THREE DIMENSIONAL FINITE ELEMENT ABLATIVE THERMAL RESPONSE ANALYSIS APPLIED TO HEATSHIELD PENETRATION DESIGN

A Dissertation
Presented to
The Academic Faculty of the School of Aerospace Engineering

by

John A. Dec

In Partial Fulfillment
of the Requirements for the Degree
Doctor of Philosophy in the
School of Aerospace Engineering

Georgia Institute of Technology
May 2010

THREE DIMENSIONAL FINITE ELEMENT ABLATIVE THERMAL RESPONSE ANALYSIS APPLIED TO HEATSHIELD PENETRATION DESIGN

Approved by:

Dr. Robert D. Braun, Advisor
School of Aerospace Engineering
Georgia Institute of Technology

Dr. Stephen M. Ruffin
School of Aerospace Engineering
Georgia Institute of Technology

Dr. Vitali Volovoi
School of Aerospace Engineering
Georgia Institute of Technology

Dr. David M. Schuster
NASA Engineering and Safety Center
NASA Langley Research Center

Mr. Bernard Laub
Thermal Protection Materials and Systems Branch
NASA Ames Research Center

Date Approved: March 29th, 2010

ACKNOWLEDGEMENTS

I consider myself fortunate to have had the opportunity to learn from and collaborate with Dr. Robert Braun during the course of this research. Dr. Braun's passion and insight into space systems design was inspirational and provided the impetus for me to push the boundaries of what I thought I could accomplish with this research. I am also thankful for membership in Dr Braun's Space Systems Design Laboratory. Since I was a distance learning student, I didn't spend as much time in the Lab as I would have liked, however, the time that I did spend there was very well spent. The Lab is filled with top-caliber graduate students and is clearly the premier space systems design laboratory in the country.

I would not have gotten to this point without the help of Dr. Jerry Seitzman. I will most likely never be able to repay Dr. Seitzman for his help in preparing for the PhD qualifying exam, but nonetheless I am very grateful for him teaching me how to "think like a PhD". I am also grateful for Dr. Seitzman putting me in touch with Dr. Paul Danehy at NASA Langley Research Center. Paul was my qual tutor while I was at home at Langley. Without Paul's help I definitely would not be writing this acknowledgment.

I am thankful for having had the opportunity to serve as the Orion Crew Exploration Vehicle's heatshield compression pad lead as part of the Thermal Protection System Advanced Development Program (TPS ADP). The compression pad subsystem provided the motivation for this research and I'd like to thank Dr. James Reuther and Dr. Ethiraj Venkatapathy of NASA Ames Research Center for having the confidence in me to lead the compression pad subsystem design effort through the programs subsystem design review while pursuing this research simultaneously.

I must also take this opportunity to thank the developers of the finite element library libMesh. Dr. Benjamin S. Kirk from NASA Lyndon B. Johnson Space Center, Dr. John

W. Peterson, and Dr. Roy H. Stogner from the University of Texas at Austin, Mr. Steffen Petersen from Hamburg University of Technology, and Mr. Derek Gaston from Sandia National Laboratories. Their finite element library saved me countless hours having to reinvent the wheel. Their work truly made the three-dimensional version of my code possible.

I'd also like to thank Mr. Bernie Laub for teaching me the "black art" that is ablative thermal response analysis. I would also like to thank the late Dr. Robert Mitcheltree for showing me the ropes on my first project at NASA and teaching me about the benefits of probabilistic design. The mentoring both Bob and Bernie provided during the early part of my NASA career stimulated my interest in this area of research and pushed me to always go the extra mile.

TABLE OF CONTENTS

LIST OF TABLES

LIST OF FIGURES

LIST OF SYMBOLS AND ABBREVIATIONS

Acronyms

ACE	Aerotherm Chemical Equilibrium Program
ADP	Advanced Development Project
CEV	Crew Exploration Vehicle
CFD	Computational Fluid Dynamics
CMA	Charring Material Thermal Response and Ablation Program
DOE	Design of Experiments
DOF	Degree of Freedom
FIAT	Fully Implicit Ablation and Thermal Response Program
MPICH2	Message Passing Interface Chameleon
OML	Outer Mold Line
PETSc	Portable, Extensible Toolkit for Scientific computation
SRC	Sample Return Capsule
FEAR	Thermal Response and Ablative Thermal Protection System Design
R&R	Retention and Release
TPS	Thermal Protection System

Symbols

A	area, m^2
B_i	pre-exponential factor for the i^{th} resin component
B'_c	non-dimensional charring rate
B'_g	non-dimensional pyrolysis gas rate at the surface
B'_{fail}	non-dimensional pyrolysis gas rate at the surface
B'_{inj}	total non-dimensional mass injected into the boundary layer
B'	total non-dimensional blowing rate
C	Capacitance matrix
C_H	Stanton number for heat transfer
C_M	Stanton number for mass transfer
c_p	solid material specific heat, J/kg-K
c_{p_g}	pyrolysis gas specific heat, J/kg-K
c_{p_v}	virgin material specific heat, J/kg-K
c_{p_c}	charred material specific heat, J/kg-K
E_{ai}	activation energy for the i^{th} resin component, Btu/lb-mole
f_{ij}	view factor to surroundings
H_r	recovery enthalpy, J/kg
H_c	total enthalpy of the virgin material, J/kg
H_v	total enthalpy of the charred material, J/kg
H_w	wall enthalpy, J/kg
$H_{air}^{T_w}$	enthalpy of air evaluated at the wall temperature, J/kg

H_g	pyrolysis gas enthalpy, J/kg
h_v^0	enthalpy of formation of the virgin material, J/kg
h_c^0	enthalpy of formation of the charred material, J/kg
h_i^0	enthalpy of formation of species i, J/kg
h_{ref}	reference enthalpy at 298K, J/kg
h_g	enthalpy of pyrolysis gas, J/kg
h_c	enthalpy of char, J/kg
h_w	enthalpy of the boundary layer edge gas evaluated at the wall temperature, J/kg
$\overline{h}$	weighted average solid enthalpy, J/kg
h	enthalpy of the solid, J/kg
i	node index, resin component index (A,B,C)
j_i	diffusional mass flux of species i, kg/m^2-s
j_{iw}	diffusional mass flux of species i at the wall, kg/m^2-s
J_i	total diffusional mass flux of species i, kg/m^2-s
k	thermal conductivity, W/m-K
K_c	Conductivity Matrix
$K_{\dot{s}}$	Convection Matrix
$\dot{m}$	mass flow rate of pyrolysis gas, kg/s
$\dot{m}_g''$	mass flux of pyrolysis gas, kg/m^2-s
$\dot{m}_c''$	mass flux of char, kg/m^2-s
$\dot{m}''^*$	mass flux due to melting and/or mechanical removal, kg/m^2-s
$\dot{m}_{inj}''$	total mass flux injected into the boundary layer, $\dot{m}_g'' + \dot{m}_c'' - \dot{m}''^*$
N	interpolation function
q	source term in the general heat equation
q^*	condensed phase energy removal, W/m^2
q_{rad}	stagnation point radiative heat flux, W/m^2
q_{conv}	stagnation point convective heat flux, W/m^2
q_{cond}	conductive heat flux, W/m^2
$\dot{q}_{cw}$	cold wall heat flux, W/m^2
$\dot{q}_{hw}$	hot wall heat flux, W/m^2
Q^*	thermochemical heat of ablation, J/kg
R	universal gas constant, J/kg-mole-°K
$\boldsymbol{R}$	load vector
$\dot{s}$	recession rate, m/s
ss	steady state
T	temperature, °C
T_w	wall temperature, °C
T_0	initial temperature, °C
T_s	surface temperature, K
T_{surr}	surrounding temperature, K
t	time, sec

U_e	boundary layer edge gas velocity, m/s
x	distance measured from the original surface of the ablating material, m
x_S	distance measured from the moving surface of the ablating material, m
Z^*_{ie}	diffusion driving potential at the boundary layer edge
Z^*_{iw}	diffusion driving potential at the wall
(e)	parameter defined only over one element
α	solar absorptivity, or thermal diffusivity
ε	emissivity
η	transpiration coefficient
ΔH_v	enthalpy of vaporization, J/kg
ΔH	enthalpy difference, J/kg
ΔH_d	heat of decomposition, J/kg
ΔT	temperature difference, °C
Γ	resin volume fraction
λ	blowing rate correlation parameter, 0.5 laminar, 0.4 turbulent
χ_v	volume fraction of virgin material
χ_i	mole fraction of species i
χ_j	mole fraction of species j
K_i	mass fraction of species i,
$\mathscr{D}_{ij}$	diffusion coefficient for species i into species j
$\mathscr{D}_{12}$	binary diffusion coefficient
$\mathscr{M}_i$	molecular weight of species i
ρ_A	density of first resin component, kg/m^3
ρ_B	density of second resin component, kg/m^3
ρ_C	density of fiber reinforcement, kg/m^3
ρ_r	residual density, kg/m^3
ρ	solid material density, instantaneous density, kg/m^3
ρ_o	initial density, kg/m^3
ρ_s	solid material density, kg/m^3
ρ_e	boundary layer edge gas density, kg/m^3
ρ_v	density of pure virgin material, kg/m^3
ρ_c	density of pure char material, kg/m^3
ρ_{resin}	density of resin component, kg/m^3
ρ_{fiber}	density of fiber reinforcement, kg/m^3
$(\rho u)_w$	total mass flux entering the boundary layer, kg/m^2-s
σ	Stephan-Boltzman constant, W/m^2-K^4
ψ_i	density exponent factor eq. (2.7) , or species source term eq. (2.48)
ϕ	transpiration correction factor
μ_1	quantity defined to simplify species conservation equation
μ_2	quantity defined to simplify species conservation equation
μ_3	quantity defined to simplify species conservation equation
$''$	denotes flux quantity, 1/m^2

SUMMARY

Heatshield design and analysis has traditionally been a decoupled process, the designer creates the geometry generally without knowledge about how the design variables affect the thermostructural response or how the system will perform under off nominal conditions. Heatshield thermal and structural response analyses are generally performed as separate tasks where the analysts size their respective components and feedback their results to the designer who is left to interpret them. The analysts are generally unable to provide guidance in terms of how the design variables can be modified to meet geometric constraints and not exceed the thermal or structural design specifications. In general, the thermal response analysis of ablative thermal protection systems has traditionally been performed using a one-dimensional finite difference calculation. The structural analyses are generally one, two, or three-dimensional finite element calculations.

In this dissertation, the governing differential equations for ablative thermal response are solved in three-dimensions using the finite element method. Darcy' Law is used to model the flow of pyrolysis gas through the ablative material. The three-dimensional governing differential equations for Darcy flow are solved using the finite element method as well. Additionally, the equations for linear elasticity are solved by the finite element method for the thermal stress using temperatures directly from the thermal response calculations.

This dissertation also links the analysis of thermal protection systems to their design. The link to design comes from understanding the variation in the thermostructural response over the range of the design variables. Material property sensitivities are performed and an optimum design is determined based on a deterministic analysis minimizing the design specification of bondline temperature subject to appropriate

constraints. A Monte Carlo simulation is performed on the optimum design to determine the probability of exceeding the design specifications. The design methodology is demonstrated on the Orion Crew Exploration Vehicle's compression pad design.

CHAPTER 1

INTRODUCTION

1.1 Robust Heatshield Design

The classical definition of a robust design is a design capable of performing its function without failure over a wide range of conditions. In terms of a spacecraft's heatshield, or, thermal protection system (TPS), a robust design is one which will survive entry even though the entry environment encountered during flight, and or its structural and thermal response to that environment, may be significantly different than that predicted in its design. The need for a robust design, or design for uncertainty, stems from the fact that during the design process, analytic predictions of the entry heating, aerodynamics, and trajectory, have uncertainties associated with them. There are also uncertainties in being able to accurately predict a TPS material's thermal response to its environment. Typically, thickness margin is added to a heatshield to account for the uncertainties in predicting its environment and material response. Thickness margin is the flight heatshield thickness minus the minimum required heatshield thickness derived from calculation; in other words, it is extra thickness above and beyond what was calculated during the design process.

TPS margin is usually calculated in one of two ways [1]. The first is a stacked worst case scenario, where all pertinent environment and material property variables are set to their worst case values and the heatshield is sized to the required bondline temperature limit. The second is a lumped uncertainties root-sum-square (RSS) approach. For this method, the uncertainties in the environment are typically lumped together and a required thickness margin is computed assuming no uncertainty in the material response to that environment. Lumping the environmental uncertainties means the trajectory dispersions, convective heat flux, and radiative heat flux uncertainties are combined as one factor

which gets applied to the input convective heat flux. Next, the required thickness margin to cover uncertainty in the material's properties to the nominal environment is computed. The RSS of these two independent margins is then defined as the required thickness margin. Additional margin due to uncertainties in surface recession, manufacturing tolerance and factor of safety may then also be added on top of that RSS value to define the final TPS thickness.

Keeping the TPS mass a minimum is always a goal for entry vehicle design, since it essentially trades against payload mass. Minimizing mass and arriving at a robust TPS design are often at odds. One of the reasons for this is the classic approach for increasing system robustness that relies on increasing thickness margin to improve robustness. While this has proven a successful design philosophy in the past, the end result is a heavier heatshield that may be over designed. Adding thickness without proper quantification gives no insight into the system reliability, and only mitigates a small portion of the possible failure modes.

While conservative and proven successful in the past, this approach provides no quantification for the amount of margin applied and says nothing about the probability the system will fail, i.e. is the system robust. Table 1 lists some recent Mars and Earth entry vehicle flight TPS thicknesses and the associated margin applied [2, 3, 4, 5, 41].

Table 1.1: Past entry vehicle flight TPS thickness and margin

Mission	TPS system	TPS thickness (cm)	Margin (%)
Stardust	PICA	5.82	21*
Mars Exploration Rover	SLA	1.57	41
Mars Pathfinder	SLA	1.91	87

Currently, there is a research effort underway to statistically quantify the input uncertainties that go into the design and analysis of TPS and to perform a probabilistic

* Relatively low since the flight thickness calculation already included the uncertainties in the aerothermal environment

analysis to size the heatshield thickness and determine the appropriate margin. [1,6,7]. For a blunt nose sphere cone entry vehicle, the simplest heatshield design would be one that was small, made of a monolithic material, and was attached to its parent spacecraft, or launch vehicle through its backshell. This type of design is generally indicative of past planetary mission entry vehicles. Figure 1.1 shows a schematic of a typical blunt nose entry vehicle.

As our desire to land larger, more advanced payloads grows, so must the size and complexity of the entry vehicle. As the size of the vehicle grows, having a monolithic TPS becomes less viable due to difficulties in manufacturing a single continuous piece of heatshield material. This implies that an advanced TPS may be constructed from blocks of material and therefore will have seams and gaps. Moreover, as the size of the vehicle grows, it becomes less efficient, from a structural and mass standpoint, to structurally attach the entry vehicle to the launch vehicle, or parent spacecraft, through the backshell. The forebody structure must be designed to carry loads associated with atmospheric entry and becomes a large fraction of the total vehicle mass for large aeroshells. If the launch vehicle were attached to the aft of the entry vehicle, then the

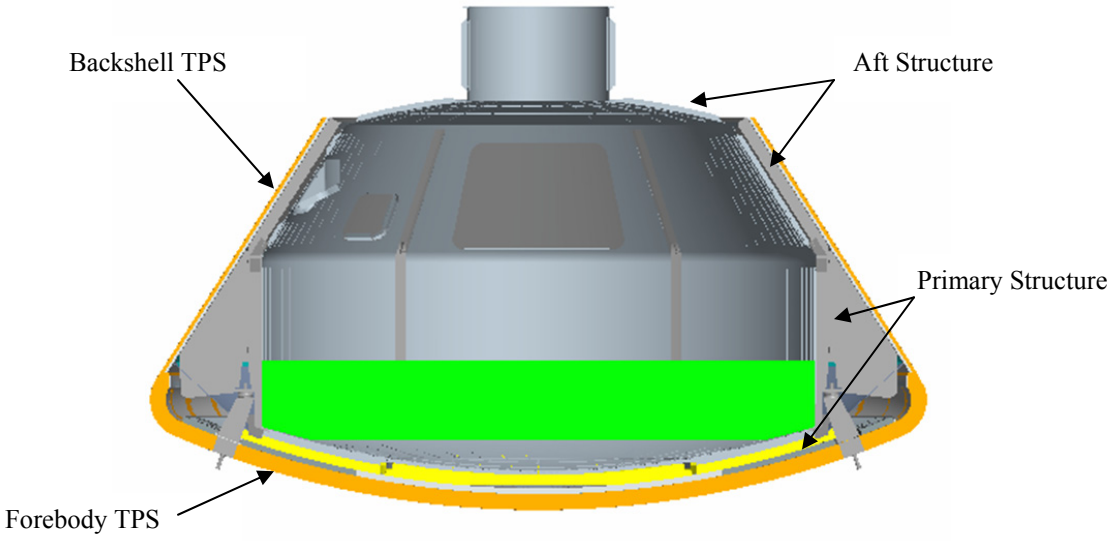

Figure 1.1: Common components of a blunt nose entry vehicle

vehicle's aft structure would need to be sized to accommodate the launch loads, thereby, increasing total mass. In order to minimize the structural mass, the most efficient method of transferring the launch loads would be to penetrate the forebody TPS and attach the parent spacecraft or launch vehicle to the entry vehicle primary structure. These penetrations are reinforced hard points on the forebody TPS usually consisting of a compression pad which is inserted into the acreage TPS and a tension tie rod that passes through the TPS or the compression pad and connects directly to the vehicle structure [8, 9]. Figure 1.2 shows a generic, simplified concept for a forebody TPS penetration. The compression pad, tension tie, and close out material make up the heatshield penetration sub-system.

Current research efforts to develop a probabilistic design methodology for the thermal protection system do not address singularities in the heatshield such as gaps, seams, joints and penetrations. A robust design philosophy must also be followed for these heatshield singularities in order to accurately quantify the required margin of the system as a whole.

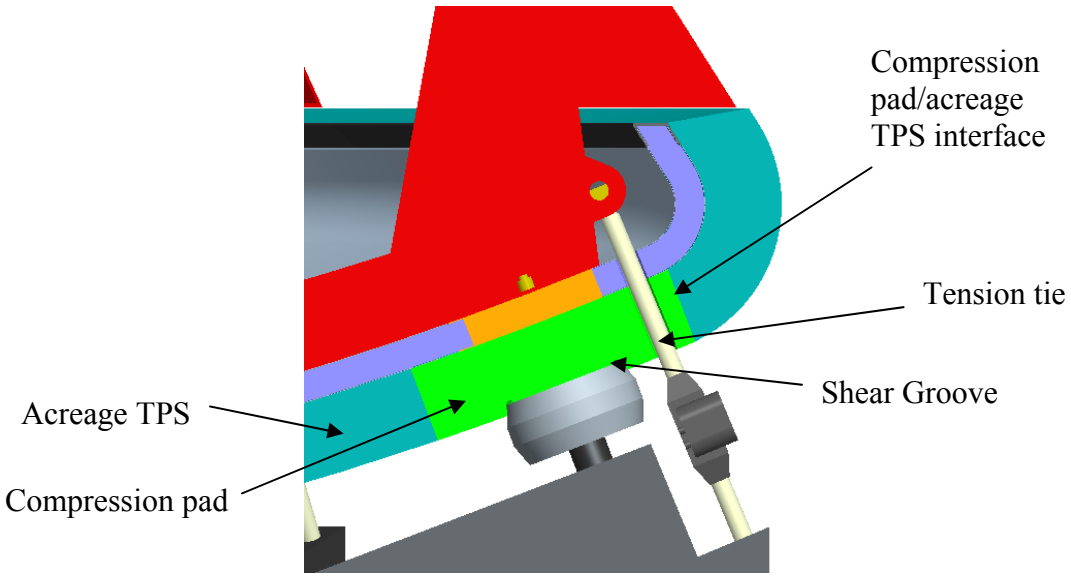

Figure 1.2: Generic heatshield penetration concept

In the case of the penetrations, the compression pad must be strong enough to carry the launch loads as well as survive reentry, which may also mean that it is constructed from a higher density material than the surrounding acreage TPS. If both the acreage

TPS and compression pads are ablative materials, the higher density material may be less susceptible to surface recession than the lower density material. This could result in surface geometric discontinuities during flight. In the region of the compression pad, there exists the potential for heating augmentation due to the disturbance in flow caused by the change in geometry. Also, due to assembly requirements, the compression pad may be set within a cavity with respect to the acreage TPS. Figure 1.3 shows the heating augmentation effect on a scale model of the Orion Crew Exploration Vehicle (CEV) which was tested in NASA Langley's Mach 6 tunnel [10]. The portions on the surface of the model that are green represent regions where no augmentation to the heating is occurring. The parts of the surface that are red and pink represent regions on the surface where heating augmentation is occurring. It is clear that significant heating augmentation is possible due to the presence of the compression pads and tension ties. This is a single

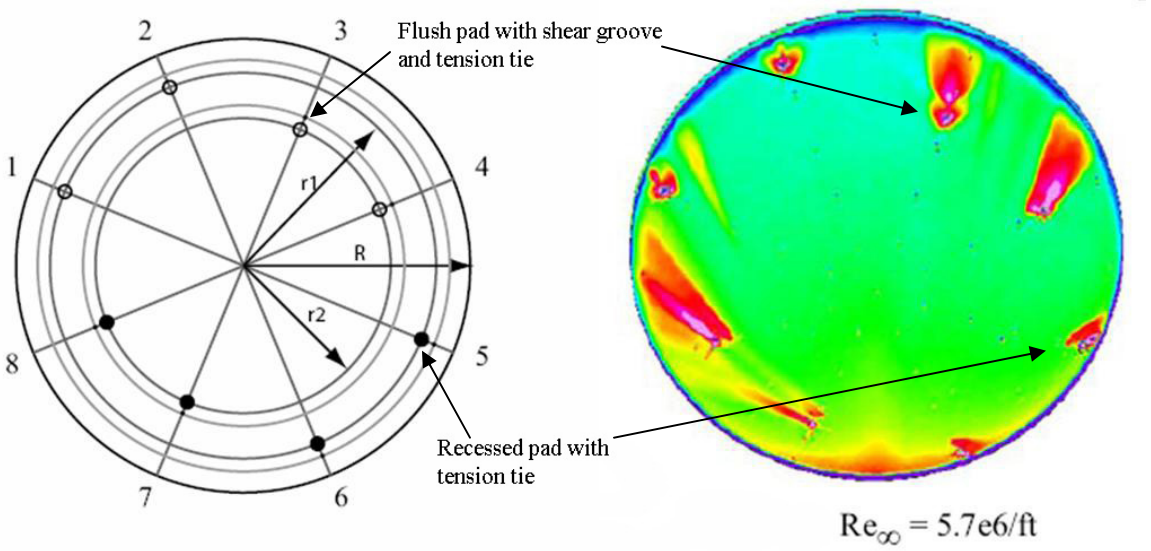

Figure 1.3: Wind tunnel heating augmentation data on the Crew Exploration Vehicle [10]

example showing that the penetrations cannot be lumped in with the acreage TPS and need an independent assessment.

Computational fluid dynamics (CFD) calculations have been performed on the CEV forebody heatshield with the detail of the heatshield compression pads added to the computational model. Results for a specific compression pad cavity depth with respect to

the heatshield outer mold line (OML) are shown in Figure 1.4 [11]. The augmented heating on the back wall of the cavity and on the acreage TPS downstream of the compression pad is apparent from Figure 1.4.

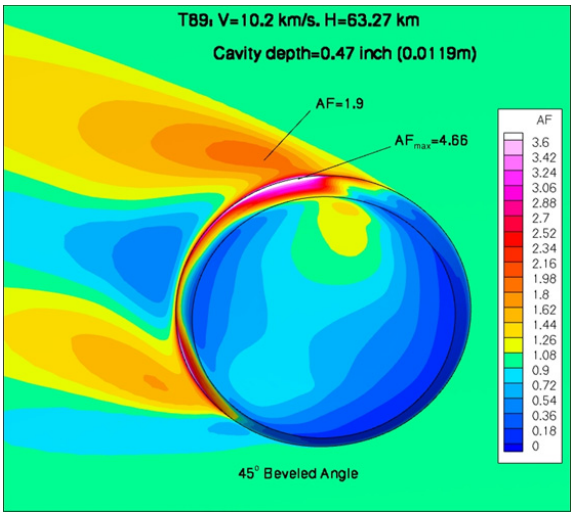

Figure 1.4: CFD calculation for heating augmentation near a CEV compression pad [11]

Figure 1.5 shows a photo of the Genesis heatshield penetration before and after arc jet testing at 460 W/cm^2. Figure 1.5 shows an increased amount of recession immediately adjacent to and downstream of the cavity. Also notice the color difference between the area downstream of the cavity and the area just below the cavity, indicating a difference in the heating levels in the two regions. These Figures (1.3, 1.4, 1.5) confirm the existence of augmented heating in the region of a forebody heatshield penetration.

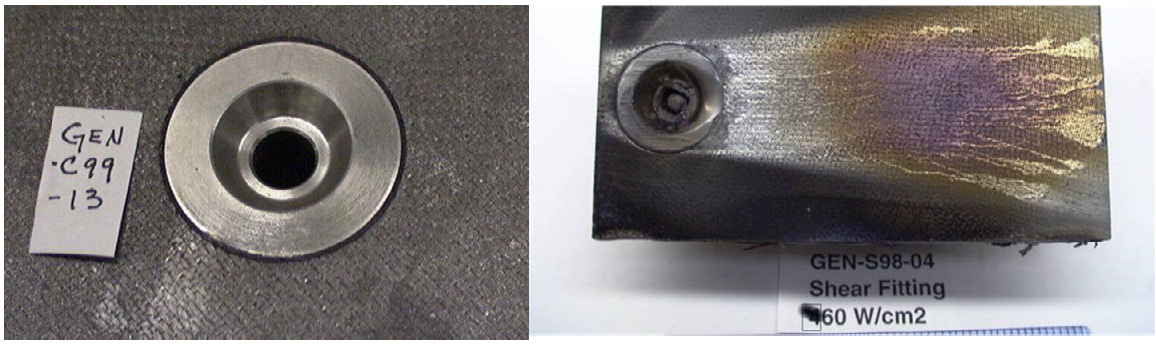

Figure 1.5: Genesis heatshield penetration pre and post arc jet testing [21]

In this dissertation, linking design uncertainty with analysis of the heatshield penetrations will be addressed; specifically, a design for uncertainty methodology will be developed.

1.2 Past Heatshield Penetration Design Concepts

To illustrate the complexity of the geometries and material combinations utilized in past forebody heatshield penetration designs, it is sensible to review the three successful past planetary entry vehicles which included them. The vehicles that have used forebody penetrations are the Apollo command module, Genesis entry capsule, and the Viking Lander aeroshell. These three vehicles utilized three different concepts for the design of their respective penetration subsystem. The three main mission parameters that drive the design of the penetration subsystem are the structural load, the peak heat flux, and total heat load encountered during flight at the penetration location. Generally speaking, these systems are typically designed using an uncoupled approach, where the thermal and structural sizing are performed independently. After the thermal and structural designs have been matured, tests are performed to verify system performance. For example, the arc jet test of the Genesis penetration with surrounding heatshield material shown in Figure 1.5, or the structural test of the Apollo compression pad with surrounding Avcoat heatshield material shown in Figure 1.6 were performed for system verification purposes [8]. In all three cases, the thermal design of the penetration system was performed using a one-dimensional analysis and or performed experimentally. Although this design philosophy has proven successful in the past; no insight was gained in terms of the robustness of the penetration system. Design and testing were performed under nominal or sometimes, worst case expected thermal and structural loads. Referring back to the definition of a robust design, the question of how these designs would perform over a range of thermal and structural loading conditions was not determined so they were not designed for uncertainty.

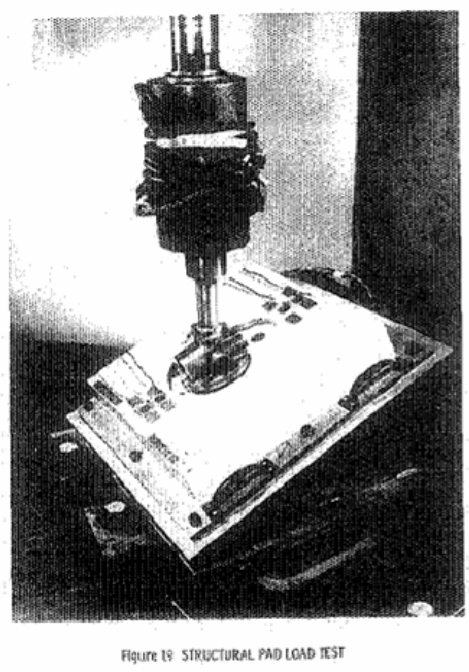

Figure 1.6: Apollo compression pad structural load test [8]

1.2.1 Apollo Heatshield Penetration Design

The Apollo heatshield design had six hard points where the command module attached to the service module. These six attachment points made up the penetration subsystem for the Apollo heatshield. As shown in Figure 1.7, the penetration subsystem consisted of six high density fiberglass phenolic compression pads with stainless steel tension ties passing through three of the pads [9]. The three pads which included the tension ties included grooves in the compression pad face to carry the shear loading. The service module had six metallic pads which served as the interface to the service module. The command module heatshield compression pads were inserted into the acreage heatshield material and bonded to the stainless steel carrier structure with RTV-560. The compression pads that included the tension ties were tear drop shaped and the tension tie passed through the section of the tear drop which had the smaller diameter. The tension tie was designed to pass through the high density ablative compression pad. The fiberglass phenolic compression pad material had a much higher strength than the

surrounding primary TPS material, Avcoat 5026. This was done to avoid placing high bearing loads on the primary ablator which could have caused damage to the acreage TPS and create gaps in the tension tie/ablator interface.

The three compression pads that only carried compressive loads were circular. Figure 1.7 shows a cross section of the Apollo compression pad with the tension tie. The

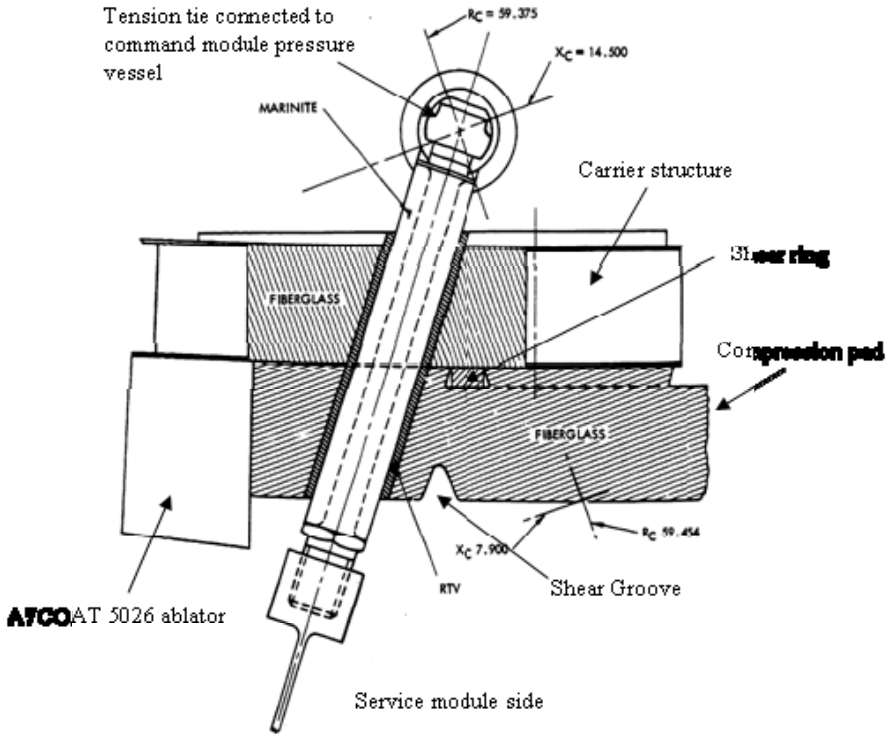

Figure 1.7: Cross section of the Apollo heatshield penetration subsystem [9]

first feature which can be seen is the groove cut into the face of the compression pad, this groove was the called the "shear groove" and was the primary means of transferring the shear load from the service module to the command module. The second feature of the design is that a Marinite insulating sleeve was placed around the tension tie in order to insulate the stainless steel carrier structure from the high temperatures surrounding it. Another feature shown is a Marinite block, labeled as fiberglass in Figure 1.7, which was placed inside the carrier structure replacing the stainless steel honeycomb in that location. Marinite is a trade name for a type of fiberglass manufactured by BNZ Materials, Inc

[12]. The Marinite block was necessary since the honeycomb was incapable of carrying the shear loads placed on it by the compression pad. Shear was transferred to the Marinite insert by way of a stainless steel ring which was embedded into the backside of the compression pad.

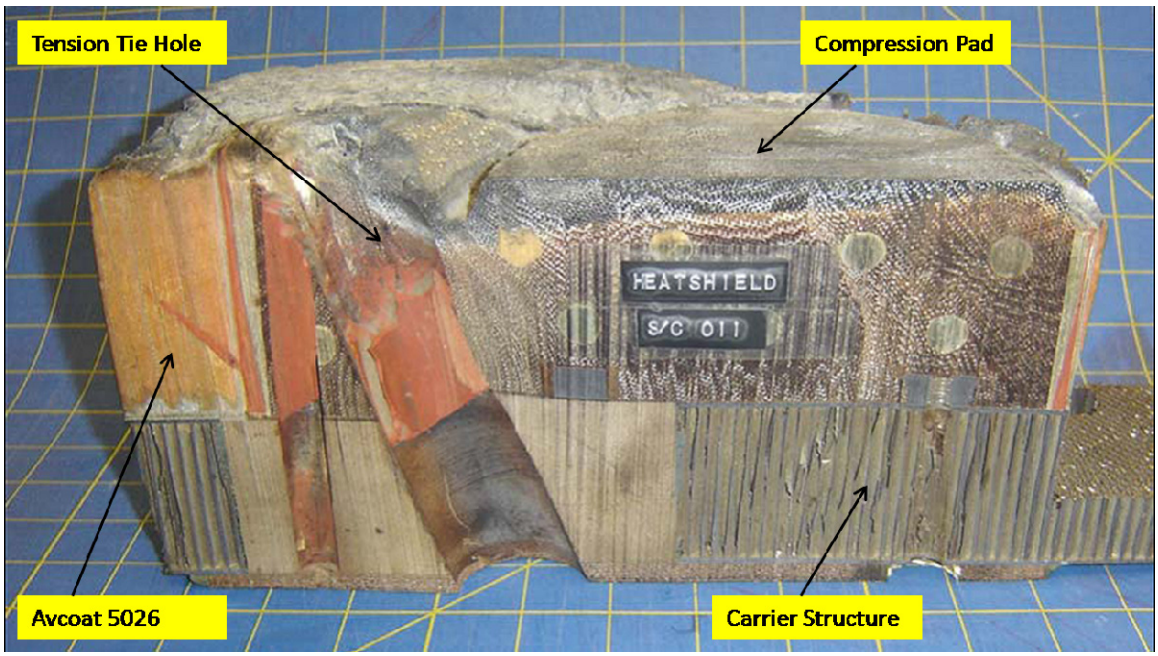

Figure 1.8: Cross section of the Apollo compression pad [13]

One design feature not shown in Figure 1.7 is the manner in which the compression pad was constructed. Figure 1.8 gives some insight into the compression pad construction [13]. The compression pad was made from several laminated fiberglass plates which were cut into the proper size and shape, then were pinned and bonded together with fiberglass rods. The entire perimeter of this assembly was then wrapped with a single layer of the same fiberglass fabric and bonded to the pads exterior with RTV-560.

The last feature of the design visible in Figure 1.7 is the fact that the compression pad is initially recessed into the acreage TPS material. Initially, the required thickness of the compression pads was determined to be more than that required for the acreage

AVOCAT 5026 in the same region [14]. The block I design, which was meant only to enter the Earth's atmosphere from low Earth orbit, included compression pads that protruded above the outer mold line of acreage TPS. The tension tie bolt also protruded above the acreage TPS, but was expected to melt flush with the acreage ablator soon after entry and not cause any problems. During the block II lunar design period, the heating augmentation in the compression pad region as well as other protuberances were studied

Figure 1.9: Apollo 4 command module recovery after entry from low Earth orbit [17]

extensively [15,16,17,18]. Figure 1.9 shows the effects of heating augmentation in the regions near the heatshield singularities. The vehicle shown in Figure 1.9 was recovered in 1966 and was one of the early Apollo flight test vehicles. This vehicle was a block I design with protruding compression pads that entered the Earth's atmosphere from low Earth orbit [17]. The effects of heating augmentation can clearly be seen near two of the compression pads.

The presence of heating augmentation causes difficulties when attempting to design both the acreage TPS and compression pads. The difficulty is that predicting heating augmentation is complex and has much uncertainty associated with it. Increased local heating can increase the bondline temperature or cause excessive recession in those

local areas. Typically there are two ways to quantify the heating augmentation, through testing and through CFD. In modern times, both of these methods are used. In the days of Apollo, engineers had to rely solely on test data. For Apollo, tests were performed either in high speed wind tunnels or in flight. In both cases the heating augmentation was assessed relative to the baseline. Conclusions were then made about the level of augmentation present and the relationship to the flight environment. Based on these results, heating augmentation "bump" factors were applied to the baseline heating.

There is uncertainty in the test measurement itself, but this is usually included in the estimate of the heating bump factors. However, the test data is generally not at flight conditions since there are no ground facilities available that can duplicate the combined heat rate, pressure, shear, and enthalpy environment of an 11 km/s entry. As mentioned above, the data must be extrapolated to the flight conditions, and thus another source of uncertainty is introduced.

As a result of the Apollo ground test and flight tests [15, 16, 17, 18], the design approach for the block II Apollo heatshield was changed to disallow any protruding singularities. In the final block II Apollo heatshield design, all special elements of the heatshield, like the compression pads were designed as either slightly recessed, or flush with the surrounding TPS. The compression pads were thus slightly recessed as shown in Figure 1.7.

All of these design features were intended to prevent a heatshield failure near the penetration region. The question of how these design features contributed to the robustness of the design and how well it could accommodate the uncertainties were not directly addressed. These questions were left unanswered in the Apollo program.

1.2.2 Viking Heatshield Penetration Design

The design of the Viking heatshield penetration subsystem was significantly different than that of Apollo. The penetration subsystem on Viking was not its own unique entity,

it was included as part of two different subsystems. The penetrations were actually pyrotechnically initiated separation nuts and were part of the pyrotechnic devices and mechanical devices subsystems.

Detailed information on the Viking penetration design is scarce and it has been stated by several of the former Viking engineers and program mangers that it was the least documented part of the design [19]. Be that as it may, Figure 1.10 shows the pyrotechnic separation nuts that were used in several locations on the Viking spacecraft, including the three aeroshell penetrations [20]. As described in [20], the separation nut had a threaded steel collet on the inside, slit nearly through, lengthwise, in four places. The nut was powered by two gas generation cartridges called Viking standard initiators, or VSI's. The closed end of the nut body was equipped with two ports by which the VSI's connected. Between the end of the collet and the blank end of the body was a piston, sealed against the body by sealing rings. Surrounding the entire assembly was a base by

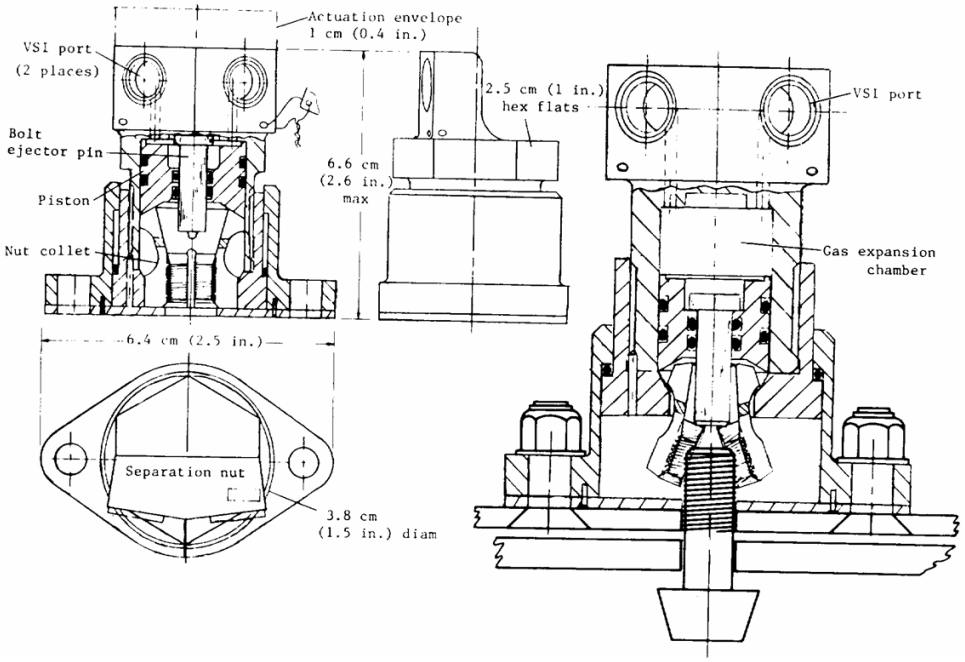

Figure 1.10: Viking aeroshell separation nut

which the separation unit could be secured to the structure of the vehicle. When the load bearing bolt was installed in the nut, the bolt engaged the internal threads in the collet.

When the power cartridges were fired, the resulting gas pressurized the space between the closed end of the body and the piston. Since the piston could not move, the body moved and disengaged the ring from the collet. At the end of the body stroke, the threaded portions of the segments pedaled outward and disengaged the bolts. The bolt size for the aeroshell separation nut was 5/16". Not shown in the figure is a push off spring used to impart a separation velocity between the lander capsule and orbiter. In the Viking literature surveyed, no mention of the impact to the forebody heating due to the presence of the penetrations could be found as well as the impact on the overall heatshield performance. Moreover, as in Apollo, the questions of uncertainty and robustness were not directly addressed.

1.2.3 Genesis Heatshield Penetration Design

The Genesis design for the compression pad, which Lockheed Martin called the sample return capsule (SRC) retention and release (R&R) mechanism, is a more complex system than both Apollo and the Viking designs. This design has both advantages and disadvantages. Genesis had three fittings equally spaced around the forebody of the sample return capsule as shown in Figure 1.11, where the third fitting is hidden behind the capsule.

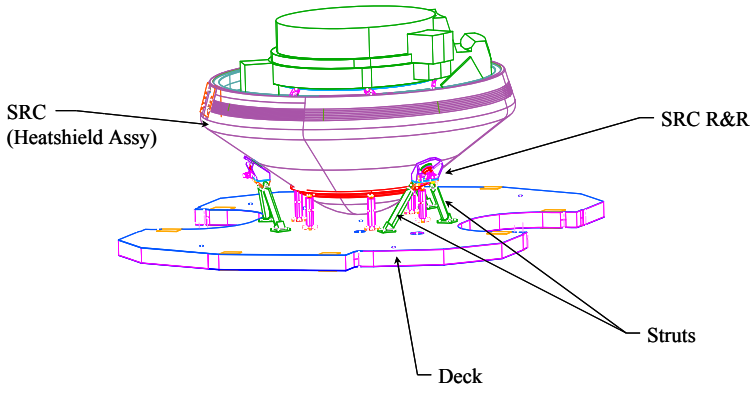

Figure 1.11: Genesis sample return capsule [21]

The most significant difference is the addition of a retracting separation bolt and its associated hardware. Figure 1.12 shows a cross section of the Genesis SRC R&R mechanism [21]. The Genesis system consists of five main components, a thick Carbon Carbon facesheet, a Molybdenum fitting, a separation bolt, a Titanium filler block, and a bolt catcher. The compression pad is preloaded to 8,500 lbs to prevent the sample return capsule from separating from the spacecraft during launch. The Molybdenum fitting carries the compressive preload, the shear and additional compression load developed during launch. The shear load is transferred from the Molybdenum shear fitting to the reinforced thickened carbon-carbon. The Genesis heatshield was constructed from a thin layer of carbon-carbon on top of a carbon based insulation called Fiberform. The major advantage of the Genesis compression pad is that the thickened carbon-carbon is made of the same material as the main heatshield. As such, the compression pad and heatshield will generally recede at the same rate during entry, reducing the likelihood of a discontinuity and potential heating augmentation failure mode. The major disadvantage

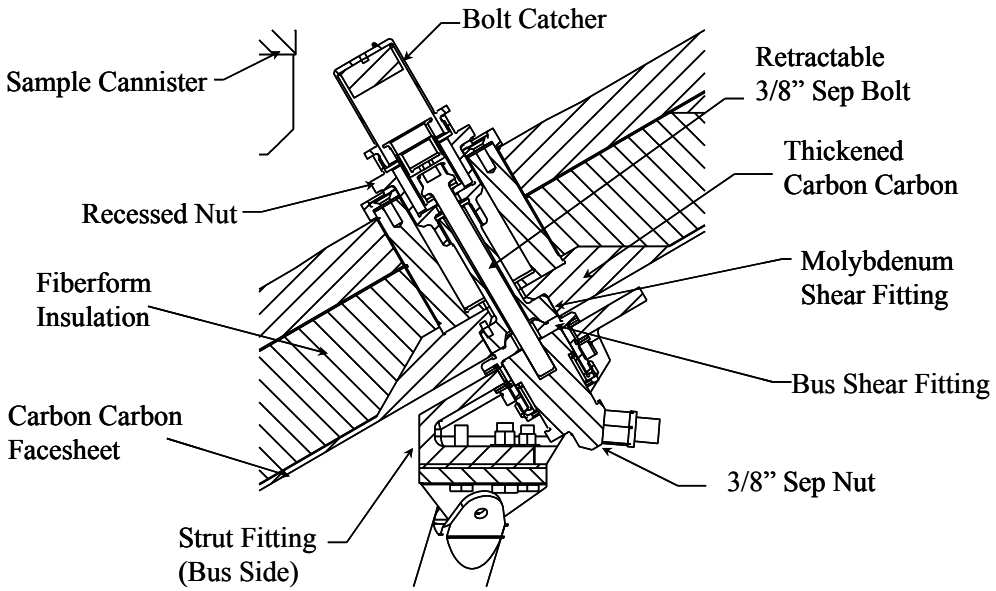

Figure 1.12: Genesis compression pad design [21]

of this approach is the metallic Molybdenum fitting which passes through the entire mechanism and provides a direct thermal path through the heatshield. Fortunately, the heat pulse for the Genesis trajectory was of short duration with a relatively low total heat load, so this design did not experience any thermal soak issues during entry. Although the Genesis design performed as intended, the robustness of the design, in particular the un-insulated Molybdenum fitting, had it encountered any significant off nominal conditions, comes into question.

As shown in Figure 1.5, the Genesis project tested the combined design of the penetration and surrounding TPS to verify the performance of this system. CFD was also performed to determine the aerodynamic heating on the capsule and the increased heating near the penetrations [22]. The arc jet test was run under controlled conditions with regard to the environmental test parameters in the NASA Ames Interactive Heating Facility using a wedge model at a heat flux of 460 W/cm^2. Even though the arc jet test was a success and the CFD proved to be helpful, the project did not directly address the question as to how the system would perform under the range of potential environmental conditions.

Arc jet testing alone cannot demonstrate a design is robust unless multiple tests are run under varying conditions. Arc jet testing models of this type becomes cost prohibitive from a model construction standpoint. In addition, because of the complexity of the penetration geometry, a typical arc jet "iso-Q" coupon will not suffice. The environmental conditions which can be simulated in the facility are also limited. Clearly some analytical means, in addition to testing, is necessary to assess robustness of a penetration system.

1.3 Thermal Protection System Design and Analysis

There are two types of thermal protection systems in use today, reusable and ablative. Use of reusable TPS, like the space shuttle tiles or a metallic heat sink, is generally

limited to low heat flux entry trajectories [23, 24]. Ablative TPS on the other hand can withstand large heat fluxes and heat loads and are generally used for vehicles which have a high entry velocity. In addition to high entry velocity, ablative TPS are also well suited where the target planet has a high atmospheric density such as Jupiter [25] since the heat rate is proportional to the density.

Ablative materials have been in use since the 1950's where they were primarily applied to the design and construction of ballistic missile nose cones. The success ablators demonstrated in re-entry applications made them attractive for use in rocket nozzle applications [26]. In general, the analysis of an ablative material's thermal response requires the solution of a differential energy transport equation [27]. In one dimension, and neglecting pyrolysis gas flow, the form of this differential equation is given by (1.1) along with an associated decomposition or charring relation given by (1.2).

$$\frac{\partial}{\partial x}\left(k\frac{\partial T}{\partial x}\right) - \rho c_p \frac{\partial T}{\partial t} + q\frac{\partial \rho}{\partial t} = 0 \tag{1.1}$$

$$\frac{\partial \rho}{\partial t} = f(\rho, T) \tag{1.2}$$

The terms of equation (1.1) have a direct physical interpretation. From left to right, the first term of (1.1) represents the energy which is conducted into the solid, the second is the amount of energy stored within the solid, and the third is the heat absorbed by the decomposition of the solid. This coupled pair of differential equations in general defies analytic solution and requires an approximate numerical solution. Koo, at el., [28] conducted a review of numerical techniques which endeavor to solve (1.1) and (1.2) for rocket nozzle and entry vehicle applications using ablative materials. The majority of work listed in ref. [28] focuses on rocket nozzle applications and their specific issues. References [26, 29, 30, 31, 32, 33, 34, 35, 36, 37, 38, 39, 84, 88, 89, 90, 91, 92, 93, 94, 95, 96] represent some of the approaches taken during the 1950's and 1960's to solve the

ablation problem for reentry heatshield and rocket nozzle applications, where reference [84] provides an extensive bibliography.

The early analysis attempts of the 1950's and early 60's at solving the thermochemical ablation problem presented in general by 1.1 and 1.2 involved coupling a simple one-dimensional heat conduction calculation with no decomposition or pyrolysis gas flow with the heat of ablation to predict surface recession [26, 34, 87, 91]. The heat of ablation, or Q^*, as it is denoted in the literature, is often incorrectly used as a material property, when in fact it is a data correlation parameter valid only during steady state ablation. For these early formulations, the 1-D heat equation for the in-depth temperatures was given by,

$$\rho c_p \frac{\partial T}{\partial t} = \frac{\partial}{\partial x}\left(k \frac{\partial T}{\partial x} \right) \tag{1.3}$$

Along with (1.3), researchers developed boundary conditions at the surface by forming an energy balance equation which described phenomenon that they knew about. The surface energy balance they developed was based on the ablation performance and the observations made during arc jet tests of Teflon and are given as,

$$-k \frac{\partial T}{\partial x} = -\dot{q}_{cw} \left(\frac{H_r - H_{air}^{T_w}}{H_r} \right) + \sigma \varepsilon T_w^4 + \rho \dot{s} \Delta H_v + \rho \dot{s} \eta \left(H_r - H_{air}^{T_w} \right) \tag{1.4}$$

The left hand side of (1.4) is the net conductive heat flux from the surface and provides the link to the in-depth energy equation (1.1). The first term on the right hand side of (1.4) represents the net convective heat flux into the surface in the absence of ablation, the second term is the net radiative heat flux away from the surface, the third represents the energy absorbed by material vaporization at the surface, and the last term represents the energy flux absorbed due to transpiration of the ablation products into the boundary layer. By making the approximation that the ablation is a steady state process it can be shown that the heat flux conducted into the material can be represented by,

$$k\left.\frac{\partial T}{\partial x}\right|_{ss} = \rho \dot{s} c_p (T_w - T_0) \tag{1.5}$$

Substituting (1.5) into (1.4), rearranging and grouping similar terms the surface energy equation for steady state ablation is obtained,

$$\dot{q}_{cw}\left(\frac{H_r - H_{air}^{T_w}}{H_r}\right) - \sigma\varepsilon T_w^4 = \rho \dot{s}\left(c_p \Delta T + \Delta H_v + \eta \Delta H\right) \tag{1.6}$$

If (1.6) is divided by the density and recession rate, all of the parameters on the right hand side are either known or can be measured in an arc jet test. The resulting equation defines the thermochemical heat of ablation,

$$Q^* = \frac{\dot{q}_{cw}\left(\frac{H_r - H_{air}^{T_w}}{H_r}\right) - \sigma\varepsilon T_w^4}{\rho \dot{s}} = c_p \Delta T + \Delta H_v + \eta \Delta H \tag{1.7}$$

Examination of (1.7) shows that Q^* is linear in ΔH; consequently, it was correlated to arc jet data and tabulated as a function of ΔH. Plotting the data, the slope of the resulting line was taken as η and the y-intercept was taken as $c_p\Delta T+\Delta H_v$. Since the specific heat and temperature are known or could be determined from a test, ΔH_v could also be derived from arc jet test data. Equation (1.4) could then be used as the surface energy balance coupled to a transient conduction solution with the additional constraint that the recession rate was equal to zero until a specified ablation temperature was reached. This formulation is approximate and not considered by modern standards to be high fidelity.

In 1961, Munson and Spindler [92] introduced in-depth thermal response modeling for organic resin composite materials which would decompose in-depth. Building on (1.3) and (1.6), their formulation for the in-depth conduction and their surface energy balance are given by,

$$\begin{aligned} \rho c_p \frac{\partial T}{\partial t} &= \frac{\partial}{\partial x}\left(k\frac{\partial T}{\partial x}\right) - c_{p_g}\dot{m}\frac{\partial T}{\partial x} + \Delta H_d \frac{\partial \rho}{\partial t} \\ \phi \dot{q}_{hw} - \sigma\varepsilon T_w^4 &= k\left(\frac{\partial T}{\partial x}\right)_w + \rho \dot{s}\left(f_1 \Delta H_{v_1} + f_2 \Delta H_{v_2}\right) \end{aligned} \tag{1.8}$$

Where the pyrolysis gas mass flux, decomposition rate and the transpiration correction, $\dot{m}, {}^{\partial\rho}/_{\partial t}, and\ \phi$, respectively were given by,

$$\dot{m}(x,t) = \int_{x}^{l} \frac{\partial \rho}{\partial t}(x,t)dx$$

$$\frac{\partial \rho}{\partial t}(x,t) = A\left(\rho(x,t) - \rho_r\right)^n \exp\left(\frac{-B}{T(x,t)}\right) \tag{1.9}$$

$$\phi = \exp\left(-f(1+\alpha f)\right),\ \ where\ \ f = \frac{\left(\eta_s \rho_w \dot{s} + \eta_g \dot{m}\right) h_s}{\dot{q}_{cw}}$$

A more rigorous approach introduced by Kratsch, Hearne, and McChesney [89] in 1963, modeled the decomposition as a mixture of organic resin and fiber reinforcement given as,

$$\rho_s = \Gamma \rho_{resin} + (1-\Gamma)\rho_{fiber} \tag{1.10}$$

The in-depth equation Kratsch, et. al. used was similar to that used by Munson and Spindler, but they recognized that some parameters involved complex chemical processes and should be expressed in terms of the enthalpy given by,

$$\frac{\partial(\rho_s H_s)}{\partial t} = \frac{\partial}{\partial y}\left[k\frac{\partial T}{\partial y}\right] + \frac{\partial}{\partial y}\left(\dot{m}_g H_g\right) + \frac{\partial \rho_s}{\partial t}\Delta H_d \tag{1.11}$$

Kratsch et. al. also adopted the transfer coefficient approach developed by Lees [85, 102] to approximate the heat transfer to the ablating surface from the chemically reacting boundary layer. Lees showed that the surface energy balance for an ablating material in a chemically reacting boundary layer could be written as,

$$\begin{aligned} -k\frac{dT}{dx} = \rho_e U_e C_H \left(H_{sr} - h_{sw}\right) + \rho_e U_e C_M \sum_i \left(Z_{ie}^* - Z_{iw}^*\right) h_i^0 + \dot{m}_c h_c + \dot{m}_g h_g \\ -(\rho v)_w h_w + q_{\underset{out}{rad}} - \alpha q_{\underset{in}{rad}} \end{aligned} \tag{1.12}$$

Assuming that the heat and mass transfer coefficients are equal and the Lewis and Prandtl numbers are unity, and defining non-dimensional ablation rates, the surface energy balance can be written as,

$$-k\frac{dT}{dx}=\rho_e U_e C_H\left(H_{sr}-h_{sw}+B'_c h_c+B'_g h_g-B'h_w\right)-q^*+q_{\underset{out}{rad}}-\alpha q_{\underset{in}{rad}} \tag{1.13}$$

In the mid to late 60's, Kendall, Rindal, and Bartlett [88], and Moyer and Rindal [27] extended the work by Kratsch et. al. to include unequal heat and mass transfer coefficients and non-unity Lewis and Prandtl numbers. They also included the work of Goldstein [98, 99] which characterized the decomposition of organic resin composites using a three reaction Arrhenius equation model. They also corrected the in-depth energy equation to account for the energy of the pyrolysis gas convection and generation within the solid and also corrected it to account for grid motion due to a coordinate system that is attached to the receding surface. Their form of the in-depth energy equation is,

$$\rho c_p\frac{\partial T}{\partial t}=\frac{\partial}{\partial x_S}\left(k\frac{\partial T}{\partial x_S}\right)+\left(h_g-\bar{h}\right)\left.\frac{\partial\rho}{\partial t}\right|_x+\dot{S}\rho c_p\frac{\partial T}{\partial x_S}+\dot{m}_g\frac{\partial h_g}{\partial x_S} \tag{1.14}$$

Kendall, Rindal, Moyer, and Bartlett were the primary authors of the Charring Material Thermal Response and Ablation Program (CMA) [56]. CMA has stood the test of time and is still widely used in industry, academia, and government. It is this form of the in-depth energy equation that will be derived in Chapter 2, in addition to the derivation of the surface boundary conditions. The Fully Implicit Ablation and Thermal Analysis Program, FIAT is also widely utilized throughout industry. FIAT is a finite difference procedure based on CMA where the primary difference is FIAT calculates the decomposition of the material implicitly, thereby making the solution fully implicit. The primary advantage is that the solution becomes insensitive to the time step

1.3.1 Design and Analysis Philosophy

Ablative materials returned to the forefront of heatshield development in the mid 1990's when planetary entry missions were designed with high entry velocity. Stardust, Genesis, Huygens, and the delayed Mars Sample Return missions, [40, 41, 42, 43, 44, 45, 46] are examples of vehicles with high entry velocity requiring ablative TPS. These high

entry velocities translate into heat rates that are about 2 orders of magnitude higher than what current reusable materials can withstand.

Throughout the classic literature, the most widely used technique in the solution of 1.1 and 1.2 is the finite difference technique. A few attempts were made in the early 1980's to solve 1.1 and 1.2 using the finite element technique [47, 48, 49]. However, in this time, the push for reusable TPS materials all but halted the development of new ablative materials as well as the analysis techniques specific to their use as entry heatshields. Moreover, all attempts in employing the finite element technique were related to rocket nozzle applications, their specific assumptions and challenges, and were limited to either one or two dimensional solutions. One of the main goals of the previously developed analysis techniques was to enable engineers to understand the behavior of ablative materials in the environment in which they are used. Moreover, they strove to provide engineers with the means to design a vehicle's TPS. However, the actual design and analysis remained detached.

In today's design environment where mission managers are seeking to increase the payload fraction, minimizing thermal protection system mass is crucial. However, sacrificing TPS robustness in order to achieve a minimum mass is unacceptable. This work focuses on linking the design to the analysis by developing a design for uncertainty framework. Within this framework, the robustness of an ablative penetration system is evaluated by determining the probability a design with fixed design variables exceeds its design criteria. This framework also links the analysis to design by creating design variable contour maps which satisfy each design criteria to within 99%. These maps provide the necessary link between the analysis and the designer and, or mission manager.

This framework makes use of a three-dimensional finite element analysis tool for entry vehicle heatshield and heatshield singularity design. Therefore, a more detailed

description of the current numerical analysis techniques and differences between the two most common techniques employed in solving 1.1 and 1.2 is warranted.

1.3.2 Finite Difference Techniques

Most of the analysis codes mentioned previously (e.g., CMA, FIAT) solved their respective sets of differential equations using the finite difference method. Finite difference techniques employ a point-wise approximation of the governing differential equations [50]. The finite difference model is formed by writing difference equations across an array of grid points. As the number of grid points is increased, the approximation of the original equation improves. There are a large number of engineering analysis tools that utilize the finite difference technique, since writing the difference equations to represent the governing equations of the problem is fairly straight forward. The finite difference technique is very well suited to one-dimensional problems and can be used in two-dimensional problems which have simple geometries, however, the technique loses its numerical simplicity when the problem is three-dimensional, involves complex geometry, has unusual boundary conditions, or has multiple materials in the cross sectional plane.

For a structured finite difference grid, the connections between nodes are restricted to being orthogonal with respect to one another. Two examples of a two-dimensional finite difference discretization are shown in Figure 1.13. If the solution region is the interior of the solid, restricting where the nodes can be placed within that solid introduces approximations near the boundaries as seen in Figure 1.13 (a), where a node has been placed outside the geometric boundary in order to capture more of the solution region. The other option available is to remove that node and leave a portion of the solid out of the solution region, shown in Figure 1.13 (b). This “stair stepping”, as it is commonly called, in addition to not exactly representing the geometry, makes it difficult to apply an accurate boundary condition to the curved boundary of the solid. In order to minimize

the approximations on the boundaries, a structured finite difference mesh would need to have an increased number of nodes in those areas. Increasing the number of nodes increases the computational time necessary to obtain a solution. With a structured grid, irregular boundaries can also be better approximated by using weighting parameters on the distance between adjacent nodes. For nodes on the curved boundary, the weighting parameters would be less than 1.0, for uniform grid point spacing the parameter would equal 1.0.

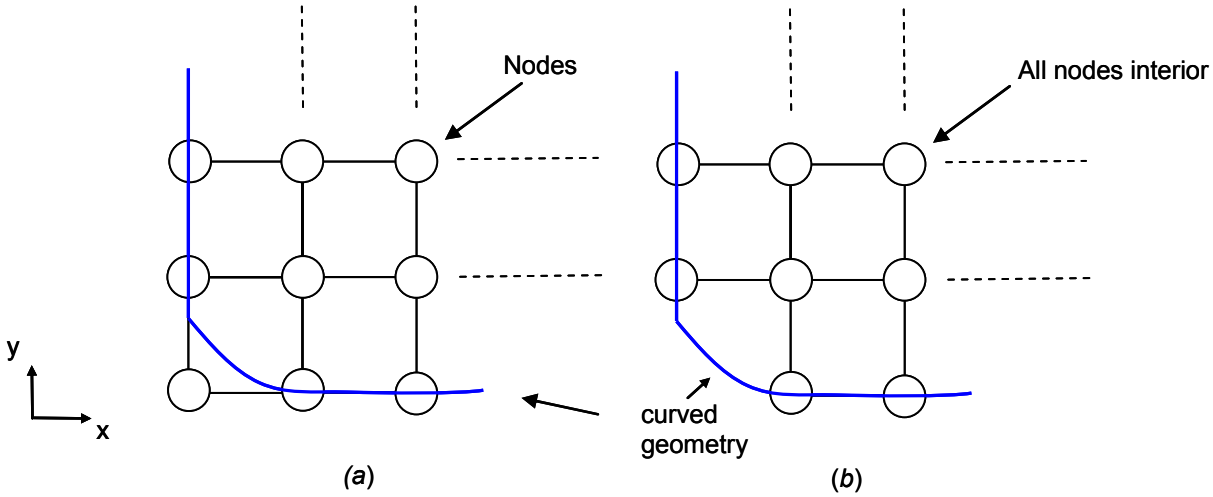

Figure 1.13: Example finite difference discretization

Another solution is to use an unstructured Cartesian finite difference grid where the nodes do not have to maintain connectivity with one another, but still must be orthogonal with adjacent nodes [51]. Figure 1.14 shows an example of an unstructured Cartesian finite difference grid. Here the curved boundary can be better approximated, but there is a disadvantage in having to define the nodal connectivity where there are cells where the nodes do not line up.

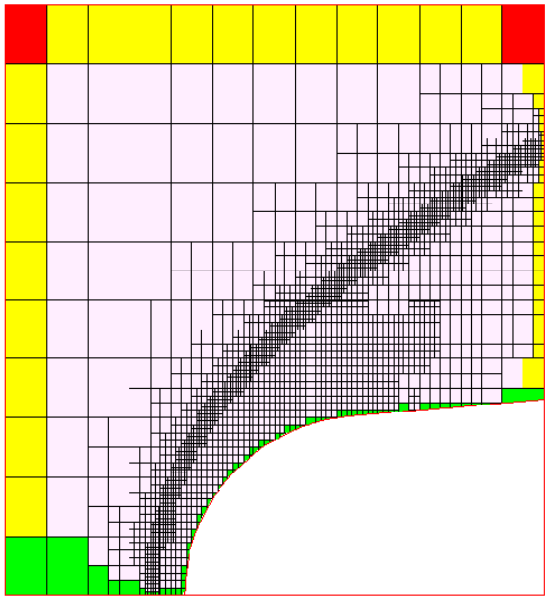

Figure 1.14: Unstructured Cartesian finite difference grid [51]

A large amount of research has been performed in the CFD community into body-fitted curvilinear coordinate grids has alleviated most of the issues associated with structured and unstructured Cartesian grid finite difference solution schemes [50, 52, 53, 54, 55]. Casting the differential equations using generalized coordinates can be accomplished using either the finite difference or finite volume techniques. An example of an airfoil meshed with a non-orthogonal gird is shown in Figure 1.15. The non-orthogonal grid in the physical domain is transformed to an orthogonal grid in the computational domain using a generalized transformation of the form shown in (1.15).

$$\begin{aligned} \xi &= \xi(x, y, z) \\ \eta &= \eta(x, y, z) \\ \zeta &= \zeta(x, y, z) \end{aligned} \tag{1.15}$$

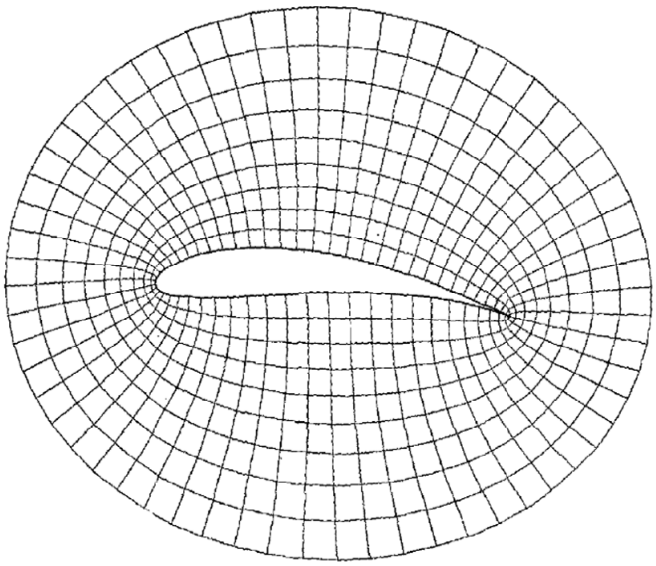

Figure 1.15: Airfoil meshed with non-orthogonal body-fitted grid [52]

There have been numerous numerical procedures developed to model the thermal response of ablative materials [27, 56, 57, 94]. Most of these codes are one-dimensional finite difference schemes; others seek semi-analytic approximate solutions to the governing differential equations. In particular the codes developed in references [27 and 57] have been very successful in predicting the one-dimensional thermal response of ablative materials under both arc jet and flight conditions. However, their success is restricted to problems in which a one-dimensional approximation is valid; for example, at the stagnation point where the geometry is planar and where the in-plane thermal conductivity does not affect the in-depth conduction.

1.3.3 Finite Element Techniques

Unlike the finite difference method which seeks to approximate the governing equations, the finite element method seeks to obtain approximate solutions to the governing differential equations [58, 59, 60, 61]. Instead of using an array of points like finite difference methods, a finite element model is built up from several small interconnected sub-regions, or elements. These elements, when assembled, form a

piecewise approximation to the governing equations; the basic premise being that the global solution can be approximated by replacing it with an assemblage of discrete elements. Since these elements can be put together in a variety of ways, they can be used to represent highly complex shapes [58]. Discretization of the solution domain can be performed with either a structured, or an unstructured grid. However, one of the main advantages is the ability to utilize an unstructured grid.

Figure 1.2, Figure 1.7, Figure 1.8, and Figure 1.12, point out that a heatshield penetration design has an inherently complex geometry. Also, due to the presence of a singularity in the heatshield, the heating boundary conditions near the penetration system are complex (as shown in Figure 1.3). These are two of the reasons that a finite element solution of the governing differential equations is sought for the thermal response of the penetration subsystem.

Another advantage of the finite element method is that it allows the use of higher order elements. Higher order elements are elements which have an increased number of nodes, and as a result have more degrees of freedom per element. For example, a standard linear quadrilateral has four nodes; a higher order quadratic quadrilateral has eight nodes where the extra four nodes are placed between the corner nodes as shown in Figure 1.16. The terms linear and quadratic refer

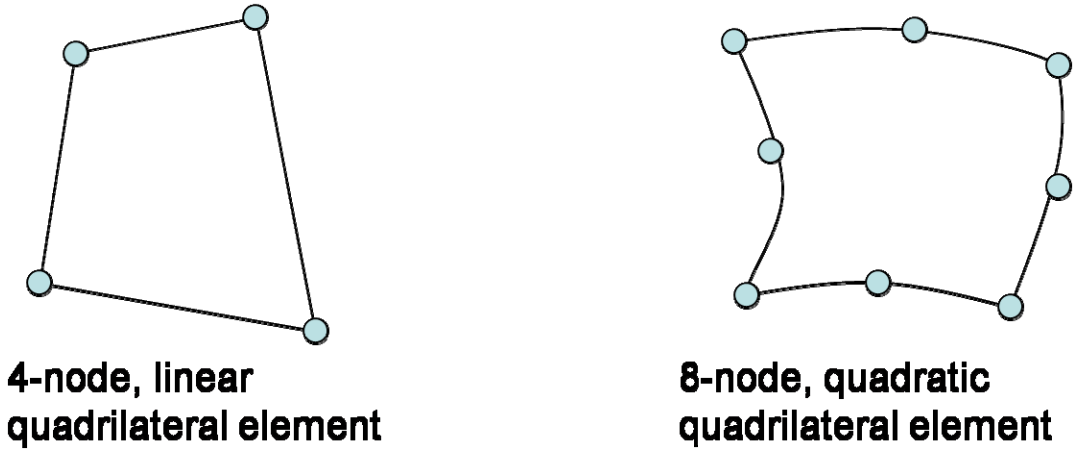

Figure 1.16: Linear and quadratic quadrilateral elements

to the order of the interpolation functions used to represent the unknown field variable between adjacent nodes. Interpolation functions will be discussed in greater detail in Chapter 3. Higher order elements have two main benefits. The first is that they add more computational degrees of freedom per element which could result in a reduction in the total number of elements required to solve a particular problem as well as increasing the accuracy of the solution. The second benefit is that it allows the element to have curved sides. Using curved sided elements allows for a more precise discretization of the geometry without having to increase the number of elements.

Most finite element computer codes have data structures that store data on an element basis, hence reducing the number of elements saves computer memory. The increased number of nodes does increase the computational time; however, the benefits mentioned above generally outweigh this disadvantage.

A cross section of the Orion CEV heatshield compression pad is shown in Figure 1.17. The finite element discretization using eight node linear hexahedral elements and higher order twenty node quadratic hexahedral elements of the compression pad are shown in Figure 1.18. Both discretizations shown in Figure 1.18 have the same number

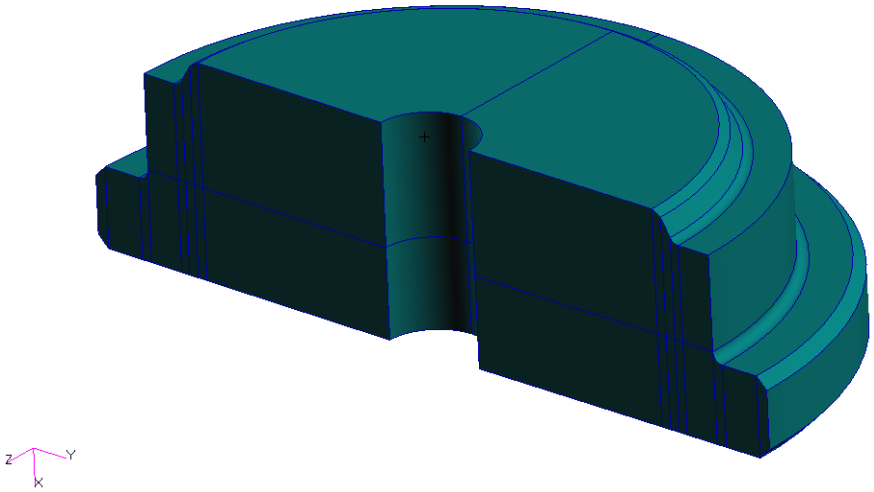

Figure 1.17: Cross section of the Orion CEV heatshield compression pad

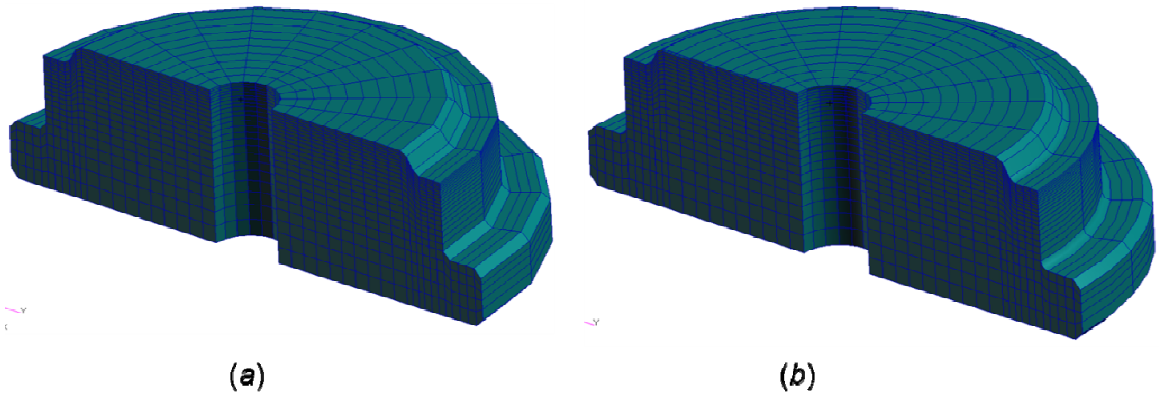

Figure 1.18: (*a*) Linear 8 node hexahedral mesh (*b*) Quadratic 20 node hexahedral mesh

of elements, but notice how the twenty node quadratic hexahedral elements more closely approximate the circular boundaries on the compression pad and the linear eight node elements with the straight sides don't quite represent the circular shape. More elements would be required for the eight node linear hexahedral mesh to represent the boundary with the same error as the quadratic element.

The main reason for seeking a finite element solution is compatibility with modern design and analysis tools. Modern design tools like ProEngineer [62] allow engineers to model complex geometries and analysis tools such as MSC Software's NASTRAN, and PATRAN Thermal [63, 64] make it practical to perform general structural and thermal analysis of these complex geometries. These design and analysis tools have become widely accepted throughout the entry vehicle design community, so compatibility with these tools would promote a multidisciplinary design process and increase the efficiency of the design process. This compatibility is the first step in linking heatshield design and analysis. It is of interest to note that while MSC Software's PATRAN Thermal is a complex piece of software with many features and capabilities in performing thermal analysis, it does not have the capability to analyze ablative heatshields. In fact, no commercially available thermal analysis software packages have the capability to perform high fidelity ablation and thermal response analysis. Cullimore and Ring's Thermal Desktop [65] software has recently implemented a heat of ablation analysis

capability; however, as mentioned in section 1.3, this is not considered a high fidelity method. There are some research codes available, (e.g. CMA, FIAT, TITIAN), but as mentioned previously, all of them are finite difference based and incompatible with modern design tools.

1.4 The Need for a Three-Dimensional Finite Element Thermal Analysis Capability

For some types of problems a one-dimensional solution may not capture all of the details necessary to fully describe the thermal response of a particular geometry or material. Regions where the geometry is highly curved, high temperature gradients exist and the in-plane thermal conductivity is significant, or pyrolysis gas flow is not normal to the heated surface, are examples where a one-dimensional solution is inadequate.

Researchers in the 1960's recognized the importance of multi-dimensional effects in rocket nozzles where the geometry is highly curved, multiple materials exist in the cross sectional plane, and high temperature gradients with significant in-plane conduction are observed [66, 67]. Although these two references were advanced from the stand point of being multi-dimensional, they lacked a general treatment of the surface energy balance. Both use heat of ablation correlation data in the form of a transpiration coefficient and a heat of vaporization term to represent the energy absorbed due to ablation. In addition, both references solve the governing differential equations using the finite difference technique.

Friedman, et. al. [67] compared 2-D temperature results to rocket firing test data for an axisymmetric rocket nozzle throat. While these temperature predictions compare very well, no recession prediction was performed and as such, verification can only be performed with test results that do not exhibit any recession.

Hurwicz, et al., [66] compared two, and three-dimensional computational results with a one-dimensional analysis of an ablative wing leading edge and a spin control fin. For the wing leading edge, they found the one-dimensional solution over predicted the

bondline temperature compared to the multi-dimensional results. For the spin control fin, they found the one-dimensional analysis under predicted the recession.

Current efforts to analyze ablation in multi-dimensions have been successful [68, 69, 70], but rely on the finite difference technique to discretize the geometry. In planar problems where the high in-plane conduction demands the multi-dimensional solution, finite difference schemes are well suited. However, in problems which have complex geometry such as the shoulder region of an entry vehicle heatshield, or forebody heatshield compression pad, a finite difference scheme may not provide the best representation. Also, in [69 and 70], the pyrolysis gas flow is assumed to be one-dimensional and normal to the heated surface. This assumption may not be valid where the geometry is highly curved, the virgin material is porous, or there are multiple materials in the cross sectional plane.

A three-dimensional finite element code which utilizes the general thermochemical formulation of the ablation problem would have the ability to address the shortcomings addressed above. In addition, a finite element code would be directly compatible with modern design and analysis tools and allow for an integrated TPS design process. Moreover, modern CFD tools are now capable of three-dimensional solutions for the aerodynamic heating; having a three-dimensional thermal response tool is vital to being able to use those aerothermal environment results directly. This feature becomes especially important near a compression pad, where a spatially distributed heating environment will be present. While a three-dimensional finite element code will be more computationally intensive than the traditional one-dimensional analysis, modern computers along with a parallel processing computational scheme will alleviate this challenge.

1.5 Reliability, Robust Design, and Uncertainty

While this dissertation does not attempt to quantify heatshield reliability, the concepts of reliability, robustness and uncertainty and how they are used in design warrants a brief review. The concept of reliability in design is not confined to the aerospace industry and in particular space vehicle TPS design. Reliability analysis in its most basic form tries to answer the question, for a given component, what is the probability that component will fail under the uncertain conditions in which it is used? In other words it is a statistical measure of how often a given component will fail. Product reliability is usually generalized and related to the quality of a product. Quality and reliability have been drivers in the automotive industry for years and in some cases designs which possess the highest reliability often give companies a competitive edge. Reliability is also present in the electronics and software industries where the competition is enormous and product reliability directly affects a company's reputation. In the aerospace industry, reliability is of very high importance because of the human element involved in air travel and human spaceflight, and the great expense at which aerospace systems are produced.

Reliability and robust design are interrelated concepts and the terms are often incorrectly used. Making a design robust, or insensitive to uncertainties, tends to increase the reliability of the design [71]. Park et. al. [71] reviewed three methodologies for robust design. The first, and earliest method developed is known as the Taguchi method. Taguchi proposed methods of determining variables to make performance insensitive to noises present in the manufacturing process [72, 73, 74]. Applying the Taguchi method to the design of a product has been accomplished by modifying the method slightly.

The second method Park et. al. [71] reviewed is called the robust optimization method. In this method, the concept of robustness is added to conventional optimization techniques. The basic premise of the method is that the objective function and constraints are redefined using robustness indices [75, 76, 77].

The third method reviewed by Park et. al., is known as the axiomatic design method. Axiomatic design is a systems design methodology which uses matrix methods to systematically analyze customer needs into functional requirements, design parameters and process variables. The method gets its name from its use of design principles or design axioms (e.g., given without proof) governing the analysis and decision making process in developing high quality system designs [78, 79].

Robust optimization can be modified to include reliability by calculating the probability of exceeding design specifications via a Monte-Carlo Simulation and using this probability as the objective function instead of the robustness indices. The constraints of the problem are either physical, such as a geometric constraint, or notional such as a bondline temperature constraint in terms of heatshield design. The constraints also take the standard form of either being equality or inequality constraints.

The key piece of information required by all of the above methods is the need to quantify the uncertainty in the design parameters of interest. Wright et. al. [6] describes three types of uncertainties that are present in the thermochemical models used in aerothermal and thermal response analysis. The types of uncertainty are: stochastic variability, structural uncertainty, and parametric uncertainty.

Stochastic uncertainties arise due to natural fluctuations that exist in the physical environment. These types of uncertainty are also known as irreducible uncertainties, since they can be characterized, but not reduced. In TPS design, natural fluctuations would include atmospheric conditions. These types of uncertainties are routinely modeled in entry trajectory simulations such as those found in POST [80].

Structural uncertainties arise in numerical simulations due to the fact that these simulations employ mathematical models to simulate physical phenomenon occurring. The mathematical models are approximations of reality where simplifying assumptions are often made to make the problem more tractable. These simplifying assumptions in general, are valid only over a limited range of conditions, and as such can be a significant

source of uncertainty. An example of a structural uncertainty is the Tauber-Sutton radiative heating correlation [116]. This correlation is valid only at the stagnation point, over a range of vehicle nose radii and atmospheric densities for Earth and Mars. Using the Tauber-Sutton radiative heating correlation for a Venus entry would be incorrect since the correlation is only valid for Earth and Mars. Other sources of structural uncertainty arise from discretizing the governing equations of the phenomenon being modeled. Discretizing the equations puts them in a form suitable for numerical simulation; however, this simplification introduces discretization, or truncation errors in the computational model. Stated another way, structural errors arise when either the physical models employed or their numerical approximations are incorrect.

Parametric uncertainty arises from the model input parameters. A typical aerothermodynamic and TPS sizing calculation requires hundreds of input parameters, such as virgin and char thermal conductivity, decomposition kinetic constants, pyrolysis gas enthalpy, chemical reaction rates, surface catalicity, shock-layer radiation emission, and many others. Only a small subset of the many input parameters required for the calculation have generally been measured experimentally, or theoretically calculated at relevant conditions. A large majority of the input parameters are estimated either by indirect or purely empirical techniques. For those that have been measured experimentally or calculated theoretically, uncertainty still exists due to the limitations of the experimental equipment used or theoretical methods employed. Parametric uncertainty can be reduced through testing or analysis, but not eliminated.

A statistical definition of uncertainty is simply the standard error of the mean of a sample of measurements [81]. Mathematically, it is the square root of the variance about the mean, or in other words the standard deviation. Wright, et. al. [6] also list six methods for estimating the parameter uncertainties.

1. Compile data from multiple sources and compute the standard error of the mean. This approach is statistically rigorous and should be used whenever possible.
2. Perform an independent assessment of a single data source. This method requires detailed analysis of the experimental setup, data reduction, and/or theoretical formulation.
3. Use recommendations from relevant review articles or compiled databases. This approach is essentially having someone else perform method 1 or 2 for us. Care should be taken that the data quoted in the reference were taken at conditions relevant to the problem being studied.
4. Use the uncertainty value quoted directly from the original data source. This approach basically skips the independent assessment as in the second approach.
5. Apply similarity rules. In this approach the uncertainty of one parameter is estimated on the basis of another related parameter whose uncertainty was determined via methods 1-4.
6. Rely on expert judgment. This approach is both the simplest and least accurate method. Most often, this approach is used out of necessity, simply because relevant data does not exist. The best way to use this method is to poll multiple experts and take an average from the quoted sources.

In this dissertation, the following approach will be used. Uncertainties for numerical model inputs for which there exists a sufficient database, method 1 will be used and the standard error will be computed directly from the data. For uncertainties for model inputs which do not have a sufficient database method 6 will be used. Specifically, a subjective Bayesian probability technique will be used to develop probability density

functions from which the uncertainty can be derived. The Bayesian technique involves polling multiple experts and taking an average from the quoted sources [82, 83].

1.6 Dissertation Organization

The following chapters of this dissertation develop the finite element formulation of the thermochemical ablation problem; present a methodology for assessing the robustness of a thermal protection system design, and present an application of its use in the design of the Crew Exploration Vehicle's heatshield compression pads.

Chapter 2 is concerned with describing the nature of the thermochemical ablation problem, formulating the governing differential equations, and establishing the boundary conditions of the problem.

Chapter 3 develops the one-dimensional finite element formulation of the governing differential equations. The solution of the one-dimensional finite element ablation problem is compared to FIAT, an existing one-dimensional finite difference numerical procedure. The development in Chapter 3 also serves as the building block for extending the solution to three dimensions, in Chapter 4.

Chapter 4 extends the one-dimensional formulation from Chapter 3 to three-dimensions. The pyrolysis gas flow is no longer assumed to be one-dimensional and is solved in three-dimensions using Darcy's law. The same verification cases run in Chapter 3 are run with the three-dimensional code operating in a one-dimensional mode. Te Genesis entry trajectory is run in full 3-D mode to illustrate the differences between the one-dimensional mode and three-dimensional solutions.

Chapter 5 links thermal protection system design with the analysis. The three-dimensional finite element ablation code is used to demonstrate probabilistic design and is illustrated by example using the CEV heatshield compression pads. The probability of exceeding design specifications for this problem is presented. Thermal response parameter sensitivities are investigated.

Chapter 6 provides conclusions drawn from the work presented in the dissertation as well as recommendations for areas of further research.

1.7 Summary of Contributions

This dissertation presents the development of a three-dimensional finite element analysis tool and its application. This dissertation also presents a method for utilizing this analysis tool in the design of thermal protection systems. The following summary lists the contributions of this work.

1.7.1 Three-Dimensional Finite Element Formulation for Ablative Thermal Response

This work develops a three-dimensional finite element formulation for the differential equations governing thermochemical ablation. Existing heatshield thermal response tools utilize the finite difference technique. The applicability of the finite element methodology is demonstrated by comparing the one-dimensional finite element formulation with existing one-dimensional finite difference solutions. The finite element formulation allows the modeling of complex three-dimensional shapes. Including the three-dimensional momentum equation, in the form of Darcy's Law, along with the conservation of mass and energy equations in the formulation allows the calculation of three-dimensional recession and recession rates. A moving mesh strategy is employed which allows post processing visualization of the ablated geometry. The governing differential equations for linear elasticity are solved with the finite element method and used for two purposes: to move the three-dimensional mesh, and calculate thermal stress. While developed for application to heatshield penetrations, this analysis approach is generally applicable to the acreage heatshield as well.

1.7.2 Linking Thermal and Structural Analysis to Design

A new methodology to probabilistically design a heatshield penetration is presented. Linking the design to analysis is demonstrated by calculating the probability of exceeding the design specifications of the heatshield penetration subsystem. The multidisciplinary nature of the problem is captured by including both the thermal and structural response. Design parameter sensitivities are determined and presented. A contour plot displaying the variation of the bondline temperature design specification over the range of the design variables is generated. The optimum heatshield penetration design is determined and a Monte Carlo simulation is performed on it to determine the probability that the design specifications are exceeded. The three-dimensional finite element tool developed for this dissertation is used to perform the coupled thermal and structural analysis.

1.7.3 Application of the Finite Element Thermal Response Tool

The finite element thermal response tool is used to analyze the thermal response of the Orion heatshield penetration subsystem. Specifically, the three-dimensional geometry of the heatshield compression pad is modeled. Spatially varying heat flux boundary conditions due to local heating augmentation are easily incorporated and applied to the compression pad. The importance of accurately modeling the local heating environment and its effect on recession around the compression pad is demonstrated. The probability of exceeding the compression pad thermal and structural design specifications is determined. The finite element thermal response tool is compared to solutions from the one-dimensional finite difference code FIAT.

CHAPTER 2

PHYSICAL DESCRIPTION OF THE THERMOCHEMICAL ABLATION PROBLEM

Ablative thermal protection systems for entry into planetary atmospheres have been an important topic of research since the late 1950's and early 1960's. As a result, numerous works exist which describe the process of ablation both physically and mathematically [26, 29-39, 84, 88-96]. Ablation is the process of absorbing energy by removal of surface material by melting, vaporization, sublimation, or chemical reaction [85]. Any or all of these mechanisms may be present depending on the specific application. Mechanical removal of the surface material may also occur, but this process does not absorb a significant amount of energy.

The fundamental problem in ablative heat and mass transfer analysis is to predict the temperature and density histories of a thermally decomposing material which is exposed to a heating environment which may also erode the material surface. Many of the early studies of ablation solve for the in-depth thermal response using the one-dimensional energy equation and make use of the semi-infinite solid assumption as well as the plane wall assumption [86, 87]. These assumptions allow the in-depth energy equation to be solved analytically which simplifies the analysis, but accuracy and generality are lost since those assumptions only apply to a narrow range of problems and boundary conditions. In these studies, attempts at predicting the density variation within the material were made using engineering approximations. Most of the early attempts at predicting surface recession were made utilizing correlations of heat of ablation data [87]. It is important to state that the heat of ablation is not a property of the material, but a data correlation parameter and is only valid at steady state ablation conditions. Comparison between steady state ablation and transient ablation results are quite different. These methods have been shown to produce reasonable results, but only for specific problems

where either the correlations are defined, there is enough data to encapsulate the surface conditions and imposed heating environment, or the condition of steady state ablation had been reached. All of these approximate methods suffer from the same shortcoming in that they lack generality.

In the mid to late 1960's, Moyer, Rindal, Kendall, and Bartlett developed a general thermochemical ablation model [27, 88, 114] which made use of the work done by Goldstein [98, 99] on material decomposition. Their general formulation solves for the in-depth temperatures, and density variations starting from first principles, and is based on the work done by Kratsch, et. al. [89]. Figure 2.1 illustrates the physical processes occurring during hypersonic reentry which make up the ablation process. It is convenient to break up the physical processes into two groups and discuss them as either part of the in-depth response or in terms of an energy balance at the surface.

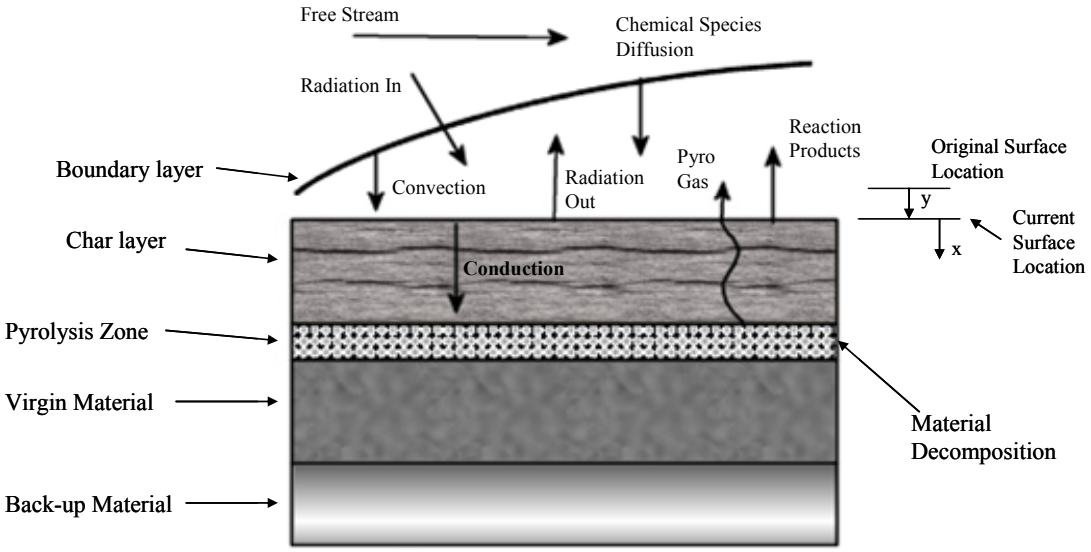

Figure 2.1: Physical processes occurring during ablation

2.1 In-Depth Thermal Response

The in-depth thermal response is the term used to group the physical phenomenon of heat conduction through the material, material decomposition and pyrolysis gas

generation, energy absorption and flow through the material. The pyrolysis gas is generated as the material undergoes decomposition, thus, the two phenomena are coupled. The decomposition of the material is a function of temperature, so it is coupled to the conduction of heat through the material. The physical processes occurring at the surface (described in Section 2.2) form the boundary conditions for conduction of heat through the material and transfer of mass to the boundary layer. Therefore, the in-depth response is coupled to the surface energy balance and any surface material removal which occurs.

Figure 2.1 shows the solid ablative material is broken into three regions. The bottom region is known as the virgin material and is generally followed by a non-ablative structural back-up material. The virgin material is the term used to describe the solid ablative material that has not been exposed to any heating and has not yet begun to decompose. The zone between the heated surface and the pyrolysis zone is known as the char zone, or char layer. The char layer is all that is left after the virgin material has completely decomposed. For most of the current ablative materials in use today, the char layer is a porous carbonaceous material, possibly reinforced with refractory fibers or cloth. The pyrolysis zone is the region where the material is no longer fully virgin and is not yet fully charred. It is an intermediate region where the material decomposition is taking place and the pyrolysis gases are being generated. During atmospheric entry, the vehicle's outer surface is heated causing the virgin material's temperature to increase. As the temperature increases, the material begins decomposing and generating pyrolysis gas. After a period of time at high temperature, the virgin material will become fully decomposed, leaving only a char residue.

Included with this basic description of the in-depth problem are a number of other complex events [27]. The pyrolysis gases flowing through the porous char layer may undergo further chemical reactions, and may react with the char, either eroding it or depositing additional residue upon it. The process of the pyrolysis gas depositing

additional residue within the char is called "coking". Coking tends to increase the density of the char layer in the regions where it is occurring, the end result being lower recession. Additionally, the char itself may collapse or fragment from mechanical or thermal stresses, and the refractory fiber reinforcements may melt or suffer mechanical damage. Various mechanical forces such as the pressure gradient developed between the internal pyrolysis gas and surface pressure may cause the char to spall, or be ejected into the boundary layer. Finally, the various species within the char structure may react chemically with each other to change the nature of the char.

Despite these complex events, the overall process may be described by the following simple relation.

$$virgin \rightarrow char + gas \tag{2.1}$$

Events such as coking, mechanical removal, melting, and subsurface reactions are less common and will be ignored in this dissertation. References [27, 85, 89, 90, 91, 92, 93, 94, 95, 96, 98] provide a representative sampling of the theory and analysis of the in-depth thermal response of charring materials, but for the remainder of this dissertation, the focus will be on the general thermochemical formulation presented in references [27, 56, 88, 103].

The control volume shown in Figure 2.2 represents an infinitesimal volume within the solid and shows the two sources of energy entering and leaving the control volume. The first energy source is due to heat conduction into and out of the control volume, q_x and q_{x+dx} respectively. The second source of energy is due to the flow of pyrolysis gas into and out of the control volume. There are three components of energy associated with the pyrolysis gas flow, the convection of sensible energy, $\dot{m}_g h_g$, the kinetic energy,

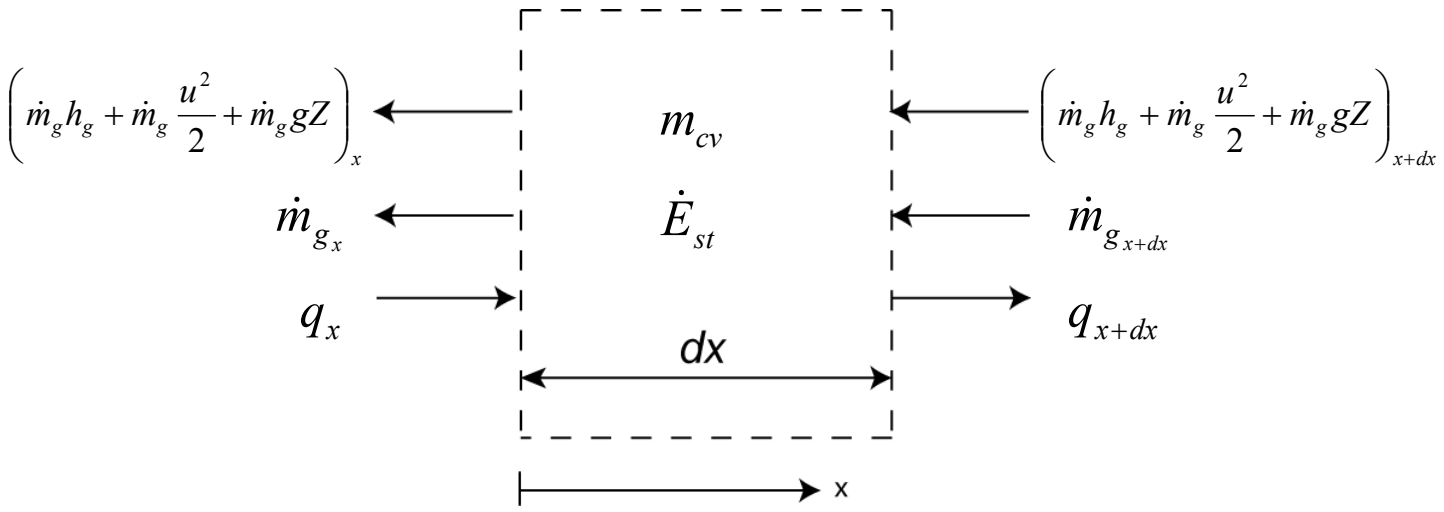

Figure 2.2: One-dimensional control volume for the in-depth thermal response

$\dot{m}_g \frac{u^2}{2}$, and the potential energy, $\dot{m}_g gZ$. The pyrolysis gas energy enters the control volume from the *x*+*dx* side and leaves from the *x* side. Figure 2.2 shows the mass flow entering and leaving the control volume as well. Notice that in this control volume the heat flux is opposite the direction of the mass flow and energy associated with the mass flow. Following the development in references [27, 89, and 98], the one-dimensional conservation of mass and energy equations, in a fixed coordinate system, can be readily formulated assuming for the time being that the conduction as well as the pyrolysis gas flow through the material is one-dimensional. The kinetic and potential energy terms will be assumed to be small in comparison to the sensible energy convection term and will be dropped from the formulation.

2.1.1 Conservation of Mass

The principle of conservation of mass states that mass can neither be created nor destroyed [97]. Figure 2.2 illustrates this principle and shows that the net mass flow into the control volume must equal rate at which mass accumulates inside the control volume. Mathematically, this can be written as,

$$\frac{\partial m_{cv}}{\partial t} = \dot{m}_{g_{x+dx}} - \dot{m}_{g_x} \tag{2.2}$$

The mass inside the control volume, m_{cv}, is related to the density of the solid material and the dimensions of the control volume as,

$$m_{cv} = \rho A dx \tag{2.3}$$

Where A is the constant cross sectional area of the control volume perpendicular to the x direction. The mass flow into the control volume can be expressed in the form of a Taylor series expansion as,

$$\dot{m}_{g_{x+dx}} = \dot{m}_{g_x} + \frac{\partial \dot{m}_{g_x}}{\partial x} dx \tag{2.4}$$

The mass flow out of the control volume is simply $\dot{m}_{g_x}$. Substituting the expressions for the mass inside the control volume, and the mass flows into and out of the control volume into (2.2) gives,

$$A \frac{\partial \rho}{\partial t} dx = \left(\dot{m}_{g_x} + \frac{\partial \dot{m}_{g_x}}{\partial x} dx \right) - \dot{m}_{g_x} \tag{2.5}$$

Canceling like terms on the right hand side, dividing by Adx, and recognizing that the mass flow per unit area, denoted by the double prime superscript, is simply the mass flux, the final form for the conservation of mass per unit volume is given as,

$$\frac{\partial \rho}{\partial t} = -\frac{\partial \dot{m}''_{g_x}}{\partial x} \tag{2.6}$$

Equation (2.6) shows that the decomposition of the virgin material is equal to the rate at which pyrolysis gas is generated. Therefore, evaluation of (2.6) requires that the decomposition rate be specified. A large amount of experimental thermogravimetric analysis (TGA) data [98, 99] have shown that the virgin material decomposition rate follows an Arrhenius type relation. In physical chemistry, an Arrhenius equation relates the rate constant to temperature change. In the case of material decomposition, it relates the rate of change of density to temperature. Following the work by Goldstein [98, 99] the form of the Arrhenius relation adopted here gives the decomposition rate as,

$$\frac{\partial \rho}{\partial t} = -\mathrm{B} e^{-E_a/RT} \rho_o \left(\frac{\rho - \rho_r}{\rho_o} \right)^{\psi} \tag{2.7}$$

Goldstein also showed that for most phenolic based resin/fiber systems, there are three independent decomposition reactions occurring over the temperature range for which decomposition occurs. Two reactions represent the resin component of the composite and one reaction represents the fibrous reinforcement. The total density of the composite material is given by,

$$\rho = \Gamma \left(\rho_A + \rho_B \right) + \left(1 - \Gamma \right) \rho_C \tag{2.8}$$

Each density component may decompose according to a relationship like (2.7). There are other ways in which to treat the density decomposition; however, (2.7) is physically realistic and straightforward numerically [27, 98, 99].

2.1.2 Conservation of Energy

The principle of conservation of energy states energy can neither be created nor destroyed only changed in form [97]. The two types of energy entering and leaving the control volume of Figure 2.2 are associated with pyrolysis gas flow and heat conduction. Some simplifying assumptions about the pyrolysis gas flow through the control volume can be made. The first assumption is that the pyrolysis gas formed is in thermal equilibrium with the material within the control volume and the second is that the residence time within the control volume is small. These assumptions imply that the temperature of the pyrolysis gas is the same as that of the solid at any given point in the control volume and that the pyrolysis gas has no time to chemically interact with the solid in the control volume respectively. Additionally, the potential energy of the pyrolysis gas may be neglected since the change in height across the control volume is negligible. The kinetic energy of the pyrolysis gas may also be neglected since it is of small magnitude relative to the pyrolysis gas enthalpy [89].

In general, the rate form of the first law of thermodynamics for a control volume may be written as,

$$\frac{dE_{cv}}{dt} = \dot{Q}_{cv} - \dot{W}_{cv} + \left[\dot{m}_{in}\left(e + Pv\right)_{in} - \dot{m}_{out}\left(e + Pv\right)_{out}\right] \tag{2.9}$$

The 1st law states that the time rate of change of energy in the control volume is equal to the net rate of heat transfer to the control volume minus the net work done by the control volume plus the net energy transported by mass flow and flow work into the control volume. The *e* in (2.9) is the total energy per unit mass and includes kinetic, potential and internal energy. Using the definition of enthalpy, the internal energy and flow work terms may be combined.

$$h = u + Pv \tag{2.10}$$

Note that there is no shaft work done by this control volume so $\dot{W}_{cv} = 0$ in (2.9). To derive the governing differential equation for the in-depth thermal response equation (2.9) will be rewritten in a simpler form,

$$\frac{dE_{cv}}{dt} = \dot{E}_{in} - \dot{E}_{out} \tag{2.11}$$

Equation (2.11) simply states that the rate at which energy is stored in the control volume is equal to the rate at which energy enters the control volume minus the rate at which energy leaves the control volume. Looking at the control volume in Figure 2.2 and recalling the assumptions made about the pyrolysis gas energy, the energy in-flow and out-flow can be written as,

$$\begin{aligned} \dot{E}_{in} &= q_x + \left(\dot{m}_g h_g\right)_{x+dx} \\ \dot{E}_{out} &= q_{x+dx} + \left(\dot{m}_g h_g\right)_x \end{aligned} \tag{2.12}$$

Expressing the heat conduction leaving the control volume and the convection of energy by the pyrolysis gas entering the control volume as Taylor series expansions give,

$$q_{x+dx} = q_x + \frac{\partial q_x}{\partial x} dx$$
$$\left(\dot{m}_g h_g\right)_{x+dx} = \left(\dot{m}_g h_g\right)_x + \frac{\partial}{\partial x}\left(\dot{m}_g h_g\right)_x dx \tag{2.13}$$

The rate of energy storage within the control volume can be expressed in terms of the density and enthalpy of the solid as,

$$\frac{dE_{cv}}{dt} = \frac{\partial}{\partial t}(\rho h) A dx \tag{2.14}$$

Substituting (2.12) into (2.11) and using the definitions in (2.13) and (2.14) gives,

$$\frac{\partial}{\partial t}(\rho h) A dx = \left[q_x + \left(\dot{m}_g h_g\right)_x + \frac{\partial}{\partial x}\left(\dot{m}_g h_g\right)_x dx \right] - \left[q_x + \frac{\partial q_x}{\partial x} dx + \left(\dot{m}_g h_g\right)_x \right] \tag{2.15}$$

Canceling like terms on the right hand side, dividing by *Adx* and recognizing that the heat rate and mass flow divided by the area are simply the heat flux and mass flux respectively gives,

$$\frac{\partial}{\partial t}(\rho h) = -\frac{\partial q''_x}{\partial x} + \frac{\partial}{\partial x}\left(\dot{m}''_g h_g\right)_x \tag{2.16}$$

Assuming that there is no mass diffusion within the control volume, the heat transfer, expressed as heat flux, can be expressed using Fourier's Law as,

$$q''_x = -k_x \frac{\partial T}{\partial x} \tag{2.17}$$

Substituting (2.17) into (2.16) gives the desired form of the governing differential energy equation for the in-depth thermal response,

$$\frac{\partial}{\partial t}(\rho h) = \frac{\partial}{\partial x}\left(k_x \frac{\partial T}{\partial x} \right) + \frac{\partial}{\partial x}\left(\dot{m}''_{g_x} h_g \right) \tag{2.18}$$

Moving from left to right, the first term in (2.18) is the energy storage, the second is the conduction through the material, and the third is the convection due to pyrolysis gas flow through the material.

2.1.3 Transformation of the Governing Equations to a Moving Coordinate System

For organic ablators, the dominate ablation mechanism, given a high enough heat flux and an oxidizing surface environment, is the chemical reaction of the char with the boundary layer gas near the surface. These oxidizing chemical reactions at the surface consume the char and cause the surface to recede [96]. For a glassy ablator, as the surface temperature reaches the melting point of the glass, the dominate ablation mechanism is vaporization of the liquid layer of glass, which will cause the surface to recede. Glassy materials may also be more susceptible to shear induced mechanical failure which removes the liquid layer. In both types of ablators, the surface of the ablator moves with respect to and towards the fixed back wall of the ablator. The back wall of the ablator is commonly referred to as the bondline since ablators are typically bonded to the spacecraft structure.

Other numerical solutions of (2.18), (2.6), (2.7), and (2.8) have found it convenient to attach the computational grid to the receding surface [27, 57, 100, 101]. Attaching the computational grid to the receding surface has several advantages. First, the solution domain remains in the physical domain of the problem. This is important because if the grid were fixed, approximations of the properties across an element would have to be made as material within an element is removed [49]. With a moving grid, these approximations do not need to be made as the material is removed. Instead the element length is simply adjusted and the properties are recomputed based on the new element size. Another advantage of the moving grid is that the grid location is tracked, making post-processing of the ablated shape straightforward. In order to solve the governing equations in a moving frame of reference, the governing equations must be transformed into the moving frame. Transforming the equations into a moving frame introduces a convective energy term into the governing differential equations.

Building off of the development in [27] and referring to Figure 2.3, the constant

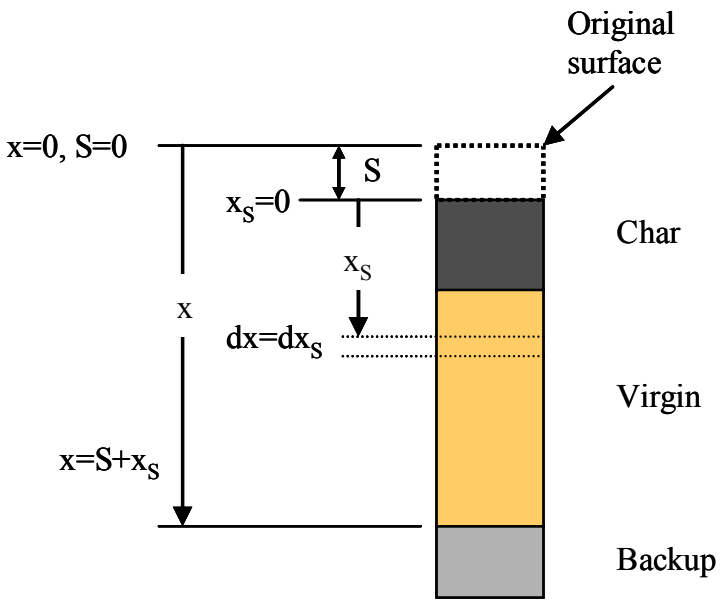

Figure 2.3: one-dimensional moving coordinate system

area, one-dimensional geometry being considered and the coordinate system being employed is illustrated. The x-coordinate is used to denote the position in the material with respect to the location of the original surface, where the origin is fixed to the location of the original surface. The coordinate x_S is the position in the material with respect to the receding surface where the origin is located at the receding surface. From Figure 2.3, the amount of surface recession, S, is related to the x and x_S coordinates by, $x = S + x_S$. Also, infinitesimal changes in x and x_S, denoted as dx and dx_S are equal at any fixed point in time.

2.1.3.1 Transformation of the Conservation of Mass

The conservation of mass stated by (2.6) was written for a control volume fixed in space where the derivatives with respect to time were taken holding x constant. Equation (2.6) must now be rewritten to relate these density changes at constant x to density changes at constant x_S. In the fixed x coordinate system, at any instant in time, the

density may be expressed as a function of position and time, $\rho = \rho(x,t)$, from which we may write using the chain rule,

$$d\rho = \left.\frac{\partial \rho}{\partial x}\right|_t dx + \left.\frac{\partial \rho}{\partial t}\right|_x dt \tag{2.19}$$

Differentiating (2.19) with respect to time at constant x_S yields

$$\left.\frac{\partial \rho}{\partial t}\right|_{x_S} = \left.\frac{\partial \rho}{\partial x}\right|_t \left.\frac{\partial x}{\partial t}\right|_{x_S} + \left.\frac{\partial \rho}{\partial t}\right|_x \tag{2.20}$$

Using the relation between the amount of recession and the x and x_S coordinates, we may write for constant x_S,

$$\begin{aligned} x &= S + x_S \\ \left.\frac{\partial x}{\partial t}\right|_{x_S} &= \frac{dS}{dt} \equiv \dot{S} \end{aligned} \tag{2.21}$$

The surface recession rate $\dot{S}$ in (2.21) is written as a total derivative since it is a function of time only. Substituting (2.21) into (2.20) and noting that $dx=dx_S$ at constant t yields,

$$\left.\frac{\partial \rho}{\partial t}\right|_{x_S} = \dot{S} \left.\frac{\partial \rho}{\partial x_S}\right|_t + \left.\frac{\partial \rho}{\partial t}\right|_x \tag{2.22}$$

Equation (2.22) along with (2.7) and (2.8) represent the conservation of mass in the moving coordinate system.

2.1.3.2 Transformation of the Conservation of Energy

Transforming the energy equation to the moving coordinate system requires the assumption that the following functional relationships are valid.

$$\begin{aligned} T &= T(x,t) \\ \rho &= \rho(x,t) \\ S &= S(t) \\ h &= h(T,\rho) \equiv h(x,t) \end{aligned} \tag{2.23}$$

Rewriting equation (2.18) to show which variables were held constant during the partial differentiation gives,

$$\left.\frac{\partial}{\partial t}(\rho h)\right|_{x} = \left.\frac{\partial}{\partial x}\left(k_x \frac{\partial T}{\partial x}\right)\right|_{t} + \left.\frac{\partial}{\partial x}\left(\dot{m}''_{g_x} h_g\right)\right|_{t} \tag{2.24}$$

The energy storage term on the left hand side which was written for a point in the fixed coordinate system will need to be related to its counterpart in the moving frame. The energy storage term can be expanded using the chain rule as:

$$\begin{aligned} &\rho h = \rho h(x,t) \\ &d(\rho h) = \left.\frac{\partial}{\partial x}(\rho h)\right|_{t} dx + \left.\frac{\partial}{\partial t}(\rho h)\right|_{x} dt \end{aligned} \tag{2.25}$$

Performing a partial differentiation with respect to time at constant x_S yields,

$$\left.\frac{\partial}{\partial t}(\rho h)\right|_{x_S} = \left.\frac{\partial}{\partial x}(\rho h)\right|_{t} \left.\frac{\partial x}{\partial t}\right|_{x_S} + \left.\frac{\partial}{\partial t}(\rho h)\right|_{x} \tag{2.26}$$

Using (2.21), rearranging, and recalling that differentiation with respect to x is equivalent to differentiation with respect to x_S at constant time yields,

$$\left.\frac{\partial}{\partial t}(\rho h)\right|_{x} = \left.\frac{\partial}{\partial t}(\rho h)\right|_{x_S} - \dot{S}\left.\frac{\partial}{\partial x_S}(\rho h)\right|_{t} \tag{2.27}$$

Substituting (2.27) into (2.24) and again recalling that differentiation with respect to x is equivalent to differentiation with respect to x_S at constant time yields,

$$\underbrace{\left.\frac{\partial}{\partial t}(\rho h)\right|_{x_S}}_{I} = \underbrace{\left.\frac{\partial}{\partial x_S}\left(k_x \frac{\partial T}{\partial x_S}\right)\right|_{t}}_{II} + \underbrace{\left.\frac{\partial}{\partial x_S}\left(\dot{m}''_{g_x} h_g\right)\right|_{t}}_{III} + \underbrace{\dot{S}\left.\frac{\partial}{\partial x_S}(\rho h)\right|_{t}}_{IV} \tag{2.28}$$

While equation (2.28) represents the energy equation in the moving coordinate system, it is convenient to express the rate of change of enthalpy in term I of (2.28) in terms of temperature and density change rates [27]. Since the enthalpy of the solid changes between fully virgin and fully charred material during the transient, a model for

the enthalpy of the partially pyrolyzed material must be established. Past flight and arc jet test experience has shown [27, 56, 57] that it is a reasonable assumption to consider the partially pyrolyzed solid as a mixture of pure virgin and pure char material. Let χ_v denote the volume fraction of undecomposed virgin material within the control volume. For pure virgin material, χ_v is 1.0, for pure char it is 0.0, and for intermediate states of decomposition it may be anywhere in between. With this definition, the density anywhere in the solid may be written,

$$\rho = \chi_v \rho_v + (1 - \chi_v)\rho_c \tag{2.29}$$

The total enthalpy per unit volume, ρh, may now be written in terms of the volume fraction χ_v and the enthalpy of the virgin and char as,

$$\rho h = \chi_v \rho_v H_v + (1 - \chi_v)\rho_c H_c \tag{2.30}$$

The total enthalpy of virgin and char material includes both the chemical and sensible enthalpies and is given as,

$$\begin{aligned} H_v &= h_v^0 + \int_0^T c_{p_v} dT \\ H_c &= h_c^0 + \int_0^T c_{p_c} dT \end{aligned} \tag{2.31}$$

Differentiating (2.30), (2.31), and (2.29) with respect to time noting that the heat of formation, and the density of the virgin and char is constant yields,

$$\frac{\partial}{\partial t}(\rho h) = \rho_v H_v \frac{\partial \chi_v}{\partial t} + \rho_v \chi_v \frac{\partial H_v}{\partial t} + \rho_c \frac{\partial H_c}{\partial t} - \rho_c H_c \frac{\partial \Gamma_v}{\partial t} - \rho_c \chi_v \frac{\partial H_c}{\partial t} \tag{2.32}$$

$$\frac{\partial H_v}{\partial t} = c_{p_v} \frac{\partial T}{\partial t} \quad and \quad \frac{\partial H_c}{\partial t} = c_{p_c} \frac{\partial T}{\partial t} \tag{2.33}$$

$$\frac{\partial \chi_v}{\partial t} = \left(\frac{1}{\rho_v - \rho_c} \right) \frac{\partial \rho}{\partial t} \tag{2.34}$$

Substituting (2.33) and (2.34) into (2.32) produces, after some algebra, the desired relation between the rate of change of enthalpy, rate of change in temperature, and rate of change in density is given as,

$$\left.\frac{\partial}{\partial t}(\rho h)\right|_{x_S} = \left[\frac{\rho_v H_v - \rho_c H_c}{\rho_v - \rho_c}\right]\left.\frac{\partial \rho}{\partial t}\right|_{x_S} + \rho_v c_{p_v}\chi_v \left.\frac{\partial T}{\partial t}\right|_{x_S} + (1-\chi_v)\rho_c c_{p_c}\left.\frac{\partial T}{\partial t}\right|_{x_S} \quad (2.35)$$

Defining mass weighted averages for the enthalpy and the specific heats of the virgin and char as,

$$\overline{h} = \left[\frac{\rho_v H_v - \rho_c H_c}{\rho_v - \rho_c}\right] \quad and \quad \rho c_p = \rho_v c_{p_v}\chi_v + (1-\chi_v)\rho_c c_{p_c} \quad (2.36)$$

Equation (2.35) may be rewritten as,

$$\left.\frac{\partial}{\partial t}(\rho h)\right|_{x_S} = \overline{h}\left.\frac{\partial \rho}{\partial t}\right|_{x_S} + \rho c_p \left.\frac{\partial T}{\partial t}\right|_{x_S} \quad (2.37)$$

Term II in equation (2.28) does not require any special modification, however, term III may be expanded as,

$$\left.\frac{\partial}{\partial x_S}\left(\dot{m}''_{g_x} h_g\right)\right|_t = \dot{m}''_{g_x}\left.\frac{\partial h_g}{\partial x_S}\right|_t + h_g \left.\frac{\partial \dot{m}''_{g_x}}{\partial x_S}\right|_t \quad (2.38)$$

Recognizing again that differentiation with respect to x and x_S are equivalent at constant time, substituting (2.6) into (2.38) yields,

$$\left.\frac{\partial}{\partial x_S}\left(\dot{m}''_{g_x} h_g\right)\right|_t = \dot{m}''_{g_x}\left.\frac{\partial h_g}{\partial x_S}\right|_t + h_g \left.\frac{\partial \rho}{\partial t}\right|_x \quad (2.39)$$

where the expression for the time rate of change of density in the fixed coordinate system is given by (2.7).

Term IV in (2.28) does not require modification, however, it is convenient to expand it to express the enthalpy per unit volume in terms of temperature and density. Differentiating (2.30), (2.31), and (2.29) with respect to x_S, dropping the "constant-t"

notation, and noting that the heat of formation, and the density of the virgin and char is constant yields,

$$\frac{\partial}{\partial x_S}(\rho h) = \rho_v H_v \frac{\partial \chi_v}{\partial x_S} + \rho_v \chi_v \frac{\partial H_v}{\partial x_S} + \rho_c \frac{\partial H_c}{\partial x_S} - \rho_c H_c \frac{\partial \chi_v}{\partial x_S} - \rho_c \chi_v \frac{\partial H_c}{\partial x_S} \tag{2.40}$$

$$\frac{\partial H_v}{\partial x_S} = c_{p_v} \frac{\partial T}{\partial x_S} \quad and \quad \frac{\partial H_c}{\partial x_S} = c_{p_c} \frac{\partial T}{\partial x_S} \tag{2.41}$$

$$\frac{\partial \chi_v}{\partial x_S} = \left(\frac{1}{\rho_v - \rho_c} \right) \frac{\partial \rho}{\partial x_S} \tag{2.42}$$

Substituting (2.41) and (2.42) into (2.40) and using the definitions from (2.36) produces,

$$\left.\frac{\partial}{\partial x_S}(\rho h)\right|_t = \bar{h} \left.\frac{\partial \rho}{\partial x_S}\right|_t + \rho c_p \left.\frac{\partial T}{\partial x_S}\right|_t \tag{2.43}$$

Now, substituting (2.37), (2.39), and (2.43) into (2.28) gives,

$$\begin{aligned} \rho c_p \left.\frac{\partial T}{\partial t}\right|_{x_S} = {} & \left.\frac{\partial}{\partial x_S}\left(k_x \frac{\partial T}{\partial x_S} \right)\right|_t + \bar{h}\left[\dot{S} \left.\frac{\partial \rho}{\partial x_S}\right|_t - \left.\frac{\partial \rho}{\partial t}\right|_{x_S} \right] + \dot{S} \rho c_p \left.\frac{\partial T}{\partial x_S}\right|_t \\ & + \dot{m}''_{g_x} \left.\frac{\partial h_g}{\partial x_S}\right|_t + h_g \left.\frac{\partial \rho}{\partial t}\right|_x \end{aligned} \tag{2.44}$$

Using the definition of the conversation of mass (2.22), dropping the constant x_S and constant t notation and only noting where differentiation is in the fixed coordinate system, (2.44) can be simplified as,

$$\boxed{\underbrace{\rho c_p \frac{\partial T}{\partial t}}_{I} = \underbrace{\frac{\partial}{\partial x_S}\left(k_x \frac{\partial T}{\partial x_S} \right)}_{II} + \underbrace{\left(h_g - \bar{h} \right) \left.\frac{\partial \rho}{\partial t}\right|_x}_{III} + \underbrace{\dot{S} \rho c_p \frac{\partial T}{\partial x_S}}_{IV} + \underbrace{\dot{m}''_{g_x} \frac{\partial h_g}{\partial x_S}}_{V}} \tag{2.45}$$

Each term in (2.45) has a specific physical meaning. Term I represents the rate of sensible energy storage, term II is the net conduction through the material, term III represents the creation of sensible energy due to pyrolysis, term IV represents the energy convected due to coordinate system movement, and term V is the energy convected away

due to pyrolysis gas generation at that point. Note that the pyrolysis gas flow rate at any point in the material, $\dot{m}''_{g_x}$, is the total flow rate per unit area past that point relative to the back face of the ablator which has zero pyrolysis gas flux.

2.2 Surface Energy Balance Yields Boundary Conditions

An energy balance at the surface may be written as the summation of all the energy fluxes entering and leaving the surface of the material and equating to zero. These energy fluxes represent the boundary conditions that are applied to the system of equations (2.22) and (2.45). The control volume in Figure 2.4 shows a detailed view of the physical phenomenon occurring at the surface of a material undergoing ablation.

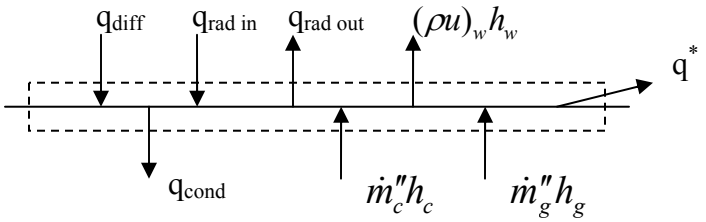

Figure 2.4: Surface energy flux terms

The physical phenomenon occurring at the surface depicted in Figure 2.4 can be grouped in terms of energy entering the control volume and energy leaving the control volume. Energy entering the control volume consists of a diffusive energy flux, q_{diff}, a radiative heat flux, $q_{rad\,in}$, energy flux due to pyrolysis gas reaching the surface, $\dot{m}''_g h_g$, and an energy flux associated with char mass flux due to char consumption, $\dot{m}_c h_c$. Energy leaving the control volume consists of a radiative flux away from the surface, $q_{rad\,out}$, conduction into the solid, q_{cond}, energy due to the flow of condensed phase material, q^*, and energy associated with gross blowing into the boundary layer,

$(\rho u)_w h_w$. The q_{cond} term is the net heat conducted into the solid and is the link between the governing in-depth differential energy equation and the surface boundary conditions. The heat conduction through the material is governed by the equations developed in Section 2.1 of this dissertation.

Using the control volume of Figure 2.4, the surface energy balance may be written as

$$-k\frac{dT}{dx} = q_{diff} + \underset{in}{q_{rad}} + \dot{m}_c'' h_c + \dot{m}_g'' h_g - \underset{out}{q_{rad}} - (\rho u)_w h_w - q^* \tag{2.46}$$

Equation (2.46) is written with the q_{cond} term in its familiar form of Fourier's Law and being in this form turns out to be convenient in terms of applying the boundary conditions in the finite element formulation which will be discussed in Chapter 3.

2.2.1 Convective Heat and Mass Transfer in a Multicomponent Boundary Layer

Equation (2.46) shows that an intimate coupling exists between the in-depth thermal response of an ablative material and the boundary layer transport phenomenon. The left hand side of this equation represents conduction into the solid material that is characterized by the differential equations presented in section 2.1. The terms on the right hand side of this equation represent the boundary layer phenomenon and energy fluxes at the surface due to material decomposition and recession. These terms in the surface energy balance must be characterized. In particular, the q_{diff} term which represents the total heat transfer rate to the wall due to molecular conduction and diffusion from the boundary layer gas must be determined. Equation (2.47) shows q_{diff} broken down into its constituent components,

$$q_{diff} = k_g \left.\frac{\partial T}{\partial y}\right|_w - \sum_i j_{iw} h_i^0 \tag{2.47}$$

To characterize the boundary layer transport terms in the surface energy balance, either the complete set of boundary layer equations must be solved and coupled to the in-depth thermal response equations, or suitable correlations to the boundary layer equations

must be employed that represent a wide range of boundary conditions and material compositions.

Generalized correlations to the boundary layer equations independent of boundary-layer-edge gas and ablation material composition have been developed assuming equal diffusion coefficients [102] and unequal diffusion coefficients [88, 103]. The approach adopted here will be that of using the correlations with unequal diffusion coefficients. There is a loss of some generality in using the correlations to the boundary layer equations, but with respect to the design problem presented in this dissertation, this approach is sufficient. This sufficiency is demonstrated by the work presented in references [56, 57, 104] where good correlation between arc jet data and the material thermal response have been demonstrated using the correlation approach, and in [105] where the correlations have been shown to match the solutions to the boundary layer equations over a wide range of boundary conditions and ablative material compositions.

The goal of the correlations is to express the q_{diff} term in the surface energy balance in terms of bulk heat and mass transfer coefficients. To develop the correlations to the boundary layer equations, we must start with the laminar, 2-D axisymmetric boundary layer conservation equations for a chemically reacting gas shown in (2.48) [103, 106, 107, 108]. Since the boundary layer equations will not be solved directly, their development from a control volume is not presented.

$$
\begin{aligned}
&\textit{Continuity}: \quad \frac{\partial \rho u}{\partial x}+\frac{\partial \rho v}{\partial y}=0 \\
&\textit{Momentum}: \quad \rho u\frac{\partial u}{\partial x}+\rho v\frac{\partial v}{\partial y}=\frac{\partial}{\partial y}\left[\mu\frac{\partial u}{\partial y}\right]-\frac{\partial p}{\partial x} \\
&\textit{Species}: \quad \rho u\frac{\partial K_i}{\partial x}+\rho v\frac{\partial K_i}{\partial y}=-\frac{\partial j_i}{\partial y}+\psi_i \\
&\textit{Energy}: \quad \rho u\frac{\partial H_T}{\partial x}+\rho v\frac{\partial H_T}{\partial y}=\frac{\partial}{\partial y}\left[\mu\frac{\partial\left(\frac{u^2}{2}\right)}{\partial y}+\frac{k}{c_p}\frac{\partial h}{\partial y}\right. \\
&\qquad \left.-\sum_i\left(j_i+\frac{k}{c_p}\frac{\partial K_i}{\partial y}\right)h_i-\frac{RT}{\rho}\sum_i\sum_j\frac{\chi_j D_i^T}{\mathscr{M}_i\mathscr{D}_{ij}}\left(\frac{j_i}{K_i}-\frac{j_j}{K_j}\right)\right]
\end{aligned}
\tag{2.48}
$$

Taking the species conservation equation and applying the Shvab-Zeldovich transformation which multiplies it by the mass of element k in molecule i, denoted by α_{ki}, and then sums over all species produces [102, 109].

$$
\begin{aligned}
&\rho u\frac{\partial \tilde{K}_k}{\partial x}+\rho v\frac{\partial \tilde{K}_k}{\partial y}=-\frac{\partial}{\partial y}\sum_i \alpha_{ki} j_i \\
&\textit{Where } \tilde{K}_k=\sum_i \alpha_{ki} K_i
\end{aligned}
\tag{2.49}
$$

In the absence of pressure diffusion and body forces, the diffusional velocity can be expressed using the Stefan-Maxwell relations as

$$
\frac{\partial \chi_i}{\partial y}=\sum_i \frac{\chi_i \chi_j}{\rho\mathscr{D}_{ij}}\left[\frac{j_j+D_j^T\dfrac{\partial \ln T}{\partial y}}{K_j}-\frac{j_i+D_i^T\dfrac{\partial \ln T}{\partial y}}{K_i}\right] \tag{2.50}
$$

In the absence of thermal diffusion and if all the diffusion coefficients, $\mathscr{D}_{ij}$, are equal, (2.50) reduces to Fick's Law which relates the diffusional mass flux explicitly to its mass fraction gradient.

$$
j_i=-\rho\mathscr{D}_{ij}\frac{\partial K_i}{\partial y} \tag{2.51}
$$

In this case the diffusion coefficients are not equal and the approximation developed by Bird [110] for the binary diffusion coefficients is used, which permits an explicit solution of (2.50) for the diffusional mass flux (j_i) in terms of gradients and properties of species *i* and the system as a whole. The approximation is in the form of,

$$\mathscr{D}_{ij} = \frac{\bar{D}}{F_i F_j} \tag{2.52}$$

where $\bar{D}$ is a property of the given multicomponent mixture and is a function of temperature and pressure. The F_i and F_j are functions of temperature only and are properties of the i^{th} species in the mixture. Equation (2.52) is essentially a correlation equation for actual binary diffusion coefficient data.

Substituting (2.52) into (2.50) and rewriting in terms of the mass fractions yields

$$\frac{\partial \chi_i}{\partial y} = \frac{\mathscr{M}^2}{\rho \bar{D}} \left(\frac{K_i F_i}{\mathscr{M}_i} \sum_j \frac{J_j F_j}{\mathscr{M}_j} - \frac{F_i J_i}{\mathscr{M}_i} \sum_j \frac{K_j F_j}{\mathscr{M}_j} \right) \tag{2.53}$$

where $\mathscr{M}$ and $\mathscr{M}_i$ represent the mixture and species molecular weights. For convenience, a total diffusional mass flux is defined as the sum of the molecular and thermal diffusion fluxes,

$$J_i = j_i + D_i^T \frac{\partial \ln T}{\partial y} \tag{2.54}$$

Multiplying each side of (2.53) by $\mathscr{M}_i / F_i$, and summing over all species, *i,* noting that the sum of all diffusive fluxes is zero and the sum of all mass fractions is unity, yields

$$\sum_j \frac{J_j F_j}{\mathscr{M}_j} = \frac{\rho \bar{D}}{\mathscr{M}^2} \sum_i \frac{\mathscr{M}_j}{F_i} \frac{\partial \chi_i}{\partial y} \equiv \frac{\rho \bar{D}}{\mathscr{M}^2} \sum_j \frac{\mathscr{M}_j}{F_j} \frac{\partial \chi_j}{\partial y} \tag{2.55}$$

Substituting (2.55) into (2.53) results in the following relation

$$\frac{\partial \chi_i}{\partial y} = \frac{K_i F_i}{\mathscr{M}_i} \sum_j \frac{\mathscr{M}_j}{F_j} \frac{\partial \chi_j}{\partial y} - \frac{\mathscr{M}^2}{\rho \bar{D}} \frac{F_i J_i}{\mathscr{M}_i} \sum_j \frac{K_j F_j}{\mathscr{M}_j} \tag{2.56}$$

To simplify (2.56), it is convenient to define several new quantities:

$$Z_i = \frac{\mathscr{M}_i \chi_i}{F_i \mu_2} \tag{2.57}$$

$$\mu_1 = \sum_j \chi_j F_j \tag{2.58}$$

$$\mu_2 = \sum_j \frac{\mathscr{M}_j \chi_j}{F_j} \tag{2.59}$$

$$\mu_3 = \sum_j \left(\frac{K_j}{F_j^2} \right) \left(\frac{dF_j}{dT} \right) \tag{2.60}$$

Multiplying (2.57) by μ_2 and differentiating with respect to *y* yields,

$$\frac{\mathscr{M}_i}{F_i} \frac{\partial \chi_i}{\partial y} - \frac{\mathscr{M}_i \chi_i}{F_i^2} \frac{\partial F_i}{\partial y} = \mu_2 \frac{\partial Z_i}{\partial y} + Z_i \frac{\partial \mu_2}{\partial y} \tag{2.61}$$

Substituting (2.54), (2.57)-(2.60), and (2.61) into (2.56) and noting the sum of Z_i over all species, *i*, is unity and that the F_i are functions of temperature only yields,

$$j_i + D_i^T \frac{\partial \ln T}{\partial y} = -\frac{\rho \bar{D}}{\mu_1} \left[\frac{\mu_2}{\mathscr{M}} \frac{\partial Z_i}{\partial y} + \frac{(Z_i - K_i)}{\mathscr{M}} \frac{\partial \mu_2}{\partial y} + K_i \left(\frac{1}{F_i^2} \frac{\partial F_i}{\partial y} - \mu_3 \right) \frac{\partial T}{\partial y} \right] \tag{2.62}$$

Equation (2.62) provides an explicit expression for the diffusional mass flux of species *i* in terms of the properties and gradients of species *i* and of the system as a whole and is the relationship which is desired. Further simplification of (2.62) can be made by assuming the F_i are constant with respect to temperature. Kendall, et al [103] constructed least-squares fits of diffusion coefficient data to obtain F_i as a function of temperature and found that if the F_i are assumed constant over a temperature range of 4000° to 16,000°R for a Carbon-Nitrogen-Oxygen system, the maximum error incurred is less than 1%. Therefore, if the F_i are assumed constant, equation (2.62) becomes,

$$j_i + D_i^T \frac{\partial \ln T}{\partial y} = -\frac{\rho \bar{D} \mu_2}{\mu_1 \mathscr{M}} \left[\frac{\partial Z_i}{\partial y} + \frac{(Z_i - K_i)}{\mu_2} \frac{\partial \mu_2}{\partial y} \right] \tag{2.63}$$

Substituting equation (2.63) into the boundary layer species conservation equation of (2.48) yields the modified boundary layer conservation equation for chemical elements in a multicomponent boundary layer with unequal diffusion coefficients and thermal diffusion.

$$\rho u \frac{\partial \tilde{K}_k}{\partial x} + \rho v \frac{\partial \tilde{K}_k}{\partial y} = \frac{\partial}{\partial y}\left[\frac{\rho \bar{D} \mu_2}{\mu_1 \mathscr{M}} \left(\frac{\partial \tilde{Z}_k}{\partial y} + (\tilde{Z}_k - \tilde{K}_k) \frac{\partial \ln \mu_2}{\partial y} \right) + D_k^T \frac{\partial \ln T}{\partial y} \right]$$

$$\tilde{K}_k = \sum_i \alpha_{ki} K_i, \qquad \tilde{Z}_k = \sum_i \alpha_{ki} Z_i, \qquad D_k^T = \sum_i \alpha_{ki} D_i^T \tag{2.64}$$

Recasting the species conservation equation in this form represents a major simplification to the set of boundary layer equations shown in (2.48) and is also a necessary step in deriving the correlations to the full set of boundary layer equations. Consider a typical graphite-air system consisting of Hydrogen, Carbon, Nitrogen, and Oxygen, where the number of significant species would be in the neighborhood of 30. Equation (2.64) permits characterizing the diffusional process in such a boundary layer using only 31 coefficients, (30 F_i diffusion factors and 1 $\bar{D}$) rather than 870 multicomponent diffusion coefficients, each of which is dependent upon species concentrations and upon 435 binary diffusion coefficients [103].

In the late 1960's the computational power available to engineers was limited, and as a result it was impractical to solve the complete set of boundary layer equations for each design application. While modern computational resources are adequate to solve the complete set of equations, development of this aspect is deferred to future work. Instead, this dissertation will focus on using the boundary layer correlation equations.

2.2.1.1 Correlation Equations to the Multicomponent Boundary Layer for an Ablating Material

In order to solve these complex thermochemical ablation problems practically, engineers of the 1960's era developed correlations to the boundary layer equations that

characterized the solutions of the complete set of equations in terms of bulk heat and mass transfer coefficients [88, 102, 103, 111]. The form chosen for these correlation equations is based on analogies between the species conservation equation given in (2.64) for unequal diffusion coefficients and the species conservation equation for equal diffusion coefficients. The requirements for the correlation equations are that they be valid for a wide range of boundary conditions and include parameters appropriate to transient ablation for both charring and non-decomposing homogenous materials. The equations should also be valid for arbitrary ablative material composition and boundary-layer-edge gas chemical composition.

In the absence of thermal diffusion effects, the species conservation equations, (2.64) take the form

$$\rho u \frac{\partial \tilde{K}_k}{\partial x} + \rho v \frac{\partial \tilde{K}_k}{\partial y} = \frac{\partial}{\partial y}\left[\frac{\rho \bar{D} \mu_2}{\mu_1 \mathscr{M}} \left(\frac{\partial \tilde{Z}_k}{\partial y} + (\tilde{Z}_k - \tilde{K}_k) \frac{\partial \ln \mu_2}{\partial y} \right) \right] \tag{2.65}$$

When all of the diffusion coefficients are equal the following are true,

$$F_i = F_j = 1.0,\ \bar{D} = \mathscr{D}_{ij},\ (\mu_1 / \mu_2) = \mathscr{M},\ and\ \tilde{Z}_k = \tilde{K}_k \tag{2.66}$$

Equation (2.65) then reduces to the conventional laminar boundary-layer species conservation for equal diffusion coefficients with no thermal diffusion:

$$\rho u \frac{\partial \tilde{K}_k}{\partial x} + \rho v \frac{\partial \tilde{K}_k}{\partial y} = \frac{\partial}{\partial y}\left(\rho \mathscr{D}_{12} \frac{\partial \tilde{K}_k}{\partial y} \right) \tag{2.67}$$

Solution of (2.67) can be correlated by an expression relating the diffusion mass flux of element *k* independent of molecular configuration, $\tilde{j}_{k_w}$, to the product of a mass transfer coefficient and mass fraction difference by [102],

$$\tilde{j}_{k_w} = \rho_e U_e C_m \left(\tilde{K}_{k_w} - \tilde{K}_{k_e} \right) \tag{2.68}$$

Where the mass transfer coefficient is approximately related to the Stanton number, or, heat transfer coefficient, by the Lewis number using the Reynolds analogy as,

$$C_M = C_H Le^{2/3} \tag{2.69}$$

Where the Lewis number is defined as,

$$Le = \mathscr{D}_{12} / \alpha \tag{2.70}$$

and α is the thermal diffusivity. The species conservation equation (2.65) may be put in the form of equation (2.67) by generalizing an approximation that Kendall, et. al. [114] found to be appropriate for a number of gas mixtures. Kendall, et. al. [114] observed that the second term on the right hand side of (2.65) is much smaller than the first,

$$\left(\tilde{Z}_k - \tilde{K}_k\right)\frac{\partial \ln \mu_2}{\partial y} << \frac{\partial \tilde{Z}_k}{\partial y} \tag{2.71}$$

Making use of this approximation and defining an effective diffusion coefficient as

$$D_{eff} \equiv \frac{\bar{D}\mu_2}{\mathscr{M}\ \mu_1} \tag{2.72}$$

The species conservation equation for unequal diffusion coefficients becomes,

$$\rho u \frac{\partial \tilde{K}_k}{\partial x} + \rho v \frac{\partial \tilde{K}_k}{\partial y} \cong \frac{\partial}{\partial y}\left(\rho D_{eff} \frac{\partial \tilde{Z}_k}{\partial y}\right) \tag{2.73}$$

The left hand sides of (2.67) and (2.73) represent flow of species due to convection, and the right hand sides due to diffusion. Based on this observation, the similarity of equations (2.67) and (2.73), and the form of the diffusional mass flux correlation equation for equal diffusion coefficients, Kendall, et. al. [88, 103] postulated that a similar correlation equation to characterize the solutions of the species equation for unequal diffusion coefficients could be written similar to equation (2.68) as,

$$\tilde{j}_{k_w} = \rho_e U_e C_m \left(\tilde{Z}^*_{k_e} - \tilde{Z}^*_{k_w}\right) \tag{2.74}$$

The previous relationship of (2.69) between the mass transfer coefficient, Stanton number and Lewis number holds, except that the Lewis number defined in (2.70) is now a function of the effective diffusion coefficient. The new variable Z_i^* is introduced to

reflect the fact that the net mass transfer is influenced by the convective terms on the left hand side of (2.73) in most boundary layer flows where the mass fractions retain significance. In order to account for the relative mass transfer by diffusional process, the driving potential for diffusion is defined on a weighted basis between Z_i *and* K_i as,

$$\tilde{Z}_k^* = \sum_i \alpha_{ki} Z_i^* \qquad\qquad Z_i^* = \frac{Z_i^{\gamma} \cdot K_i^{1-\gamma}}{\sum_j Z_j^{\gamma} \cdot K_j^{1-\gamma}} \tag{2.75}$$

Kendall, et. al. proposed a value for γ of $\frac{2}{3}$ for boundary layer flows, based on analogy with the relative magnitudes of the conductive and convective terms in the energy equation. Figure 2.5 shows the elemental mass balance at the surface of a charring ablative material.

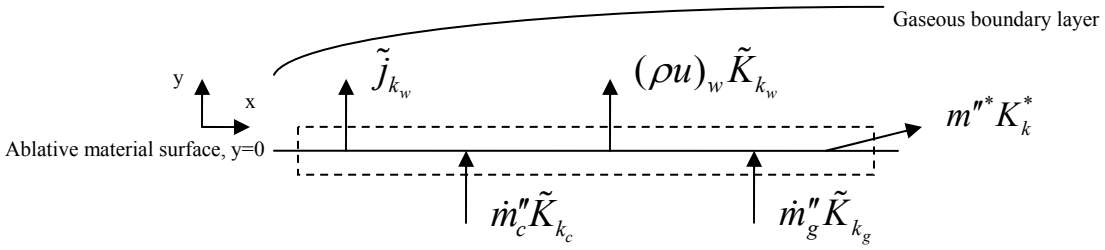

Figure 2.5: Surface elemental mass balance

The conservation of chemical elements at the surface of the ablator can be written from Figure 2.5 using equation (2.74) to express the diffusional mass flux as,

$$\dot{m}_c \tilde{K}_{k_c} + \dot{m}_g \tilde{K}_{k_g} = \rho_e U_e C_M \left(\tilde{Z}_{k_w}^* - \tilde{Z}_{k_e}^* \right) + (\rho u)_w \tilde{K}_{k_w} + m^* \tilde{K}_k^* \tag{2.76}$$

In a similar manner to the conservation of species, a correlation equation for the multicomponent, chemically reacting boundary layer conservation of energy, with unequal diffusion coefficients may be developed by drawing analogies with those correlations used for equal diffusion coefficients. Rosner [111] used a chemical

engineering approach and proposed the following correlation equation for conservation of energy assuming equal diffusion coefficients and a non-ablating surface based on similitude theory,

$$q_w = k_g \left.\frac{\partial T}{\partial y}\right|_w - \sum_i j_{iw} h_i^0 = \rho_e U_e C_H \left(H_{sr} - h_{sw}\right) + \rho_e U_e C_M \sum_i \left(K_{ie} - K_{iw}\right) h_i^0 \quad (2.77)$$

The terms on the left hand side make up the total heat transfer rate to the wall by molecular conduction and diffusion, and are in fact the same as the q_{diff} energy flux shown in Figure 2.4. The terms on the right represent the sensible chemical energy transfer, where the first is characterized by a heat transfer coefficient and enthalpy difference between the wall and boundary layer edge, the second by a mass transfer coefficient, a mass fraction difference between the wall and boundary layer edge, and the species chemical enthalpies. Rosner compared the correlation equation given in (2.77) to detailed boundary layer calculations performed by Fay and Riddell [112] at the stagnation point for a fully catalytic surface and found it to be accurate to within 5%. For unequal diffusion coefficients, making arguments similar to those used to derive the correlation in (2.77) yields,

$$q_w = k_g \left.\frac{\partial T}{\partial y}\right|_w - \sum_i j_{iw} h_i^0 = \rho_e U_e C_H \left(H_{sr} - h_{sw}\right) + \rho_e U_e C_M \sum_i \left(Z_{ie}^* - Z_{iw}^*\right) h_i^0 \quad (2.78)$$

For unequal diffusion coefficients, (2.78) shows the chemical transport is characterized by the Z-driving potential for mass transfer. Referring back to Figure 2.4 and equation (2.46), the surface energy balance may be rewritten substituting the relation given by (2.78) for the boundary layer heat transfer term, q_{diff}, as

$$\begin{aligned} -k\frac{dT}{dx} = {} & \rho_e U_e C_H \left(H_{sr} - h_{sw}\right) + \rho_e U_e C_M \sum_i \left(Z_{ie}^* - Z_{iw}^*\right) h_i^0 + \dot{m}_c'' h_c + \dot{m}_g'' h_g \\ & -(\rho u)_w h_w - q^* + q_{\substack{rad \\ out}} - \alpha q_{\substack{rad \\ in}} \end{aligned} \quad (2.79)$$

It is convenient to define non-dimensional ablation rates based on the mass transfer coefficient as,

$$B' = \frac{(\rho v)_w}{\rho_e U_e C_M}, \quad B'_g = \frac{\dot{m}''_g}{\rho_e U_e C_M}, \quad B'_c = \frac{\dot{m}''_c}{\rho_e U_e C_M}, \quad B'_{fail} = \frac{\dot{m}''^*}{\rho_e U_e C_M} \tag{2.80}$$

Where B' is the total normalized ablation rate, B'_g is the normalized ablation rate due pyrolysis gas liberation, B'_c is the normalized ablation rate due to char consumption, and B'_{fail} is the normalized ablation rate due to mechanical removal. For further clarification, the total mass blowing into the boundary layer can be expressed as the sum of the individual mass fluxes entering the surface as,

$$\left(\rho u\right)_w = \dot{m}''_g + \dot{m}''_c - \dot{m}''^* \tag{2.81}$$

Looking at equation (2.81) the following observation can be made with regard to the total normalized ablation rate,

$$B' = \frac{(\dot{m}_g + \dot{m}_c - m^*)}{\rho_e U_e C_M} = B'_g + B'_c - B'_{fail} \tag{2.82}$$

Making use of the definitions in (2.80) the surface energy balance may be written for unequal diffusion coefficients and $C_M \neq C_H$ as,

$$\begin{aligned} -k\frac{dT}{dx} = \rho_e U_e C_H \left(H_{sr} - h_{sw}\right) + \rho_e U_e C_M \left(\sum_i \left(Z^*_{ie} - Z^*_{iw}\right) h_i^0 + B'_c h_c + B'_g h_g - B' h_w \right) \\ -q^* + q_{\underset{out}{rad}} - \alpha q_{\underset{in}{rad}} \end{aligned} \tag{2.83}$$

Equation (2.83) is also valid for homogeneous materials for which case the gas generation rate, $\dot{m}''_g = 0$. If the diffusion coefficients are assumed to be equal, then $Z^*_k = K_k$ by the definitions in (2.57)-(2.60) and therefore, $\sum_i Z^*_{i_e} h_i^{T_w} = h_{e_w}$ and $\sum_i Z^*_{i_w} h_i^{T_w} = h_w$. If it is also assumed that the Lewis and Prandtl numbers are unity, then by (2.69) $C_M = C_H$. With both of the assumptions, (2.83) simplifies to,

$$-k\frac{dT}{dx} = \rho_e U_e C_H \left(H_{sr} - h_{sw} + B_c' h_c + B_g' h_g - B' h_w \right) - q^* + q_{\underset{out}{rad}} - \alpha q_{\underset{in}{rad}} \quad (2.84)$$

Equation (2.84) is the form of the surface energy balance that is most commonly used in solving ablative thermal response problems. Deriving the less common, more general surface energy balance (2.83) increases the flexibility and applicability of the design tool and methodology to be presented in this dissertation.

2.2.1.2 Heat Transfer Coefficient

The heat transfer coefficient $\rho_e U_e C_H$, given in equations (2.83) and (2.84) is typically calculated using a cold wall heat flux, q_{cw} and recovery enthalpy, H_r, by,

$$\rho_e U_e C_H = \frac{q_{cw}}{H_r}$$
$$\text{where} \quad H_r = r\frac{u^2}{2} - \sum_i K_i h_i^0, \quad and \quad h_w = 0 \quad (2.85)$$

The recovery factor, r, can be approximated by $\sqrt{\Pr}$ [106, 108], and is typically between about 0.82-0.85 for air. Often times, the hot wall heat flux is known, q_{hw}, in which case the hot wall heat transfer coefficient is calculated as,

$$\rho_e U_e C_H = \frac{q_{hw}}{\left(H_r - h_w \right)} \quad (2.86)$$

where h_w is the enthalpy at the wall at an assumed wall temperature. The assumption of radiative equilibrium at the surface is typically used to approximate wall temperature at the given hot wall heat flux. The underlying assumption of radiative equilibrium temperature is that all the incoming energy is reradiated, neglecting the effects of conduction and ablation. Ideally, there would be iteration between the surface temperature and the calculation of the hot wall heat transfer coefficient since radiative equilibrium results in surface temperatures higher than reality.

Up to now the dependence of C_H on the actual mass transfer rate to the boundary layer has been ignored. The assumption has been that C_H may be determined by the boundary layer edge conditions alone. In practice, this is known to be incorrect, with the value of C_H being strongly dependant on the value of $\dot{m}''$, the total mass flux entering the boundary layer. This total mass flux $\dot{m}''$ is known as blowing and if the unblown ($\dot{m}$ =0) heat transfer coefficient is denoted as C_{H_0}, the dependence has been shown by data correlation and analysis to be represented by the following relation [104],

$$\frac{C_H}{C_{H_0}} = \frac{\ln(1+2\lambda B'_{inj})}{2\lambda B'_{inj}} \tag{2.87}$$

2.2.1.3 Non-Dimensional Ablation Rates and Chemical Equilibrium

Returning to equation (2.76), substituting in the expressions for the non-dimensional ablation rates (2.80), assuming equal diffusion coefficients, and solving for the mass fraction of element *k* at the wall gives,

$$\tilde{K}_{k_w} = \frac{B'_c \tilde{K}_{k_c} + B'_g \tilde{K}_{k_g} + B'_f \tilde{K}_{k_f} + \tilde{K}_{k_e}}{1+B'} \tag{2.88}$$

Given the relative amounts of the chemical elements in the char and pyrolysis gas, the chemical and thermodynamic state of the gases adjacent to the ablating surface may be calculated using equilibrium relations. For unequal diffusion coefficients, equation (2.76) contains two unknowns $\tilde{Z}^*_{k_w}$ *and* $\tilde{K}_{k_w}$. Fortunately, $\tilde{Z}^*_{k_w}$ *and* $\tilde{K}_{k_w}$ may be expressed in terms of the species partial pressures using equilibrium relations as,

$$\begin{aligned} \tilde{K}_{k_w} &= \frac{\mathscr{M}_k}{P\mathscr{M}_g} \sum_{i=1}^{m} C_{ki} P_i \\ \tilde{Z}^*_{k_w} &= \frac{\mathscr{M}_k \overline{F}}{P\mathscr{M}_g} \sum_{i=1}^{m} \frac{C_{ki} P_i}{F_i^{\gamma}} \end{aligned} \tag{2.89}$$

Where $\mathscr{M}_k$ is the molecular weight of element *k*, $\mathscr{M}_g$ is the mean molecular weight of the gas phase, and $\overline{F}$ is the mean of F_i^{γ} defined as,

$$\overline{F} = \frac{\sum_{i=1}^{m} \mathscr{M}_i P_i}{\sum_{i=1}^{m} \frac{\mathscr{M}_i P_i}{F_i^{\gamma}}} \tag{2.90}$$

Substituting (2.89) into (2.76) and using the definitions of the non-dimensional ablation rates in (2.80) gives,

$$B' \sum_{i=1}^{m} C_{ki} P_{i_w} + \overline{F} \sum_{i=1}^{m} \frac{C_{ki} P_{i_w}}{F_i^{\gamma}} = \frac{P_w \mathscr{M}_g}{\mathscr{M}_k} \left(\tilde{Z}_{k_e}^{*} + B_g' \tilde{K}_{k_g} + B_g' \tilde{K}_{k_g} \right) \tag{2.91}$$

The assumption of chemical equilibrium is the basis for both equation (2.88) and (2.91). It is also possible to calculate the species concentrations and hence the non-dimensional ablation rates using the species rate equations. Using the rate equations would allow calculation of non-equilibrium ablation rates. This would be especially important at low temperatures where the equilibrium assumption begins to break down. In this dissertation, the equilibrium assumption is used exclusively and the incorporation of the non-equilibrium rate equations is left as future work.

Typically, an equilibrium chemistry code such as Aerotherm's Chemical Equilibrium Program (ACE) [113, 114] is used to solve (2.88) or (2.91) for the chemical state at the surface of the ablator. A parametric table of the non-dimensional ablation rates along with the pressure, temperature, and relative amounts of the elements in the virgin, char and pyrolysis gas is input into ACE and a "surface thermochemistry" table is output which contains solutions for $\sum_{i}^{m} \tilde{Z}_{i_w}^{*} h_i^{T_w}$ and h_w as a function of pressure, temperature, B_g', and B_c'. For equal diffusion coefficients and unity Lewis and Prandtl numbers the thermochemistry table contains h_w as a function of pressure, temperature, B_g', and B_c'.

The char mass flux is computed using the value of B'_c obtained during the solution of the in-depth and surface energy balances. The amount of surface recession is related to B'_c and hence the char mass flux by,

$$\rho_e U_e C_M \cdot B'_c = \dot{m}''_c = \rho \dot{S} \tag{2.92}$$

where ρ is the density at the surface where the recession is occurring and $\dot{S}$ is the recession rate.

If the material experiences melting, and liquid layer removal, the liquid layer mass flux ($\dot{m}''^*$) can also be calculated using the same chemical equilibrium, or kinetic procedure as defined for the char mass flux [27].

The pyrolysis gas flow rate, $\dot{m}''_g$, is calculated from the conservation of mass and the governing decomposition model given in (2.22) and (2.7). The pyrolysis gas and char enthalpies at the surface are both a function of the temperature at the surface. The boundary layer gas enthalpy at the wall is a function of the surface temperature, pressure, and chemical species concentrations. Calculating the pyrolysis gas enthalpy is a complex problem. The simplest model is to assume that the pyrolysis gas is in thermal equilibrium with the char and compute the enthalpy as a function of temperature and pressure. This assumption requires that the pyrolysis gas elemental composition be known. The pyrolysis gas composition can be calculated based on measurements of the virgin and char elemental compositions as well as the virgin and char densities [27, 114]. With the elemental gas composition known, the thermodynamic properties can be determined assuming chemical equilibrium, or using detailed reaction kinetic relations [113, 114].

2.2.2 Radiative Heat Flux

Radiation away from the surface follows the non-linear Stefan-Boltzmann relation given as [115],

$$q_{\substack{rad \\ out}} = f_{ij}\varepsilon\sigma\left(T_s^4 - T_{surr}^4\right) \tag{2.93}$$

Radiation from the boundary layer gas to the surface is a complex function of gas temperature, chemical composition, and vehicle geometry (which contributes to the shock shape around the body). In this dissertation, the radiative heat flux input to the surface will be approximated by the Tauber-Sutton stagnation point relation for Earth and Mars atmospheric entries [116] given as,

$$q_r = Cr_n^a \rho_\infty^b f(V) \tag{2.94}$$

The actual amount of radiation absorbed by the surface is governed by the surface absorptivity, α, and is related to the boundary layer gas radiation as,

$$q_{rad\,in} = \alpha q_r \tag{2.95}$$

The Tauber-Sutton relation in (2.94) has only been defined for entry in either Earth or Mars atmospheres and is valid over finite ranges of nose radius, velocity, and free stream density. The valid ranges for these quantities are summarized in Table 2.1.

Table 2.1: Range of validity for the Tauber-Sutton relation

	Earth		Mars	
	Lower Limit	Upper Limit	Lower Limit	Upper Limit
Velocity (km/s)	10	16	6.5	9
Density (km/m^3)	$6.66\text{x}10^{-5}$	$6.31\text{x}10^{-4}$	$1.0\text{x}10^{-4}$	$1.0\text{x}10^{-3}$
Nose radius (m)	0.3	3.0	1.0	23.0

CHAPTER 3

ONE-DIMENSIONAL FINITE ELEMENT FORMULATION OF THE GOVERNING DIFFERENTIAL EQUATIONS, VERIFICATION, ASSUMPTIONS, AND LIMITATIONS

3.1 The Finite Element Method

The finite element method seeks to find approximate solutions to the governing differential equations of continuum problems. Huebner, et. al., [58] define a continuum as body of matter either solid, liquid, or gas, in which some kind of phenomenon is occurring. In a continuum problem of any dimension, the field variable, be it pressure, temperature, displacement, stress, etc., possesses an infinite number of values since it is a spatial function throughout the body. The problem then has an infinite number of unknowns. The finite element discretization process reduces the problem to one with a finite number of unknowns by dividing the continuum into elements and expressing the unknown field variables in terms of assumed known approximating functions within each element. The approximating functions are called interpolation functions and are defined in terms of the nodal values of the field variables and their spatial coordinates within the element. The nodal values of the field variable and the interpolation functions completely define the behavior of the field variable over the element. The nodal values of the field variable become the unknowns of the problem and upon their solution along with the interpolation functions, define the field variable over the entire assemblage of elements and hence the solution over the continuum.

The power and advantage of the finite element method over other numerical procedures comes from the ability to formulate solutions for individual elements before putting them together in a global system to represent the entire continuum. At its core, the finite element method takes a complex problem and reduces it to a series of much simpler problems. These solutions over the element are referred to as the element

equations. There are two main methods by which to formulate the element equations for individual elements, the variational approach and the method of weighted residuals.

The variational approach relies on using calculus of variations and involves rendering a functional stationary. In solid mechanics, the functional turns out to be the potential energy, complimentary energy, or some variant of these. The variational approach can only be used when a corresponding variational principle exists, as in the examples stated for solid mechanics. For heat transfer problems, anything more complex then the basic nonlinear heat conduction equation does not possess a variational principle and therefore requires some other means to obtain the element formulation. Since the problem being solved here is highly nonlinear and includes numerous additional energy terms associated with the ablation process, no variational principle exists. Therefore, the method of weighted residuals will be used to derive the element equations.

Regardless of the method used to derive the element equations, the finite element method follows a logical, step-by-step process. The logical steps of the finite element method will be briefly introduced here and discussed in greater detail in the sections that follow.

The first step in the finite element method is to discretize the continuum. That is, the solution region needs to be divided into a series of elements. The solution region may be divided by any number or types of elements, usually determined by engineering judgment.

The second step in the finite element method is to select interpolating functions. Interpolation functions will be developed further in Section 3.2.2.

The third step is to derive the element equations. In this dissertation, the method of weighted residuals will be used due to the nature of the differential equations being solved.

The fourth step is to assemble the element equations into a global system of equations. A unique feature of the finite element method is that the system equations are

generated by assembling individual element equations. In contrast, in the finite difference method the system equations are generated by writing individual nodal equations.

The fifth step in the process is to impose the boundary conditions of the problem on the system of equations. This is the step where known values of the nodal variables are assigned and surface energy balances are applied.

The final step is to solve the system of equations. The set of equations that need be solved can be linear steady state, non-linear steady state, linear transient, or non-linear transient. The ablation thermal response problem being solved here is of the non-linear transient type. Non-linear solution algorithms such as the Newton-Raphson method and the non-linear conjugate gradient method are common methods used to solve the non-linear set of equations.

3.1.1 The Method of Weighted Residuals

The method of weighted residuals is a general technique for obtaining approximate solutions to linear and non-linear partial differential equations [58, 59]. There are two steps in applying the method of weighted residuals. The first involves assuming a functional form of the dependent variable which satisfies the differential equation and boundary conditions. In the case of the ablation problem, the dependent variable is the temperature. Substituting this assumed function into the differential equation and boundary conditions results in an error. This error or residual is then required to vanish in an average sense over the solution domain.

Solving the equations developed in step one transforms the assumed function to a specific function, which becomes the sought after approximate solution. To be more specific, consider the following general differential equation,

$$A(\Phi) - f = 0 \tag{3.1}$$

where A is a differential operator, f is the forcing function, and Φ is the unknown field variable. Let the domain of this differential equation be denoted as Ω bounded by the surface Γ. The function f is a known function of the independent variables and the boundary conditions are prescribed on Γ. Applying the method of weighted residuals, the exact solution Φ, is approximated by $\tilde{\Phi}$ given as,

$$\Phi \approx \tilde{\Phi} = N_0 + \sum_{i=1}^{m} N_i C_i \tag{3.2}$$

Where N_0 and N_i are the assumed functions, called interpolation, or shape functions and the C_i are either unknown functions or parameters of one of the independent variables. The upper limit m specifies the number of known N_i functions and the number of unknown C_i functions. The functions N_0 and N_i are chosen in such a way as to satisfy the boundary conditions. When (3.2) is substituted back into (3.1), it is likely that (3.1) will not be satisfied and there will be some error, or residual R which results from approximating Φ by $\tilde{\Phi}$.

$$A(\tilde{\Phi}) - f = R \tag{3.3}$$

Step two of the method of weighted residuals is to solve for the C_i unknowns such that R is small over the entire solution domain. This is accomplished by forming a weighted average of the error and requiring that it vanish over the solution domain.

$$\int_{\Phi} \left[A(\tilde{\Phi}) - f \right] \cdot W_i d\Omega = \int_{\Omega} R \cdot W_i d\Omega = 0, \quad i = 1, 2, ...m \tag{3.4}$$

Therefore m, linearly independent weighting functions, W_i, are chosen such that $R \approx 0$. In order to obtain a solution for the unknown C_i's and hence an approximation for the unknown variable Φ, we must choose the form of the weighting functions.

There are a variety of weighting functions to choose from, however, one of the more traditional used in deriving finite element equations is the Bubnov-Galerkin method [58]. The Bubnov-Galerkin method, or more commonly called Galerkin's method,

chooses the weighting functions to be the same as the functions used to approximate Φ, in other words $W_i = N_i$. Therefore Galerkin's method requires that,

$$\int_{\Omega} \left[A(\Phi) - f \right] \cdot N_i d\Omega = 0, \quad i = 1, 2, ..., m \tag{3.5}$$

The method of weighted residuals and hence Galerkin's method deal with the entire solution domain. However, because (3.1) holds for any point in the domain, it also holds for any number of points which define a subdomain, or element of the whole domain. For this reason Galerkin's method may be applied to a single element to define a local approximation of the governing equations. The familiar finite element representations of the unknown variable now become available and the functions N_i become the interpolating functions defined over a single element $N_i^{(e)}$ and the C_i's are the values of the unknown parameters which may be the nodal values of the dependent variable, or its derivative. The superscript notation (e) will be used throughout to denote when a function or parameter is defined over only a single element.

3.1.2 Galerkin's Weak Form of the Governing Partial Differential Equations

The goal is to transform the governing differential equations developed in Chapter 2 for the ablation problem into a form suitable to be solved by the finite element method. To accomplish this Galerkin's method will be used. The first step is to assume a functional form for the temperature, which is the dependent variable in this application. Hence we write,

$$T^{(e)} = \sum_{i=1}^{n} N_i T_i \tag{3.6}$$

Next we write the weighted residual statement of equation (2.45) with $W_i = N_i$ for one element, where "i" is the number of nodes in one element.

$$\int_{\Omega^{(e)}} \left[\frac{\partial}{\partial x_S}\left(k_x \frac{\partial T^{(e)}}{\partial x_S} \right) + \left(h_g - \bar{h} \right) \frac{\partial \rho^{(e)}}{\partial t}\bigg|_x + \dot{S}\rho c_p \frac{\partial T^{(e)}}{\partial x_S} + \dot{m}''_{g_x} \frac{\partial h_g^{(e)}}{\partial x_S} - \rho c_p \frac{\partial T^{(e)}}{\partial t} \right] N_i d\Omega = 0 \tag{3.7}$$

It is desirable to reduce the order of the equation in (3.7) which reduces the inter-element continuity requirements on the interpolation functions. To eliminate the second derivative with respect to temperature, the first term in (3.7) must be integrated by parts. Noting that in one-dimension $d\Omega = dx$ gives,

$$N_i k_x \frac{\partial T^{(e)}}{\partial x_S}\bigg|_{x_{S_1}}^{x_{S_2}} - \int_{x_{S_1}}^{x_{S_2}} k_x \frac{\partial T^{(e)}}{\partial x_S}\frac{\partial N_i}{\partial x_S} dx_S + \int_{x_{S_1}}^{x_{S_2}} (h_g - \bar{h}) N_i \frac{\partial \rho^{(e)}}{\partial t}\bigg|_{xi} dx_S$$
$$+ \int_{x_{S_1}}^{x_{S_2}} \dot{S}\rho c_p N_i \frac{\partial T^{(e)}}{\partial x_S} dx_S + \int_{x_{S_1}}^{x_{S_2}} \dot{m}''_{g_x} N_i \frac{\partial h_g^{(e)}}{\partial x_S} dx_S - \int_{x_{S_1}}^{x_{S_2}} \rho c_p N_i \frac{\partial T^{(e)}}{\partial t} dx_S = 0 \tag{3.8}$$

Integrating by parts reduces the order of differentiation on the governing equation and reduces, or weakens the continuity restrictions on the interpolating functions. Therefore the integral equation in (3.8) is referred to as Galerkin's weak form. Integration by parts also introduces the natural boundary conditions into the formulation which are represented by the first term of (3.8).

Equation (3.8) can be simplified by using the approximate definition for the temperature in an element given in (3.6), where its derivative can be expressed as,

$$\frac{\partial T^{(e)}}{\partial x_S} = \sum_{i=1}^{n} \frac{\partial N_i}{\partial x_S} T_i \tag{3.9}$$

Further simplification can be achieved by expressing (3.6) and (3.9) in matrix notation given as,

$$T^{(e)} = \left[N\right]^T \left\{T\right\}$$
$$\frac{\partial T^{(e)}}{\partial x_S} = \left[B\right]^T \left\{T\right\} \tag{3.10}$$

The matrix ***N*** is called the temperature interpolation matrix and the matrix ***B*** is called the temperature gradient interpolation matrix. ***B*** is calculated for a general three dimensional problem by,

$$\left[B\right] = \begin{bmatrix} \frac{dN_1}{dx} & \frac{dN_2}{dx} & \cdots & \frac{dN_r}{dx} \\ \frac{dN_1}{dy} & \frac{dN_2}{dy} & \cdots & \frac{dN_r}{dy} \\ \frac{dN_1}{dz} & \frac{dN_2}{dz} & \cdots & \frac{dN_r}{dz} \end{bmatrix} \tag{3.11}$$

where r is the number of nodes in the element.

Similarly, the pyrolysis gas enthalpy and its derivative with respect to x_S over an element can be expressed as,

$$h_g^{(e)} = \sum_{i=1}^{n} N_i h_{g_i} = \left[N\right]^T \left\{h_g\right\}$$
$$\frac{\partial h_g^{(e)}}{\partial x_S} = \sum_{i=1}^{n} \frac{\partial N_i}{\partial x_S} h_{g_i} = \left[B\right]^T \left\{h_g\right\} \tag{3.12}$$

Substituting (3.10) and (3.12) into (3.8) gives Galerkin's weak form of the governing differential equations for one-dimensional ablation thermal response in matrix form,

$$\int_{x_{S_1}}^{x_{S_2}} \rho c_p \left[N\right]\left[N\right]^T \left\{\dot{T}\right\} dx_S + \int_{x_{S_1}}^{x_{S_2}} \left[B\right]^T \left[k\right]\left[B\right]\left\{T\right\} dx_S - \int_{x_{S_1}}^{x_{S_2}} \dot{S}\rho c_p \left[N\right]\left[B\right]\left\{T\right\} dx_S$$
$$= \left[N\right] k_x \frac{\partial T^{(e)}}{\partial x_S}\bigg|_{x_{S_1}}^{x_{S_2}} + \int_{x_{S_1}}^{x_{S_2}} \left[\dot{m}_g''\right]\left[B\right]^T \left[N\right]^T \left\{h_g\right\} dx_S + \int_{x_{S_1}}^{x_{S_2}} \left[(h_g - \overline{h})\right]\left[N\right]\left\{\dot{\rho}\right\} dx_S \tag{3.13}$$

3.2 Element Equations

With the governing differential equations written in Galerkin's weak form, the individual element equations can be expressed and the natural boundary condition term introduced by the integration by parts procedure may be evaluated. Formation of the element equations requires examination of not only the surface boundary conditions, but also the appropriate form of the interpolations functions. Before the interpolation functions can be specified, the solution domain must be discretized into elements and the element topology defined.

3.2.1 Discretization and Element Topology

In this Chapter we are dealing with a one-dimensional problem which can be shown schematically in Figure 3.1. In this example, the solid is broken down, or discretized, into six elements of equal length with seven nodes. The global numbering scheme for the nodes and elements is arbitrary. However, following a sequential numbering scheme minimizes the global matrix bandwidth and is beneficial from a computer memory storage and computation time standpoint [58]. The process of discretizing a given geometry, commonly called meshing, is highly dependent on the particular problem

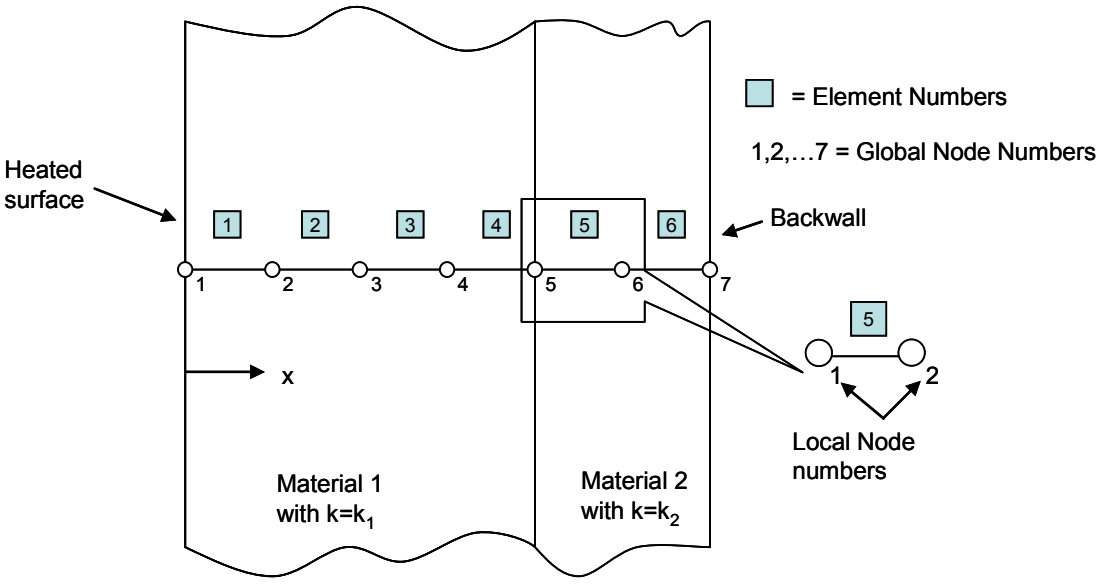

Figure 3.1: One-dimensional finite element discretization

being solved. Some problems can be solved without a great loss in accuracy with only a few elements and nodes. Other problems, where the unknown variables are changing rapidly as a function of both time and space, require a much finer mesh. A general rule of thumb for finite element meshing of thermal problems is to increase the number of nodes and elements in regions where there are large temperature gradients. In the context of the ablation thermal response problem being solved here, that region would be near the heated surface.

Selecting the proper mesh density is a tradeoff between solution accuracy, computational time, and convergence. For the ablation problem, a proper mesh density is developed based on past experience in solving problems where the gradients are large, the material properties are functions of temperature, and the boundary conditions are non-linear. Increasing the number of elements reduces the spacing between nodes, which increases the solution accuracy. This is due to the fact that the approximation to the differential equation introduced by the interpolation functions becomes closer to the exact solution as the distance between nodes decreases. There is a limit as to how fine a mesh can be analyzed. Increasing the number of elements in a problem requires additional computer memory in order to store the data associated with those elements. In addition, computational time is adversely affected by the number of elements since each element added to the system introduces more unknowns that must be solved. Convergence can also be an issue in selecting mesh size and will be further explored in section 3.5. Once the geometry has been satisfactorily meshed, the element topology is defined.

On the element level, topology refers to the ordered numbering of the nodes within an element. On a more global scale, topology is the record of which nodes belong to each of the elements, in other words it defines how the elements are connected to one another. Each element has its own local numbering scheme as shown in Figure 3.1, as well as a global numbering scheme. For one-dimensional elements, the nodes are numbered 1 and 2, for two-dimensional quadrilaterals, the nodes are numbered 1 through 4, and for three-

dimensional hexahedral elements, 1 through 8. Table 3.1 shows the relation between the local node numbers within an element and the global node numbering scheme for the example mesh in Figure 3.1.

Most commercial finite element programs accomplish both the task of meshing the geometry and determining the element topology automatically within the software. For example, in MSC software's PATRAN Thermal, the user meshes the geometry using built-in functions within the software, then internally, the software numbers the nodes and elements and determines the connectivity, or topology. In developing the finite element code for this dissertation, the geometric meshing was performed using PATRAN Thermal. After meshing, a data file containing the element and nodal coordinate data as well the element topology was exported from PATRAN and is used as input to the code developed here. This is the first step in assuring compatibility with PATRAN for design applications. The next step is to remap results back to PATRAN and NASTRAN for use in other thermal and structural analyses. The mesh from other software packages may also be used; however a conversion routine would be needed to convert to the proper format.

Table 3.1: Topology for the example finite element mesh in Figure 3.1

Element	Numbering Scheme	
	Local	Global
1	1 2	1 2
2	1 2	2 3
3	1 2	3 4
4	1 2	4 5
5	1 2	5 6
6	1 2	6 7

3.2.2 Interpolation Functions

Once the finite element mesh and topology have been defined, the behavior of the unknown field variable over each element must be approximated. The behavior of the temperature over the element is approximated by a continuous function expressed in terms of the nodal values of the temperature and the nodal spatial coordinates. It is the collection of these approximating functions over the solution domain that provides the piecewise approximation to the temperature and is the heart of the finite element method. These interpolation functions will now be more thoroughly defined.

In order to ensure that the approximate solution converges to the correct solution as the number of elements increases and to ensure that the expression for the variation of temperature across an element shown in (3.6) holds, the interpolation functions, N_i, must meet certain requirements. Rewriting (3.6) in a more general form,

$$\phi^{(e)} = \left[N^{(e)} \right]^T \phi^{(e)}, \qquad e = 1, 2, \ldots . m \tag{3.14}$$

where ϕ is any unknown field variable. The interpolation functions, $N^{(e)}$ must be chosen such that the following requirements are met [58, 117]:

1. At the element boundaries, the field variable ϕ and any of its partial derivatives should be one order less than the highest-order derivative appearing in the weak form of the governing differential equations.
2. All uniform states of ϕ and its partial derivatives up to the highest order appearing in the weak form of the governing differential equations should have representation in $\phi^{(e)}$ when, in the limit, the element size shrinks to zero.

These requirements were put forth in reference [117], justified in reference [118], and are known as the compatibility and completeness requirements, respectively. Since the highest order derivative that appears in (3.13) is a first-order derivative, the simplest

interpolation function that satisfies both the compatibility and completeness requirements is a linear function.

Interpolation functions can take a variety of forms, but generally, polynomials are chosen due to the ease at which they can be manipulated mathematically. In one dimension, a general nth order polynomial can be written as,

$$P_n(x) = \sum_{k=1}^{q_n} \alpha_k x^i, \quad i \le n \tag{3.15}$$

Where $q_n = n+1$ and for a linear polynomial, $n = 1$, which gives,

$$P_1(x) = \alpha_1 + \alpha_2 x \tag{3.16}$$

The order of the polynomial used and the number of degrees of freedom assigned to the element are related. Notice from (3.16) that there are two unknown coefficients which means there needs to be two independent equations to uniquely define them. The unknown field variable ϕ, expressed in terms of the polynomial in (3.16) over the element gives,

$$\phi^{(e)}(x) = \alpha_1{}^{(e)} + \alpha_2{}^{(e)} x \tag{3.17}$$

Physically, (3.17) gives the linear variation of ϕ, in terms of the coefficients α_i, which are known as the generalized coordinates of the element. The generalized coordinates are independent parameters and describe the magnitude of the variation of ϕ across the element, where the order of the polynomial describes the shape of the variation. The coefficients $\alpha_1^{(e)}$ *and* $\alpha_2^{(e)}$, may then be expressed in terms of the nodal values of ϕ and the spatial coordinates of each node by evaluating (3.17) at each node as,

$$\begin{aligned} \phi_1 &= \alpha_1 + \alpha_2 x_1 \\ \phi_2 &= \alpha_1 + \alpha_2 x_2 \end{aligned} \tag{3.18}$$

For convenience, (3.18) can be placed in matrix notation as,

$$\{\phi\} = [G]\{\alpha\}$$

$$\text{where,} \qquad \{\phi\} = \begin{bmatrix} \phi_1 \\ \phi_2 \end{bmatrix}, \quad [G] = \begin{bmatrix} 1 & x_1 \\ 1 & x_2 \end{bmatrix}, \quad \{\alpha\} = \begin{bmatrix} \alpha_1 \\ \alpha_2 \end{bmatrix} \tag{3.19}$$

Solving (3.19) for the generalized coordinates gives,

$$\{\alpha\} = [G]^{-1}\{\phi\} \tag{3.20}$$

If the original polynomial expression for ϕ (3.17), is written in terms of the product of a row vector and a column vector we can write,

$$\phi^{(e)} = \{P\}\{\alpha\}$$

$$\text{where} \qquad P = \begin{bmatrix} 1 & x \end{bmatrix} \tag{3.21}$$

Substituting (3.20) into (3.21) yields,

$$\phi^{(e)} = \{P\}[G]^{-1}\{\phi\}$$

$$\text{where} \qquad \{P\}[G]^{-1} = [N] \tag{3.22}$$

The matrix ***N***, contains the interpolation functions we seek. Using the symbolic matrix manipulation capability of Mathematica [119], the interpolations functions can be found by their definition in (3.22) as,

$$N_1 = \frac{x - x_2}{x_1 - x_2}, \quad N_2 = \frac{x - x_1}{x_2 - x_1} \tag{3.23}$$

The procedure outlined above is general and will work for one, two, or three dimensional problems. The result for the interpolation functions in one-dimension is relatively simple and computing the inverse of the ***G*** matrix is fairly simple; however, moving to two and three-dimensions makes calculating the inverse more challenging, and the resulting relations become complex functions of the nodal coordinates. For

convenience and to simplify the form of the interpolation functions, these terms can be expressed in terms of natural coordinates. Natural coordinates are local coordinates based on the element geometry and who's nodal coordinates range between zero and unity. Natural coordinates describe the location of a point within an element in terms of that elements nodal coordinates. For the one dimensional problem presented above the local coordinates are, x_1=0, and x_2=L, where L is the length of the element. Substituting the local coordinates into (3.23) and rearranging gives,

$$N_1 = 1 - \frac{x}{L}, \qquad N_2 = \frac{x}{L}$$

$$\text{in matrix form} \quad [N] = \begin{bmatrix} 1 - \dfrac{x}{L} \\ \dfrac{x}{L} \end{bmatrix} \tag{3.24}$$

Each of the interpolation functions in (3.24) varies from zero to unity, which is the desired result. Both components of the interpolation matrix in (3.24) are simple polynomial expressions which satisfy the compatibility and completeness requirements. Furthermore, they can be easily differentiated to obtain the gradient interpolation matrix ***B*** as,

$$[B] = \begin{bmatrix} -\dfrac{1}{L} & \dfrac{1}{L} \end{bmatrix} \tag{3.25}$$

The interpolation functions and gradient matrix for the one dimensional problem have been developed. Further development of the interpolation functions and gradient matrices in two and three dimensions will be presented in Chapter 4.

3.2.3 Surface Boundary Conditions

Returning back to Galerkin's weak form of the governing differential equation in (3.13), definitions for every term have been described with the exception of the natural boundary condition term that was introduced as a result of the integration by parts. With the interpolation functions defined, the natural boundary condition terms may now be evaluated. The boundary condition term is evaluated at the element end points where the interpolation functions are either zero or unity. Using the definition of the interpolation functions and the local coordinates given in (3.24), the natural boundary condition term is evaluated as,

$$\begin{aligned} i=1, \quad & N_i k_x \frac{\partial T}{\partial x_S}\bigg|_{x_{S_1}}^{x_{S_2}} = \cancel{N_1(L)^0} k_x \frac{dT}{dx_S} - \cancel{N_1(0)^1} k_x \frac{dT}{dx_S} = -k_x \frac{dT}{dx_S} \\ i=2, \quad & N_i k_x \frac{\partial T}{\partial x_S}\bigg|_{x_{S_1}}^{x_{S_2}} = \cancel{N_2(L)^1} k_x \frac{dT}{dx_S} - \cancel{N_2(0)^0} k_x \frac{dT}{dx_S} = k_x \frac{dT}{dx_S} \end{aligned} \tag{3.26}$$

Placing (3.26) in matrix form gives,

$$\{Q_{bc}\} = \begin{bmatrix} -k_x \dfrac{dT}{dx_S} \\ k_x \dfrac{dT}{dx_S} \end{bmatrix} \tag{3.27}$$

The terms at each of the nodal points in (3.26) and (3.27) physically represent the net amount of energy conducted into the material from the surroundings.

Assembly of the element equations into the global system of equations will not be fully discussed until section 3.3; however, we state here without proof that the boundary condition terms for all interior nodes will cancel leaving only the boundary condition terms on the external nodes exposed at the surface. Referring back to Figure 3.1, if it is further specified that the back wall is insulated, then there is no heat conducted into the

solid from the surroundings at that point and therefore the only term left is the one on the heated surface. Returning now to the surface energy balance given in equation (2.83) and the simplified form for equal diffusion coefficients in (2.84), the link between the finite element method and the ablation surface boundary conditions is now evident.

3.2.4 Final Form of the Element Equations

The element equations can now be written substituting the definition of the boundary condition term and changing the integration bounds to use the local coordinates,

$$\begin{aligned}\int_0^L \rho c_p [N][N]^T \{\dot{T}\} dx_S + \int_0^L [B]^T [k][B]\{T\} dx_S - \int_0^L \dot{S}\rho c_p [N][B]\{T\} dx_S \\ = \{Q_{bc}\} + \int_0^L \left[\dot{m}_g\right][B]^T [N]^T \{h_g\} dx_S + \int_0^L \left[(h_g - \bar{h})\right][N]\{\dot{\rho}\} dx_S\end{aligned} \tag{3.28}$$

Further simplification of (3.28) can be achieved by combining the matrix multiplications and integrations into single matrices as,

$$[C]^{(e)} \{\dot{T}\}^{(e)} + \left([K_c]^{(e)} - [K_{\dot{s}}]^{(e)}\right)\{T\}^{(e)} = \{R\}^{(e)} \tag{3.29}$$

Where the matrices in (3.29) are defined as,

$$\begin{aligned}[C]^{(e)} &= \int_0^L \rho c_p [N][N]^T dx_S \\ [K_c]^{(e)} &= \int_0^L [B]^T [k][B] dx_S, \qquad \text{where } [k] = k_x \text{ for 1-D} \\ [K_{\dot{s}}]^{(e)} &= \int_0^L \dot{S}\rho c_p [N][B] dx_S \\ \{R\}^{(e)} &= \{Q_{bc}\} + \{Q_p\} + \{Q_d\}\end{aligned} \tag{3.30}$$

and the vectors in the residual vector are defined as,

$$\left\{Q_{bc}\right\}^{(e)} = \begin{bmatrix} -k_x \dfrac{dT}{dx_S} \\ k_x \dfrac{dT}{dx_S} \end{bmatrix}$$

$$\left\{Q_p\right\}^{(e)} = \int_0^L \left[\dot{m}_g\right]\left[B\right]^T \left[N\right]^T \left\{h_g\right\} dx_S \tag{3.31}$$

$$\left\{Q_d\right\}^{(e)} = \int_0^L \left[(h_g - \bar{h})\right]\left[N\right]\left\{\dot{\rho}\right\} dx_S$$

The matrices $\boldsymbol{C}$, $\boldsymbol{K_c}$, and $\boldsymbol{R}$ are standard matrices that appear in every finite element formulation for heat transfer [58, 59, 61]. The matrix $\boldsymbol{C}$, is referred to as the capacitance matrix, $\boldsymbol{K_c}$ is the conductivity matrix, and $\boldsymbol{R}$ is the load vector. The matrix $\boldsymbol{K_{\dot{s}}}$ and the matrices $\boldsymbol{Q_p}$ and $\boldsymbol{Q_d}$ in the load vector are specific to the finite element formulation of the ablation thermal response problem. $\boldsymbol{K_{\dot{s}}}$ arises because the finite element grid moves as the material recedes and it is analogous to a convection matrix that would arise from the finite element formulation of a fluid flow problem. Hence, $\boldsymbol{K_{\dot{s}}}$ will be referred to as the convection matrix. $\boldsymbol{Q_p}$ is the load vector due to the pyrolysis gas flow through the material and will be referred to as the pyrolysis load vector. $\boldsymbol{Q_d}$ contains the term $(h_g - \bar{h})$ which is known as the heat of decomposition; hence $\boldsymbol{Q_d}$ will be referred to as the decomposition load vector.

The matrix multiplications and integrations for (3.30) and (3.31) are provided in Appendix B. For simplicity, the components of the matrices will be referred to symbolically herein. For example the conductivity matrix for an element would be referred to as,

$$\left[K_c\right] = \begin{bmatrix} K_{c_{11}} & -K_{c_{12}} \\ -K_{c_{12}} & K_{c_{22}} \end{bmatrix} \tag{3.32}$$

Notice that the conductivity matrix is symmetric. Also note that the negative signs are a result of the matrix multiplication and integration.

3.3 Global System of Equations

With the element equations defined, the task is now to take all of the element equations and assemble them into a global system of equations. The assembly procedure developed in [58 and 59] is followed here and is based on the insistence of compatibility at the element nodes. At the nodes, where elements are connected, the value of the unknown field variable is the same for all elements connected by that node. This rule forms the basis for the assembly procedure.

3.3.1 Assembly of the Element Equations

The element matrices and load vectors developed in section 3.2 can simply be thought of as submatrices and subvectors for the entire global system. The assembly procedure integrates the element submatrices and subvectors together. This is not done in a random fashion, since matrix addition is only defined for matrices and vectors of the same size. Therefore, before the element matrices can be added, they must be expanded to the size of the global system matrix. In Figure 3.1 there are 6 elements and 7 nodes. If the unknown field variable is the temperature, then each node has one degree of freedom and therefore for the 7 node example there needs to be 7 equations. Therefore the system matrix would be a square $n \times n$ matrix with n=7. The expanded element matrices are constructed using the original element matrices, only the coefficients of the original matrices are placed into the proper position within the expanded matrix using the element topology. For example consider the conductivity matrix for element number 3 in Figure 3.1. Using the topology defined in Table 3.1 for element number 3, the relationship between the local coefficients in the local element conductivity matrix and the global expanded conductivity matrix can be obtained directly,

$$
\begin{array}{lcl}
\textit{Local} & & \textit{Global} \\
K^{(3)}_{c_{11}} & \rightarrow & K_{c_{33}} \\
K^{(3)}_{c_{22}} & \rightarrow & K_{c_{44}} \\
K^{(3)}_{c_{12}} & \rightarrow & K_{c_{34}} \\
K^{(3)}_{c_{21}} & \rightarrow & K_{c_{43}}
\end{array}
\tag{3.33}
$$

In matrix notation, using the expanded matrix, the contribution of element number 3 to the global system becomes,

$$
\left[K_c\right]^{(3)} = \begin{bmatrix}
0 & 0 & 0 & 0 & 0 & 0 & 0 \\
0 & 0 & 0 & 0 & 0 & 0 & 0 \\
0 & 0 & K_{c_{33}} & K_{c_{34}} & 0 & 0 & 0 \\
0 & 0 & K_{c_{43}} & K_{c_{44}} & 0 & 0 & 0 \\
0 & 0 & 0 & 0 & 0 & 0 & 0 \\
0 & 0 & 0 & 0 & 0 & 0 & 0 \\
0 & 0 & 0 & 0 & 0 & 0 & 0
\end{bmatrix}
\tag{3.34}
$$

The above procedure can be followed for all of the elements in Figure 3.1 and the global conductivity matrix is then just the sum of all the expanded element conductivity matrices which gives,

$$
\left[K_c\right] = \begin{bmatrix}
K^{(1)}_{c_{11}} & K^{(1)}_{c_{12}} & 0 & 0 & 0 & 0 & 0 \\
K^{(1)}_{c_{21}} & K^{(1)}_{c_{22}} + K^{(2)}_{c_{22}} & K^{(2)}_{c_{23}} & 0 & 0 & 0 & 0 \\
0 & K^{(2)}_{c_{32}} & K^{(2)}_{c_{33}} + K^{(3)}_{c_{33}} & K^{(3)}_{c_{34}} & 0 & 0 & 0 \\
0 & 0 & K^{(3)}_{c_{43}} & K^{(3)}_{c_{44}} + K^{(4)}_{c_{44}} & K^{(4)}_{c_{45}} & 0 & 0 \\
0 & 0 & 0 & K^{(4)}_{c_{54}} & K^{(4)}_{c_{55}} + K^{(5)}_{c_{55}} & K^{(5)}_{c_{56}} & 0 \\
0 & 0 & 0 & 0 & K^{(5)}_{c_{65}} & K^{(5)}_{c_{66}} + K^{(6)}_{c_{66}} & K^{(6)}_{c_{67}} \\
0 & 0 & 0 & 0 & 0 & K^{(6)}_{c_{76}} & K^{(6)}_{c_{77}}
\end{bmatrix}
\tag{3.35}
$$

For clarity, the superscript numbers in parenthesis refer to the element from which that coefficient came. This procedure is the same for all of the element matrices and applies

to the element load vectors as well. Writing the assembly procedure mathematically gives,

$$[K] = \sum_{e=1}^{m} [K]^{(e)}$$
$$\{R\} = \sum_{e=1}^{m} \{R\}^{(e)} \tag{3.36}$$

Where $\boldsymbol{K}$ and $\boldsymbol{R}$ are any matrix and load vector and m is the number of elements in the system.

The assembly procedure was demonstrated for a simple 6 element example. In practice, there will be many more elements to assemble. Typically the assembly procedure is automated within the computer program used to solve the global system of equations. The assembly procedure summarized by Huebner, et. al. [58] is as follows:

1. Setup n x n and n x 1 matrices with zero entries, where n is the number of system nodal variables.
2. Starting with one element, transform the element equations from local coordinates to global coordinates if these two coordinate systems are coincident.
3. Perform any necessary matrix operations on the element matrices.
4. Using the element topology relating the local element node numbers to the global node numbers, change the subscript indices of the coefficients in the element matrices and the single subscript index of the element load vectors
5. Insert those terms in the corresponding n x n and n x 1 matrices in the locations designated by their new indices. Each time a term is placed in a location where another term has already been placed, it is added to whatever value is there.

6. Return to step 2 and repeat this procedure for all the elements in the system. The result will be the global system of equations expressed mathematically as,

$$\overset{nxn}{[K]}\overset{nx1}{\{x\}} = \overset{nx1}{\{R\}} \tag{3.37}$$

After assembly, the global system of equations becomes,

$$[C]\{\dot{T}\} + \left([K_c] - [K_{\dot{s}}]\right)\{T\} = \{R\} \tag{3.38}$$

The system of equations in (3.38) are in the same form as the element equations in (3.29) and the matrices retain their meaning, only now they are all global matrices and vectors. The system of equations in (3.38) are highly non-linear for several reasons. First, the surface energy balance on the heated surface boundary includes re-radiation to the surroundings. Radiation to the surroundings is a function of the nodal unknown temperature on the boundary raised to the fourth power, producing a non-linear response. Second, the material properties and ablation parameters are functions of temperature which also causes the response to be non-linear. Specifically, the thermal conductivity *k,* specific heat c_p, h_w, h_g, $\overline{h}$, $\sum Z_i^*$, $B_g^{'}$, and $B_c^{'}$ are functions of temperature. $\sum Z_i^*$, $B_g^{'}$, $B_c^{'}$, and h_g are also functions of pressure, but this pressure dependence does not contribute to the nonlinearity since the pressure is constant at any given point in time. Finally, the density, which in most heat transfer problems is a constant, is a temperature dependant variable in the ablation problem.

3.4 Nonlinear Transient Solution

The system of equations presented in (3.38) is a set of non-linear equations in which a transient solution is sought. To solve the transient problem, a time marching scheme is needed. There are two main methods used to solve transient finite element problems, the method of mode superposition and numerical integration [58]. Mode superposition is

better suited for second-order matrix equations than for first-order equations, and is widely used in structural dynamics. The matrix equations here are first-order and since it is also desirable to output results at discrete points in time, a numerical integration time marching scheme will be used.

3.4.1 Numerical Integration

Numerical integration relies on recurrence relations developed by making finite difference approximations in the time domain. Let t_n denote a time in the transient response, such that $t_{n+1} = t_n + \Delta t$, where Δt is the time step. If an intermediate time is defined within a time step, denoted t_θ, then a general family of algorithms results such that $t_\theta = t_n + \theta \cdot \Delta t$, where $0 \le \theta \le 1$ [58, 120]. The system of equations is then evaluated at time t_θ and written in a form to indicate which matrices have a functional dependence on temperature and time,

$$\left[C(T_\theta)\right]\left\{\dot{T}\right\}_\theta + \left[\left[K_c(T_\theta, t_\theta)\right] - \left[K_{\dot{s}}(T_\theta, t_\theta)\right]\right]\left\{T\right\}_\theta = \left\{R(T_\theta, t_\theta)\right\} \tag{3.39}$$

The subscript θ indicates the temperature vector is evaluated at time θ. Defining the temperature vector and the derivative of the temperature with respect to time as,

$$\begin{aligned} \left\{\dot{T}\right\}_\theta &= \frac{\left\{T\right\}_{n+1} - \left\{T\right\}_n}{\Delta t} \\ \left\{T\right\}_\theta &= (1-\theta)\left\{T\right\}_n + \theta\left\{T\right\}_{n+1} \end{aligned} \tag{3.40}$$

Substituting (3.40) into (3.39) gives,

$$\begin{aligned} &\left(\theta\left[\left[K_c(T_\theta, t_\theta)\right] - \left[K_{\dot{s}}(T_\theta, t_\theta)\right]\right] + \frac{1}{\Delta t}\left[C(T_\theta)\right]\right)\left\{T\right\}_{n+1} \\ &= \left(-(1-\theta)\left[\left[K_c(T_\theta, t_\theta)\right] - \left[K_{\dot{s}}(T_\theta, t_\theta)\right]\right] + \frac{1}{\Delta t}\left[C(T_\theta)\right]\right)\left\{T\right\}_n + \left\{R(T_\theta, t_\theta)\right\} \end{aligned} \tag{3.41}$$

Where $\{T\}_{n+1}$ and $\{T\}_{\theta}$ are unknowns and $\{T\}_{n}$ is known from the previous time step. The family of algorithms represented by (3.41) can be classified as either explicit or implicit based on the value of θ. If θ=0, the algorithm is explicit and reduces to a set of uncoupled algebraic equations. If θ>0, the algorithm is implicit and requires solution of a set of coupled algebraic equations. Hughes [121] shows (3.41) to be unconditionally stable when $\theta \geq \frac{1}{2}$. When $\theta < \frac{1}{2}$, (3.41) becomes conditionally stable and is subject to time step restraints. In other words, the time step must be chosen such that it is smaller than a critical time step given as,

$$\Delta t_{cr} = \frac{2}{1-2\theta}\frac{1}{\lambda_m} \tag{3.42}$$

where λ_m is the largest eigenvalue of the system. Since the solution of these equations will be used in a repetitive design calculation, it is desirable to avoid issues related to the time step and make the solution insensitive (from a computational standpoint) to the time step chosen. Therefore the fully implicit, or backward difference algorithm was chosen for this implementation (θ=1). With θ=1, the transient system of equations becomes,

$$\left(\left[\left[K_c(T_{n+1},t_\theta)\right]-\left[K_{\dot{s}}(T_{n+1},t_\theta)\right]\right]+\frac{1}{\Delta t}\left[C(T_{n+1})\right]\right)\{T\}_{n+1} = \frac{1}{\Delta t}\left[C(T_{n+1})\right]\{T\}_{n}+\{R(T_{n+1},t_\theta)\} \tag{3.43}$$

where $\{T\}_{\theta} = \{T\}_{n+1}$

3.4.2 Newton-Raphson Method

Since the coefficient matrices in (3.43) are functions of temperature and therefore are nonlinear, an iterative solution must be used. The Newton-Raphson method is an iterative scheme used to solve non-linear equations and is one of the most common methods for solving nonlinear sets of equations due to the ease at which it can be

implemented. The details of the Newton-Raphson Method are given in Appendix A [58, 109, 122, 123].

3.4.3 Sparse Matrix Solver PARDISO

The matrices developed as a result of the global matrix assembly process contain a large number of elements that are zero. In mathematical terms, this is known as a sparse matrix. In order to efficiently utilize computer memory, only the non-zero elements of the matrix should be stored and manipulated by the solver. To accomplish this, the matrix is stored in Compression Sparse Row, or CSR sparse matrix format and the solver PARDISO is used to solve the linear matrix that arises from the Newton-Raphson method. PARDISO is an acronym which stands for Parallel Sparse Direct Solver and is included as part of the Intel Math Kernel Library [124].

3.5 Comparison of the One-Dimensional Analysis with FIAT

In this investigation, a numerical procedure for the solution of the one-dimensional finite element ablation problem and has been written in a mixture of C++ and FORTRAN. C++ was chosen to control the data management and input/output operations of the program over FORTRAN because of its superior capabilities in this area, albeit at the expense of some efficiency. The matrix computations and solver are written in FORTRAN due its superior numerical computation speed and the ease at which computations can be parallelized.

In this section the present tool is compared with the industry standard, one-dimensional finite difference tool FIAT for series of verification cases that exercise various components of the code. The approach taken was to exercise this new analysis method starting with a simple case then moving forward to validate cases with increased complexity. The first case is a simple transient conduction problem where the material is Titanium, a non-ablator. The second case examines reinforced carbon-carbon, a material

that will ablate, but is not a pyrolyzing material. The third case analyzes MX4926N carbon phenolic which is a material that will both pyrolyze and ablate. A low peak heat flux entry trajectory is used for this case because it will not cause the material to ablate and only pyrolysis will occur. The final verification test case is an arc jet test boundary condition on MX4926N carbon phenolic. The arc jet test condition is a severe test case that will cause the material to both ablate and pyrolyze. The boundary conditions in all cases, except the arc jet case, consist of an applied heat flux as a function of time and radiation away from the surface. In the arc jet case the applied heat flux is a constant and there is also radiation away from the surface. For all the cases run, both codes have the same number of computational nodes, but the physical depth of the interior nodes varies slightly. A summary of the test problems and their conditions is shown in Table 3.2 and the corresponding heating boundary condition profiles for the first three cases are provided in Figure 3.2. The geometry chosen for each verification case consisted of a one-dimensional slice through the material which was 7.62cm in length and had 39 elements and 40 nodes. The same number of nodes was used for the FIAT solution in each verification case.

Table 3.2: Verification case summary

Case	Description	Material	Boundary Conditions
1	Entry trajectory	Titanium (Ti-6Al-4V), thermal properties a function of temperature	Input convective and radiative heat flux a function of time, surface radiation away from the heated surface, no pyrolysis, no ablation
2	Entry trajectory	Reinforced Carbon-Carbon, thermal properties a function of temperature	Input convective and radiative heat flux a function of time, surface radiation away from the heated surface, no pyrolysis, ablation
3	Entry trajectory	MX4926N Carbon Phenolic, thermal properties a function of temperature	Input convective and radiative heat flux a function of time, surface radiation away from the heated surface, pyrolysis, no ablation
4	Arc jet test, i.e. constant heat flux	MX4926N Carbon Phenolic, thermal properties a function of temperature	Input convective and radiative heat flux constant, surface radiation away from the heated surface, pyrolysis, ablation

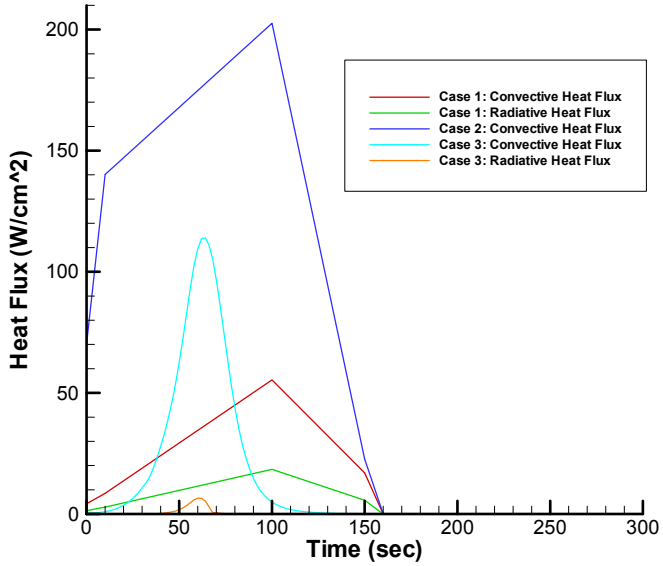

Figure 3.2: Verification case heat flux profiles

3.5.1 Verification Case 1: Low Peak Heat Flux Trajectory, No Ablation, No Pyrolysis

The first verification case is a simple heat conduction problem which eliminates the complicating effects of surface recession and pyrolysis. The goal of this case was to demonstrate that the finite element codes' conduction model and the non-linear sparse matrix solver were functioning correctly. The non-linearity in the problem arises due to the surface radiation boundary condition and the thermal properties that are functions of temperature.

The material chosen for this verification run was Ti-6Al-4V titanium alloy, which is a metallic, non-ablative material. The heating environment consisted of a simulated trajectory containing both convective and radiative heating. The peak heat flux for this trajectory is 73 W/cm^2 which is low enough to avoid the complicating effects of melting.

The heat flux was applied over 160 seconds, and was followed by a cool down period of 640 seconds where surface radiation away was the only active boundary condition.

Comparison of the time history of the surface temperature and selected in-depth temperatures for the present tool with FIAT is shown in Figure 3.3. In Figure 3.3, there is no difference in temperature between the present tool and FIAT. This case validates a number of features in the present tool. It validates the internal conduction calculations and the implementation of the non-linear solver. This comparison also validates the application of boundary conditions and the interpolation of the temperature dependent material properties.

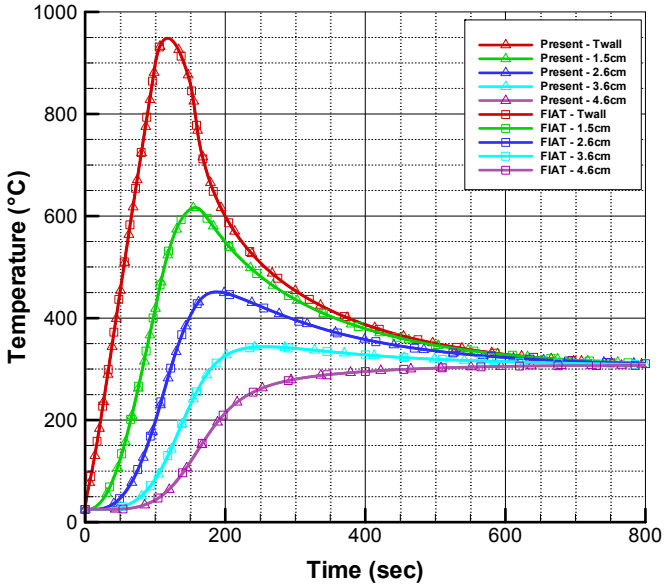

Figure 3.3: Temperature comparison for Titanium alloy, 73 W/cm^2 peak heat flux

3.5.2 Verification Case 2: Moderate Peak Heat Flux Trajectory, With Ablation, No Pyrolysis

The second verification case analyzes a reinforced carbon-carbon specimen. This case demonstrates that the present tool accurately calculates surface recession and exercises the code's moving grid scheme in the absence of the complicating effects of decomposition and pyrolysis gas flow. In this case, there was no radiative heating input as a surface boundary condition, only convective heating input as a simulated trajectory. The peak heat flux was 200 W/cm^2 and was chosen so that the material would reach a

temperature regime where recession would occur. The results from this analysis match closely to those generated by FIAT. A graphical comparison of the temperatures is provided in Figure 3.4

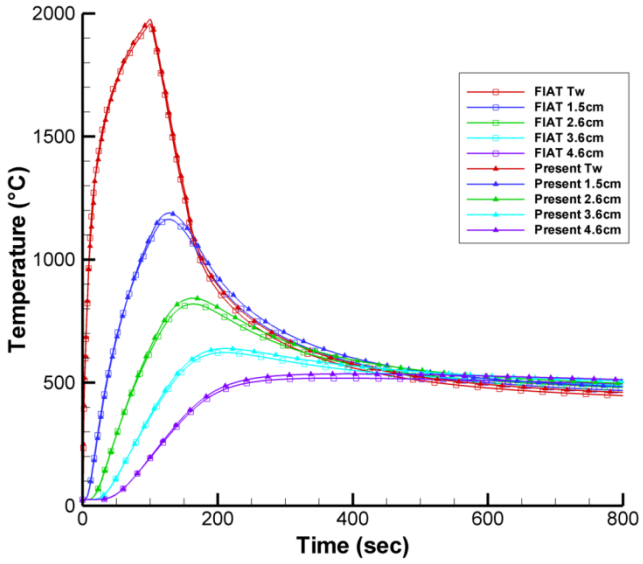

Figure 3.4: Temperature comparison for reinforced carbon-carbon, ablation, no pyrolysis

The root mean square (RMS) errors for the surface and in-depth temperatures over the entire 800 second trajectory are summarized in Table 3.3. The percent difference in peak temperature for the surface and the selected in-depth locations are given in Table 3.3 as well. The total recession predicted by the present tool matches the total recession predicted by FIAT well. A comparison of the recession and recession rate is provided in Figure 3.5. The recession rates also match, albeit there is some jaggedness in the FIAT recession rate. This is an artifact of calculating the rate after the fact using the FIAT recession output which does not contain enough significant figures to provide a smooth recession rate. The recession calculated by the present tool was 1.434mm, and that calculated by FIAT was 1.435mm. This case demonstrates that the present tool

Table 3.3: Temperature error and percent difference in peak temperature

	Surface	1.5 cm	2.6 cm	3.6 cm	4.6 cm
RMS	11.7°C	13.4°C	14.3°C	13.5°C	12.5°C
Peak diff.	0.65%	2.31%	3.46%	3.25%	2.79%

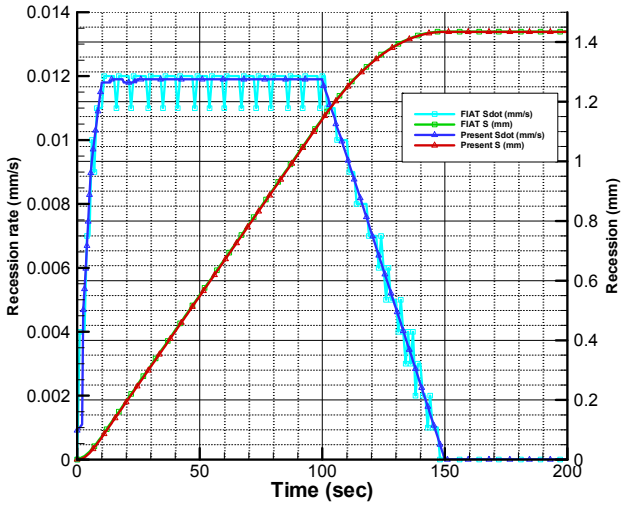

Figure 3.5: Recession and recession rate comparison for reinforced carbon-carbon, 130 W/cm^2

is calculating B'_c and using it correctly in the surface boundary conditions.

It is important to point out a significant difference between the present tool and FIAT. In FIAT, the set of nodal equations developed do not solve for the nodal temperatures, but solve for the nodal heat flux. FIAT forms the surface energy balance given in (2.84) which has been repeated here for convenience as (3.44). The left hand side of (3.44) is the net conductive flux into the material at the surface. For each iteration within a given time step, FIAT solves for this conductive flux at the surface. FIAT uses

$$-k\frac{dT}{dx} = \rho_e U_e C_H \left(H_{sr} - h_{sw} + B'_c h_c + B'_g h_g - B' h_w \right) - q^* + q_{\underset{out}{rad}} - \alpha q_{\underset{in}{rad}} \qquad (3.44)$$

the conductive flux at the surface as a boundary condition for the in-depth solution. The in-depth solution in FIAT simultaneously solves for each of the nodal heat fluxes. Then, the nodal temperatures are calculated using Fourier's law. The resulting surface temperature is fed back into the surface energy balance to update the terms that are functions of temperature. This series of calculations is repeated until convergence is achieved. In the present tool, the surface energy balance is included directly in the matrix

equations which solve simultaneously for the nodal temperatures. The boundary condition terms that are functions of temperature are updated every iteration and the simultaneous solution is repeated. This process continues until convergence is achieved.

While the two methods are fundamentally similar and reach the same desired result of computing temperatures, the numerical path taken to achieve that goal is different. This difference makes it unlikely that the present tool and FIAT will achieve an exact match for the temperatures. If the surface temperatures don't match exactly, then as a result, the recession and recession rates will be slightly different. If different amounts of material are being removed from the surface, the in-depth temperatures will be affected since there is a different amount of thermal mass in each mesh. Note however that the character of the curves is the same.

3.5.3 Verification Case 3: Low Peak Heat Flux Trajectory, No Ablation, With Pyrolysis

Comparison of the temperatures for the present tool with FIAT for a low peak heat flux trajectory is shown in Figure 3.6. The material chosen for this verification run was MX4926N carbon phenolic, which is a high density carbon based ablator. The carbon phenolic was 7.33cm thick and was stacked on top of 0.635cm of Ti-6Al-4V titanium alloy. The peak heat flux of 110 W/cm^2 was not high enough in this case to cause the material to recede, but was high enough to cause material decomposition and pyrolysis gas flow. The goal of this verification case was to verify the finite element code was calculating the in-depth decomposition and pyrolysis gas flow correctly in the absence of the complicating effects of surface recession.

The present solution over predicts the peak surface temperature by 23.5°C (less than 2%), but the character of the curves are the same and the difference away from the peak is minimal. The in-depth temperatures match well, even though there is a difference in the surface temperature at the peak. There are two small anomalies in the surface

temperature, one near the peak, the other at about 155 seconds. Both the present solution and FIAT show sudden temperature discontinuities at those locations. These anomalies are due to sudden changes in the heating boundary conditions at those times (see Figure 3.2). Near the peak, the radiative heating drops sharply to zero. At 155 seconds, the recovery enthalpy component of the convective heating drops rapidly.

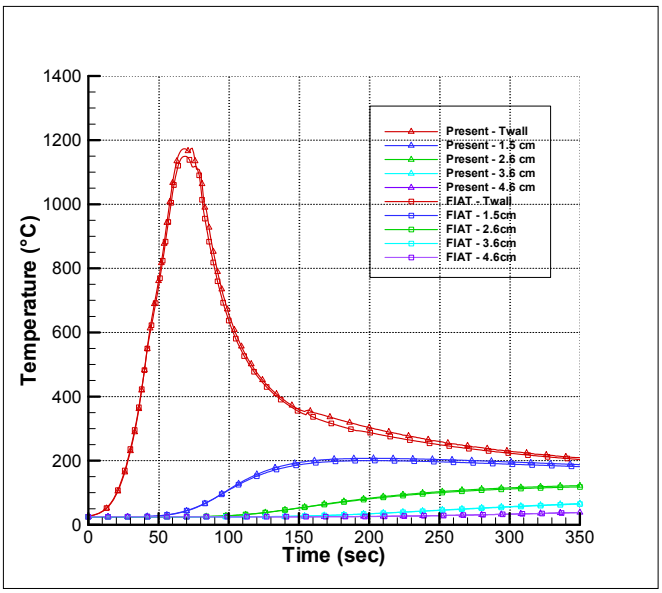

Figure 3.6: Temperature comparison for MX4926N carbon phenolic, no ablation, with pyrolysis

Figure 3.7 shows the pyrolysis gas flow at the surface of the material over the entire trajectory. The shape and timing between the two solutions matches quite well with the exception near the peak where the finite element solution shows oscillatory behavior. The finite element solution for the pyrolysis gas mass flux oscillates because it is calculated explicitly. In the solution of the finite element equations, the temperatures are calculated implicitly, however, the decomposition of the material is calculated first using the temperature at the beginning of the time step, i.e. the old temperatures. This explicit decomposition rate is then used to calculate the pyrolysis gas flow. FIAT on the

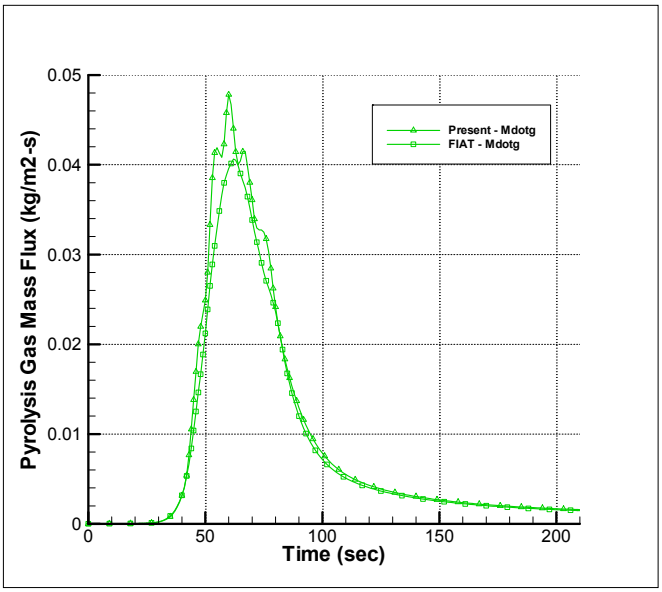

Figure 3.7: Pyrolysis gas mass flux at the surface

other hand, solves for the decomposition rates and pyrolysis gas mass flux simultaneously with the calculation of the nodal heat flux; as a result it is fully implicit and oscillates much less. The consequence of the explicit decomposition calculation is that these pyrolysis gas mass flux oscillations will be transferred to B'_g when it is calculated via equation (2.80) and as a result, the recession calculation between the two codes will be slightly different. The oscillating decomposition may also cause the in-depth temperatures to be different as well since the char and pyrolysis depths will not match exactly which will cause small differences in the in-depth densities, thermal conductivity and specific heat.

The oscillation in the pyrolysis gas mass flux is a limitation of the current method that can be mitigated by using a finer mesh in the finite element code. The affect of the time step on the oscillations will be discussed in Section 3.5.5. For this case as well as the previous two verification cases, the mesh used in both the present tool and FIAT were the same and contained 40 nodes. The mesh in both the FIAT solution and the present solution are biased towards the heated surface so there are more nodes near the region where pyrolysis is occurring. For this current verification case, the mesh was refined and

31 elements were added to the mesh. After mesh refinement the same biased grid strategy was used. The improved pyrolysis gas mass flux calculation is presented in Figure 3.8. The temperatures for the refined mesh case did not change appreciably. This result demonstrates that a finer mesh density, as required for the decomposition calculation, is not required to increase the accuracy of the temperature predictions. The surface temperature and the temperature at the 2.6cm in-depth location are shown in Figure 3.9 for the coarse and refined mesh runs. As seen in Figure 3.9, the temperature is insensitive to the mesh density for this verification case.

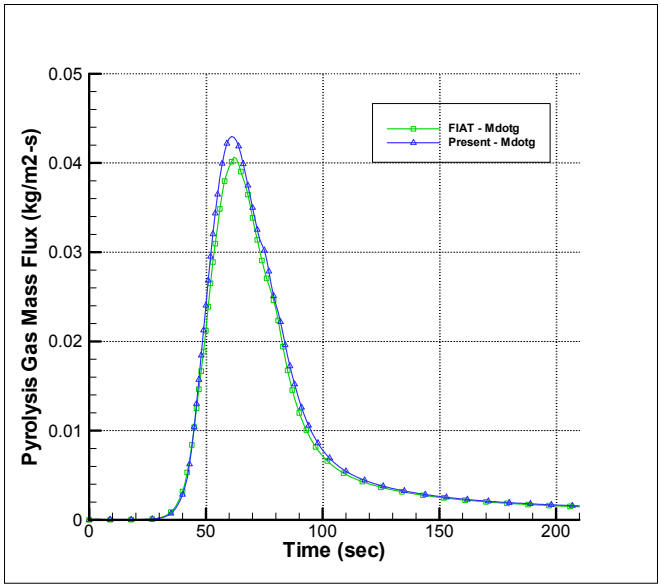

Figure 3.8: Pyrolysis gas mass flux at the surface with the refined mesh

In lieu of increasing the mesh density which can have a detrimental effect on the computational run time, there are two possible solutions to this oscillation problem. Evaluation of these potential solutions is considered as future work. The first approach is to make the decomposition calculation implicit along with the temperature calculation. The second is to develop higher order elements where the number of nodes per element is increased. Both of these options will be expanded upon in Chapter 6 in the future work section.

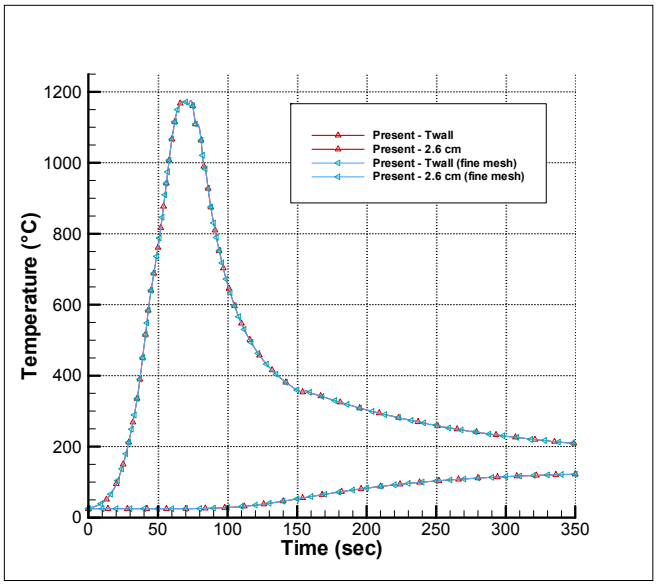

Figure 3.9: Temperature sensitivity to mesh density

3.5.4 Verification Case 4: High Heat Flux Arc Jet Test Condition

The final verification case compares the present tool and FIAT with data from an arc jet test at a high heat flux for a 200 second exposure, followed by a 400 second cool down period. The centerline enthalpy for the test was estimated from facility correlation equations to be approximately 80 MJ/kg. The pressure achieved during the test was less than 0.1 atm. In addition, a simple Monte Carlo simulation was run using the present tool and the results compared to the data. The material exposed in the arc jet test was MX4926N carbon phenolic with a thickness of 6.35cm. For insulation, 6.02cm of LI-2200 was placed behind the carbon phenolic. The arc jet model used for the test series is shown in Figure 3.10.

The arc jet condition provides a constant heat flux boundary condition environment which is high enough in magnitude and long enough in duration to cause surface recession for this material. The heat flux is input as a step function, so it is also a good test of the solution algorithms' stability under a high gradient condition. During the cool down, the material radiates heat away and conducts heat into the material away from the

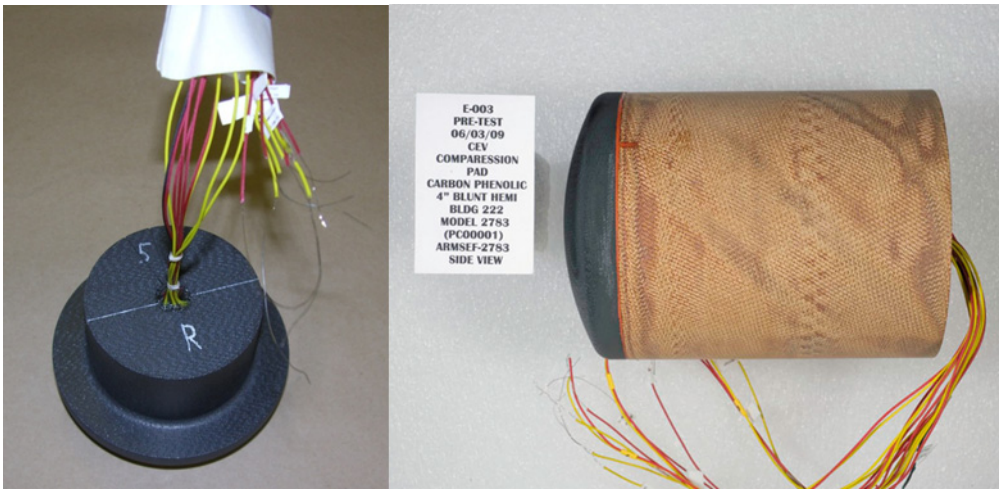

Figure 3.10: MX4926N carbon phenolic arc jet test model

exposed surface. During cool down a significant temperature gradient develops through the thickness of the material and allows comparison of in-depth temperatures.

The temperatures calculated by both the present tool and FIAT are shown along with the data taken from test number 2784 in Figure 3.11. The surface temperatures predicted during the heated portion of the run for the present tool match FIAT quite well, differing by less than 4.0°C over the duration of the exposure Comparing with the pyrometer data, both FIAT and the present tool match well until the pyrometer becomes

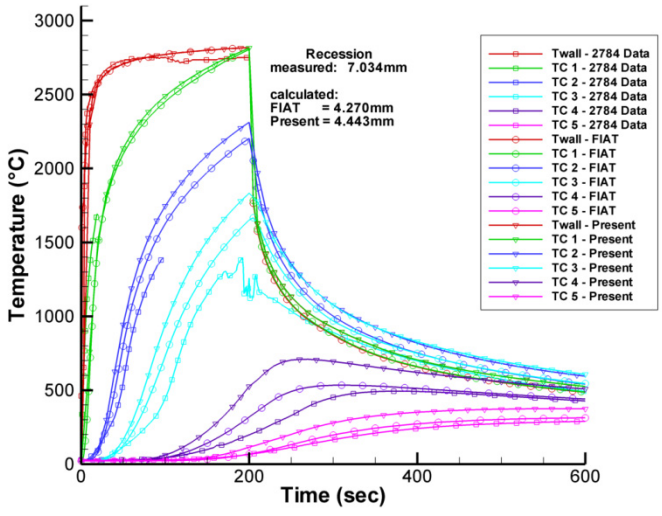

Figure 3.11: Temperature comparison for MX4926N arc jet test condition

unstable and drops suddenly at around 90 seconds into the run. It is important to note that small differences in surface temperature can lead to significant differences in the calculation of B'_c and hence the predicted recession. For example, for MX4926N carbon phenolic at 0.1 atm, and a B'_g equal to 0.4, a 25°C temperature difference causes a 12.5% difference in B'_c. In this verification case, the magnitude of the difference in the surface temperature does not appear to have adversely affected B'_c and the calculated recession which differed by less than 4% between the present tool and FIAT. There was a fairly significant difference between the measured recession and the calculated recession which can be attributed to the arc jet test conditions.

The actual arc jet test conditions are estimated via correlation equations and calorimeter data taken during the testing. The two most important parameters related to the recession are the estimated centerline enthalpy and the heat flux. Recall from Section 2.2.1.2 that the heat transfer coefficient is calculated by dividing the heat flux by the recovery enthalpy. More importantly, recall from Section 2.2.1.3, the non-dimensional ablation rate is calculated by dividing the char mass flux at the surface by the heat transfer coefficient. There is a large amount of uncertainly in estimating the centerline enthalpy with a correlation equation; this uncertainly propagates into the calculation of the heat transfer coefficient and into the recession calculation. Given that the actual test conditions have some uncertainty associated with them, it is not surprising the calculated recession differs from the measured value.

The in-depth temperatures at five different locations are shown in Figure 3.11 as well. The depths for this case are provided in Table 3.4 and correspond to the actual locations of the thermocouples in the arc jet model. The in-depth temperatures, without the surface temperature plotted, are shown in Figure 3.12 and show that, in general, the present tool compares well with the FIAT results showing the same character in the curves. Relative to FIAT, the present tool however over predicts the temperatures slightly and the over prediction becomes larger as you move from the surface towards the

Table 3.4: In-depth thermocouple locations for arc jet test specimen

Location Designation	Depth (cm)
TC1	0.442
TC2	1.153
TC3	1.786
TC4	3.208
TC5	4.265

bondline. This behavior is a result of the manner in which the present tool and FIAT calculate decomposition, leading to different char and pyrolysis penetration depths.

The char penetration depth at any instant in time is the location where the fraction of virgin material present is less than 2%. The pyrolysis front is the location where there is still greater than 98% virgin material remaining. In the present tool, the char penetration depth is 2.57cm after the 200 second exposure period, which is 12.89% deeper than that predicted by FIAT. By the end of the 600 second run, the char in the present tool has penetrated to a depth of 2.98cm, or 13.70% deeper than the FIAT

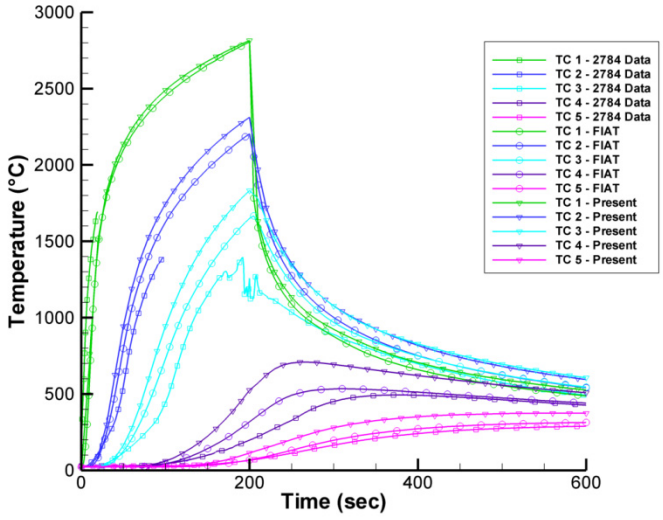

Figure 3.12: In-depth temperature comparison for MX4926N arc jet test condition

prediction. The thermal conductivity of the char is much greater than that of the virgin material and allows more heat to be conducted through it, so the consequence of having the char penetrate deeper into the specimen is higher in-depth temperatures.

The first in-depth location for the present tool, TC1, compares well with the results from FIAT and both the present tool and FIAT compare well with the arc jet data. Moving from TC1 to TC5 the over prediction between the present tool and FIAT grows because of the difference in char depth. Additionally, both the present tool and FIAT over predict the in-depth thermocouple data. This over prediction is likely caused by the difference in the material property model being used in the calculation and in the actual material being tested. The material response model was derived from arc jet test data for a different version of carbon phenolic known as FM5055. This type of carbon phenolic is made from different precursor rayon fibers and a different phenolic resin than the MX4926N. Although the two versions of carbon phenolic are very similar, there are small differences in the decomposition kinetics and the virgin and char thermal conductivities which could very well lead to the differences seen here.

Figure 3.13 shows the surface recession and recession rates calculated by the present tool and FIAT. Also given in Figure 3.13 is the average recession history for the arc jet test calculated using an average recession rate and the total measured recession. As the plot shows, the total recession calculated by the present tool compares well with the FIAT prediction and is 0.173mm, or 4.05% higher. This small difference can be attributed to the small difference in surface temperature. Both the present tool and FIAT under predict the experimentally measured recession by 2.591mm and 2.764mm respectively.

Figure 3.14 shows a comparison of the pyrolysis gas flow rate at the surface. Figure 3.15 shows a close up view of the pyrolysis gas flow during the first 60 seconds of the arc jet exposure. This plot is consistent with the behavior observed in the third

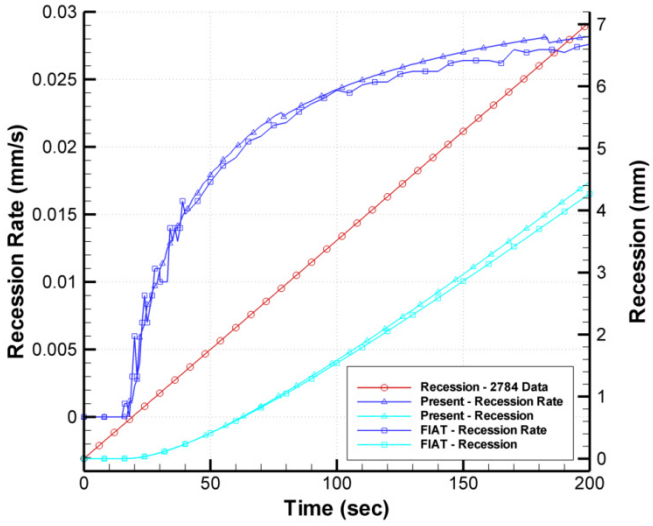

Figure 3.13: Recession and recession rate comparison for MX4926N arc jet test condition

verification case, and in large part the third verification case proved valuable in choosing an appropriate mesh density for this case. One interesting feature is that although FIAT is fully implicit, this extreme boundary condition causes its pyrolysis gas flow to oscillate as well which can be seen in Figure 3.15. For this verification case, there were 18 more nodes in the present tool's grid than in the FIAT grid. This suggests that the implicit solution scheme alone cannot totally eliminate the oscillations in the pyrolysis gas flow calculation and that there is also dependency on the computational grid size.

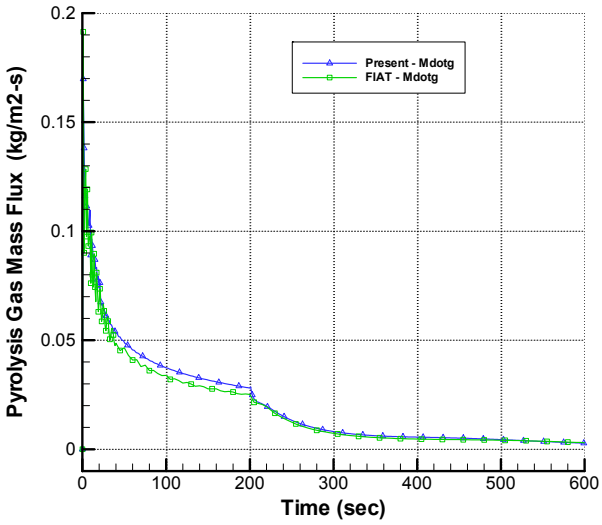

Figure 3.14: Pyrolysis gas flow rate comparison at the surface for MX4926N arc jet test condition

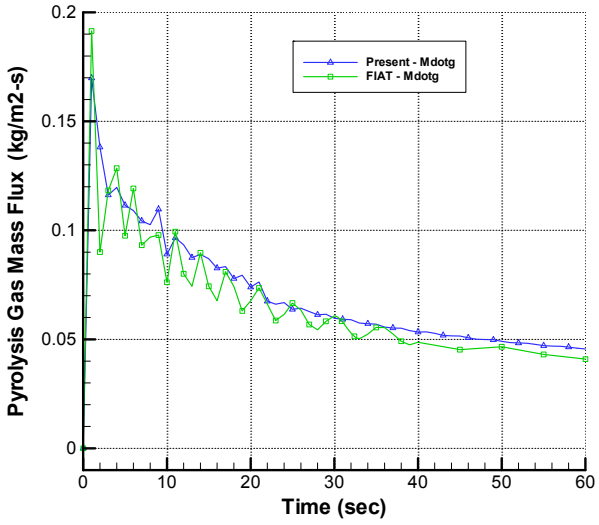

Figure 3.15: Pyrolysis gas flow rate comparison at the surface for MX4926N, first 60 seconds

3.5.4.1 Arc Jet Monte Carlo Simulation

In addition to comparing the results from the present tool and FIAT with the arc jet data, a 2000 sample Monte Carlo simulation was performed with the present tool. The goal was to determine whether the arc jet data could be bounded by the $\pm 3\sigma$ temperatures for the thermocouples and surface temperature. To keep the analysis

simple, five parameters were chosen to be statistically varied and are summarized in Table 3.5.

Table 3.5: Summary of statistically varied parameters

Property	3σ Uncertainty	Uncertainty Evaluation Method
Virgin thermal conductivity	±0.45 W/m-K	1
Char thermal conductivity	±0.88 W/m-K	1
Virgin density (room temp)	±6.3% kg/m^3	1
Char Emissivity	±0.06375	1
Heat transfer coefficient	±20.00% kg/m^2-s	6

The surface temperature upper and lower bounds compared to the data are given in Figure 3.16. The surface temperature pyrometer data is bounded by the $\pm 3\sigma$ temperature bounds, and more importantly, the calculated recession also bounds the measured recession.

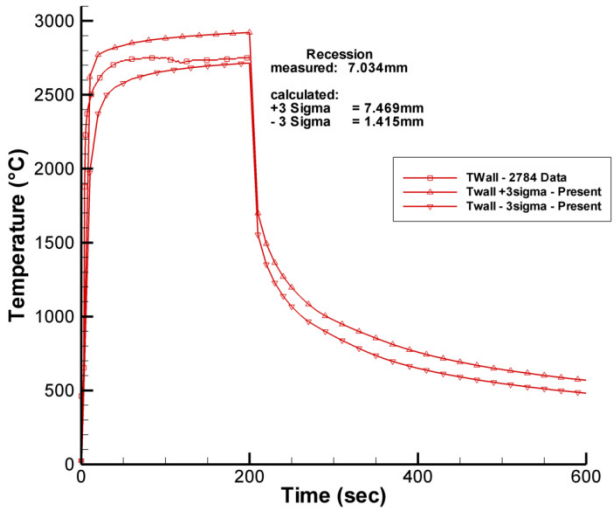

Figure 3.16: Surface temperature bounds

The in-depth temperature data along with the $\pm 3\sigma$ temperature bounds are given in Figure 3.17. In general the data is bounded by the $\pm 3\sigma$ temperature, however, it is very close to the lower bound. This is due once again to the differences in the material response model and the actual material being tested. Furthermore, the Monte Carlo simulation only varied five parameters. Many more parameters could have been statistically varied and accounted for additional uncertainty and served to widen the $\pm 3\sigma$ temperature bounds.

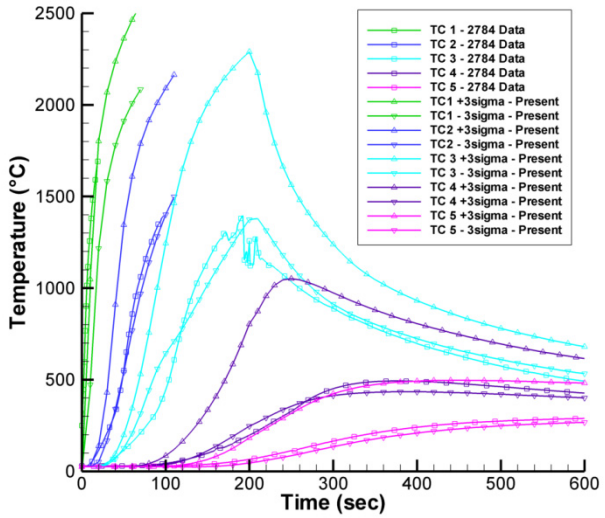

Figure 3.17: In-depth temperature bounds

3.5.5 One-Dimensional Mesh and Time Step Sensitivity

The element length, as well as the time step can directly affect the convergence and numerical stability of the solution. Non-linearities, such as material properties that are a function of temperature, radiation boundary conditions, and high temperature gradients may also affect convergence. In Section 3.5.3, it was observed that an increased number of elements decreased the oscillations in the pyrolysis gas flow solution. It was also observed that the temperature difference between the two different mesh densities was negligible but the heat flux for that case was fairly benign. In this section the effect of

the mesh density and also time step will be examined under a high heat flux boundary condition.

A simulation using the Genesis entry vehicle trajectory was run using three different one-dimensional mesh densities. Then the medium mesh density case was run for three different constant time steps. The combined Genesis entry heating reaches 608 W/cm^2 and is given in Figure 3.18. The one-dimensional geometry was a 7.62cm thick MX4926N carbon phenolic rod. The mesh for the first case had 24 elements of equal length (25 nodes), the second had 42 elements of equal length (43 nodes), and the third had 79 elements of equal length (80 nodes).

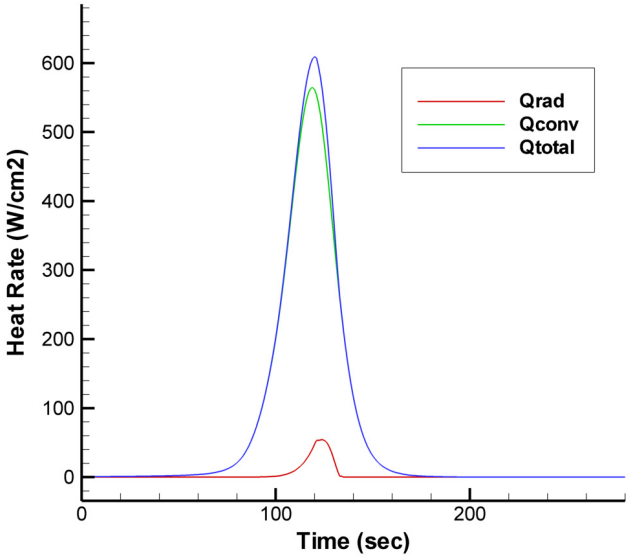

Figure 3.18: Genesis convective and radiative heating

The pyrolysis gas flow for the three mesh densities is shown in Figure 3.19. It can be clearly seen that for each successive mesh refinement, the oscillation in the pyrolysis gas mass flux diminishes. This shows the decomposition and hence the pyrolysis gas flow calculations are highly sensitive to the element length. This is mainly due to the explicit nature in which these calculations are made.

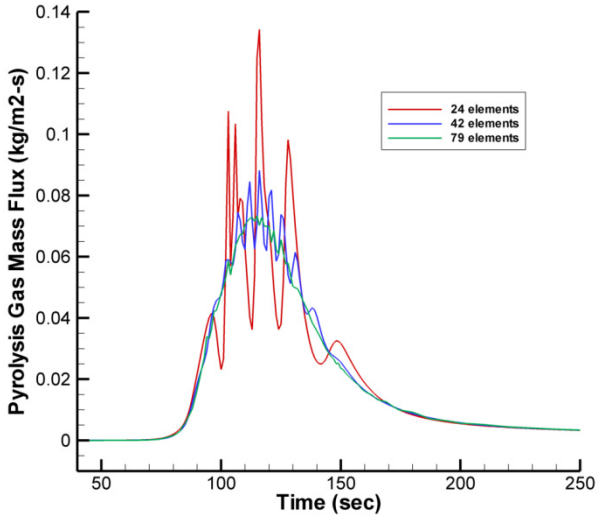

Figure 3.19: Comparison of the pyrolysis gas mass flux at the surface

The temperature comparisons between the three mesh densities are provided in Figure 3.20. The temperatures for the 42 and 79 element cases are nearly identical with the largest difference occurring at the peak on the surface by 3.2°C. The temperature for the

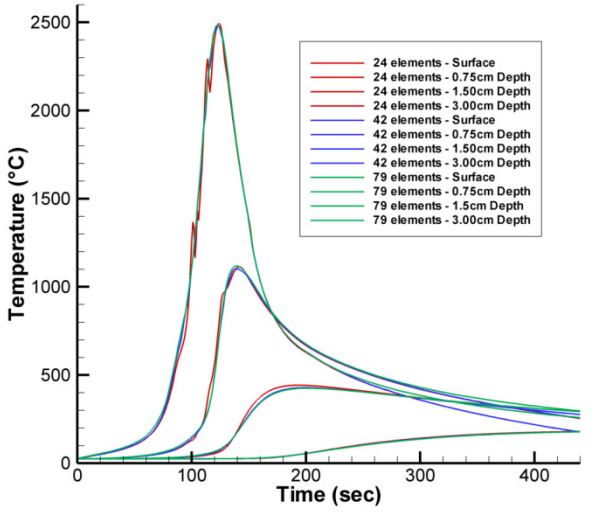

Figure 3.20: Temperature comparison between three different mesh densities

24 element case, when compared to the 79 element case at the peak for the surface node, differs by 15.42°C and occurs 1 second later in the simulation. The surface temperature

for the 24 element case oscillates a bit due to the highly oscillating pyrolysis gas flow. A zoomed in view of the surface temperatures and the temperatures at a depth of 0.75cm is provided in Figure 3.21. At the surface, the oscillations in the temperature for the 24 element case can be clearly seen as well as the subtle oscillation in the 42 element case. At a depth of 0.75cm, the 24 element case still shows some oscillation, while the 42 and 79 element cases show no oscillations.

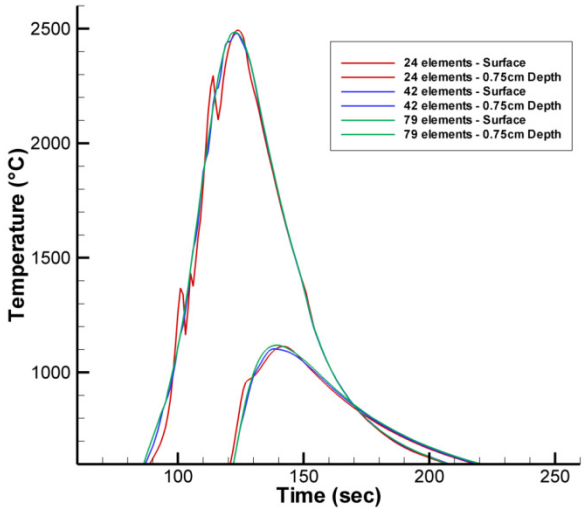

Figure 3.21: Temperature comparison at the surface and 0.75cm depth

The 42 element mesh was run using the same Genesis entry trajectory using three different fixed time steps. The time steps chosen were 0.5, 0.1, and 0.05 seconds under a fully implicit time marching scheme ($\theta = 1.0$). The variation in the oscillation in the pyrolysis gas mass flux as a function of the time step appears to be negligible and is shown in Figure 3.22. The temperature remained virtually unchanged for each time step and was nearly identical to the temperature shown in Figure 3.20 and Figure 3.21 confirming that it is also insensitive to time step.

The conclusion that can be made is that the pyrolysis gas flow calculation is more sensitive to mesh density than the temperature and as such will be the determining factor when preparing a mesh within PATRAN or any other meshing software. Furthermore,

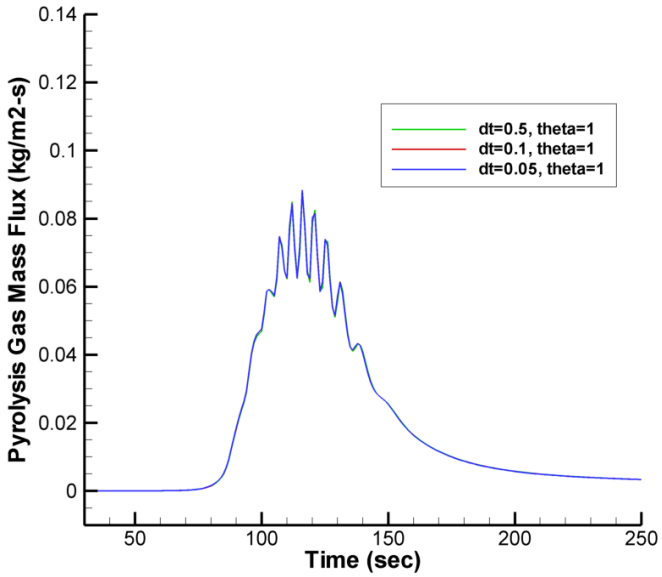

Figure 3.22: Pyrolysis gas mass flux as a function of time step

the solution for both the pyrolysis gas mass flux and the temperature were found to be insensitive to the time step being used. It can also be concluded that some pyrolysis gas oscillation can be tolerated without an adverse affect on the temperature as seen in the 42 element and 79 element cases. The case of choice would be the 42 element case because the computational time would be lower since there are fewer nodes and elements, and most importantly, the temperatures are not adversely affected.

3.6 Limitations of the One-Dimensional Finite Element Formulation

The one-dimensional code developed here has several limitations and caution should be exercised by those inexperienced in solving thermochemical ablation thermal response problems.

First of all, the code (in its present) form does not include an automatic mesh generation routine. Meshing is left up to the user with the assumption that the user is also performing related analysis in either NASTRAN or PATRAN Thermal. Mesh generation for the thermal response problem takes practice and experience. The best advice to the novice is to learn by trial and error; keeping in mind the basic principle in finite element

analysis is that more elements are usually required in regions of high temperature gradients.

The second limitation of the code is the fact that it is one-dimensional. The reasons for needing a three-dimensional finite element code have already been discussed and the effort to correct this limitation is presented in Chapter 4 of this dissertation.

Another limitation is in the choice of applying the heating boundary conditions. There are two options, one is to read a trajectory output file and calculate the recovery enthalpy and heat transfer coefficient based on the trajectory. The other input option is a CMA and FIAT style input where the user supplies a table of recovery enthalpy, pressure, radiative heating, and heat transfer coefficient as a function of time. The trajectory option is extremely useful in performing design and mission trade studies, but the heating information extracted from these types of codes generally employs Chapman's, or the Sutton-Graves' equations which are valid at the stagnation point only.

Another limitation already mentioned in detail is the explicit calculation of the decomposition and pyrolysis gas mass flux. The solution to this limitation is to add the density, decomposition rates, and pyrolysis gas mass flux to the nodal degrees of freedom and simultaneously solve for all of the unknowns.

Finally, there is a limitation inherent in supplying a pre-calculated table of B'_g, and B'_c. Using a table introduces interpolation and extrapolation errors. Since extrapolation is in general not a good engineering practice, the solutions for B'_g, and B'_c are bounded by the table itself, which is another possible source of error. In general a separate analysis must be performed to generate the thermochemistry data when it doesn't currently exist. This limitation will be addressed in the future work section of Chapter 6 where a discussion on computing the surface chemistry directly during the solution will be made. Implementing surface chemistry as a subroutine increases the flexibility of the

code and makes it straight forward to implement kinetic reaction rate chemistry models in addition to the standard equilibrium model being used.

CHAPTER 4

EXTENSION OF THE FINITE ELEMENT FORMULATION TO THREE-DIMENSIONS

In Chapter 2, the governing differential equations for the thermochemical ablation problem were developed in one dimension. In Chapter 3, the method of weighted residuals was used to derive the one-dimensional element equations from the governing equations. In this chapter, following the same general procedure developed in Chapters 2 and 3, the governing differential equations for the three-dimensional thermochemical ablation problem will be developed and the method of weighted residuals will be used once again to derive the three-dimensional element equations. In addition, the concept of isoparametric elements will be introduced and utilized in the solution of the three-dimensional finite element equations.

4.1 Governing Differential Equations of the Three Dimensional Thermochemical Ablation Problem

Starting with a three-dimensional differential control volume, and following the same procedure developed in Chapter 2, the governing differential equations for the three-dimensional thermochemical ablation problem will be developed. The three dimensional control volume is given in Figure 4.1. This control volume represents an infinitesimal volume within the solid. The two energy terms and the mass flux term are exactly the same as in the one-dimensional case, the difference now being that energy and mass are allowed to flow in the y and z directions in addition to the x direction. Similarly, for the three dimensional control volume it is assumed that the kinetic and potential energy terms are small in comparison to the sensible energy convection terms in the x, y, and z directions and will be dropped from the formulation.

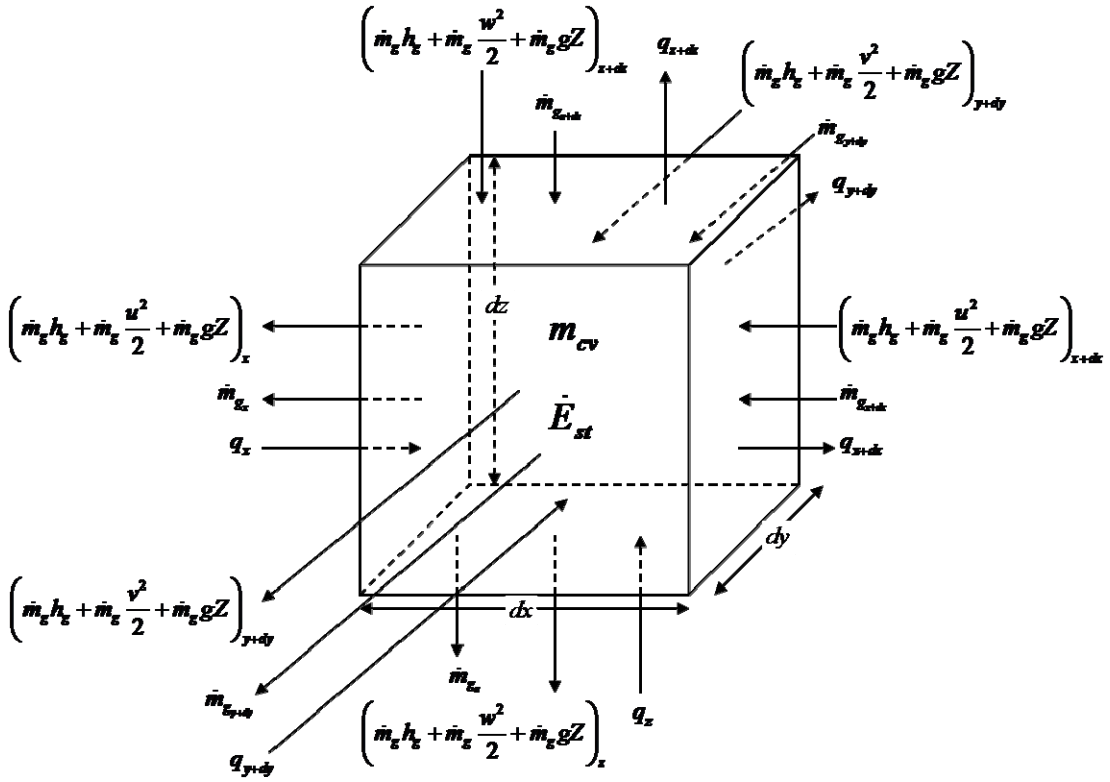

Figure 4.1: Three-dimensional control volume for the in-depth thermal response

4.1.1 Conservation of Mass

Using the principle of conservation of mass, Figure 4.1 shows that the net mass flow into the control volume must equal rate at which mass accumulates inside the control volume. Mathematically, this can be written as,

$$\frac{\partial m_{cv}}{\partial t} = \sum \dot{m}_{in} - \sum \dot{m}_{out} \tag{4.1}$$

The mass inside the control volume, m_{cv}, is related to the density of the solid material and the dimensions of the control volume as,

$$m_{cv} = \rho dx dy dz \tag{4.2}$$

The flow of mass per unit time and area, or mass flux through a surface is the product of the velocity normal to the surface and the density. In the x direction, the product of

velocity and density leaving the control volume is expressed in Figure 4.1 as $\rho u = \dot{m}''_{g_x}$. Similarly, the mass flux out of the control volume in the y and z directions respectively is $\dot{m}''_{g_y}$, $\dot{m}''_{g_z}$. The components of mass flux into the control volume in the x, y, and z directions can be expressed in the form of Taylor series expansions as,

$$\begin{aligned} \dot{m}''_{g_{x+dx}} &= \dot{m}''_{g_x} + \frac{\partial \dot{m}''_{g_x}}{\partial x} dx \\ \dot{m}''_{g_{y+dy}} &= \dot{m}''_{g_y} + \frac{\partial \dot{m}''_{g_y}}{\partial y} dy \\ \dot{m}''_{g_{z+dz}} &= \dot{m}''_{g_z} + \frac{\partial \dot{m}''_{g_z}}{\partial z} dz \end{aligned} \tag{4.3}$$

Summing all of the mass fluxes into and out of the control volume, and substituting the expressions for the mass inside the control volume, and the mass flux into and out of the control volume into (4.1) gives,

$$\begin{aligned} \frac{\partial \rho}{\partial t} dxdydz = &\left(\dot{m}''_{g_x} + \frac{\partial \dot{m}''_{g_x}}{\partial x} dx \right) dydz + \left(\dot{m}''_{g_y} + \frac{\partial \dot{m}''_{g_y}}{\partial y} dy \right) dxdz \\ &+ \left(\dot{m}''_{g_z} + \frac{\partial \dot{m}''_{g_z}}{\partial z} dz \right) dxdy - \dot{m}''_{g_x} dydz - \dot{m}''_{g_y} dxdz - \dot{m}''_{g_z} dxdy \end{aligned} \tag{4.4}$$

Canceling like terms on the right hand side, and dividing by *dxdydz*, (4.4) becomes,

$$-\frac{\partial \rho}{\partial t} = \frac{\partial \dot{m}''_{g_x}}{\partial x} + \frac{\partial \dot{m}''_{g_y}}{\partial y} + \frac{\partial \dot{m}''_{g_z}}{\partial z} \tag{4.5}$$

The three component Arrhenius relation developed in Chapter 2 for the density decomposition and the relation for total density given in equations (2.7) and (2.8) respectively are still valid for the three dimensional case, the only difference here is that now there are two additional directions mass may flow as the solid material is converted to pyrolysis gas.

4.1.2 Conservation of Momentum

In the one-dimensional finite element formulation, three assumptions were made about the flow of pyrolysis gas through the charred ablator. The first was that the pyrolysis gas was in thermal equilibrium with the char and the residence time within the char was small. The second was that the potential and kinetic energies of the pyrolysis gas could be neglected. The third was the pyrolysis gas flows in one-dimension, normal to the heated surface, i.e. along the line of nodes in the one-dimensional discretization of the problem, and the drop in pressure through the char is negligible.

In the three-dimensional formulation, the first two assumptions will be retained. The third assumption however, will be dropped requiring solution of the momentum equation simultaneously with conservation of mass. The result of this approach is that, along with the magnitude of the pyrolysis gas flux, the direction of flow and the pressure within the material can be determined. Determining the direction of gas flow is especially critical in regions where the both the virgin and char forms of the ablative material are porous and the material's permeability is orthotropic. Two additional factors could cause the pyrolysis gas to flow in multiple directions. One would be a pressure gradient along the surface of the ablator and the other a temperature gradient in the in-plane direction of the material causing localized differences in the pyrolysis gas generation rate.

In 1856 Henri Darcy established experimentally that the instantaneous discharge rate through a porous medium is proportional to the pressure drop over a given distance and inversely proportional to the dynamic viscosity of the fluid. This assumes that the flow is both fully developed and steady. In one-dimension, Darcy's law may be written as,

$$q = \frac{-\kappa_p}{\mu}\frac{\partial P}{\partial x} \tag{4.6}$$

The constant of proportionality, κ_p, is known as the permeability and q is the discharge flux with units of length per unit time which is also known as the Darcy flux. The Darcy flux is not the velocity which the fluid passing through the pores is experiencing. The pore velocity is related to the Darcy flux through the material's porosity given in (4.7).

$$u = \frac{q}{\phi} \tag{4.7}$$

Darcy's Law may be written in terms of the mass flux by substituting (4.7) into (4.6) and multiplying both sides of the equation by the fluid density. Equation (4.6) in terms of the mass flux becomes,

$$\dot{m}''_{g_x} = \frac{-\kappa_{p_x}}{\nu\phi}\frac{\partial P}{\partial x} \tag{4.8}$$

In equation (4.8), the dynamic viscosity has been replaced by the kinematic viscosity which is simply the dynamic viscosity divided by the density. In three dimensions, Darcy's Law is given by (4.9),

$$\begin{aligned} m''_{gx} &= -\frac{\kappa_{px}}{\nu\phi}\frac{\partial P}{\partial x} \\ m''_{gy} &= -\frac{\kappa_{py}}{\nu\phi}\frac{\partial P}{\partial y} \\ m''_{gz} &= -\frac{\kappa_{pz}}{\nu\phi}\frac{\partial P}{\partial z} \end{aligned} \tag{4.9}$$

where the major difference is that the pressure gradient is three-dimensional and permeability is a tensor.

4.1.3 Conservation of Energy

Conservation of energy in three dimensions is similar to that for the one-dimensional case developed in Chapter 2; the difference is that there is energy flow in the y and z directions in addition to the x direction. The additional energy fluxes are

identical to those in the x-direction as shown in the control volume of Figure 4.1. The same simplifying assumptions about the pyrolysis gas used in Chapter 2 are retained here; specifically, the pyrolysis gas formed is in thermal equilibrium with the material within the control volume and the residence time within the control volume is small. The kinetic and potential energies of the pyrolysis gas are neglected for the same reasons as stated in Chapter 2.

The general form of the first law of thermodynamics for a three-dimensional control volume is the same as that given for the one-dimensional case in Chapter 2; only here, all the vector quantities have three directional components. The simplified form of the first law of thermodynamics given in (2.11) is rewritten here for convenience,

$$\frac{dE_{cv}}{dt} = \sum \dot{E}_{in} - \sum \dot{E}_{out} \tag{4.10}$$

Equation (4.10) simply states that the rate at which energy is stored in the control volume is equal to the rate at which energy enters the control volume minus the rate at which energy leaves the control volume. Looking at the control volume in Figure 4.1 and recalling the assumptions made about the pyrolysis gas energy, the energy in-flow and out-flow per unit area normal to each surface of the control volume can be identified and summed as follows,

$$\begin{aligned}
\dot{E}_{in} &= \left[q''_x + \left(\dot{m}''_{g_x} h_g \right)_{x+dx} \right] dydz + \left[q''_y + \left(\dot{m}''_{g_y} h_g \right)_{y+dy} \right] dxdz + \left[q''_z + \left(\dot{m}''_{g_z} h_g \right)_{z+dz} \right] dxdy \\
\dot{E}_{out} &= \left[q''_{x+dx} + \left(\dot{m}''_{g_x} h_g \right)_x \right] dydz + \left[q''_{y+dy} + \left(\dot{m}''_{g_y} h_g \right)_y \right] dxdz + \left[q''_{z+dz} + \left(\dot{m}''_{g_z} h_g \right)_z \right] dxdy
\end{aligned} \tag{4.11}$$

The components of the heat conduction vector leaving the control volume can be expressed as a Taylor series expansion by,

$$q''_{x+dx} = q''_x + \frac{\partial q''_x}{\partial x} dx$$
$$q''_{y+dy} = q''_y + \frac{\partial q''_y}{\partial y} dy \tag{4.12}$$
$$q''_{z+dz} = q''_z + \frac{\partial q''_z}{\partial z} dz$$

Similarly, the components of the pyrolysis gas convection vector can be written as Taylor series expansions as follows,

$$\left(\dot{m}''_{g_x} h_g\right)_{x+dx} = \left(\dot{m}''_{g_x} h_g\right)_x + \frac{\partial}{\partial x}\left(\dot{m}''_{g_x} h_g\right)_x dx$$
$$\left(\dot{m}''_{g_y} h_g\right)_{y+dy} = \left(\dot{m}''_{g_y} h_g\right)_y + \frac{\partial}{\partial y}\left(\dot{m}''_{g_y} h_g\right)_y dy \tag{4.13}$$
$$\left(\dot{m}''_{g_z} h_g\right)_{z+dz} = \left(\dot{m}''_{g_z} h_g\right)_z + \frac{\partial}{\partial z}\left(\dot{m}''_{g_z} h_g\right)_z dz$$

The rate of energy storage within the control volume can be expressed in terms of the density and enthalpy of the solid as,

$$\frac{dE_{cv}}{dt} = \frac{\partial}{\partial t}(\rho h)\, dxdydz \tag{4.14}$$

Substituting (4.11) into (4.10) and using the definitions in (4.12), (4.13), and (4.14) gives,

$$\begin{aligned}\frac{\partial}{\partial t}(\rho h)\, dxdydz = &\left[q''_x + \left(\dot{m}''_{g_x} h_g\right)_x + \frac{\partial}{\partial x}\left(\dot{m}''_{g_x} h_g\right)_x dx\right] dydz + \left[q''_y + \left(\dot{m}''_{g_y} h_g\right)_y + \frac{\partial}{\partial y}\left(\dot{m}''_{g_y} h_g\right)_y dy\right] dxdz \\ &+ \left[q''_z + \left(\dot{m}''_{g_z} h_g\right)_z + \frac{\partial}{\partial z}\left(\dot{m}''_{g_z} h_g\right)_z dz\right] dxdy - \left[q''_x + \frac{\partial q''_x}{\partial x} dx + \left(\dot{m}''_{g_x} h_g\right)_x\right] dydz \\ &- \left[q''_y + \frac{\partial q''_y}{\partial y} dy + \left(\dot{m}''_{g_y} h_g\right)_y\right] dxdz - \left[q''_z + \frac{\partial q''_z}{\partial z} dz + \left(\dot{m}''_{g_z} h_g\right)_z\right] dxdy\end{aligned} \tag{4.15}$$

Cancelling like terms and dividing by *dxdydz* gives,

$$\frac{\partial}{\partial t}(\rho h) = -\frac{\partial q''_x}{\partial x} - \frac{\partial q''_y}{\partial y} - \frac{\partial q''_z}{\partial z} + \frac{\partial}{\partial x}\left(\dot{m}''_{g_x} h_g\right)_x + \frac{\partial}{\partial y}\left(\dot{m}''_{g_y} h_g\right)_y + \frac{\partial}{\partial z}\left(\dot{m}''_{g_z} h_g\right)_z \tag{4.16}$$

Once again as in Chapter 2, assuming there is no mass diffusion within the control volume, the components of the heat flux vector can be written, using Fourier's Law, as,

$$\begin{aligned} q''_x &= -k_x \frac{\partial T}{\partial x} \\ q''_y &= -k_y \frac{\partial T}{\partial y} \\ q''_z &= -k_z \frac{\partial T}{\partial z} \end{aligned} \tag{4.17}$$

Substituting (4.17) into (4.16) gives the desired form of the governing differential energy equation for the in-depth thermal response in three dimensions,

$$\begin{aligned} \frac{\partial}{\partial t}(\rho h) = &\frac{\partial}{\partial x}\left(k_x \frac{\partial T}{\partial x}\right) + \frac{\partial}{\partial y}\left(k_y \frac{\partial T}{\partial y}\right) + \frac{\partial}{\partial z}\left(k_z \frac{\partial T}{\partial z}\right) \\ &+ \frac{\partial}{\partial x}\left(\dot{m}''_{g_x} h_g\right) + \frac{\partial}{\partial y}\left(\dot{m}''_{g_y} h_g\right) + \frac{\partial}{\partial z}\left(\dot{m}''_{g_z} h_g\right) \end{aligned} \tag{4.18}$$

Notice now that orthotropic material properties have been introduced into the governing differential equations by including directional dependant thermal conductivity.

4.1.4 Transformation of the Governing Equations to a Moving Coordinate System

The governing differential equations developed in the previous section are valid for a fixed coordinate frame. As in Chapter 2, the governing differential equations must be transformed into a moving coordinate frame to account for the material's motion due to ablation. Figure 4.2 shows the three-dimensional control volume after a time, t, where the material has ablated in all three directions. The x, y, z-coordinates are used to denote the position in the material with respect to the location of the control volume in the fixed coordinate system. The coordinates x_S, y_S, and z_S are the position in the material with respect to the receding surface where the origin is located at the corner of the receded control volume. From Figure 4.2 the amount of surface recession in all three directions, S_x, S_y, S_z is related to the x, y, z, x_S, y_S, and z_S coordinates by the following relations,

$$x = S_x + x_S$$
$$y = S_y + y_S \qquad (4.19)$$
$$z = S_z + z_S$$

Also, infinitesimal changes in x, x_S, y, y_S, z and z_S are denoted as dx, dx_S, dy, dy_S, dz and dz_S respectively and are equal at any fixed point in time.

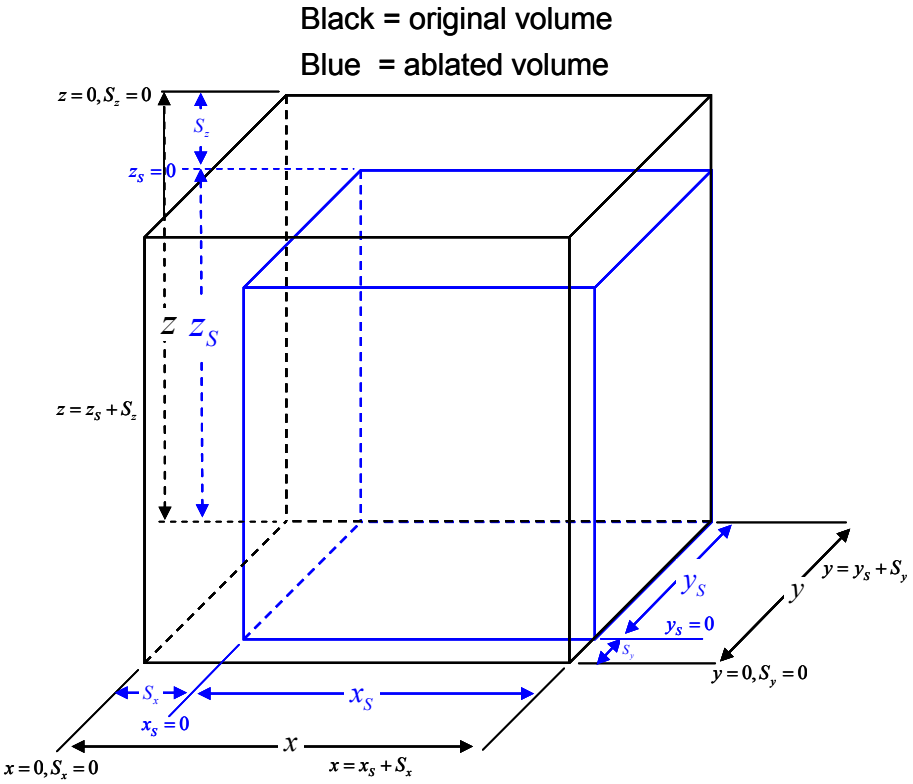

Figure 4.2: Three-dimensional control volume at time, t, after ablation

4.1.4.1 Transformation of the Three-Dimensional Conservation of Mass

The conservation of mass given by (4.5) was written for a control volume fixed in space where the derivatives with respect to time were taken holding x, y, and z constant. Equation (4.5) must now be rewritten to relate these density changes at constant x, y, and z to density changes at constant x_S, y_S, and z_S. In the fixed coordinate system, at any instant in time, the density may be expressed as a function of position and time, $\rho = \rho(x, y, z, t)$, from which we may write using the chain rule,

$$d\rho = \left.\frac{\partial \rho}{\partial x}\right|_t dx + \left.\frac{\partial \rho}{\partial y}\right|_t dy + \left.\frac{\partial \rho}{\partial z}\right|_t dz + \left.\frac{\partial \rho}{\partial t}\right|_{x,y,z} dt \tag{4.20}$$

Differentiating (4.20) with respect to time at constant x_S, y_S, and z_S gives,

$$\left.\frac{\partial \rho}{\partial t}\right|_{x_S,y_S,z_S} = \left.\frac{\partial \rho}{\partial x}\right|_t \left.\frac{\partial x}{\partial t}\right|_{x_S} + \left.\frac{\partial \rho}{\partial y}\right|_t \left.\frac{\partial y}{\partial t}\right|_{y_S} + \left.\frac{\partial \rho}{\partial z}\right|_t \left.\frac{\partial z}{\partial t}\right|_{z_S} + \left.\frac{\partial \rho}{\partial t}\right|_{x,y,z} \tag{4.21}$$

Using the relationships between the components of recession and the fixed and moving coordinates, we may write for constant x_S, y_S, and z_S,

$$\begin{aligned} x &= S_x + x_S & y &= S_y + y_S & z &= S_z + z_S \\ \left.\frac{\partial x}{\partial t}\right|_{x_S} &= \frac{dS_x}{dt} \equiv \dot{S}_x & \left.\frac{\partial y}{\partial t}\right|_{y_S} &= \frac{dS_y}{dt} \equiv \dot{S}_y & \left.\frac{\partial z}{\partial t}\right|_{z_S} &= \frac{dS_z}{dt} \equiv \dot{S}_z \end{aligned} \tag{4.22}$$

The recession rates are written as total derivatives since they are functions of time only. Substituting (4.22) into (4.21) and recalling that $dx=dx_S$, $dy=dy_S$, and $dz=dz_S$ at a fixed point in time yields,

$$\left.\frac{\partial \rho}{\partial t}\right|_{x_S,y_S,z_S} = \dot{S}_x \left.\frac{\partial \rho}{\partial x}\right|_t + \dot{S}_y \left.\frac{\partial \rho}{\partial y}\right|_t + \dot{S}_z \left.\frac{\partial \rho}{\partial z}\right|_t + \left.\frac{\partial \rho}{\partial t}\right|_{x,y,z} \tag{4.23}$$

Equation (4.23) along with (4.5), (2.7), and (2.8) represent the three-dimensional conservation of mass in a moving coordinate system.

4.1.4.2 Transformation of the Three-Dimensional Conservation of Momentum

Since the steady flow assumption was made, no derivatives with respect to time appear in the Darcy flow equations. Therefore transformation to the moving coordinate system is not required for this set of equations.

4.1.4.3 Transformation of the Three-Dimensional Conservation of Energy

Transforming the energy equation to the moving coordinate system requires the assumption that the following functional relationships are valid.

$$
\begin{aligned}
T &= T(x,y,z,t) \\
\rho &= \rho(x,y,z,t) \\
S &= S(t) \\
h &= h(T,\rho) \equiv h(x,y,z,t)
\end{aligned}
\tag{4.24}
$$

Rewriting equation (4.18) to denote which variables are held constant during the partial differentiation gives,

$$
\begin{aligned}
\left.\frac{\partial}{\partial t}(\rho h)\right|_x = &\left.\frac{\partial}{\partial x}\left(k_x \frac{\partial T}{\partial x}\right)\right|_t + \left.\frac{\partial}{\partial y}\left(k_y \frac{\partial T}{\partial y}\right)\right|_t + \left.\frac{\partial}{\partial z}\left(k_z \frac{\partial T}{\partial z}\right)\right|_t \\
&+ \left.\frac{\partial}{\partial x}\left(\dot{m}''_{g_x} h_g\right)\right|_t + \left.\frac{\partial}{\partial y}\left(\dot{m}''_{g_y} h_g\right)\right|_t + \left.\frac{\partial}{\partial z}\left(\dot{m}''_{g_z} h_g\right)\right|_t
\end{aligned}
\tag{4.25}
$$

The energy storage term, written for a point in the fixed coordinate system will need to be related to its counterpart in the moving coordinate system. Using the functional relationships given in (4.24), the energy storage term may be expanded using the chain rule as,

$$
\begin{aligned}
&\rho h = \rho h(x,y,z,t) \\
&d(\rho h) = \left.\frac{\partial}{\partial x}(\rho h)\right|_t dx + \left.\frac{\partial}{\partial y}(\rho h)\right|_t dy + \left.\frac{\partial}{\partial z}(\rho h)\right|_t dz + \left.\frac{\partial}{\partial t}(\rho h)\right|_{x,y,z} dt
\end{aligned}
\tag{4.26}
$$

Performing a partial differentiation with respect to time at a point constant in the moving coordinate frame, (constant x_S, y_S, z_S) yields,

$$
\left.\frac{\partial}{\partial t}(\rho h)\right|_{x_S,y_S,z_S} = \left.\frac{\partial}{\partial x}(\rho h)\right|_t \left.\frac{\partial x}{\partial t}\right|_{x_S} + \left.\frac{\partial}{\partial y}(\rho h)\right|_t \left.\frac{\partial y}{\partial t}\right|_{y_S} + \left.\frac{\partial}{\partial z}(\rho h)\right|_t \left.\frac{\partial z}{\partial t}\right|_{z_S} + \left.\frac{\partial}{\partial t}(\rho h)\right|_{x,y,z} \tag{4.27}
$$

Using the relations in (4.22), recalling that differentiation with respect to x, y, and z is equivalent to differentiation with respect to x_S, y_S, and z_S at constant time yields,

$$
\left.\frac{\partial}{\partial t}(\rho h)\right|_{x,y,z} = \left.\frac{\partial}{\partial t}(\rho h)\right|_{x_S,y_S,z_S} - \dot{S}_x \left.\frac{\partial}{\partial x_S}(\rho h)\right|_t - \dot{S}_y \left.\frac{\partial}{\partial y_S}(\rho h)\right|_t - \dot{S}_z \left.\frac{\partial}{\partial z_S}(\rho h)\right|_t \tag{4.28}
$$

Substituting (4.28) into (4.25) and recalling that differentiation with respect to x, y, and z is equivalent to differentiation with respect to x_S, y_S, and z_S at constant time yields,

$$\underbrace{\frac{\partial}{\partial t}\left(\rho h\right)\Big|_{x_S,y_S,z_S}}_{I} = \underbrace{\frac{\partial}{\partial x_S}\left(k_x\frac{\partial T}{\partial x_S}\right)\Big|_t + \frac{\partial}{\partial y_S}\left(k_y\frac{\partial T}{\partial y_S}\right)\Big|_t + \frac{\partial}{\partial z_S}\left(k_z\frac{\partial T}{\partial z_S}\right)\Big|_t}_{II}$$
$$+\underbrace{\frac{\partial}{\partial x_S}\left(\dot{m}''_{g_x}h_g\right)\Big|_t + \frac{\partial}{\partial y_S}\left(\dot{m}''_{g_y}h_g\right)\Big|_t + \frac{\partial}{\partial z_S}\left(\dot{m}''_{g_z}h_g\right)\Big|_t}_{III} \tag{4.29}$$
$$+\underbrace{\dot{S}_x\frac{\partial}{\partial x_S}\left(\rho h\right)\Big|_t + \dot{S}_y\frac{\partial}{\partial y_S}\left(\rho h\right)\Big|_t + \dot{S}_z\frac{\partial}{\partial z_S}\left(\rho h\right)\Big|_t}_{IV}$$

Equation (4.29) represents the three-dimensional conservation of energy in a moving coordinate system. As in the one-dimensional case it is convenient to express the rate of change of enthalpy in term I in terms of the temperature and density rates of change. The expansion and simplification of term I is identical to that derived in Chapter 2, so the final result may be written as,

$$\frac{\partial}{\partial t}\left(\rho h\right)\Big|_{x_S,y_S,z_S} = \overline{h}\,\frac{\partial \rho}{\partial t}\Big|_{x_S,y_S,z_S} + \rho c_p\,\frac{\partial T}{\partial t}\Big|_{x_S,y_S,z_S} \tag{4.30}$$

Similarly, term II in (4.29) does not require any modification and term III may be expanded as,

$$\frac{\partial}{\partial x_S}\left(\dot{m}''_{g_x}h_g\right)\Big|_t + \frac{\partial}{\partial y_S}\left(\dot{m}''_{g_y}h_g\right)\Big|_t + \frac{\partial}{\partial z_S}\left(\dot{m}''_{g_z}h_g\right)\Big|_t = \dot{m}''_{g_x}\frac{\partial h_g}{\partial x_S}\Big|_t + h_g\frac{\partial \dot{m}''_{g_x}}{\partial x_S}\Big|_t$$
$$+\dot{m}''_{g_y}\frac{\partial h_g}{\partial y_S}\Big|_t + h_g\frac{\partial \dot{m}''_{g_y}}{\partial y_S}\Big|_t + \dot{m}''_{g_z}\frac{\partial h_g}{\partial z_S}\Big|_t + h_g\frac{\partial \dot{m}''_{g_z}}{\partial z_S}\Big|_t \tag{4.31}$$

Recognizing that differentiation with respect to x, y, and z is equivalent to differentiation with respect to x_S, y_S, and z_S at constant time, and rearranging (4.31) gives,

$$\frac{\partial}{\partial x_S}\left(\dot{m}''_{g_x}h_g\right)\Big|_t + \frac{\partial}{\partial y_S}\left(\dot{m}''_{g_y}h_g\right)\Big|_t + \frac{\partial}{\partial z_S}\left(\dot{m}''_{g_z}h_g\right)\Big|_t = \dot{m}''_{g_x}\frac{\partial h_g}{\partial x_S}\Big|_t + \dot{m}''_{g_y}\frac{\partial h_g}{\partial y_S}\Big|_t$$
$$+\dot{m}''_{g_z}\frac{\partial h_g}{\partial z_S}\Big|_t + h_g\left(\frac{\partial \dot{m}''_{g_x}}{\partial x_S}\Big|_t + \frac{\partial \dot{m}''_{g_y}}{\partial y_S}\Big|_t + \frac{\partial \dot{m}''_{g_z}}{\partial z_S}\Big|_t\right) \tag{4.32}$$

Notice that the term in parenthesis that is multiplied by the pyrolysis gas enthalpy, h_g, is the expression for the time rate of change of density in the fixed coordinate system given by (4.5). Substituting (4.5) into (4.32) gives,

$$\left.\frac{\partial}{\partial x_S}\left(\dot{m}''_{g_x} h_g\right)\right|_t + \left.\frac{\partial}{\partial y_S}\left(\dot{m}''_{g_y} h_g\right)\right|_t + \left.\frac{\partial}{\partial z_S}\left(\dot{m}''_{g_z} h_g\right)\right|_t = \dot{m}''_{g_x}\left.\frac{\partial h_g}{\partial x_S}\right|_t + \dot{m}''_{g_y}\left.\frac{\partial h_g}{\partial y_S}\right|_t + \dot{m}''_{g_z}\left.\frac{\partial h_g}{\partial z_S}\right|_t + h_g\left.\frac{\partial \rho}{\partial t}\right|_{x,y,z} \tag{4.33}$$

Term IV in (4.29) does not require expansion, but again it is now convenient to express the enthalpy per unit volume in terms of temperature and density gradients. The expansion and simplification process is identical to that shown in Chapter 2; except here, there are two additional terms associated with the y and z directions. The result of the expansion and simplification is,

$$\begin{aligned}
\left.\frac{\partial}{\partial x_S}(\rho h)\right|_t &= \bar{h}\left.\frac{\partial \rho}{\partial x_S}\right|_t + \rho c_p\left.\frac{\partial T}{\partial x_S}\right|_t \\
\left.\frac{\partial}{\partial y_S}(\rho h)\right|_t &= \bar{h}\left.\frac{\partial \rho}{\partial y_S}\right|_t + \rho c_p\left.\frac{\partial T}{\partial y_S}\right|_t \\
\left.\frac{\partial}{\partial z_S}(\rho h)\right|_t &= \bar{h}\left.\frac{\partial \rho}{\partial z_S}\right|_t + \rho c_p\left.\frac{\partial T}{\partial z_S}\right|_t
\end{aligned} \tag{4.34}$$

Substituting (4.30), (4.33), and (4.34) into (4.29) and rearranging gives,

$$\begin{aligned}
\rho c_p\left.\frac{\partial T}{\partial t}\right|_{x_S,y_S,z_S} &= \left.\frac{\partial}{\partial x_S}\left(k_x\frac{\partial T}{\partial x_S}\right)\right|_t + \left.\frac{\partial}{\partial y_S}\left(k_y\frac{\partial T}{\partial y_S}\right)\right|_t + \left.\frac{\partial}{\partial z_S}\left(k_z\frac{\partial T}{\partial z_S}\right)\right|_t + h_g\left.\frac{\partial \rho}{\partial t}\right|_{x,y,z} \\
&+ \dot{m}''_{g_x}\left.\frac{\partial h_g}{\partial x_S}\right|_t + \dot{m}''_{g_y}\left.\frac{\partial h_g}{\partial y_S}\right|_t + \dot{m}''_{g_z}\left.\frac{\partial h_g}{\partial z_S}\right|_t + \bar{h}\left[\dot{S}_x\left.\frac{\partial \rho}{\partial x_S}\right|_t + \dot{S}_y\left.\frac{\partial \rho}{\partial y_S}\right|_t + \dot{S}_z\left.\frac{\partial \rho}{\partial z_S}\right|_t - \left.\frac{\partial \rho}{\partial t}\right|_{x_S,y_S,z_S}\right] \\
&+ \dot{S}_x\rho c_p\left.\frac{\partial T}{\partial x_S}\right|_t + \dot{S}_y\rho c_p\left.\frac{\partial T}{\partial y_S}\right|_t + \dot{S}_z\rho c_p\left.\frac{\partial T}{\partial z_S}\right|_t
\end{aligned} \tag{4.35}$$

Using the definition of the conservation of mass in the moving coordinate system, (4.23) and dropping the notation for constant differentiation, except where it occurs in the fixed

coordinate system, the final form of the three-dimensional conservation of energy in a moving coordinate system may be written as,

$$\rho c_p \frac{\partial T}{\partial t} = \frac{\partial}{\partial x_S}\left(k_x \frac{\partial T}{\partial x_S}\right) + \frac{\partial}{\partial y_S}\left(k_y \frac{\partial T}{\partial y_S}\right) + \frac{\partial}{\partial z_S}\left(k_z \frac{\partial T}{\partial z_S}\right) + \left(h_g - \bar{h}\right)\left.\frac{\partial \rho}{\partial t}\right|_{x,y,z} + \dot{m}''_{g_x}\frac{\partial h_g}{\partial x_S} + \dot{m}''_{g_y}\frac{\partial h_g}{\partial y_S} + \dot{m}''_{g_z}\frac{\partial h_g}{\partial z_S} + \dot{S}_x \rho c_p \frac{\partial T}{\partial x_S} + \dot{S}_y \rho c_p \frac{\partial T}{\partial y_S} + \dot{S}_z \rho c_p \frac{\partial T}{\partial z_S} \tag{4.36}$$

The terms in equation (4.36) have the exact same meaning as in the one-dimensional version; only now, energy transport occurs in all three directions.

4.2 Three-Dimensional Finite Element Formulation of the Governing Partial Differential Equations

In Chapter 2, the theory and procedure for the finite element method was introduced. Specifically the method of weighted residuals and Galerkin's weak form for the one-dimensional thermochemical ablation problem was discussed. In this section, the method of weighted residuals will be used once again and Galerkin's weak form for the three-dimensional governing differential equations will be developed.

4.2.1 Galerkin's Weak Form of the Three-Dimensional Energy Equation

The procedure to put the governing differential equations into Galerkin's weak form is essentially the same as that for the one-dimensional problem. The biggest difference in going from 1-dimension to 3-dimensions is the method used to perform the integration. For the one-dimensional problem the weighted residual statement of the governing differential equations could be integrated by part to reduce the order of the equation. For the three-dimensional problem, integration by parts is known as Gauss's theorem and is slightly different than the standard one-dimensional integration by parts formula. Gauss's theorem for integration by parts is,

$$\int_\Omega u\left(\nabla \cdot \mathbf{v}\right) d\Omega = \int_\Gamma u\left(\mathbf{v} \cdot \hat{n}\right) d\Gamma - \int_\Omega \mathbf{v} \cdot \nabla u d\Omega \tag{4.37}$$

As in the one-dimensional problem, the first step in arriving at Galerkin's weak form is to assume a functional form for the dependent variable. Hence we write for the dependent variable and its derivatives showing their functional relationships,

$$
\begin{aligned}
T^{(e)}(x,y,z,t) &= \sum_{i=1}^{n} N_i(x,y,z)T_i(t) \\
\frac{\partial T}{\partial x_S}^{(e)}(x,y,z,t) &= \sum_{i=1}^{n} \frac{\partial N_i}{\partial x_S}(x,y,z)T_i(t) \\
\frac{\partial T}{\partial y_S}^{(e)}(x,y,z,t) &= \sum_{i=1}^{n} \frac{\partial N_i}{\partial y_S}(x,y,z)T_i(t) \\
\frac{\partial T}{\partial z_S}^{(e)}(x,y,z,t) &= \sum_{i=1}^{n} \frac{\partial N_i}{\partial z_S}(x,y,z)T_i(t)
\end{aligned}
\tag{4.38}
$$

Next, the weighted residual statement of equation (4.36) is written with $W_i = N_i$ for one element, where "i" is the number of nodes in one element.

$$
\iiint_{\Omega^{(e)}} \left[\begin{array}{l}
\dfrac{\partial}{\partial x_S}\left(k_x \dfrac{\partial T^{(e)}}{\partial x_S}\right) + \dfrac{\partial}{\partial y_S}\left(k_y \dfrac{\partial T^{(e)}}{\partial y_S}\right) + \dfrac{\partial}{\partial z_S}\left(k_z \dfrac{\partial T^{(e)}}{\partial z_S}\right) + \left(h_g - \bar{h}\right)\dfrac{\partial \rho^{(e)}}{\partial t}\Bigg|_{x,y,z} \\
+ \dot{m}''_{g_x} \dfrac{\partial h_g^{(e)}}{\partial x_S} + \dot{m}''_{g_y} \dfrac{\partial h_g^{(e)}}{\partial y_S} + \dot{m}''_{g_z} \dfrac{\partial h_g^{(e)}}{\partial z_S} + \dot{S}_x \rho c_p \dfrac{\partial T^{(e)}}{\partial x_S} + \dot{S}_y \rho c_p \dfrac{\partial T^{(e)}}{\partial y_S} \\
+ \dot{S}_z \rho c_p \dfrac{\partial T^{(e)}}{\partial z_S} - \rho c_p \dfrac{\partial T^{(e)}}{\partial t}
\end{array} \right] N_i \, d\Omega = 0 \tag{4.39}
$$

Now using Gauss's theorem to integrate the term shown in (4.40),

$$
\frac{\partial}{\partial x_S}\left(k_x \frac{\partial T^{(e)}}{\partial x_S}\right) + \frac{\partial}{\partial y_S}\left(k_y \frac{\partial T^{(e)}}{\partial y_S}\right) + \frac{\partial}{\partial z_S}\left(k_z \frac{\partial T^{(e)}}{\partial z_S}\right) \tag{4.40}
$$

Setting $u=N_i$ and

$$
\mathbf{v} = k_x \frac{\partial T^{(e)}}{\partial x_S}\hat{i} + k_y \frac{\partial T^{(e)}}{\partial y_S}\hat{j} + k_z \frac{\partial T^{(e)}}{\partial z_S}\hat{k} \tag{4.41}
$$

The result of the integration is the Galerkin's weak form,

$$\iiint_{\Omega^{(e)}}\left(k_x\frac{\partial T^{(e)}}{\partial x_S}\frac{\partial N_i}{\partial x_S}+k_y\frac{\partial T^{(e)}}{\partial y_S}\frac{\partial N_i}{\partial y_S}+k_z\frac{\partial T^{(e)}}{\partial z_S}\frac{\partial N_i}{\partial z_S}\right)dx_S dy_S dz_S+\iiint_{\Omega^{(e)}}\dot{m}''_{g_x}\frac{\partial h_g^{(e)}}{\partial x_S}N_i dx_S dy_S dz_S$$
$$+\iiint_{\Omega^{(e)}}\dot{m}''_{g_y}\frac{\partial h_g^{(e)}}{\partial y_S}N_i dx_S dy_S dz_S+\iiint_{\Omega^{(e)}}\dot{m}''_{g_z}\frac{\partial h_g^{(e)}}{\partial z_S}N_i dx_S dy_S dz_S+\iiint_{\Omega^{(e)}}\dot{S}_x\rho c_p\frac{\partial T^{(e)}}{\partial x_S}N_i dx_S dy_S dz_S$$
$$+\iiint_{\Omega^{(e)}}\dot{S}_y\rho c_p\frac{\partial T^{(e)}}{\partial y_S}N_i dx_S dy_S dz_S+\iiint_{\Omega^{(e)}}\dot{S}_z\rho c_p\frac{\partial T^{(e)}}{\partial z_S}N_i dx_S dy_S dz_S-\iiint_{\Omega^{(e)}}\rho c_p\frac{\partial T^{(e)}}{\partial t}N_i dx_S dy_S dz_S \quad (4.42)$$
$$+\iint_{\Gamma^{(e)}}(\mathbf{q}\cdot\hat{n})N_i d\Gamma=0$$

The surface integral introduced by the integration by parts provides the connection to the surface boundary conditions present on any surface of the element. The surface integral represents the net conductive flux into the volume, $\Omega^{(e)}$, from any surface bounded by Γ and can be expanded to represent any number of boundary conditions by summation over all surfaces bounded by Γ. Since equation (4.42) is for one element, Γ includes all of the surfaces of the element. For example, in the case of an ablative material, the surface boundary conditions are given by equation (2.84) for any element surface exposed to the aerodynamic heating. Equation (2.84) written in terms of the surface integral of (4.42) is,

$$\iint_{\Gamma^{(e)}}(\mathbf{q}\cdot\hat{n})N_i d\Gamma=\rho_e U_e C_H\left(H_{sr}-h_{sw}+B'_c h_c+B'_g h_g-B'h_w\right)-q^*+q_{\underset{out}{rad}}-\alpha q_{\underset{in}{rad}} \quad (4.43)$$

Equation (4.42) can be simplified by expressing the temperature and its spatial derivatives in matrix notation as,

$$T^{(e)}=\left[N\right]^T\left\{T\right\}$$
$$\begin{bmatrix}\dfrac{\partial T^{(e)}}{\partial x_S}\\ \dfrac{\partial T^{(e)}}{\partial y_S}\\ \dfrac{\partial T^{(e)}}{\partial z_S}\end{bmatrix}=\left[B\right]\left\{T\right\} \quad (4.44)$$

The pyrolysis gas enthalpy and its spatial derivatives may also be expressed in matrix notation as,

$$h_g^{(e)} = \sum_{i=1}^{n} N_i h_{g_i} = \left[N\right]^T \left\{h_g\right\}$$

$$\begin{bmatrix} \dfrac{\partial h_g^{(e)}}{\partial x_S} \\ \dfrac{\partial h_g^{(e)}}{\partial y_S} \\ \dfrac{\partial h_g^{(e)}}{\partial z_S} \end{bmatrix} = \begin{bmatrix} \displaystyle\sum_{i=1}^{n} \frac{\partial N_i}{\partial x_S} h_{g_i} \\ \displaystyle\sum_{i=1}^{n} \frac{\partial N_i}{\partial y_S} h_{g_i} \\ \displaystyle\sum_{i=1}^{n} \frac{\partial N_i}{\partial z_S} h_{g_i} \end{bmatrix} = \left[B\right]\left\{h_g\right\} \tag{4.45}$$

The components of the pyrolysis gas mass flux and the recession rates may be combined into a pyrolysis gas mass flux and a recession rate vector as follows,

$$\left[\dot{m}_g''\right] = \begin{bmatrix} \dot{m}_{g_x}'' \\ \dot{m}_{g_y}'' \\ \dot{m}_{g_z}'' \end{bmatrix} \qquad \left[\dot{S}\right] = \begin{bmatrix} \dot{S}_x \\ \dot{S}_y \\ \dot{S}_z \end{bmatrix} \tag{4.46}$$

Substituting (4.44), (4.45), and (4.46) into (4.42) and rearranging gives the three-dimensional matrix equations for the thermochemical ablation problem for one element,

$$\begin{aligned} &\iiint_{\Omega^{(e)}} \rho c_p \left[N\right]\left[N\right]^T \left\{\dot{T}\right\} dx_S dy_S dz_S + \iiint_{\Omega^{(e)}} \left[B\right]^T \left[k\right]\left[B\right]\left\{T\right\} dx_S dy_S dz_S \\ &\quad - \iiint_{\Omega^{(e)}} \rho c_p \left[\dot{S}\right]\left[N\right]\left[B\right]\left\{T\right\} dx_S dy_S dz_S = \iint_{\Gamma^{(e)}} \left(\mathbf{q}\cdot\hat{n}\right) N_i d\Gamma \\ &+ \iiint_{\Omega^{(e)}} \left[\dot{m}_g\right]\left[B\right]^T \left[N\right]^T \left\{h_g\right\} dx_S dy_S dz_S + \iiint_{\Omega^{(e)}} \left[\left(h_g - \bar{h}\right)\right]\left[N\right]\left\{\dot{\rho}\right\} dx_S dy_S dz_S \end{aligned} \tag{4.47}$$

Where the matrix ***B*** is the three-dimensional gradient interpolation matrix defined in (3.11) and ***N*** is the element interpolation matrix which will be discussed in the next section.

The thermal conductivity tensor is defined for an orthotropic material as,

$$k = \begin{bmatrix} k_x & 0 & 0 \\ 0 & k_y & 0 \\ 0 & 0 & k_z \end{bmatrix} \tag{4.48}$$

This definition for thermal conductivity assumes that the local element axes are aligned with the material principle directions. For elements where the local axes are not aligned with the material principle axes, the thermal conductivity tensor must be rotated by a direction cosine matrix, (***C***),

$$k = \begin{bmatrix} C_{11} & C_{12} & C_{13} \\ C_{21} & C_{22} & C_{23} \\ C_{31} & C_{32} & C_{33} \end{bmatrix} \begin{bmatrix} k_x & 0 & 0 \\ 0 & k_y & 0 \\ 0 & 0 & k_z \end{bmatrix} \begin{bmatrix} C_{11} & C_{12} & C_{13} \\ C_{21} & C_{22} & C_{23} \\ C_{31} & C_{32} & C_{33} \end{bmatrix} \tag{4.49}$$

Performing the matrix multiplications results in a symmetric anisotropic thermal conductivity matrix with respect to the element,

$$k = \begin{bmatrix} k_{11} & k_{12} & k_{13} \\ k_{12} & k_{22} & k_{23} \\ k_{13} & k_{23} & k_{33} \end{bmatrix} \tag{4.50}$$

4.2.2 Galerkin's Weak Form of the Conservation of Mass and Momentum Equations

To solve the conservation of mass and Darcy Flow equations, we choose the velocity components, *u, v, w*, in the x, y, z directions respectively and the pressure, p as the field variables. Using the three velocity components along with the pressure in the development of Galerkin's weak form is known as the mixed velocity-pressure formulation [58]. The first step in developing Galerkin's weak form is to assume a functional form for the field variables. The functional form for the mass flux components and pressure over one element are given by,

$$
\begin{aligned}
m''^{(e)}_{g_x} &= \sum_{i=1}^{n} N^u{}_i m''_{g_x i} = \left[N^u \right]^T \left\{ m''_{g_x} \right\}, \qquad \frac{\partial m''^{(e)}_{g_x}}{\partial x} = \sum_{i=1}^{n} \frac{\partial N^u_i}{\partial x} m''_{g_x i} = \left[\frac{\partial N}{\partial x} \right] \left\{ m''_{g_x} \right\} \\
m''^{(e)}_{g_y} &= \sum_{i=1}^{n} N^v{}_i m''_{g_y i} = \left[N^v \right]^T \left\{ m''_{g_y} \right\}, \qquad \frac{\partial m''^{(e)}_{g_y}}{\partial y} = \sum_{i=1}^{n} \frac{\partial N^v_i}{\partial y} m''_{g_y i} = \left[\frac{\partial N}{\partial y} \right] \left\{ m''_{g_y} \right\} \\
m''^{(e)}_{g_z} &= \sum_{i=1}^{n} N^w{}_i m''_{g_z i} = \left[N^w \right]^T \left\{ m''_{g_z} \right\}, \qquad \frac{\partial m''^{(e)}_{g_z}}{\partial z} = \sum_{i=1}^{n} \frac{\partial N^w_i}{\partial z} m''_{g_z i} = \left[\frac{\partial N}{\partial z} \right] \left\{ m''_{g_z} \right\} \\
P^{(e)} &= \sum_{i=1}^{n} N^P{}_i P_i = \left[N^P \right]^T \left\{ P \right\}
\end{aligned}
\tag{4.51}
$$

The interpolation functions N_i^u, N_i^v, N_i^w are identical to the interpolation functions used to describe the temperature and enthalpy in the energy equation. Several different approaches [125, 126, 127] have established that the interpolation functions for the pressure should be one order lower than the velocity components. The interpolation functions for the velocity components are linear, therefore the interpolation functions, N_i^P , are constant. The consequence of choosing interpolation functions in this manner is that while the velocity components maintain C^0 continuity from element to element, the pressure from element to element is discontinuous. For example, for an 8-noded hexahedral element, there would be three unknown velocity components at each node and the variation of the velocity would be described by the functions given in (4.51); whereas for each hexahedral element there would only be one unknown for the pressure. In order to maintain continuity for the pressure, high order elements would need to be utilized making the velocity component interpolation quadratic and the pressure interpolation linear. The formulation presented in this dissertation will utilize linear, 8-node hexahedral elements so the pressure interpolation functions are constant and discontinuous.

The next step is to write the weighted residual statement of (4.5) and (4.9) using the Bubnov-Galerkin approach, where $W_i = N_i^{u,v,w}$ and $H_i = N_i^P$,

$$\iiint_\Omega \left[m''^{(e)}_{g_x} + \frac{\kappa_{px}}{\nu\phi}\frac{\partial P^{(e)}}{\partial x} \right] N_i^u \, d\Omega = 0$$

$$\iiint_\Omega \left[m''^{(e)}_{g_y} + \frac{\kappa_{py}}{\nu\phi}\frac{\partial P^{(e)}}{\partial y} \right] N_i^v \, d\Omega = 0$$

$$\iiint_\Omega \left[m''^{(e)}_{g_z} + \frac{\kappa_{pz}}{\nu\phi}\frac{\partial P^{(e)}}{\partial z} \right] N_i^w \, d\Omega = 0 \tag{4.52}$$

$$\iiint_\Omega \left[\frac{\partial \dot{m}''^{(e)}_{g_x}}{\partial x} + \frac{\partial \dot{m}''^{(e)}_{g_y}}{\partial y} + \frac{\partial \dot{m}''^{(e)}_{g_z}}{\partial z} - \frac{\partial \rho}{\partial t} \right] N_i^P \, d\Omega = 0$$

To eliminate the pressure derivatives, Gauss's theorem is used to integrate the three components of the momentum equation by parts. Setting $u = N_i$ for each component and

$$\mathbf{v}_x = \frac{\kappa_{px}}{\nu\phi}\frac{\partial P^{(e)}}{\partial x}, \quad \mathbf{v}_y = \frac{\kappa_{py}}{\nu\phi}\frac{\partial P^{(e)}}{\partial y}, \quad \mathbf{v}_z = \frac{\kappa_{pz}}{\nu\phi}\frac{\partial P^{(e)}}{\partial z} \tag{4.53}$$

The result is Galerkin's weak form given as,

$$\iiint_\Omega \left(m''^{(e)}_{g_x} N_i^u \right) dxdydz + \iiint_\Omega \frac{\kappa_{px}}{\nu\phi}\frac{\partial N_i^u}{\partial x} P^{(e)} dxdydz = \iint_\Gamma N_i^u \left(P \cdot \hat{\mathbf{n}} \right) d\Gamma + \iint_\Gamma N_i^u V_n d\Gamma$$

$$\iiint_\Omega \left(m''^{(e)}_{g_y} N_i^v \right) dxdydz + \iiint_\Omega \frac{\kappa_{py}}{\nu\phi}\frac{\partial N_i^v}{\partial y} P^{(e)} dxdydz = \iint_\Gamma N_i^v \left(P \cdot \hat{\mathbf{n}} \right) d\Gamma + \iint_\Gamma N_i^v V_n d\Gamma$$

$$\iiint_\Omega \left(m''^{(e)}_{g_z} N_i^w \right) dxdydz + \iiint_\Omega \frac{\kappa_{pz}}{\nu\phi}\frac{\partial N_i^w}{\partial z} P^{(e)} dxdydz = \iint_\Gamma N_i^u \left(P \cdot \hat{\mathbf{n}} \right) d\Gamma + \iint_\Gamma N_i^u V_n d\Gamma \tag{4.54}$$

$$\iiint_\Omega \left[\frac{\partial \dot{m}''^{(e)}_{g_x}}{\partial x} + \frac{\partial \dot{m}''^{(e)}_{g_y}}{\partial y} + \frac{\partial \dot{m}''^{(e)}_{g_z}}{\partial z} \right] N_i^P \, dxdydz = \iiint_\Omega \frac{\partial \rho}{\partial t} N_i^P$$

The surface integrals on the right hand side of the momentum equation components were introduced by the integration by parts procedure. The first surface integral represents the surface tractions and the second represents a specified mass flow boundary condition. Substituting the definitions from (4.51) yields,

$$
\begin{aligned}
&\iiint_{\Omega}[N][N]\left\{m''_{g_x}\right\}dxdydz+\iiint_{\Omega}\frac{\kappa_{px}}{\nu\phi}\left[\frac{\partial N}{\partial x}\right]\{P\}\,dxdydz=\iint_{\Gamma}[N](P\cdot\hat{\mathbf{n}})d\Gamma+\iint_{\Gamma}[N]V_n d\Gamma\\
&\iiint_{\Omega}[N][N]\left\{m''_{g_y}\right\}dxdydz+\iiint_{\Omega}\frac{\kappa_{py}}{\nu\phi}\left[\frac{\partial N}{\partial y}\right]\{P\}\,dxdydz=\iint_{\Gamma}[N](P\cdot\hat{\mathbf{n}})d\Gamma+\iint_{\Gamma}[N]V_n d\Gamma\\
&\iiint_{\Omega}[N][N]\left\{m''_{g_z}\right\}dxdydz+\iiint_{\Omega}\frac{\kappa_{pz}}{\nu\phi}\left[\frac{\partial N}{\partial z}\right]\{P\}\,dxdydz=\iint_{\Gamma}[N](P\cdot\hat{\mathbf{n}})d\Gamma+\iint_{\Gamma}[N]V_n d\Gamma\\
&\iiint_{\Omega}\left[\frac{\partial N}{\partial x}\right]\left\{m''_{g_x}\right\}dxdydz+\iiint_{\Omega}\left[\frac{\partial N}{\partial y}\right]\left\{m''_{g_y}\right\}dxdydz+\iiint_{\Omega}\left[\frac{\partial N}{\partial z}\right]\left\{m''_{g_z}\right\}dxdydz=\iiint_{\Omega}[N]\left[\frac{\partial \rho}{\partial t}\right]dxdydz
\end{aligned}
\tag{4.55}
$$

Equation (4.55) can be expressed more compactly in matrix form as,

$$
\iiint_{\Omega}\begin{bmatrix}
[N][N] & 0 & 0 & \frac{\kappa_{px}}{\nu\phi}\left[\frac{\partial N}{\partial x}\right]\\
0 & [N][N] & 0 & \frac{\kappa_{py}}{\nu\phi}\left[\frac{\partial N}{\partial y}\right]\\
0 & 0 & [N][N] & \frac{\kappa_{pz}}{\nu\phi}\left[\frac{\partial N}{\partial z}\right]\\
\left[\frac{\partial N}{\partial x}\right]^T & \left[\frac{\partial N}{\partial y}\right]^T & \left[\frac{\partial N}{\partial z}\right]^T & 0
\end{bmatrix}\cdot\begin{bmatrix}
\left[m''_{g_x}\right]\\
\left[m''_{g_y}\right]\\
\left[m''_{g_z}\right]\\
[P]
\end{bmatrix}dxdydz=\iiint_{\Omega}\begin{bmatrix}
[F_x]\\
[F_y]\\
[F_z]\\
[N]\left[\frac{\partial \rho}{\partial t}\right]
\end{bmatrix}dxdydz
\tag{4.56}
$$

4.3 Isoparametric Element Formulation

In the one-dimensional formulation of Chapter 3, a simple two node bar element was developed. The simple 1-D bar element, while equivalent to a 1-D finite difference mesh, does not quite capture the power of the finite element method. The simplest forms of elements for three-dimensional problems are the four-noded tetrahedral and the eight-noded hexahedral element. To ensure that we may apply the finite element method to complex geometries, the three-dimensional formulation must go beyond these simple representations. To accomplish this, a class of elements known as isoparametric elements that are based on the simple tetrahedral and hexahedral elements will be developed. These isoparametric elements are formed by distorting the edges of the simple elements thereby producing curved sided elements. With curved sided elements, it is possible to better fit the boundaries of complex geometries with fewer elements. As a practical

matter, reducing the number of elements for a 3-D problem can lessen the computational burden.

In this dissertation, the general formulation for eight-noded isoparametric elements will be presented. In the implementation of the finite element solution however, this dissertation will be limited to eight-noded hexahedral elements with straight sides because the code relies on the mesh from Patran which does not have the ability to produce curved sided elements. In addition to curve-sided elements, the general isoparametric formulation is valid for straight sided elements and will still be in place for a future higher order curve-sided element upgrade.

4.3.1 Coordinate Transformation

The underlying idea in developing isoparametric elements of any order is to transform, or map simple geometric shapes in some local coordinate system into distorted shapes in the global Cartesian coordinate system; then, evaluate the resulting element equations [58, 60, 61]. In the following discussion, the terms *distorted* and *mapped* will be used to identify the element in the global Cartesian coordinate system and the local element coordinate system respectively.

Figure 4.3 shows a distorted eight-noded general hexahedral element in the global coordinate frame and its mapped counterpart in the local coordinate frame.

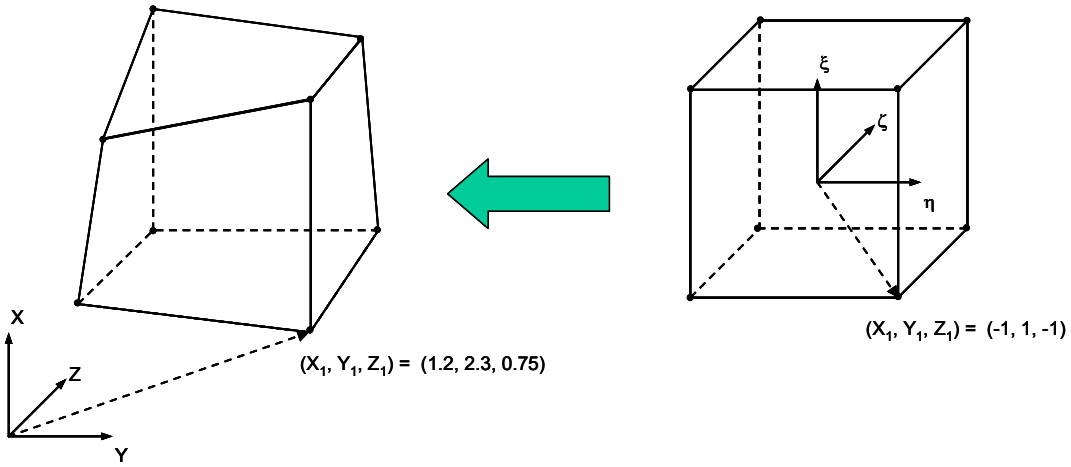

Figure 4.3: Isoparametric coordinate transform

The local nodal coordinates range from -1 to +1 and are related to the global coordinates through the element interpolation functions as follows,

$$x(\xi,\eta,\zeta) = \sum_{i=1}^{n} N_i(\xi,\eta,\zeta)x_i$$
$$y(\xi,\eta,\zeta) = \sum_{i=1}^{n} N_i(\xi,\eta,\zeta)y_i \tag{4.57}$$
$$z(\xi,\eta,\zeta) = \sum_{i=1}^{n} N_i(\xi,\eta,\zeta)z_i$$

Where x_i, y_i, and z_i are the nodal coordinates in the global coordinate system. Incidentally, the dependant variable is also written in terms of the local coordinates as,

$$T(\xi,\eta,\zeta) = \sum_{i=1}^{n} N_i(\xi,\eta,\zeta)T_i \tag{4.58}$$

Unlike the one-dimensional interpolation functions developed in Chapter 3 which were based on simple polynomials written in terms of global coordinates between two nodes, the interpolation functions for the three-dimensional isoparametric formulation are written in terms of the local coordinates. The interpolation functions are formed by writing products of Lagrange interpolating polynomials. The definition of a Lagrange interpolating polynomial in the global and local coordinate systems written for the x and ξ coordinates respectively is,

$$L_k(x) = \prod_{\substack{m=0 \\ m\neq k}}^{n} \frac{x - x_m}{x_k - x_m}, \qquad L_k(\xi) = \prod_{\substack{m=0 \\ m\neq k}}^{n} \frac{\xi - \xi_m}{\xi_k - \xi_m} \tag{4.59}$$

The Lagrange polynomials for the y, z and η, ζ coordinates are identical to those in (4.59); one simply needs to insert the respective coordinate. Lagrange polynomials possess the desired property of either being a unit value when evaluated at the node they are defined for, or zero when evaluated at any other node. The Lagrange polynomials are products of *n* factors and are clearly polynomials of order *n*. In relation to an element and its nodes, the order of the polynomial is related to the element order. The eight-noded

hexahedral element shown in Figure 4.3 is linear since there are only nodes in the corners. If there where nodes placed between each of the corner nodes, there would be 20 total nodes and the element and its subsequent Lagrange polynomial would both be quadratic. Since a curve is defined by a minimum of three points, in order to support curve-sided elements, the order of the element must be at least quadratic.

In three-dimensions, the interpolating functions are formed by writing the product,

$$N_i(\xi,\eta,\zeta) = L_i(\xi)L_i(\eta)L_i(\zeta) \tag{4.60}$$

Evaluating (4.60) for the linear eight-noded hexahedral element shown in Figure 4.3 in which i=1 to 8, gives the interpolation functions for the isoparametric formulation,

$$N_i(\xi,\eta,\zeta) = \tfrac{1}{8}(1+\xi\xi_i)(1+\eta\eta_i)(1+\zeta\zeta_i) \tag{4.61}$$

In matrix notation, the transpose of ***N*** may be written,

$$\left[N\right]^T(\xi,\eta,\zeta) = \begin{bmatrix} \tfrac{1}{8}(1-\xi)(1-\eta)(1-\zeta) \\ \tfrac{1}{8}(1-\xi)(1+\eta)(1-\zeta) \\ \tfrac{1}{8}(1-\xi)(1+\eta)(1+\zeta) \\ \tfrac{1}{8}(1-\xi)(1-\eta)(1+\zeta) \\ \tfrac{1}{8}(1+\xi)(1-\eta)(1-\zeta) \\ \tfrac{1}{8}(1+\xi)(1+\eta)(1-\zeta) \\ \tfrac{1}{8}(1+\xi)(1+\eta)(1+\zeta) \\ \tfrac{1}{8}(1+\xi)(1-\eta)(1+\zeta) \end{bmatrix} \tag{4.62}$$

4.3.2 Evaluation of the Element Matrices

After expressing the interpolation functions and the dependant variable in terms of the local coordinates, the task now is to evaluate the element equations which in general will be in the following form,

$$\int_{\Omega^{(e)}} f\left(T, \frac{\partial T}{\partial x}, \frac{\partial T}{\partial y}, \frac{\partial T}{\partial z}\right) dxdydz \tag{4.63}$$

Where $\Omega^{(e)}$ is the volume of the distorted element in the global coordinate system. Since the dependant variable, *T* has been expressed in terms of the local coordinates, the spatial derivatives of *T* and *dxdydz* must also be expressed in the local coordinates. From (4.58) the derivatives can be written as,

$$\frac{\partial T^{(e)}}{\partial x} = \sum_{i=1}^{n} \frac{\partial N_i}{\partial x} T_i, \qquad \frac{\partial T^{(e)}}{\partial y} = \sum_{i=1}^{n} \frac{\partial N_i}{\partial y} T_i, \qquad \frac{\partial T^{(e)}}{\partial z} = \sum_{i=1}^{n} \frac{\partial N_i}{\partial z_S} T_i \tag{4.64}$$

Hence, $\partial N_i/\partial x$, $\partial N_i/\partial y$, and $\partial N_i/\partial z$ must be expressed in terms of ξ, η, and ζ. Using the chain rule ,

$$\begin{aligned} \partial N_i &= f(\xi,\eta,\zeta) \\ \frac{\partial N_i}{\partial \xi} &= \frac{\partial N_i}{\partial x}\frac{\partial x}{\partial \xi} + \frac{\partial N_i}{\partial y}\frac{\partial y}{\partial \xi} + \frac{\partial N_i}{\partial z}\frac{\partial z}{\partial \xi} \\ \frac{\partial N_i}{\partial \eta} &= \frac{\partial N_i}{\partial x}\frac{\partial x}{\partial \eta} + \frac{\partial N_i}{\partial y}\frac{\partial y}{\partial \eta} + \frac{\partial N_i}{\partial z}\frac{\partial z}{\partial \eta} \\ \frac{\partial N_i}{\partial \zeta} &= \frac{\partial N_i}{\partial x}\frac{\partial x}{\partial \zeta} + \frac{\partial N_i}{\partial y}\frac{\partial y}{\partial \zeta} + \frac{\partial N_i}{\partial z}\frac{\partial z}{\partial \zeta} \end{aligned} \tag{4.65}$$

or in matrix notation as,

$$\begin{bmatrix} \frac{\partial N_i}{\partial \xi} \\ \frac{\partial N_i}{\partial \eta} \\ \frac{\partial N_i}{\partial \zeta} \end{bmatrix} = \begin{bmatrix} \frac{\partial x}{\partial \xi} & \frac{\partial y}{\partial \xi} & \frac{\partial z}{\partial \xi} \\ \frac{\partial x}{\partial \eta} & \frac{\partial y}{\partial \eta} & \frac{\partial z}{\partial \eta} \\ \frac{\partial x}{\partial \zeta} & \frac{\partial y}{\partial \zeta} & \frac{\partial z}{\partial \zeta} \end{bmatrix} \begin{bmatrix} \frac{\partial N_i}{\partial x} \\ \frac{\partial N_i}{\partial y} \\ \frac{\partial N_i}{\partial z} \end{bmatrix} = [J] \begin{bmatrix} \frac{\partial N_i}{\partial x} \\ \frac{\partial N_i}{\partial y} \\ \frac{\partial N_i}{\partial z} \end{bmatrix} \tag{4.66}$$

Where the matrix ***J*** defines a Jacobian matrix,

$$[J] = \begin{bmatrix} \frac{\partial x}{\partial \xi} & \frac{\partial y}{\partial \xi} & \frac{\partial z}{\partial \xi} \\ \frac{\partial x}{\partial \eta} & \frac{\partial y}{\partial \eta} & \frac{\partial z}{\partial \eta} \\ \frac{\partial x}{\partial \zeta} & \frac{\partial y}{\partial \zeta} & \frac{\partial z}{\partial \zeta} \end{bmatrix} \tag{4.67}$$

The Jacobian is evaluated by using the coordinate transformations given in equation (4.57). Finally, to find the desired derivative of the dependant variable in terms of the local coordinates, the inverse of the Jacobian must be calculated and therefore the derivatives may be expressed as,

$$\begin{bmatrix} \frac{\partial T}{\partial x} \\ \frac{\partial T}{\partial y} \\ \frac{\partial T}{\partial z} \end{bmatrix} = [J]^{-1} \begin{bmatrix} \frac{\partial N_1}{\partial \xi} & \frac{\partial N_2}{\partial \xi} & \cdots & \frac{\partial N_n}{\partial \xi} \\ \frac{\partial N_1}{\partial \eta} & \frac{\partial N_2}{\partial \eta} & \cdots & \frac{\partial N_n}{\partial \eta} \\ \frac{\partial N_1}{\partial \zeta} & \frac{\partial N_2}{\partial \zeta} & \cdots & \frac{\partial N_n}{\partial \zeta} \end{bmatrix} \begin{bmatrix} T_1 \\ T_2 \\ \vdots \\ T_n \end{bmatrix} \tag{4.68}$$

To complete the evaluation of the integrals in the element equations, *dxdydz* needs to be expressed in terms of ξ,η, and ζ. Text books on advanced calculus show that [140],

$$dxdydz = |J| d\xi d\eta d\zeta \tag{4.69}$$

Where $|J|$ is the determinant of the Jacobian matrix. The final form of the element equations in terms of the local coordinates may now be written as,

$$\begin{aligned} &\int_{-1}^{1}\int_{-1}^{1}\int_{-1}^{1} \rho c_p [N][N]^T \{\dot{T}\} |J| d\xi_S d\eta_S d\zeta_S + \int_{-1}^{1}\int_{-1}^{1}\int_{-1}^{1} [B]^T [k][B]\{T\} |J| d\xi_S d\eta_S d\zeta_S \\ &\quad - \int_{-1}^{1}\int_{-1}^{1}\int_{-1}^{1} \rho c_p [\dot{S}][N][B]\{T\} |J| d\xi_S d\eta_S d\zeta_S = \iint_{\Gamma^{(e)}} (\mathbf{q}\cdot\hat{n})[N] d\Gamma \\ &+ \int_{-1}^{1}\int_{-1}^{1}\int_{-1}^{1} [\dot{m}_g][B]^T [N]^T \{h_g\} |J| d\xi_S d\eta_S d\zeta_S + \int_{-1}^{1}\int_{-1}^{1}\int_{-1}^{1} [(h_g - \bar{h})][N]\{\dot{\rho}\} |J| d\xi_S d\eta_S d\zeta_S \end{aligned} \tag{4.70}$$

Where the interpolation functions ***N*** have been defined in equation (4.62) and the gradient interpolation matrix is now defined as,

$$[B(\xi,\eta,\zeta)] = [J]^{-1} \begin{bmatrix} \frac{\partial N_1}{\partial \xi} & \frac{\partial N_2}{\partial \xi} & \cdots & \frac{\partial N_n}{\partial \xi} \\ \frac{\partial N_1}{\partial \eta} & \frac{\partial N_2}{\partial \eta} & \cdots & \frac{\partial N_n}{\partial \eta} \\ \frac{\partial N_1}{\partial \zeta} & \frac{\partial N_2}{\partial \zeta} & \cdots & \frac{\partial N_n}{\partial \zeta} \end{bmatrix} \tag{4.71}$$

The integrals present in the matrix equations of (4.70) cannot be evaluated analytically. They must be evaluated numerically. The numerical integration scheme used is described in detail in several texts on the finite element method [58, 60, 61], and is called Gauss-Legendre integration.

4.4 Three-Dimensional Grid Movement and Coupled Structural Analysis

In the formulation presented here the mesh is attached to the ablating surface and moves with the surface. Unlike the one-dimensional mesh where the adjacent nodes were all aligned with the x-axis, the three-dimensional mesh may have nodes that do not align with the axes, i.e. an unstructured mesh. For the one-dimensional mesh, it was relatively easy to move the mesh as the surface receded. The mesh was contracted linearly from the surface to the last ablating node, where the last ablating node was fixed in position. For the three-dimensional case, it is not as straightforward since the mesh may not be aligned with any particular coordinate axes and the points on the surface may be ablating at different rates due to variable surface boundary conditions. Building on the work of Lynch and O'Neil [128], and Hogan, et al., [100] the mesh movement in this dissertation will be modeled assuming the mesh behaves as a linear elastic solid.

It is a fortuitous coincidence that the grid movement scheme makes use of the linear elastic equations to displace the mesh. Having already included the logic necessary to implement the linear elastic equations, solving for the thermal stress during the thermal response transient becomes trivial. In this section the three-dimensional finite element equations for thermal stress will be presented. Since the structural problem being analyzed in this dissertation is a relatively standard engineering problem, the governing differential equations will not be derived in detail.

4.4.1 Grid Movement Scheme

Although the approaches developed by Lynch and O'Neil, and Hogan et al., are for a two-dimensional problem, their scheme can be extended to three-dimensions by using the three-dimensional versions of the linear elasticity equations. The goal is to write the governing three-dimensional differential equations for linear elasticity and put them into Galerkin's weak form in terms of forces and displacements.

After a converged solution of the finite element thermal code over a time interval Δt, the surface recession calculated during that interval for each ablating surface node becomes the displacement boundary condition for the linear elasticity solution. Nodes of the ablative material that are on the boundary of a non-ablative backup structural material are fixed with zero displacement. Additionally, all non-ablative material nodes are fixed with zero displacement. The linear elasticity finite element equations are then solved for the remaining nodal displacements and the nodal coordinates are altered according to that solution.

The first step is to write the governing differential equations for linear elasticity. For linear elasticity, the governing equations are the equilibrium equations [58, 60],

$$\begin{aligned}
\frac{\partial \sigma_x}{\partial x} + \frac{\partial \tau_{xy}}{\partial y} + \frac{\partial \tau_{xz}}{\partial z} + F_x &= 0 \\
\frac{\partial \tau_{xy}}{\partial x} + \frac{\partial \sigma_y}{\partial y} + \frac{\partial \tau_{yz}}{\partial z} + F_y &= 0 \\
\frac{\partial \tau_{xz}}{\partial x} + \frac{\partial \tau_{yz}}{\partial y} + \frac{\partial \sigma_z}{\partial z} + F_z &= 0
\end{aligned} \tag{4.72}$$

Writing (4.72) in matrix form gives,

$$\left[L\right]^T \left\{\sigma\right\} - \left\{F_b\right\} = 0 \tag{4.73}$$

Where $\left[L\right]$ is a differential operator, $\left\{\sigma\right\}$ is the vector of stress components, and $\left\{F_b\right\}$ is the vector of body force components per unit volume and are defined as,

$$[L]=\begin{bmatrix} \frac{\partial}{\partial x} & 0 & 0 \\ 0 & \frac{\partial}{\partial y} & 0 \\ 0 & 0 & \frac{\partial}{\partial z} \\ \frac{\partial}{\partial y} & \frac{\partial}{\partial x} & 0 \\ \frac{\partial}{\partial z} & 0 & \frac{\partial}{\partial x} \\ 0 & \frac{\partial}{\partial z} & \frac{\partial}{\partial y} \end{bmatrix}, \qquad \{\sigma\}=\begin{bmatrix} \sigma_x \\ \sigma_y \\ \sigma_z \\ \tau_{xy} \\ \tau_{xz} \\ \tau_{yz} \end{bmatrix}, \qquad \{F_b\}=\begin{bmatrix} F_x \\ F_y \\ F_z \end{bmatrix} \tag{4.74}$$

The second equation needed is the strain-displacement relationship given by,

$$\{\varepsilon\}=[L]\{\delta\} \tag{4.75}$$

Where the strain vector $\{\varepsilon\}$ and displacement vector $\{\delta\}$ are defined as,

$$\{\varepsilon\}=\begin{bmatrix} \varepsilon_x \\ \varepsilon_x \\ \varepsilon_z \\ \varepsilon_{xy} \\ \varepsilon_{xz} \\ \varepsilon_{yz} \end{bmatrix}, \quad \{\delta\}=\begin{bmatrix} u(x,y,z) \\ v(x,y,z) \\ w(x,y,z) \end{bmatrix} \tag{4.76}$$

The third relation needed is Hooke's law which relates the stress to the strain given in matrix form as,

$$\{\sigma\}=[C_e]\{\varepsilon\}-[C_e]\{\varepsilon_0\} \tag{4.77}$$

Where the matrix $[C_e]$is the 6x6 linear elastic modulus matrix and $\{\varepsilon_0\}$ is the vector of initial strains due to non-uniform temperature distribution. The components of the elastic modulus matrix vary depending on whether the material is isotropic, orthotropic, or anisotropic (see Appendix B)[129]. For the purposes of the grid movement scheme, the elastic modulus matrix will be assumed to be isotropic. For the grid movement scheme,

the actual stresses and strains are of no consequence so this simplification posses no real problems.

The next step is to substitute equation (4.75) into (4.77) which gives,

$$\{\sigma\} = [C_e][L]\{\delta\} - [C_e]\{\varepsilon_0\} \tag{4.78}$$

Equation (4.78) is then substituted into the governing differential equations of (4.73) to yield,

$$[L]^T \left([C_e][L]\{\delta\} - [C_e]\{\varepsilon_0\} \right) - \{F_b\} = 0 \tag{4.79}$$

Equation (4.79) is the matrix form of the three-dimensional equilibrium equations of linear elasticity. The weighted residual statement of (4.79) can now written as,

$$\iiint_{\Omega} [W][L]^T \left([C_e][L]\{\delta\} - [C_e]\{\varepsilon_0\} \right) d\Omega - \iiint_{\Omega} [W]\{F_b\}\, d\Omega = 0 \tag{4.80}$$

Where the 3x3 matrix $[W]$ is the weighting function matrix defined as,

$$[W] = \begin{bmatrix} W_1 & 0 & 0 \\ 0 & W_2 & 0 \\ 0 & 0 & W_3 \end{bmatrix} \tag{4.81}$$

Next, the first term of (4.80) is integrated by parts using Gauss's theorem and yields the weak form,

$$\begin{aligned} \iiint_{\Omega} \left([L][W]^T \right)^T [C_e][L]\{\delta\}\, d\Omega - \iiint_{\Omega} \left([L][W]^T \right)^T [C_e]\{\varepsilon_0\} d\Omega \\ + \iiint_{\Omega} [W]\{F_b\}\, d\Omega - \iint_{\Gamma} [W]\{T_c\}\, d\Gamma = 0 \end{aligned} \tag{4.82}$$

The integration by parts has introduced a surface integral which includes surface tractions which are defined by,

$$\{T_c\} = [n][C_e][L]\{\delta\} \tag{4.83}$$

Where $[n]$ is a 3x3 matrix with the diagonal elements equal to the components of a unit vector, $\boldsymbol{n}$. Equation (4.82) is the global system equation valid for the entire volume, to

obtain the equations for an individual element; the displacement field is approximated using the interpolation functions N_i as,

$$\{\delta\}^{(e)} = [N]\{\delta\} \tag{4.84}$$

The weighting functions are set equal to the interpolation functions and the product of the interpolation matrix and the differential operator $\boldsymbol{L}$, is the element strain interpolation matrix defined as,

$$[B_e] = \begin{bmatrix} \frac{\partial N_1}{\partial x} & 0 & 0 & \frac{\partial N_2}{\partial x} & 0 & 0 & \cdots & \frac{\partial N_i}{\partial x} & 0 & 0 \\ 0 & \frac{\partial N_1}{\partial y} & 0 & 0 & \frac{\partial N_2}{\partial y} & 0 & \cdots & 0 & \frac{\partial N_i}{\partial y} & 0 \\ 0 & 0 & \frac{\partial N_1}{\partial z} & 0 & 0 & \frac{\partial N_2}{\partial z} & \cdots & 0 & 0 & \frac{\partial N_i}{\partial z} \\ \frac{\partial N_1}{\partial y} & \frac{\partial N_1}{\partial x} & 0 & \frac{\partial N_2}{\partial y} & \frac{\partial N_2}{\partial x} & 0 & \cdots & \frac{\partial N_i}{\partial y} & \frac{\partial N_i}{\partial x} & 0 \\ \frac{\partial N_1}{\partial z} & 0 & \frac{\partial N_1}{\partial x} & \frac{\partial N_2}{\partial z} & 0 & \frac{\partial N_2}{\partial x} & \cdots & \frac{\partial N_i}{\partial z} & 0 & \frac{\partial N_i}{\partial x} \\ 0 & \frac{\partial N_1}{\partial z} & \frac{\partial N_1}{\partial y} & 0 & \frac{\partial N_2}{\partial z} & \frac{\partial N_2}{\partial y} & \cdots & 0 & \frac{\partial N_i}{\partial z} & \frac{\partial N_i}{\partial y} \end{bmatrix} \tag{4.85}$$

Substituting (4.84) and (4.85) into (4.82) yields Galerkin's weak form for one element,

$$\begin{aligned} \iiint_{\Omega^{(e)}} [B_e]^T [C_e][B]\{\delta\}^{(e)}\, d\Omega - \iiint_{\Omega^{(e)}} [B_e]^T [C_e]\{\varepsilon_0\}^{(e)} d\Omega \\ + \iiint_{\Omega^{(e)}} [N]^T \{F_b\}^{(e)}\, d\Omega - \iint_{\Gamma^{(e)}} [N]^T \{T_c\}^{(e)}\, d\Gamma = 0 \end{aligned} \tag{4.86}$$

For the grid motion scheme, the initial strains are zero and there are no body forces and no surface tractions. The boundary conditions for each ablating node are of the form,

$$\begin{bmatrix} u \\ v \\ w \end{bmatrix} = \begin{bmatrix} \dot{s}_x \Delta t \hat{n}_x \\ \dot{s}_y \Delta t \hat{n}_y \\ \dot{s}_z \Delta t \hat{n}_z \end{bmatrix} \tag{4.87}$$

Upon assembly, (4.86) represent a linear system and can be solved by any direct linear solver.

4.4.2 Thermal Stress Analysis

Having developed Galerkin's weak form in the previous section, it is straight forward to repeat that result here,

$$\begin{aligned}\iiint_{\Omega^{(e)}}\left[B_e\right]^T\left[C_e\right]\left[B\right]\left\{\delta\right\}^{(e)}d\Omega-\iiint_{\Omega^{(e)}}\left[B_e\right]^T\left[C_e\right]\left\{\varepsilon_0\right\}^{(e)}d\Omega\\+\iiint_{\Omega^{(e)}}\left[N\right]^T\left\{F_b\right\}^{(e)}d\Omega-\iint_{\Gamma^{(e)}}\left[N\right]^T\left\{T_c\right\}^{(e)}d\Gamma=0\end{aligned}\tag{4.88}$$

The difference now is that the initial strain vector is non-zero and if surface tractions and body forces are present they may be included as well. Another difference is that for the thermal stress solution, the material properties used are the actual properties which for most ablative materials are orthotropic material properties. Therefore the elastic modulus matrix will be the orthotropic modulus matrix (see Appendix B).

Unlike the grid movement scheme, for the thermal stress analysis, the stresses are the desired result. After solving (4.88) for the nodal displacements due to thermal expansion, body forces, and surface tractions, the resulting stresses for any element may be calculated by,

$$\left\{\sigma\right\}^{(e)}=\left[C_e\right]^{(e)}\left[B\right]^{(e)}\left\{\delta\right\}^{(e)}-\left[C_e\right]^{(e)}\left\{\varepsilon_0\right\}^{(e)}\tag{4.89}$$

4.5 Verification of the Three-Dimensional Analysis Code

In this dissertation, the three-dimensional code has been written in a mixture of C++ and FORTRAN with its foundation being the one-dimensional code developed in Chapter 3. The three-dimensional code is built around the finite element library libMesh and the Portable, Extensible Toolkit for Scientific computation (PETSc) [130, 131, 132, 133]. The libMesh library provides data structures and routines that aid in creating the sparse global finite element matrices and provides an interface to the PETSc suite of linear and non-linear sparse matrix solvers. PETSc includes the routines and data structures necessary to solve sparse matrix problems. In this section, the three-dimensional code

has been exercised in a similar fashion as the one-dimensional code. The first case is a thick square, metallic, plate with constant thermal properties and a constant heat flux boundary condition and is compared to the transient analytic solution for a semi-infinite solid. The second case is a metallic, square plate with constant thermal properties and is compared to NASTRAN Thermal. The boundary conditions for this case consist of a constant heat flux on one surface and radiation away from the opposite surface. The third verification case is identical to the third verification case from Chapter 3, Section 3.5.3. The fourth verification case is identical to the second verification case of Chapter 3, Section 3.5.2. The final verification case is identical to the fourth verification case of Chapter 3, Section 3.5.4. The heat flux profiles for cases 3-5 are shown in Figure 3.2. A summary of the test problems and their conditions is shown in Table 4.1. The geometry for the first two cases is identical and consists of a 7.62 x 7.62 x 7.62cm square cube. The geometry for cases 3-5 consists of a 2.54 x 2.54 x 7.62cm rectangular block, with the 7.62cm dimension being the through the thickness direction. All cases are planar so that relevant comparisons to the one-dimensional FIAT results can be made.

Table 4.1: Summary of verification cases

Case	Description	Material	Boundary Conditions
1	Planar, semi-infinite solid, linear	Titanium (Ti-6Al-4V), constant thermal properties	Constant input convective heat flux, no pyrolysis, no ablation
2	Planar, non-linear	Titanium (Ti-6Al-4V), constant thermal properties	Constant input convective heat flux, no pyrolysis, no ablation, surface radiation away from the backwall
3	Planar, non-linear, entry trajectory	Reinforced Carbon-Carbon, thermal properties a function of temperature	Input convective and radiative heat flux a function of time, surface radiation away from the heated surface, no pyrolysis, ablation
4	Planar, non-linear, entry trajectory	MX4926N Carbon Phenolic, thermal properties a function of temperature	Input convective and radiative heat flux a function of time, surface radiation away from the heated surface, pyrolysis, no ablation
5	Planar, non-linear, arc jet condition	MX4926N Carbon Phenolic, thermal properties a function of temperature	Input convective and radiative heat flux constant, surface radiation away from the heated surface, pyrolysis, ablation

4.5.1 Verification Case 1: Constant Heat Flux, Constant Thermal Properties, Semi-Infinite Solid

The first verification case is a thick square block of Ti-6Al-4V Titanium alloy. The thermal properties are constant and isotropic and there is no pyrolysis or ablation. Since the slab is very thick, for short transients, the material can be considered a semi-infinite solid. A semi-infinite solid is one in which the material extends to infinity in all but one direction. Under the semi-infinite solid assumption, the in-depth energy equation (4.36) reduces to,

$$\rho c_p \frac{\partial T}{\partial t} = k_x \frac{\partial^2 T}{\partial x^2} \tag{4.90}$$

With a constant heat flux boundary condition and initial condition of,

$$\begin{aligned} -k_x \left.\frac{\partial T}{\partial x}\right|_{x=0} &= q_0'' \\ T(x,0) &= T_i \end{aligned} \tag{4.91}$$

For the semi-infinite solid, an analytic solution exists for the transient thermal response of equations (4.90) and (4.91) and is given as,

$$T(x,t) - T_i = \frac{2q_0''\left(\frac{\alpha t}{\pi}\right)^{\frac{1}{2}}}{k} \exp\left(\frac{-x^2}{4\alpha t}\right) - \frac{q_0'' x}{k} erfc\left(\frac{x}{2\sqrt{\alpha t}}\right) \tag{4.92}$$

$$where, \qquad \alpha = \frac{k}{\rho c_p}$$

Equation (4.92) is solved for the temperature as a function of time. A comparison of the three-dimensional finite element solution to this analytic solution is presented in Figure 4.4. The temperature comparison between the 3-D finite element code and the analytic solution for this case is almost an exact match at the surface and at a chosen depth of 3.81cm. At depths inside the solid towards the backwall, this comparison begins to break

down as the semi-infinite solid assumption starts to deteriorate. This case demonstrates that the 3-D conduction solution and the application of boundary conditions are working properly.

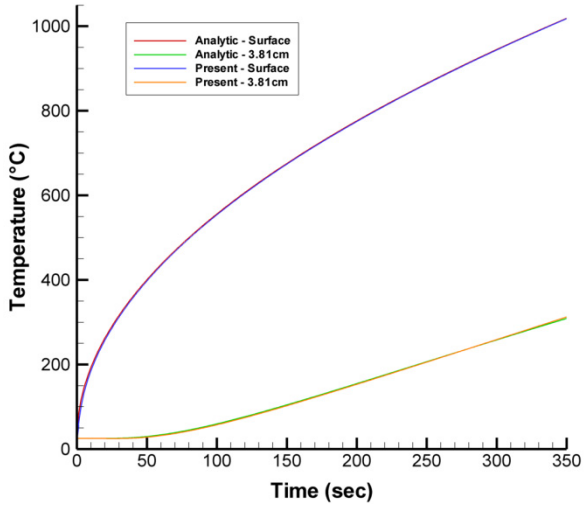

Figure 4.4: Temperature comparison between 3-D finite element and analytic solutions

4.5.2 Verification Case 2: Constant Heat Flux, Constant Thermal Properties, Radiation Away (Non-Linear)

The second case is a square plate made of Ti-6Al-4V Titanium alloy. The thermal properties are constant and isotropic and there is no pyrolysis or ablation. There is a radiation boundary condition placed on the surface directly opposite to that which has the constant heat flux applied. The radiation boundary condition makes the problem non-linear and requires the use of a non-linear solution scheme. There is no analytic solution for this case, so a comparison is made between the current finite element solution and NASTRAN Thermal, a commercially available finite element code. The nodal temperature plotted in Figure 4.5 corresponds to the node at the exact center of the top surface and is compared to the NASTRAN solution of a node at the same location. This is possible since both codes used the same mesh. The nodal temperature plotted in Figure 4.6 corresponds to the node at the exact center of the bottom surface.

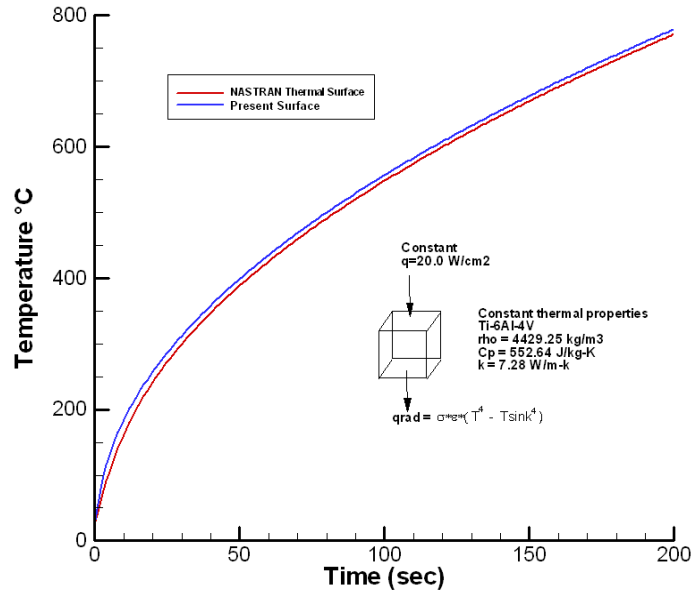

Figure 4.5: Surface temperature comparison between present solution and NASTRAN Thermal

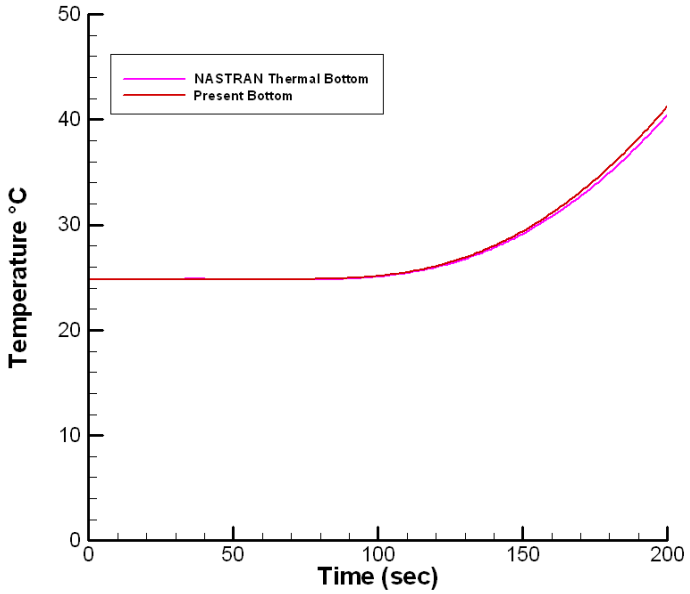

Figure 4.6: Temperature comparison on the bottom surface between present and NASTRAN Thermal

4.5.3 Verification Case 3: Low Peak Heat Flux Trajectory, No Ablation, With Pyrolysis

The boundary conditions and material choice for this verification case are identical to verification case 3 from Chapter 3. In this section, the problem is solved with the three-dimensional tool in a simulated one-dimensional mode. To simulate one-dimensional behavior, the thermal conductivity for the y and z directions was set equal to the thermal conductivity in the x-direction. The pyrolysis gas flow calculation is active, but the permeability for the y and z directions was set artificially low so that the flow would be constrained to flow only in the x-direction. The temperature for the three-dimensional tool running in a one-dimensional mode is compared to both the FIAT results and the result from the one-dimensional finite element tool developed in Chapter 3 in Figure 4.7.

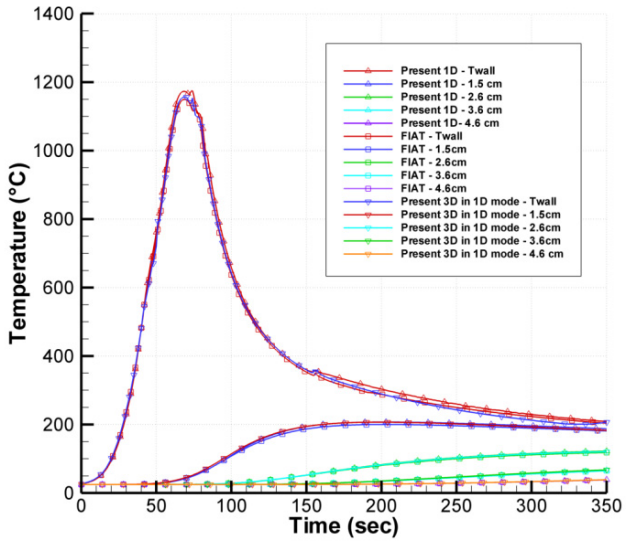

Figure 4.7: Temperature comparison for MX4926N carbon phenolic, pyrolysis, with no recession

The surface temperature of the three-dimensional tool matches FIAT well and is a better match than that of the one-dimensional finite element tool. The in-depth temperatures match quite well and the character of the curves are similar; however the in-

depth temperatures for the present one-dimensional and three-dimensional solutions are slightly higher. The temperature difference reaches a peak of 3.7% at the 1.5cm location.

Although it had little effect on the in-depth temperatures for this verification case, in the three-dimensional calculation, it is possible for the gas to travel in both the positive and negative x direction because of the approach used to compute the pyrolysis gas pressure and mass flow. Since the peak pressure occurs at the in-depth location where the decomposition rate is the largest, a pressure gradient is formed with respect to that location and the surface as well as that location and the bottom surface of the ablator. Even though there is a solid boundary at the backface of the ablator which is a no flow boundary condition, the permeability in the y and z directions, albeit very small, was non-zero. This allows the gas to flow towards the backface eventually reaching zero at the backface. Since the pyrolysis gas traveling towards the backface is at a higher temperature than the material it passes through in that direction, heat can be transferred from the gas to material via the pyrolysis gas convection term in the governing equations; hence for cases that have large pressure gradients and high flow rates towards the backface, the in-depth temperatures could potentially be higher.

A comparison of the pyrolysis gas flux at the surface is provided in Figure 4.8. Notice that like the present one-dimensional solution, the three-dimensional solution also exhibits oscillations. The oscillations are present since the Darcy flow and conservation of mass equation systems are solved explicitly. As described in Chapter 3, Section 3.5.3, the oscillations can be reduced by making the calculation implicit or refining the mesh by adding nodes and elements near the surface. The affect of mesh refinement on the pyrolysis gas flux will be illustrated in Section 4.5.6. Although there are oscillations, the three-dimensional pyrolysis mass flux is similar in character and magnitude to the FIAT result and the present one-dimensional result. This validates that the Darcy flow system of equations are being solved correctly.

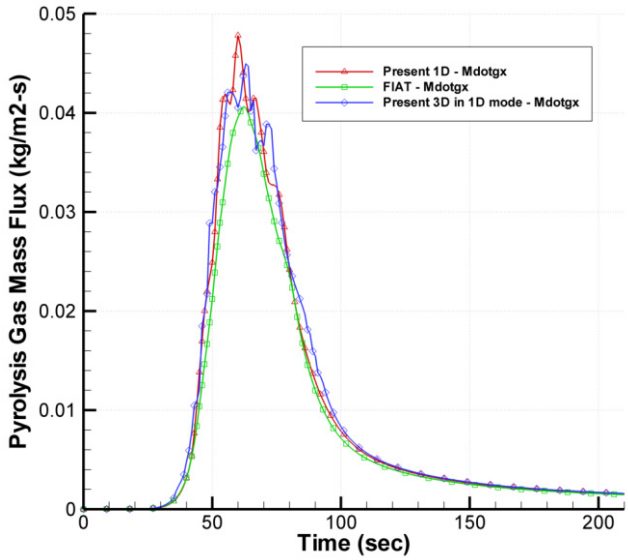

Figure 4.8: Pyrolysis gas mass flux at the surface

4.5.4 Verification Case 4: Moderate Peak Heat Flux Trajectory, With Ablation, No Pyrolysis

This verification case is the same as verification case 2 from Chapter 3. The three-dimensional code was run in a one-dimensional mode so as to compare the results with the one-dimensional FIAT results. This case demonstrates that the present tool accurately calculates surface recession and exercises the code's moving grid scheme in the absence of the complicating effects of decomposition and pyrolysis gas flow. In this case, there was no radiative heating input as a surface boundary condition, only convective heating input as a simulated trajectory. The peak heat flux was 200 W/cm^2 and was chosen so that the material would reach a temperature regime where recession would occur. The temperature for the three-dimensional tool running in a one-dimensional mode is compared FIAT and is shown in Figure 4.9. The surface temperature for this case matches the FIAT solution well. The in-depth temperatures for this case are slightly higher than FIAT, as was the case for the one-dimensional solution.

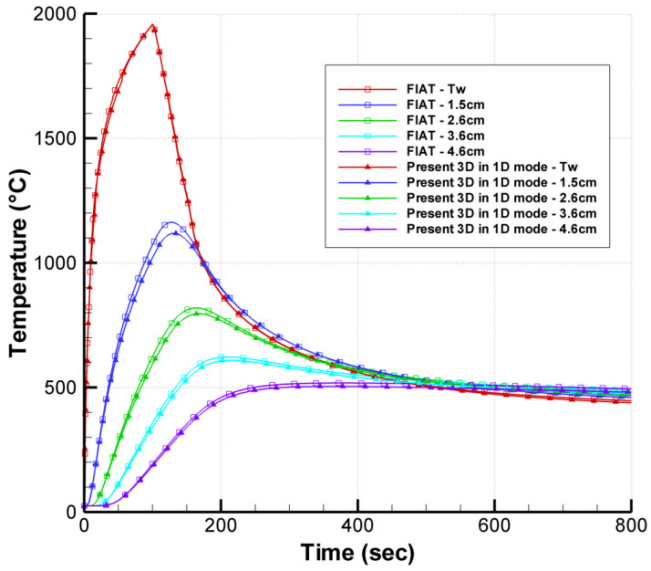

Figure 4.9: Temperature comparison for reinforced carbon-carbon, recession with no pyrolysis

4.5.5 Verification Case 5: High Heat Flux Arc jet Test Condition

This verification case is the same as verification case 4 from Chapter 3. Here the three-dimensional code was run in a one-dimensional mode so as to compare the results with the one-dimensional FIAT results. This case is an arc jet test condition with a high heat flux for a 200 second exposure, followed by a 400 second cool down period. The material exposed to the arc jet condition was MX4926N carbon phenolic with a thickness of 6.35cm. For insulation, 6.02cm of LI-2200 was placed behind the carbon phenolic. The arc jet condition provides a constant heat flux boundary condition environment which is high enough in magnitude and long enough in duration to cause surface recession for this material. The heat flux is input as a step function, so it is also a good test of the solution algorithms' stability under a high gradient condition. During the cool down, the material reradiates and heat soaks into the material away from the exposed surface. During cool down a significant temperature gradient develops through the thickness of the material and allows comparison of in-depth temperatures. The surface temperatures calculated by the present tool and FIAT are shown in Figure 4.10. The surface temperatures match

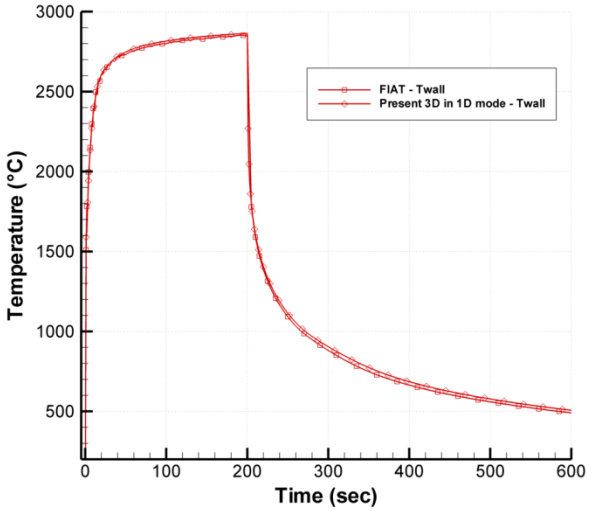

Figure 4.10: Surface temperature comparison for MX4926N arc jet test condition

well. However, the surface temperature calculated by the present three-dimensional tool is 6°C higher than that calculated by the one-dimensional version of the present tool which may have been caused by differences in the mesh densities. In the three-dimensional mesh it was not known a priori what mesh density at the surface would be sufficient, so a finer mesh density at the surface was chosen for this three-dimensional case. The in-depth temperatures are match well and are presented in Figure 4.11. It is

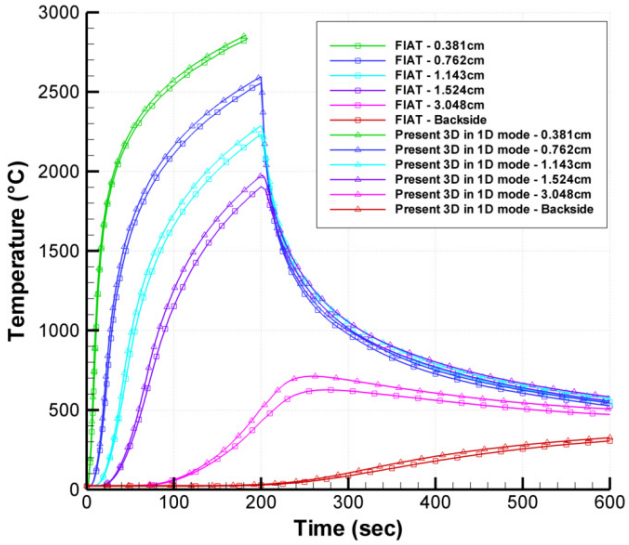

Figure 4.11: In-depth temperature comparison for MX4926N arc jet test condition

interesting to note that the overall match between the present three-dimensional tool and FIAT is better than the one-dimensional tool. This can be attributed to the more robust non-linear solver provided by PETSc as well as a better treatment of the pyrolysis gas flow solution via Darcy's Law which oscillates less.

4.5.5.1 Mesh Movement Verification

The equations for linear elasticity are solved after every time step in which recession was calculated. The linear elastic properties used in the mesh movement calculation are constant, isotropic properties for Titanium. The mesh is moved by imposing the calculated recession as a fixed displacement boundary condition. In this dissertation, verification of the mesh movement scheme was performed by inspecting the x,y,z coordinates in the output file, and comparing with the total amount of recession calculated during the arc jet case simulation. Additionally, a simple case of displacement due to thermal expansion was run and compared to the displacement calculated with MSC Software's NASTRAN.

For the arc jet case, the boundary conditions were applied uniformly over the top surface of the mesh where the initial value for the x-coordinate of all the nodes on that surface was 0.0. If the mesh movement scheme is working correctly, all the nodes on the surface should move uniformly and have a new x-coordinate value equal to the total amount of recession calculated. The initial surface location at the beginning of the simulation and the final ablated shape at the end of the simulation are shown in Figure 4.12. Visually, it can be seen that all of the surface nodes have moved uniformly. Within the output file, the x-coordinate location at the end of the simulation was moved to 0.004268 m compared to the actual calculated recession of 0.0042682 m, is a 0.468% difference.

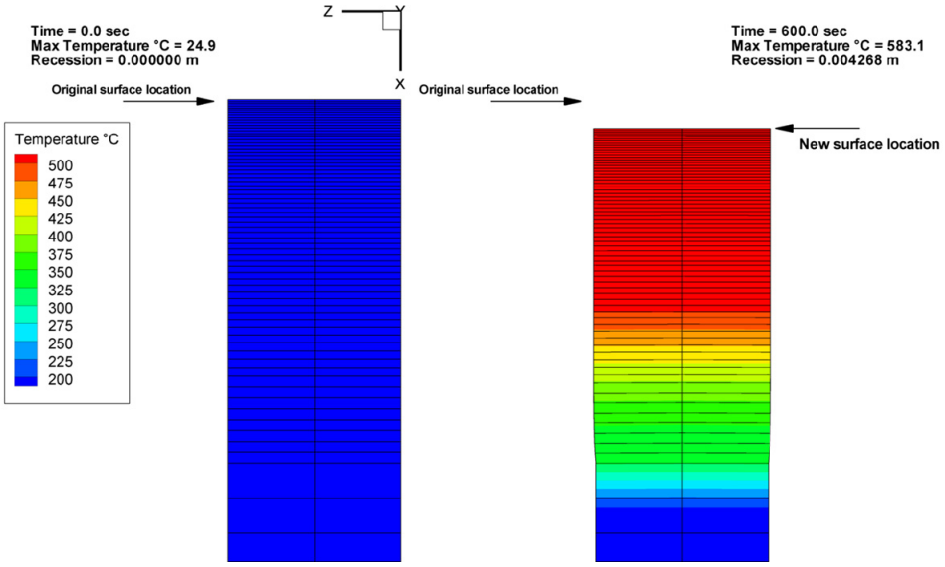

Figure 4.12: Grid movement scheme verification

The NASTRAN and present 3D tool models were simple columns with 24 equally spaced elements each. Since the grid movement scheme utilizes the material properties of Titanium, it was used as the material for this case as well. The column was constrained in all degrees of freedom on the bottom surface and a uniform temperature of 500K was applied to each element. The reference temperature for this case was 298K. The displacement for both the present tool and NASTRAN are given in Figure 4.13. The x-component of displacement, shown in Figure 4.13, shows the present solution matches the displacement calculated by NASTRAN well. The percent difference between the present solution and NASTRAN for the maximum x-component displacement was 0.97%. The y and z displacements were identical to each other and differed from NASTRAN by 2.87%.

Comparing the stress between the present code and NASTRAN becomes problematic since the present code only includes three degrees of freedom for the displacement components for each node. NASTRAN on the other hand includes six degrees of freedom, three for displacement and three for rotation. Given this current limitation in the present code, to validate the stress calculation, the problem had to be fully constrained

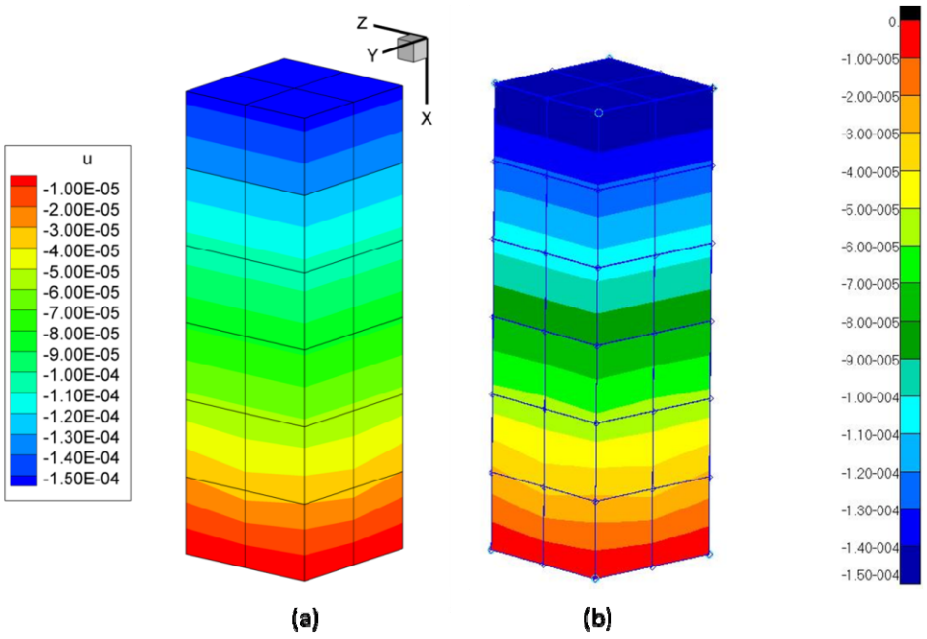

Figure 4.13: X-component displacement comparison, (a) present, (b) NASTRAN

so that there would be no displacement and no rotation. For a fully constrained problem the stress in the column is constant and a comparison between the present tool and NASTRAN is provided in Figure 4.14. There is a slight difference between the two solutions which is very much less than 0.1%. This partial verification will suffice for this dissertation since fully constrained problems produce conservative results. The important point to note is the displacement calculation is validated which is of the utmost importance for the mesh movement scheme in the thermal response solution.

Not having the three additional rotational degrees of freedom in the current formulation is a limitation of the current code. Adding those degrees of freedom to the elasticity equations will be handled as part of the future work. Full verification of the stress calculation will be deferred until that is accomplished. Adding those degrees of freedom will allow more general structural problems to be solved. For example, a distributed pressure load on the surface of a heatshield could be included in addition to the thermal loading.

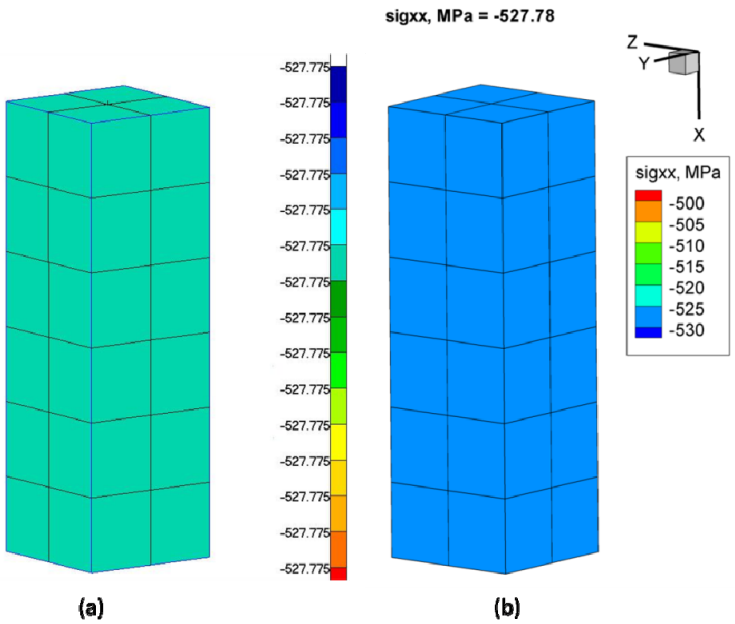

Figure 4.14: Fully constrained stress distribution (MPa), (a) NASTRAN, (b) present

4.5.6 Three-Dimensional Mesh and Time Step Sensitivity

As in Section 3.5.5, the sensitivity to mesh density and time step was run using the Genesis entry trajectory for three different mesh densities and three different time steps. The convective and radiative heating for this trajectory were provided in Figure 3.18. The three-dimensional geometry used here was the same as verification cases 3-5 which consisted of a 2.54 x 2.54 x 7.62cm MX4926N carbon phenolic column. The mesh for the first case had 96 elements and 255 nodes, the second had 378 elements and 688 nodes, and the third had 2844 elements 3920 nodes. Three different time steps were examined with the 378 element mesh. Additionally, for each time step, the fully implicit time marching scheme ($\theta = 1.0$) and the Crank-Nicholson time marching scheme ($\theta = 0.5$) were examined. Using the lessons learned from previous verification cases about proper meshing, each mesh was biased towards the heated surface. The three different meshes with arrows pointing to and away from the surfaces where the boundary conditions were applied are shown in Figure 4.15. Each column was meshed with 8-noded linear hexahedral elements. As shown in Figure 4.15, the coarse mesh case had

four elements in the Y-Z plane, the medium case had nine elements in the Y-Z plane, and the fine mesh case had 36 elements in the Y-Z plane.

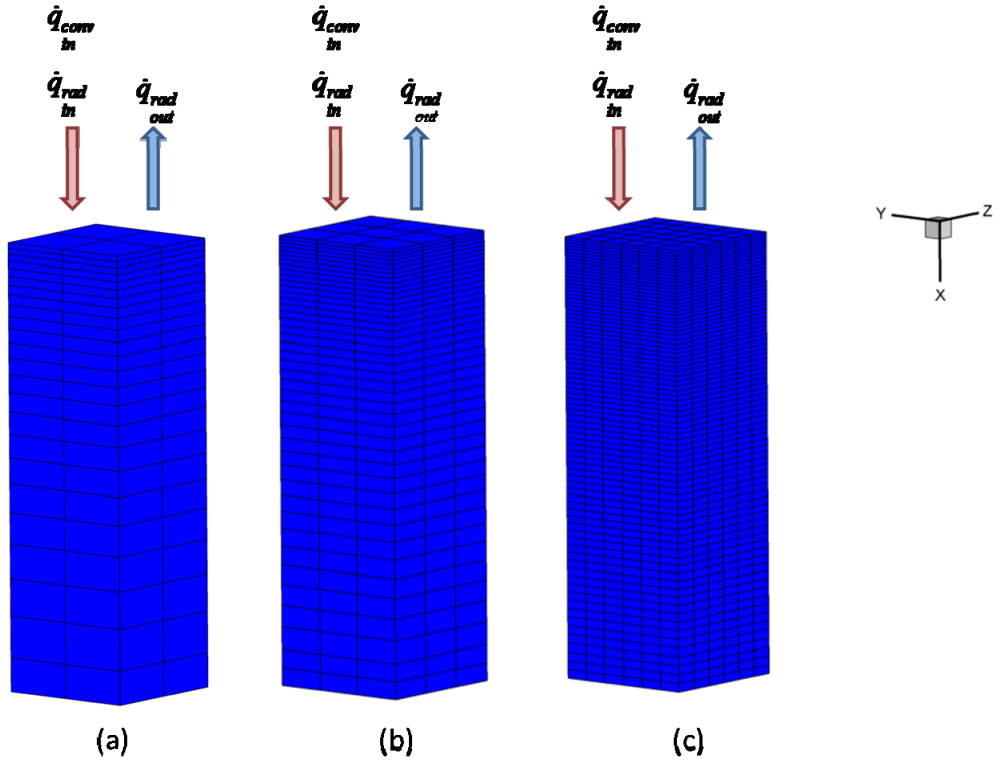

Figure 4.15: Mesh and geometry for mesh sensitivity, (a) coarse, (b) medium, (c) fine

A comparison of the pyrolysis gas mass flux at the surface in the center of each column is provided in Figure 4.16. The mesh sensitivity cases were all run in 1-D mode and as a result there was no variation in the pyrolysis gas flux in the Y-Z plane. A plot showing the pyrolysis gas mass flux distribution at 123 seconds into the simulation is provided in Figure 4.17. Notice that the mass flux in the Figure 4.17 is negative; this is a result of calculating the pyrolysis gas mass flux using Darcy's Law. The pyrolysis gas mass flux is now a vector quantity where the sign indicates the direction of the mass flux. All the two dimensional plots showing the pyrolysis gas mass flux thus far have had their negative values changed to positive in order to be compared to FIAT which always outputs this quantity as positive. Also note that had these cases not been run in 1-D

mode, i.e. constraining the gas to flow only in the x-direction, plots of the pyrolysis gas mass flux distribution for the y, and z directions could have also been displayed.

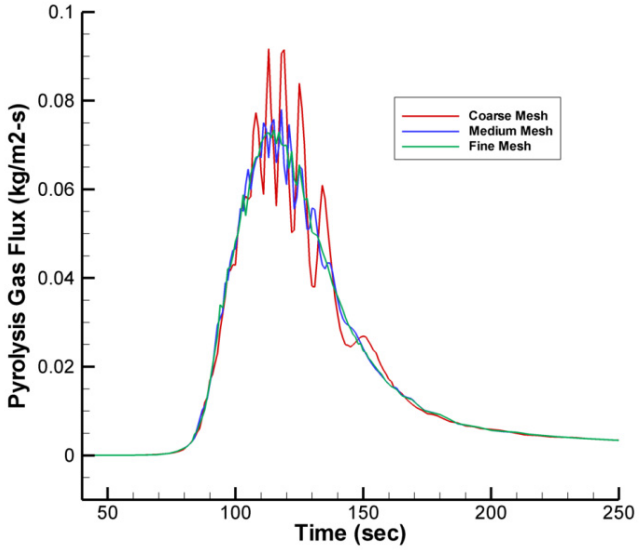

Figure 4.16: Pyrolysis gas mass flux at the surface at column center

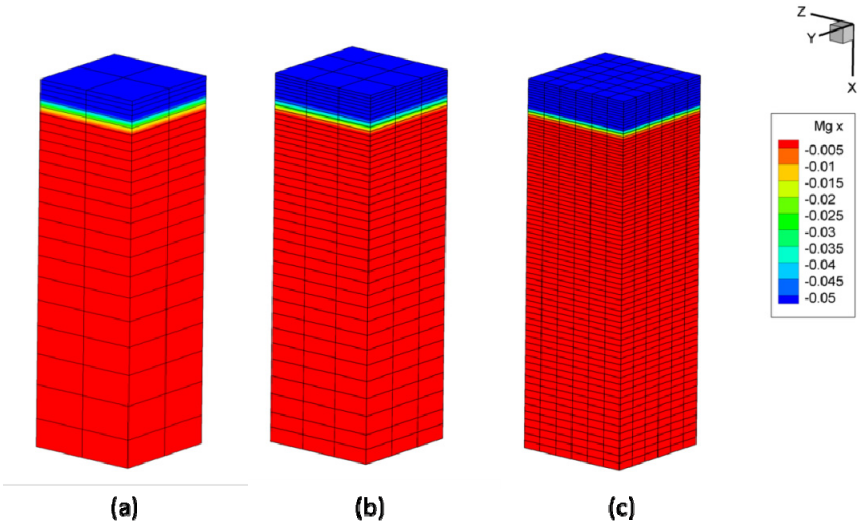

Figure 4.17: x-Direction pyrolysis gas mass flux distribution at 123 seconds, (a) coarse mesh, (b) medium mesh, (c) fine mesh

As in Section 3.5.5, the pyrolysis gas at the surface oscillates for each of the three cases and diminishes as the mesh is refined. Unlike the one-dimensional pyrolysis gas

mass flux, the three-dimensional flux oscillations are much less in magnitude. This can be attributed to three things. First, the governing equations for Darcy flow are solved using the finite element method for the pyrolysis gas mass flux. Here, the density decomposition rate is input as a source term in the resulting system of equations. Solving for the flux in this manner appears much more stable than in the one-dimensional case where the pyrolysis gas flux is determined by integrating the decomposition rate over the line of nodes from the backside to the surface. Second, the three-dimensional cases have more nodal points in plane which adds stability to the calculation. The pyrolysis gas flux in CMA is calculated similarly to the one-dimensional calculation presented here, however, CMA creates artificial nodelets around each node in the solution domain. Adding the nodelets proved to add stability to the pyrolysis gas mass flux [27]. Finally, the biased mesh towards the surface provides smaller elements near the surface which increases the stability of the Darcy flow and decomposition calculations.

A comparison of the temperatures, given in Figure 4.18, shows that like the one-dimensional cases of Section 3.5.5, the temperature is mostly affected by the oscillations in the pyrolysis gas mass flux. A zoomed in view of the surface temperatures and the

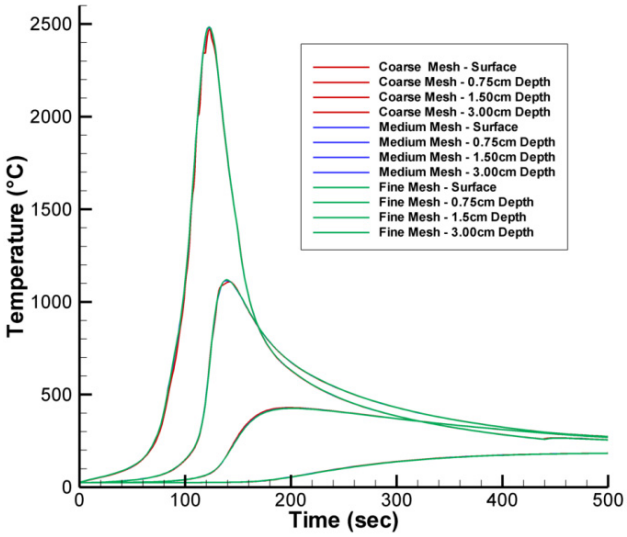

Figure 4.18: Temperature comparison between three different mesh densities

temperatures at a depth of 0.75cm is provided in Figure 4.19. Notice that due to the lower magnitude oscillations in the pyrolysis gas mass flux, the temperatures for the three cases are very close, with the difference in the surface temperature between the fine and medium being only 3.5°C. The temperature for the coarse case shows some minor oscillations and doesn't quite reach the same peak temperature being 9.5°C lower than the fine mesh case. Since the heating and radiation boundary conditions were applied uniformly across the surface in the Y-Z plane and the pyrolysis gas mass flux did not vary in-plane, the temperature distribution were also invariant in the Y-Z plane.

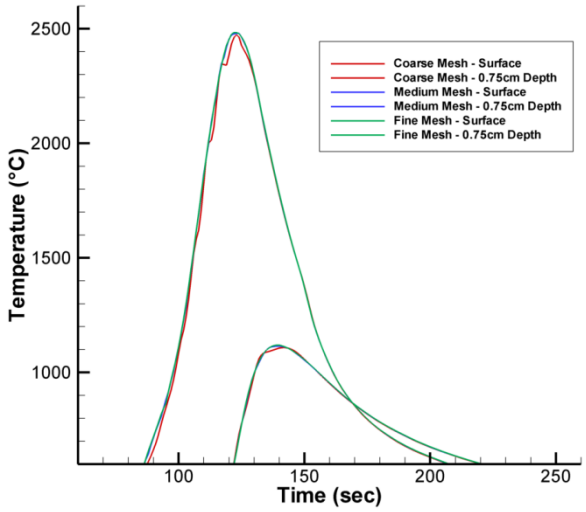

Figure 4.19: Temperature comparison at the surface and a depth of 0.75cm

As in the one-dimensional cases, the three-dimensional solution for pyrolysis gas mass flux appears to be insensitive to the time step used for the problem. Additionally, there also appears to be no dependence on the time marching scheme being used as there was virtually no difference between the fully implicit and Crank-Nicholson time marching schemes. The pyrolysis gas mass flux as a function of the time step is shown in Figure 4.21. Like the pyrolysis gas mass flux, the temperatures was also insensitive to the time step and the time marching scheme and varied very little from that shown in Figure 4.18 and Figure 4.19.

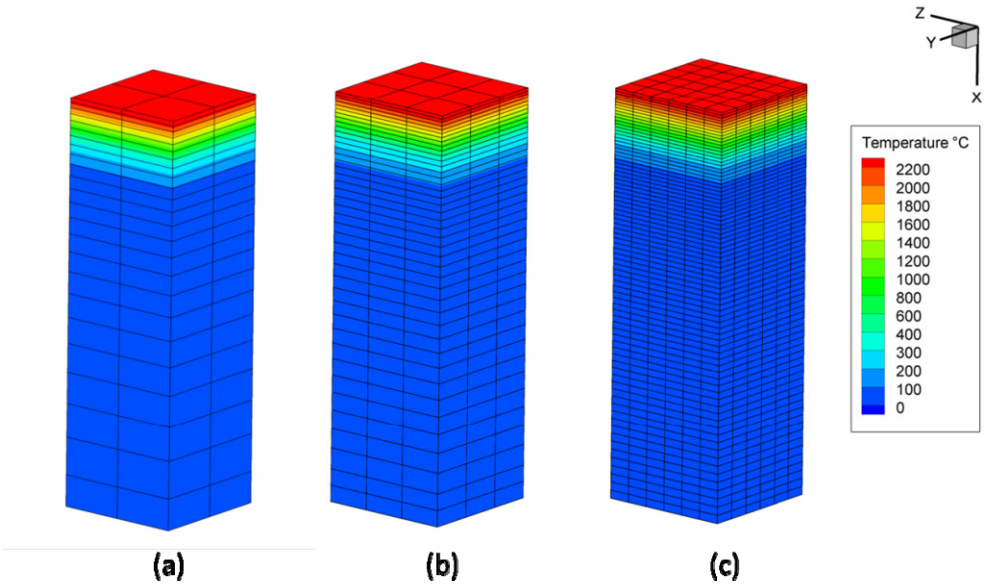

Figure 4.20: Temperature distribution at 123 seconds, (a) coarse mesh, (b) medium mesh, (c) fine mesh

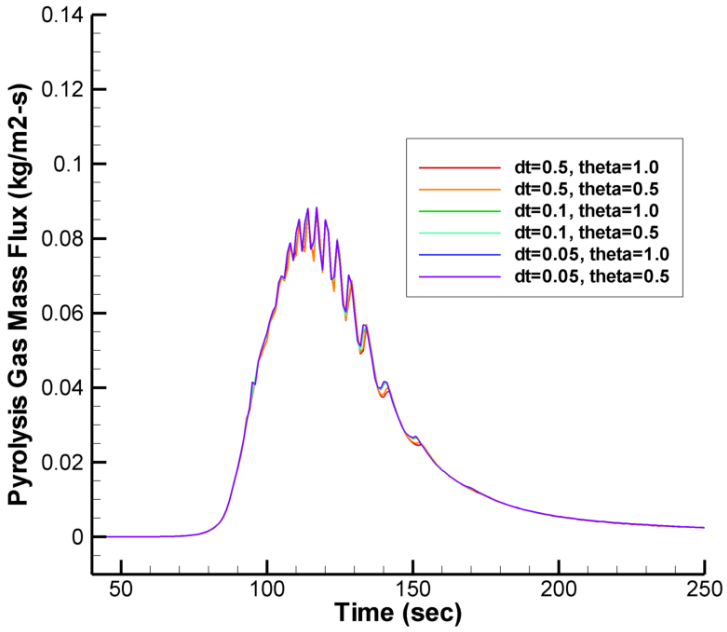

Figure 4.21: Pyrolysis gas mass flux as a function of time step and time marching scheme

The conclusion here is the same as that from Section 3.5.5, the pyrolysis gas flow calculation is more sensitive to mesh density than the temperature and as such will be the determining factor when preparing a mesh within PATRAN or any other meshing

software. It has also been shown both the pyrolysis gas mass flux and the temperature are insensitive to the time step and time marching scheme being used for the problem. Again, it can be concluded that some pyrolysis gas oscillation can be tolerated without an adverse affect on the temperature as seen in all three cases. For the three-dimensional solution any of these meshes would suffice. For 1-D mode and uniformly distributed boundary conditions, the best mesh would be a combination of the coarse mesh and medium mesh. Combining the four in-plane elements of the coarse mesh with the element distribution through the thickness of the medium mesh would minimize computational costs and increase solution fidelity.

4.6 Comparison of the "1-D Mode" with the Full 3-D Solution

The verification cases and mesh sensitivity have been run in a 1-D mode where the pyrolysis gas was constrained to flow only in the x-direction and the thermal properties were isotropic. Using the medium dense mesh from the previous section, the genesis entry trajectory was run once again, however, this time orthotropic material properties were used. There is no data available for the permeability for the in-plane components of the MX4926N material, so it was assumed that the in-plane permeability was half that of the across ply permeability. The across ply direction was inclined 30° with respect to the y-z plane. The temperature distribution for the orthotropic case at 123 seconds is compared to the 1-D mode case in Figure 4.22. Notice that the temperature for the orthotropic case is inclined with respect to the y-z plane and that it reaches a peak temperature 135.9°C higher than the 1-D mode case. The temperature inclination becomes more pronounced towards the end of the trajectory as the heat soaks into the material as shown in Figure 4.23.

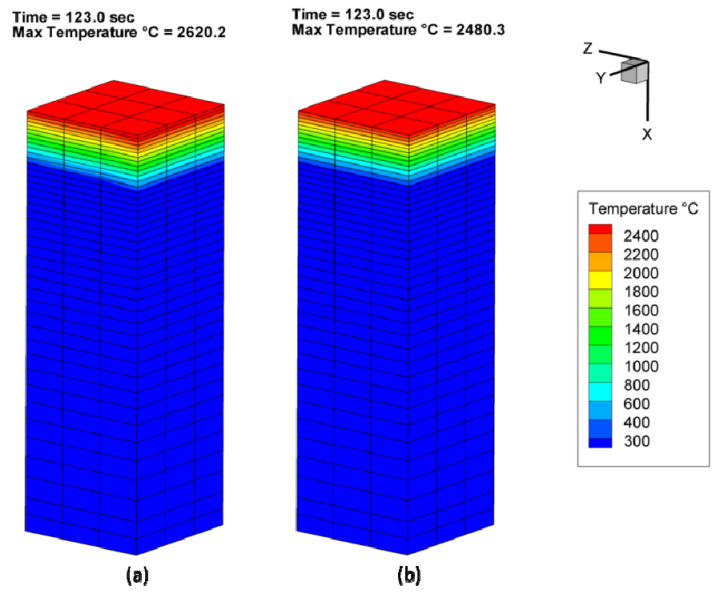

Figure 4.22: Temperature distribution at 123 seconds, (a) orthotropic, (b) 1-D mode

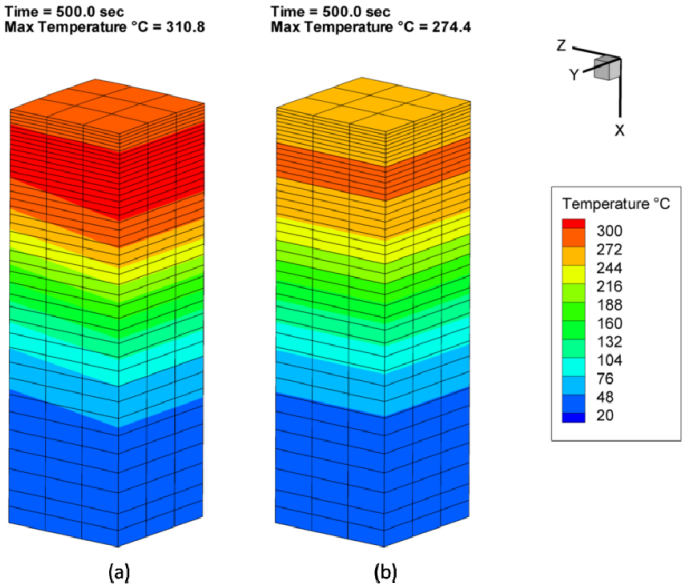

Figure 4.23: Temperature distribution at 500 seconds, (a) orthotropic, (b) 1-D mode

The higher peak temperature is related to the pyrolysis gas flow. Since the gas is no longer constrained to flow only in the x-direction, some of the gas is flowing out the sides in the y and z directions. With the pyrolysis gas flowing in all directions, less gas reaches the surface and therefore there is less cooling. The pyrolysis gas flow in the x, y, and z directions is provided in Figure 4.24. It is interesting to note that since the virgin porosity

and permeability are non-zero, there is a small amount of pyrolysis gas that flows towards the bondline. This phenomenon was not observed in the 1-D mode cases again because it was constrained to flow only in the x-direction. Also notice that the y and z pyrolysis gas flow are similar, but are not the same. This is due to the across ply direction of the material being inclined 30° with respect to the y-z plane.

The recession for the 1-D mode was calculated to be 0.118 mm, for the orthotropic case it was 0.53 mm. The difference here is due to the both the higher temperature and the lack of gas reaching the surface.

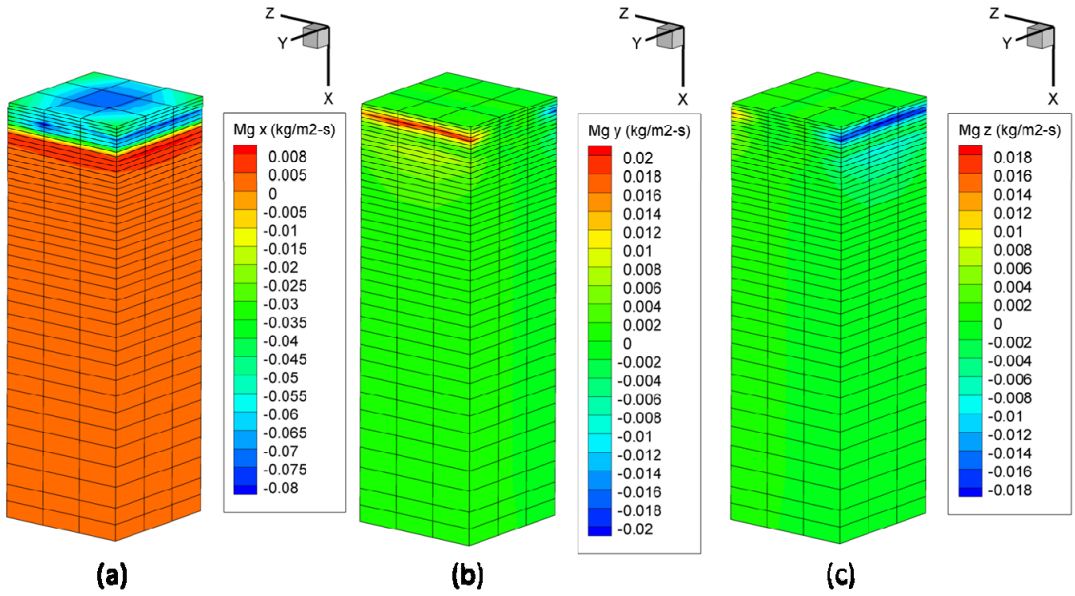

Figure 4.24: Pyrolysis gas mass flux, (a) x-component, (b) y-component, (c) z-component

4.7 Limitations of the Three-Dimensional Finite Element Formulation

The limitations of the three-dimensional code developed here are the same as those described in Section 3.6, with the except that the one-dimensionality and the pyrolysis gas being restricted to flow in only one direction are no longer limitations. Additionally, a limitation, which is not the fault of the code itself, is the fact that most materials are missing key orthotropic material properties in their databases, especially the properties required for the Darcy flow calculation. Given that limitation, assumptions about the properties must be made by the user. The code is currently limited to 8-noded hexahedral

elements. Future work will focus on allowing the use of other families of elements including higher order elements.

As described in Section 4.5.5.1, the stress due to thermal expansion has been validated only for the case where the component is fully constrained. This is a limitation of the current implementation but over all produces conservative results for the induced thermal stresses. The additional rotational degrees of freedom will need to be included to provide a more general framework for stress calculations.

Another limitation is that the Message Passing Interface Chameleon (MPICH2) must be configured properly on the computer or cluster being used otherwise the code will only operate in serial mode. PETSc, libMesh, and the present tool are capable of parallel processing; however, the Linux cluster available for this work was did not have MPICH2 properly configured to take advantage of that capability.

CHAPTER 5

LINKING ANALYSIS TO DESIGN

5.1 Introduction

Design of a heatshield and its penetration subsystem is multidisciplinary in nature; it includes both the structural response to the flight loads, and the thermal response to the entry heating. Entry heating can also induce thermal stresses in the materials due to thermal expansion. To perform heatshield and compression pad thickness sizing, the analyst relies on trajectory inputs from the guidance, navigation, and control team, aerodynamic heating distribution inputs from the aerothermodynamics team, and the geometric configuration from the mechanical design team. To perform the structural sizing of a compression pad, the analyst relies on the loads inputs from the loads and dynamics team, and again the geometric configuration from the mechanical design team.

The structural analyst generally takes advantage of the fact that the three-dimensional CAD geometry from the mechanical design team can be imported directly into the finite element analysis codes. Currently there is no commercially available three-dimensional thermal analysis code capable of performing high fidelity analysis and sizing of heatshield materials. The thermal analyst typically uses the three-dimensional geometric configuration to create a one-dimensional slice through the geometry at a specific point on the heatshield or compression pad and performs a one-dimensional analysis using FIAT or some other analogous solution method. This one-dimensional analysis is repeated until the thickness is such that the sizing constraint, typically bondline temperature, is satisfied. The thermal analyst repeats this process for multiple locations on the heatshield to develop a thickness distribution, often without regard to any geometric constraints that exist. On a blunt body, sphere-cone type of vehicle, the points selected generally lie along radial lines emanating from the stagnation point to the vehicle shoulder. The mechanical design team is left to interpret these results and incorporate

them into the system design. The analyst is generally unable to provide guidance in terms of how the design variables can be modified to meet geometric constraints and not exceed the thermal design specifications.

To perform a thermostructural analysis to assess thermal stresses, the structural analyst must interpolate the one-dimensional temperature data onto the larger three-dimensional structural model. Interpolating the thermal results from a limited set of points on the heatshield can cause sharp gradients when mapped to the structural model. These sharp gradients can lead to erroneous thermal stresses and cause the design team to modify the design in a suboptimal way.

Uncertainties exist in the parameters that are used as inputs to the thermal and structural response and yield uncertainty in the results of any subsequent analysis. Uncertainty in the numerical modeling of the associated physical phenomenon also contributes to the uncertainty of the results. Designing systems to meet their operational requirements and design specifications under these uncertain conditions is difficult and often factors of safety, or margin, are introduced to both the inputs and the results of the analysis to mitigate the effect of uncertainty. Applying margin to the design has proven to be successful in the past, but often produces design solutions that are massive, suboptimal and lacking in insight into the probability that a system will exceed its design specifications or meet its operational requirements.

The Finite Element Ablation and Thermal Response Design and Analysis Program, or FEAR, developed for this dissertation will be used to analyze the thermal response of a heatshield compression pad. For the structural response, the finite element equations for linear elasticity have been integrated into FEAR. These analysis tools are then integrated into a Monte-Carlo simulation where the probability of exceeding design specifications can be assessed, parameter sensitivities can be performed, and probabilistic ranges of the design variables can be examined.

5.1.1 Motivation: Orion Heatshield Compression Pad

The Orion Crew Exploration Vehicle will be the first entry vehicle built by NASA to have a man-rated ablative heatshield since the Apollo program. Like Apollo, the vehicle includes six hard-point compression pads that must transfer the launch loads to the command module during launch as well as survive the thermal environment during reentry.

There is a striking similarity between the Apollo and the Orion command modules. However, the Apollo Program had a different set of design requirements and a different risk posture than the Orion Program. The Orion Program has tested its engineers with quantifying the risks associated with the design each system. One of the most scrutinized systems is the heatshield. There is no redundancy built into the heatshield system; it must work and must work even under uncertain operating conditions. The use of legacy heatshield sizing tools such as CMA and FIAT provide no insight into the ability of the heatshield to perform its function under off-nominal environmental conditions or variable material properties.

A new design approach must be utilized to answer the question of how a heatshield or compression pad performs under uncertain conditions. In addition, the push to reduce the heatshield mass fraction must be considered. Simply adding heatshield thickness, which directly translates into mass, to increase the designs robustness is not generally acceptable. This is particularly true for the Orion vehicle where arguments over tenths of kilograms are commonplace. Given this desire, the current one-dimensional ablative thermal analysis and design process is inadequate, especially when considering the Orion heatshield compression pads. The compression pad subsystem is a complex three-dimensional system which interfaces with many different materials. The boundary conditions near the compression pad are complex, and spatially varying in the plane normal to the compression pad's external surface as shown in Figure 5.1 [134]. The flow

is assumed to be turbulent so the augmentation factors shown are the factors for turbulent flow.

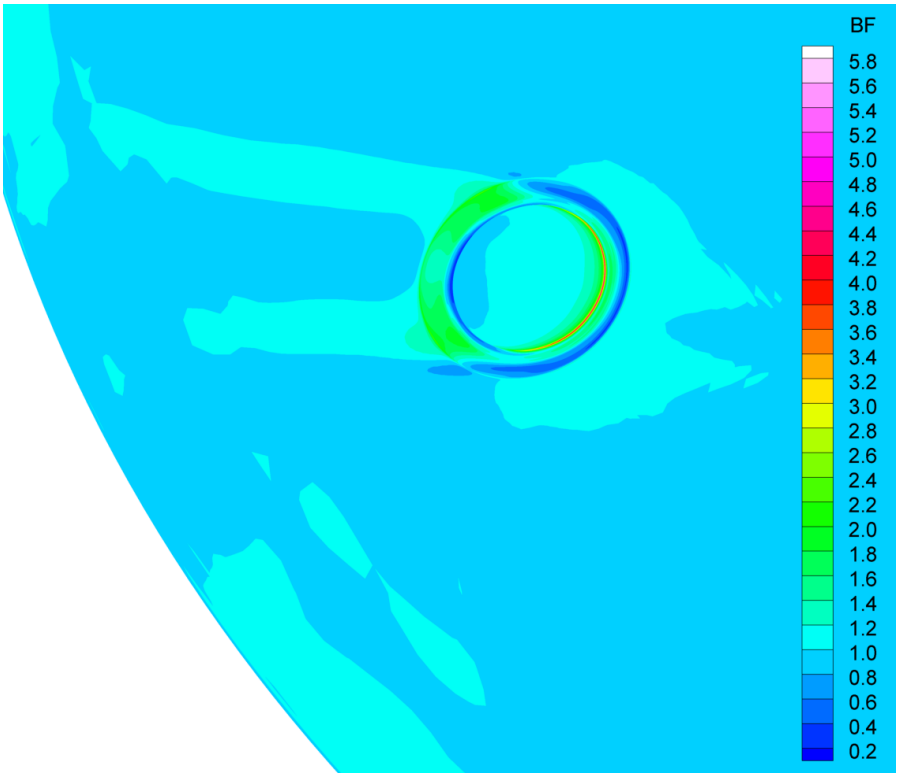

Figure 5.1: DAC-3 heating augmentation near the 120° compression pad location [134]

The Orion CEV smooth body heating reaches a peak combined convective and radiative heat rate of 829 W/cm2. The heating augmentation factors show in Figure 5.1 are applied to the smooth body convective heating rate only The trajectory used in this dissertation comes from the third Orion CEV Design and Analysis Cycle (DAC-3) lunar return and is provided Figure 5.2. The nominal trajectory heating is anchored to a CFD solution at discrete time points and is for a smooth body vehicle which does not account for any shape change. The complexity of the heatshield compression pads, the requirements placed on them, and the complex boundary conditions around them provides the motivation for this dissertation.

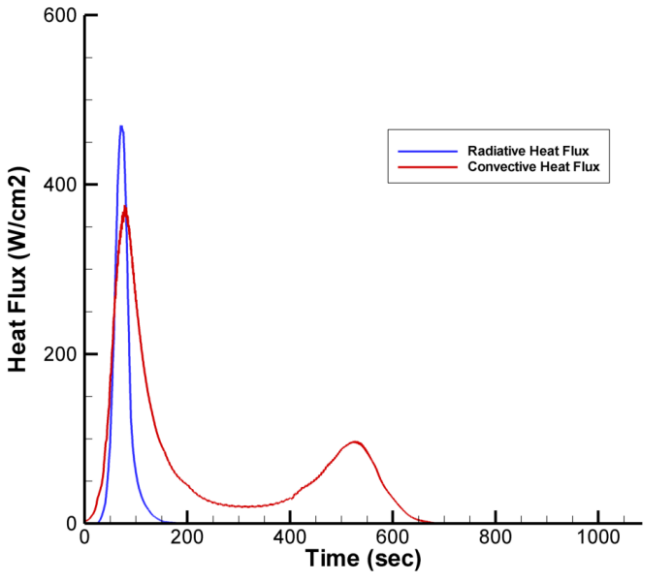

Figure 5.2: CEV DAC-3 lunar return trajectory heating near the 120° compression pad

5.1.2 Objectives

The objective of this design methodology is to link the design of the compression pad to its thermostructural analysis. The link to the analysis includes both the thermal and structural response of the compression pads. The analysis parameters of interest in this application, which could also be thought of as the driving design specifications, are the bondline temperature and the maximum thermal stress. The link to design comes from understanding the variation in the thermostructural response over the range of the design variables. The design variables of interest are the compression pad thickness, material ply layup inclination angle, and the Titanium insert structure thickness behind the pad. These are only a small subset of analysis parameters and design variables available to the designer; many others may be included in the methodology. However, for demonstration purposes, we limit the selection to these five.

It is important to mention that a link to the fluid flow analysis is not directly made in this dissertation. The link to the flow environment represents an important aspect of heatshield and compression pad design but is beyond the scope of this dissertation and is a topic for future work. For this work, it is assumed that a high fidelity computational

fluid dynamic (CFD) solution for the flow field exists at several discrete time points along the entry trajectory for the three-dimensional entry vehicle. It is further assumed that the heating from the entry trajectory code has been modified to match the results of the CFD at those discrete time points. Additionally, it is assumed that the augmented heating near the compression pads has been calculated and exists in the form of spatially distributed scale factors, also known as bump factors. These bump factors are simply multipliers to the smooth body heating.

Uncertainties in the CFD calculations and in the trajectory are also assumed to exist. In this dissertation, the heating and trajectory will be inputs to the analysis and already include their associated uncertainties. Using the bondline temperature and thermal stress as the measure, sensitivities to the analysis input parameters provide insight into how much the uncertainty in each input contributes to the response of the system. Moreover, characterizing the sensitivity to each input helps determine which uncertainties and input parameters should be included in a Monte Carlo simulation. As an example, sensitivities to the material properties will be assessed for a three-dimensional compression pad under CEV lunar return entry conditions. This is the first step in the design process.

The next step is to examine how the thermostructural response varies over the ranges of the design variables. As mentioned above, for the Orion CEV compression pad, the pad thickness, ply angle and Titanium insert backup structure thickness were chosen as the design variables. The objective is to discretize the design space by selecting discrete points for each design variable from within the range of its variation. For example, breaking the ply angle into three levels one could choose the minimum, maximum, and a value in the middle of the range. Once the design space has been discretized, a matrix of designs is created where each one represents a different combination of the design variables. The process of systematically varying the design variables is known as design of experiments and there are many ways it can be performed. In this dissertation a full factorial scheme will be utilized since it covers all possible combinations in the

discretized space, albeit at the expense of having to run a maximum number of cases in the analysis. Other schemes such as the central-composite design reduce the number of runs, but at the expense of not using all possible combinations of the design variables. FEAR is run for each design in the matrix and the bondline temperature and thermal stress are recorded.

After the matrix of designs has been analyzed, a contour plot showing the variation in bondline temperature over the design space is generated. Within the contour of bondline temperature any design constraints present can be superimposed on it. Utilizing the plot, the optimum design based on minimizing the objective function, in this case the bondline temperature can be determined.

To design for uncertainty, the input parameters and their associated uncertainties must be incorporated into the design and analysis. The most influential uncertainties, as determined by the sensitivity study are selected for use in a Monte Carlo simulation. The optimum design determined above, is the candidate design that the Monte Carlo simulation is performed on. From the results of the simulation, the probability that the design will exceed its design specification can be quantitatively determined. A histogram showing the distribution of the bondline and thermal stress can be generated and the 99%, 95%, and 90% bondline temperature and thermal stress can be displayed. If the probabilities are satisfactory then the process is complete. If they are not satisfactory, the constraints can be modified and the process of finding the optimum design and running the Monte Carlo are repeated. The design process is summarized in Figure 5.3.

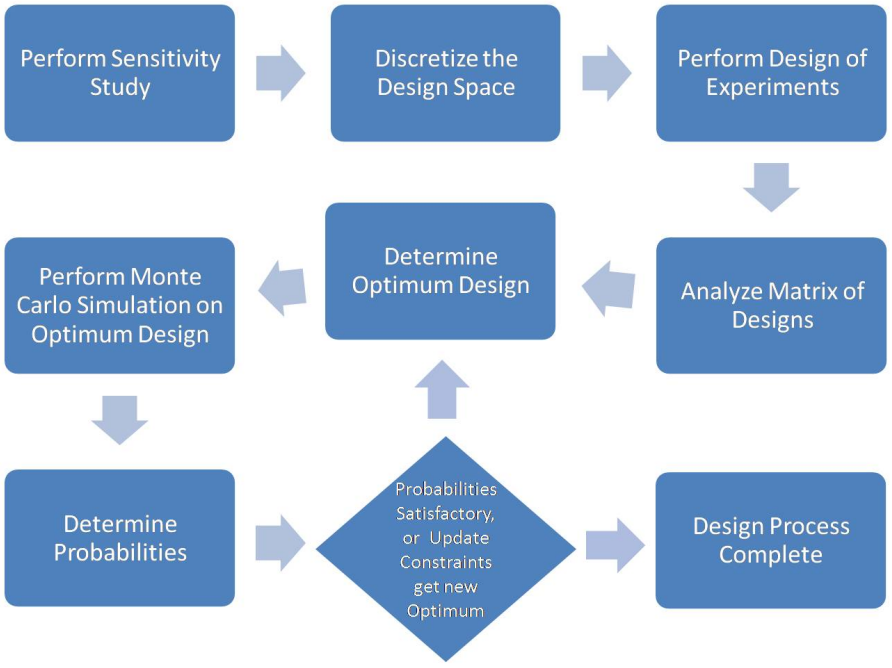

Figure 5.3: Design process flow

5.1.3 Orion Crew Exploration Vehicle Heatshield and Penetration Subsystem

In Chapter 1, a general heatshield penetration system was described. The Orion CEV heatshield possesses a similar system. Specifically, the Orion penetration subsystem is made up of six reinforced hard points on the forebody TPS. Each hard point consists of an MX4926N carbon phenolic compression pad and an Inconel tension tie. The MX4926N plies are inclined 20° with respect to the bottom of the pad and aligned with the centerline flow streamline. The compression pad is inserted into the Titanium carrier structure, then the acreage Avcoat TPS is built up around it. There is a 20° bevel cut into the Avcoat both to provide clearance for the service module connection and to minimize the effects of heating augmentation. The tension tie rod passes through the center of the pad and connects directly to the vehicle structure. The tension tie is preloaded to balance the weight of the vehicle plus added factors of safety. The preload is distributed over the six compression pad/tension tie subsystems. The compression pad is bonded and bolted to its Titanium carrier structure. There is a small gap between the compression pad and

the Avcoat and the gap is filled with a compliant gap filler material. The gap reduces the stress in the surrounding materials by allowing for a small amount of differential thermal expansion. A cross section of the Orion heatshield compression pad with its surrounding Titanium structure and Avcoat heatshield is shown in Figure 5.4 where the tension tie has been removed for clarity.

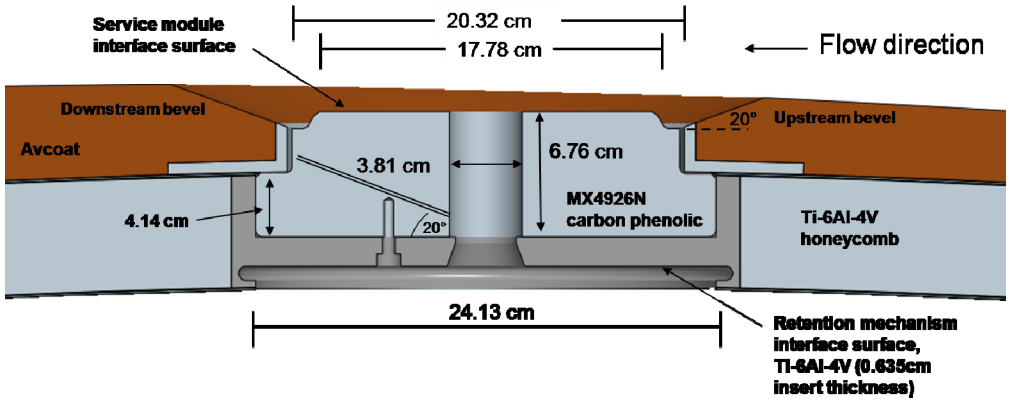

Figure 5.4: Cross section of the Orion heatshield compression pad, surrounding structure, and acreage heatshield

From Figure 5.4 it is clear that the compression pad design, with its surrounding structure, and TPS has a complex geometric shape. The geometry along with a distributed heating boundary condition similar to that shown in Figure 1.4, and orthotropic material properties makes this system difficult to characterize with a one-dimensional analysis.

5.2 Analysis Tool Runtime Evaluation

The finite element code FEAR is a high fidelity code which solves up to four different equation systems per time step and may have excessive run times, especially in the three-dimensional version, which could preclude it from being effectively used in a Monte Carlo simulation. The first two equation systems are the Darcy flow and thermal response equation systems and are required at every time step. The other two equation systems are for the thermal stress and the grid motion. The grid motion is run whenever there is any recession. The thermal stress system is solved at user specified intervals.

The run time for the one-dimensional version of FEAR was evaluated in Chapter 3 and was found to be no more expensive to run then FIAT. In this section the run time for the three-dimensional genesis cases used during the mesh sensitivity as well as a full scale compression pad under a CEV lunar return trajectory are evaluated.

5.2.1 Evaluation of the Three-Dimensional Finite Element Code Computation Cost

The computational time for FEAR was evaluated on an Intel 2.93GHz Xeon quad core processor running 64 bit Fedora Core 9 Linux operating system. FEAR was run in serial mode meaning only one processor was used. As mentioned in Chapter 4 Section 4.7, libMesh, PETSc, and FEAR have parallel processing capabilities, however, the cluster available for this work was not properly configured to take advantage of this. This limitation will be corrected in the future. The genesis entry trajectory was chosen since it produces heating high enough to cause recession, so every equation system would be active. Comparison of the computational time for the three different mesh densities described in Chapter 4, Section 4.5.5.1 is provided in Figure 5.5.

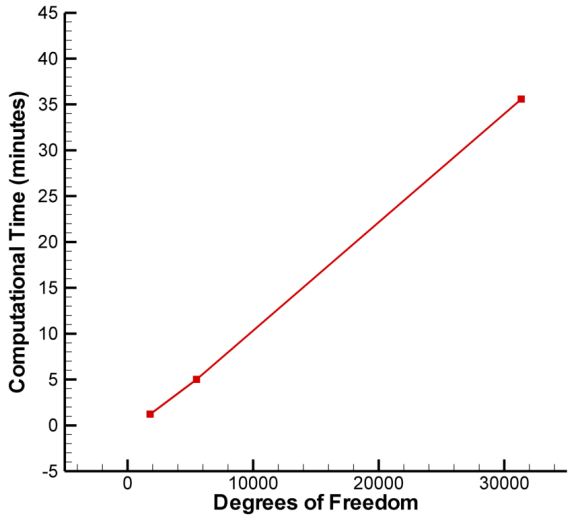

Figure 5.5: Computational cost for the simple column geometry with the Genesis entry trajectory

The computational time, shown in Figure 5.5, increases nearly linearly as the number of degrees of freedom increases. Recall that four equation systems are being solved and that for every 8-noded hexahedral element the Darcy flow equations contribute four degrees of freedom, the stress and grid motion contribute three, and the thermal response contributes one, for a total of eight degrees of freedom for every node in the mesh.

The full scale compression pad along with the Titanium insert structure was meshed with two different mesh densities using 8-noded hexahedral elements. The first was a coarse mesh with 9,744 elements and 11,016 nodes. The second had 19,240 elements and 21,560 nodes. Both meshes were biased towards the heating surface. A cross section

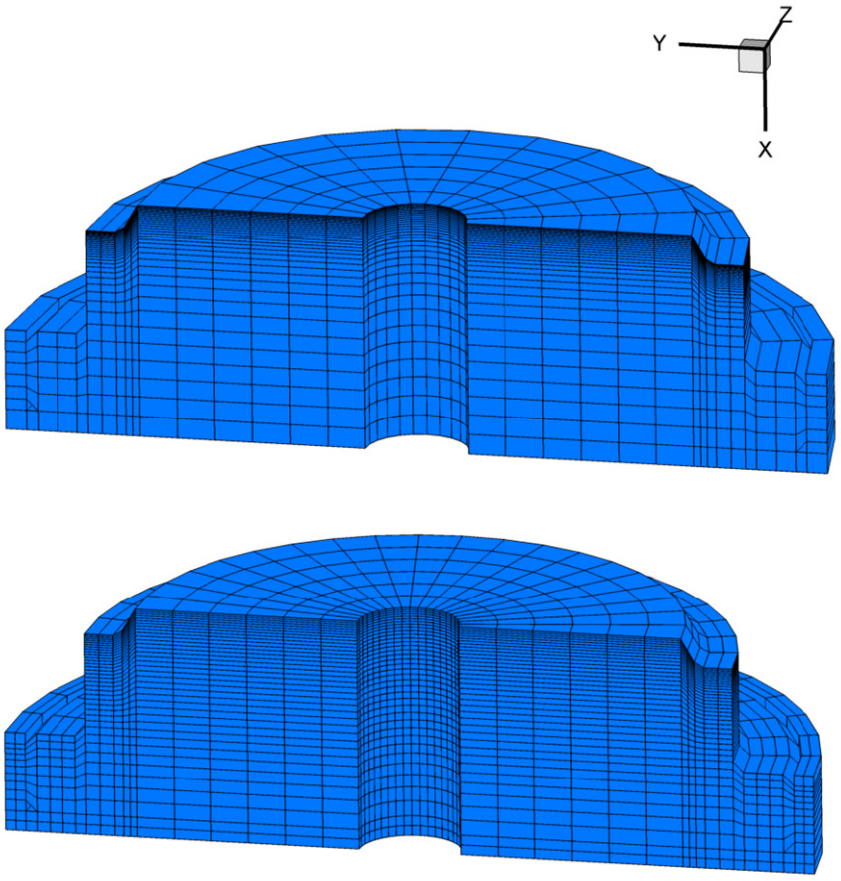

Figure 5.6: Compression pad mesh, coarse mesh (top), fine mesh (bottom)

of each mesh showing the element distribution through the thickness is provided in Figure 5.6. The main difference is that the coarse mesh has fewer elements circumferentially and slightly less elements through the thickness. Both compression pad models were run with FEAR in serial mode using the smooth body heating from the trajectory given in Figure 5.2. Heating augmentation was not included for this run time evaluation. The computational costs of running the compression pad models are given in Figure 5.7.

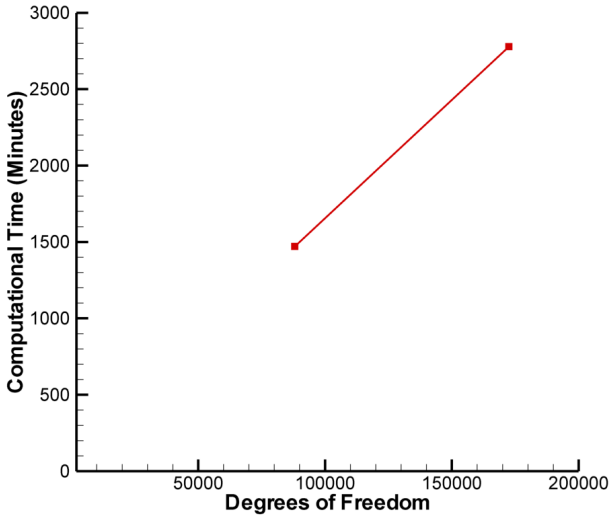

Figure 5.7: Compression pad computation cost using DAC-3 lunar return trajectory

Comparing the run times between the simple column geometry and the compression pad geometries shown in Figure 5.8, the slope of the lines as the number of degrees of freedom increases is quite different. There are a few factors that are influencing this, one reason is because there are a lot more element faces in the compression pad models that have boundary conditions applied. For each non-linear iteration during every time FEAR must loop through each of the elements that have boundary conditions applied. Another reason is due to the CEV trajectory which is a skip trajectory that has two peaks in the heating. It has been observed that near peak heating conditions the time step being used

by FEAR becomes small so therefore the compression pads experience two instances where the solution is marching through time slowly.

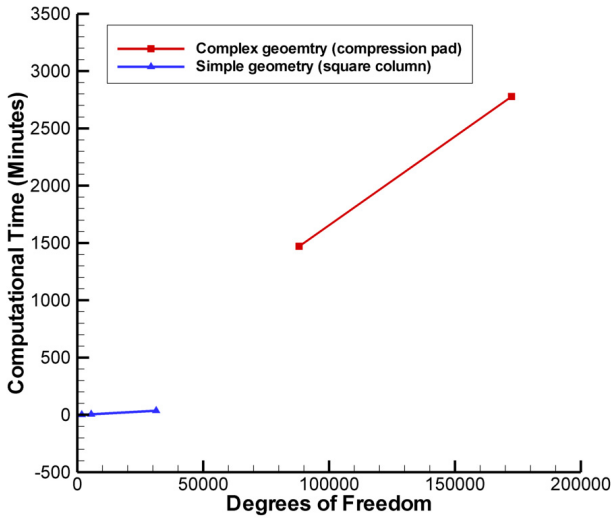

Figure 5.8: Comparison of run times for different geometries

5.3 Thermal Response Sensitivity to Material Properties

One of the objectives discussed in section 5.1.2 was to demonstrate how sensitivity studies could be performed using the high fidelity one-dimensional and three-dimensional finite element codes. In this section the sensitivity to variations in the material properties is examined. Along with the properties, Table 5.1 lists each property's associated 3-σ uncertainty and by which method the uncertainty was determined, as described in Chapter 1, Section 1.5. The uncertainties listed are for the MX4926N carbon phenolic. Material property data for the MX4926N carbon phenolic was obtained from an extensive database developed by ATK Launch Systems and NASA [135]. The data in this report falls under the purview of the U.S. Munitions List as defined in the International Traffic in Arms Regulations (ITAR) and therefore cannot be presented in this dissertation.

To establish the relationship between the material properties, their uncertainty, and their affect on the thermal and structural response, the three-dimensional compression pad using the DAC-3 lunar return entry given in Figure 5.2 is examined. For this

material property sensitivity study heating augmentation was not applied to the compression pad model. Moreover the compression pad model chosen was the coarsely meshed model which had 9,744 elements and 11,016 nodes.

Table 5.1: Sensitivity study properties and associated uncertainties

Property†	3σ Uncertainty	Uncertainty Evaluation Method
Virgin thermal conductivity	±0.45 W/m-K	1
Char thermal conductivity	±0.88 W/m-K	1
Virgin specific heat	±19.1 J/kg-K	1
Char specific heat	±30.7 J/kg-K	1
Virgin density (room temp)	±6.3% kg/m^3	1
Char Emissivity	±0.06375	1
Virgin heat of formation	±15% J/kg	6
Pyrolysis gas enthalpy	±15% J/kg	6
Permeability – Log (Kp)	±10.2% cm^2	1
Porosity	±8.7%	1
Coefficient of thermal expansion (CTE)	±46.17% m/m/°C	1
Compressive Modulus	±28.98% Pa	1

†Uncertainties calculated in the database are given as functions of temperature and principle direction they are given as average values here unless otherwise noted

5.3.1 Compression Pad Material Property Sensitivity

Using the property variations listed in Table 5.1 FEAR was run 24 times where each run a single property was set to its minimum or maximum 3-σ uncertainty which isolated that property as being the only factor influencing the bondline temperature and thermal stress. Results of the material property sensitivity are shown in Figure 5.9 and Figure 5.10. The bondline temperature is most sensitive to the variations in the virgin and char thermal conductivity, and to a lesser extent by the virgin density and virgin heat of formation variations. The pyrolysis gas enthalpy, char emissivity, and the virgin specific heat have only a minor influence on the bondline temperature influencing it less than 1.0%. The compressive modulus, permeability, porosity, and CTE have little to no affect

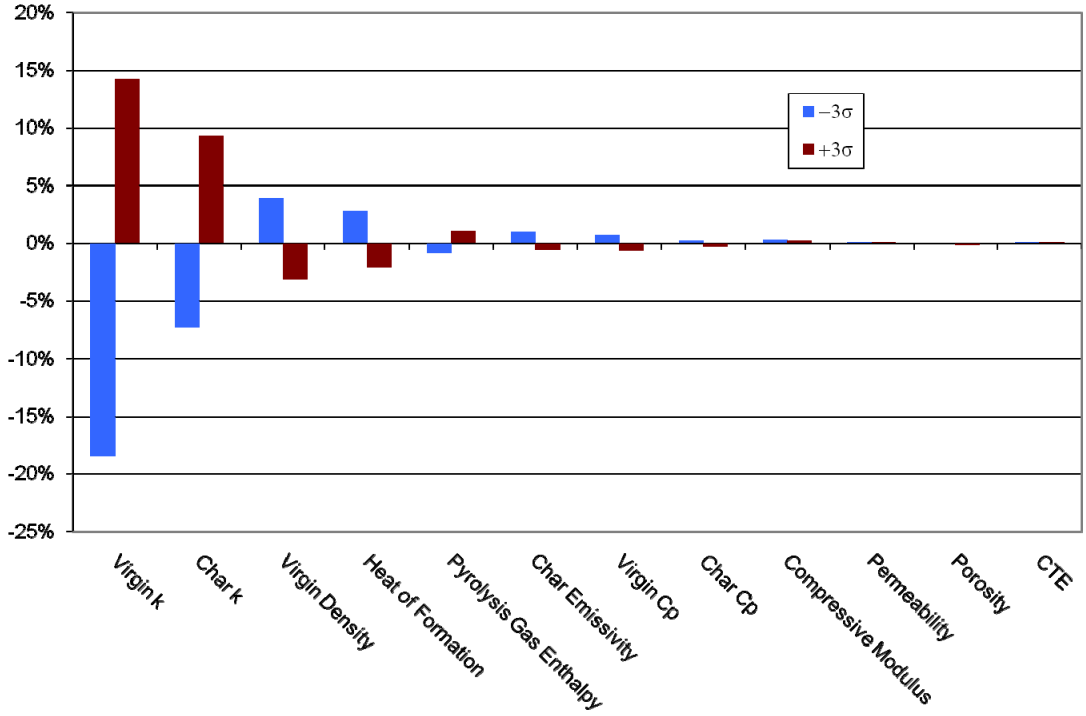

Figure 5.9: Bondline temperature sensitivity

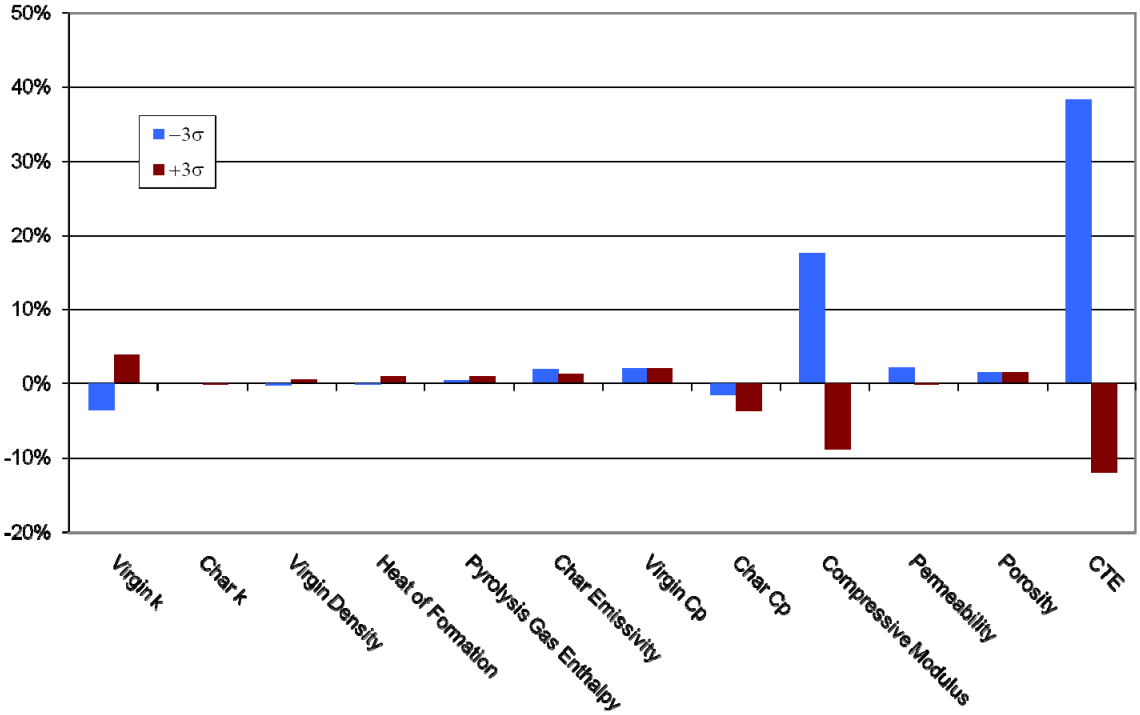

Figure 5.10: Across-ply tensile stress sensitivity

on the bondline temperature each influencing it less than 0.20%. The across-ply tensile stress is most sensitive to the CTE, compressive modulus, and virgin thermal conductivity. All other property variations produced less than a 2.5% change in the across-ply tensile stress.

As a result of the material property sensitivity study, the input parameters having the most influence on the design specifications have been identified for use in the final step in the design process outlined in Figure 5.3. The material property input parameters that have been selected for the Monte Carlo simulation of the optimum compression pad design are summarized in Table 5.2.

Table 5.2: Most influential material property inputs

Material Property	Change in Design Specification			
	Bondline Temperature		Across-ply Tensile Stress	
	-3σ	+3σ	-3σ	+3σ
Virgin thermal conductivity	-18.40%	14.02%	3.50%	-3.80%
Char thermal conductivity	-7.20%	9.30%	-0.09%	0.17%
Virgin density	3.90%	-3.10%	-0.28%	0.50%
Virgin heat of formation	2.80%	-2.10%	-0.13%	0.96%
CTE	0.09%	0.06%	-38.39%	11.99%
Compressive modulus	0.26%	0.25%	-17.63%	8.85%

5.3.2 High Fidelity Thermal Response Models

It is important to discuss how the inputs for a thermal response model are assembled and how the quality and level of uncertainty of those inputs affects the solution. A high fidelity thermal response model contains the material property inputs which go into high fidelity ablation and thermal response analysis. The performance of any high fidelity thermal response code and its ability to predict the thermal response of a material under test or flight conditions is directly related to the quality of its inputs.

If the inputs have high uncertainties or were poorly measured, it is likely the temperature and recession predictions will not match the test or flight data. In the early stages of a project, knowledge about the material properties and its performance under its planned environment is generally lacking. This is one of the main sources of uncertainty in the material response model. Uncertainties in the heating environment and planned entry trajectory are also present and impact material performance, but are not attributable to the material itself. Through the life of a project, knowledge about the material, its mission, and the entry environment is gained through analysis, ground and sometimes flight tests. Through testing, the uncertainties shrink over the lifecycle of the project, but do not vanish. The most common tests are material property tests, arc jet tests, wind tunnel tests, and structural tests. It is from material property and arc jets tests that the high fidelity thermal response model is constructed.

The properties that go into a high fidelity thermal response model can be separated into four groups: the density and decomposition parameters, thermophysical properties, pyrolysis gas properties, and surface thermochemistry. Some of the properties can be measured in a laboratory; others have to be derived from other known quantities or calculated.

The virgin density is typically measured by either a water displacement test, or by weighing a specimen of the material, measuring the dimensions, and then dividing the weight by the volume. The decomposition kinetic constants that are used in the Arrhenius equation (2.7), are derived from Thermo-Gravimetric Analysis (TGA experiments). A sample of the material is heated in an inert gas, usually at 10°C/min. The mass loss as a function of temperature is recorded and the residual mass at the end of the experiment defines the char yield and char density. The derivative of mass loss with respect to temperature is subsequently used to determine the remaining Arrhenius constants.

Table 5.3 summarizes the thermophysical properties and how they are generally obtained. The pyrolysis gas enthalpy is calculated using the elemental composition and data from the TGA experiment. Typically, the elemental composition is input into an equilibrium chemistry code and the enthalpy is calculated as a function of pressure and temperature. While the equilibrium assumption is valid at high temperatures, it begins to deteriorate at low temperatures and its use could predict

Table 5.3: Thermophysical properties

Property	How Determined
Virgin thermal conductivity	Measured as a function of temperature using a comparative rod apparatus and radial inflow apparatus
Virgin specific heat	Measured as a function of temperature using an adiabatic calorimeter, ice calorimeter, or differential scanning calorimeter
Virgin emissivity	Measured as a function of temperature by measuring the total normal emittance and comparing it to the black body total normal emittance
Virgin absorptivity	Measured as a function of temperature by measuring the total normal absorptivity and comparing it to the black body total normal absorptivity
Virgin elemental composition	Measured by mass spectrometry
Virgin heat of combustion	Measured using a bomb calorimeter
Virgin heat of formation	Derived from heat of combustion
Char elemental composition	Derived from known constituents and char yield data
Char heat of formation	Derived from known constituents and existing data
Char specific heat	Derived from elemental composition and using method of mixtures
Char thermal conductivity	Measured as a function of temperature, with great difficulty since oven char is different than in-situ char
Pyrolysis gas elemental composition	Derived from virgin and char elemental composition

unrealistic exothermic decomposition reactions in some materials. This is where the TGA data is generally used. If the TGA apparatus is outfitted with a digital scanning calorimeter, the heat of reaction of the pyrolysis reactions can be measured as a function of temperature. Ladacki, at el [136] found that for phenolic resin composites, the low temperature pyrolysis gas enthalpy can be represented by $(\bar{h} + \Delta H_p)$, where $\bar{h}$ is the weighted average solid enthalpy defined in (2.36) and ΔH_p is the heat of pyrolysis. Curve fits of the heat of pyrolysis data can be constructed and the quantity $(\bar{h} + \Delta H_p)$ can

be plotted along with the equilibrium pyrolysis gas enthalpy as a function of temperature. The high temperature equilibrium enthalpy is then merged with the low temperature $(\bar{h} + \Delta H_p)$ solution between 1500 – 2200K depending upon the pressure.

The surface thermochemistry data is calculated using the virgin, char, and pyrolysis gas elemental composition and is typically obtained using the equilibrium assumption similar to the pyrolysis gas enthalpy. The surface thermochemistry data includes the quantities $\sum_{i}^{m} \tilde{Z}_{i_w}^{*} h_i^{T_w}$ and h_w as a function of pressure, temperature, B'_g, and B'_c. As in the pyrolysis gas composition, the equilibrium assumption also affects the surface thermochemistry data at low temperatures. A plot of the non-dimensional char rate as a function of temperature at 1 atm for a phenolic resin composite is given in Figure 5.11. There are three distinct regions on this plot, the sublimation region where the

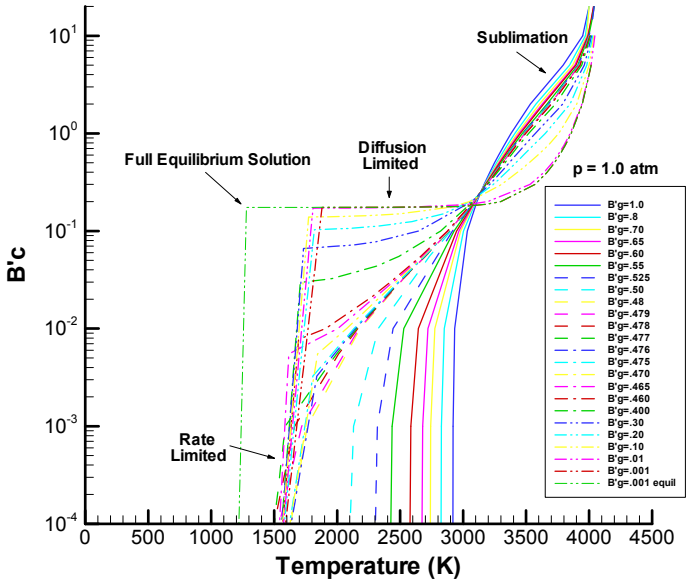

Figure 5.11: Non-dimensional char rate as a function of surface temperature for a phenolic resin composite

char is being instantly converted to gas, the diffusion limited plateau where the rate of char consumption is limited by the amount of oxygen diffusion to the surface, and the

rate limited region where the char consumption is limited by the actual chemical reaction rates. A full equilibrium solution, as shown in the plot extends the diffusion limited plateau to unrealistically low temperatures. As a result, the full equilibrium solution would then over predict the amount of recession that occurs below 2000K. To correct this, reaction rate data must be used and a non-equilibrium solution must be generated. This is not typically done and most experienced engineers either use the full equilibrium solution as a conservative approach or, as in the case of Figure 5.11, modify the data manually based on experience.

It is fortuitous for the Orion CEV TPS compression pads that MX4926N carbon phenolic possesses an extensive database which includes properties in all three principle directions. It also includes permeability and porosity data which is vital to the Darcy flow pyrolysis gas flux calculation. Most materials do not possess this level of detail in their material property database. With the advent of the three-dimensional tool developed in this dissertation, it must be emphasized that future material property testing must include mechanical and thermal tests in all three principle directions and porosity and permeability measurements. The consequence of not performing these tests is that assumptions with large uncertainty would have to be used in regard to these material properties.

5.4 Design for Uncertainty

Uncertainty is present in almost any aerospace vehicle system; in particular, for heatshield and penetration system design, there are many uncertainties. Some of the largest uncertainties pertaining to heatshield and penetration design are the CFD calculation of the entry heating environments, and the entry trajectory parameters, which directly affects the heating environment. The other uncertainties that are present come from the material response to that environment by way of the material properties. Given

that uncertainties are present, the goal is to account for them in the design. Such a design would increase the robustness of the system and increase system reliability.

5.4.1 Deterministic Analysis

5.4.1.1 As Designed Compression Pad Analysis

The 1-D compression pad sizing for the DAC-3 lunar return entry environment was been performed by the CEV TPS Advanced Development Project (ADP) compression pad team [137], which the author of this dissertation was the lead of. The compression pad design at the TPS Subsystem Design Review (SSDR) is shown in Figure 5.4 and shows all the pertinent dimensions and features. The mass of the as designed compression pad and Titanium insert system is 5.39kg. The as designed DAC-3 compression pad was analyzed with FEAR and is the baseline for comparing to the optimum design which will be determined in Section 5.4.1.3 The boundary conditions applied to the compression pad are shown in Figure 5.12. The heating augmentation factors are mapped to the FEAR mesh from the CEV Aerosciences Project (CAP)

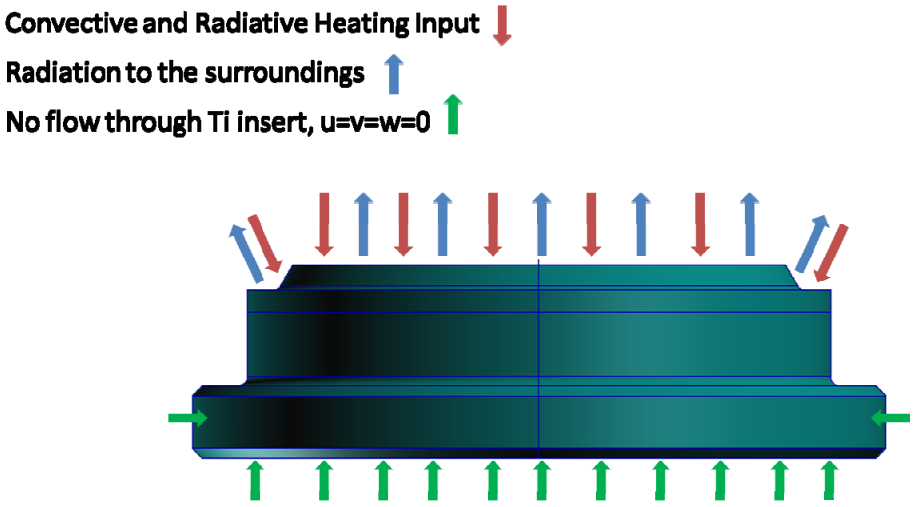

Figure 5.12: Compression pad boundary conditions

team's aeroheating database using Tecplot's internal inverse distance interpolation routine [138]. The augmentation factors used are shown in Figure 5.1 and the result of the

mapping can be visualized in either Tecplot or MSC PATRAN. The mapped augmentation factors are shown from within PATRAN in Figure 5.13. Notice that the coarse circumferential mesh of the compression pad provides a low resolution of the augmentation factors on the FEAR mesh. Unfortunately, to minimize the run time this limitation will have to be endured until parallel processing can be utilized.

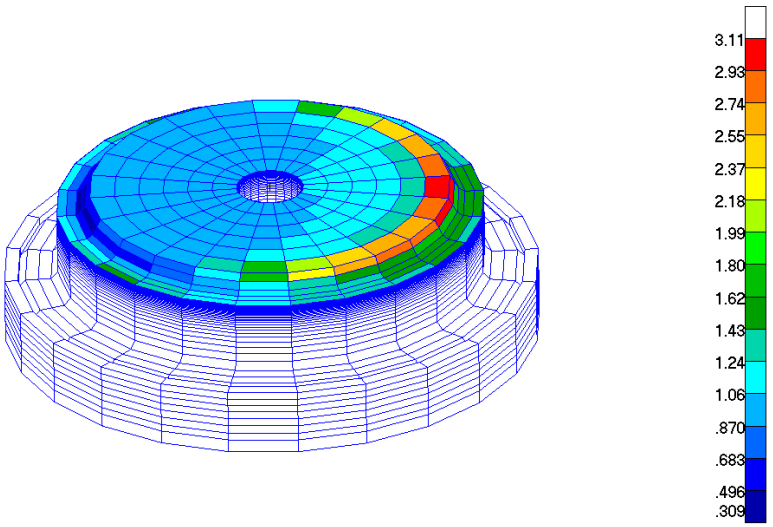

Figure 5.13: Heating augmentation factors mapped to FEAR

The resultant temperature distribution through the compression pad at peak heating and at the end of the trajectory is given in Figure 5.14 and Figure 5.15 respectively. The bondline temperature limit for the compression pad is 315.2°C, it is interesting to observe that the maximum bondline temperature even under augmented heating conditions was only 152.8°C. There are several reasons for this which demonstrates the reason a three-dimensional analysis of the pad and a new design methodology are required.

The first reason has to do with the current design philosophy and way the compression pad's 1-D sizing is performed. The pad is sized using FIAT with three different cases. The first sizing case uses the nominal smooth body heating and applies trajectory dispersion factors to the convective and radiative heating. The second case

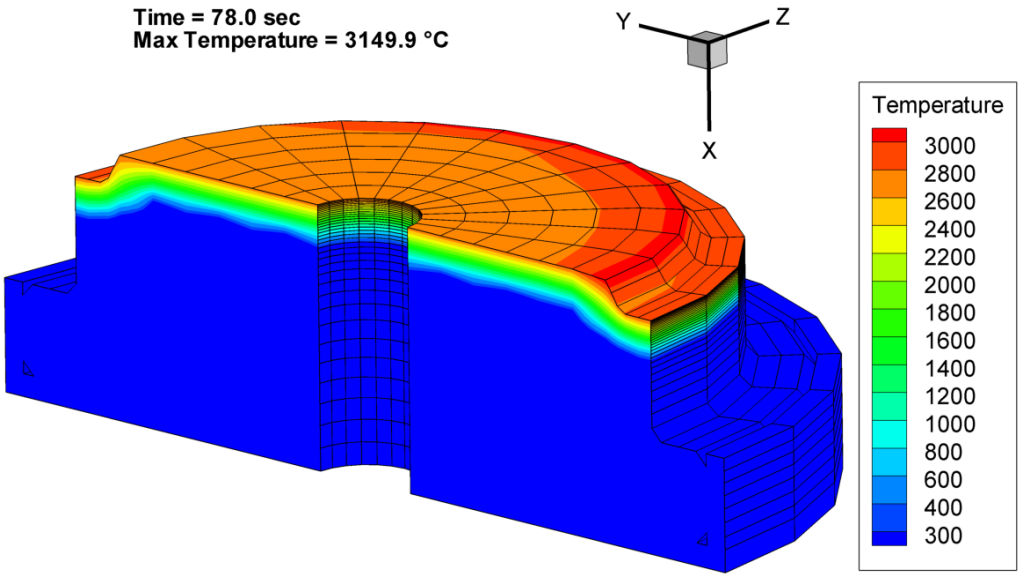

Figure 5.14: Compression pad temperature distribution 4 seconds after peak heating

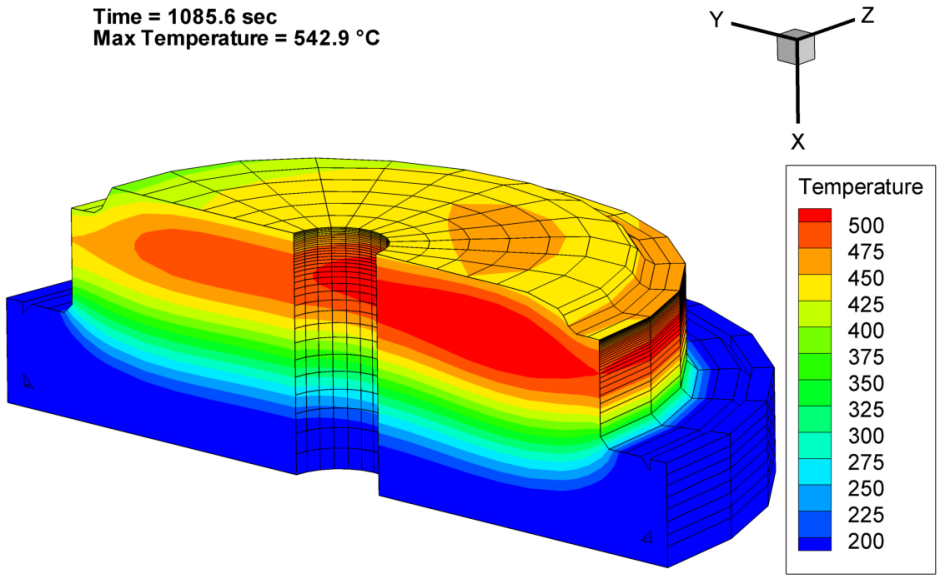

Figure 5.15: Compression pad temperature distribution at parachute deployment

uses the smooth body heating and applies the trajectory dispersions factors and factors due to the uncertainty in the aeroheating CFD calculations. The third case uses the same environment as the first case, but this time the pad is sized to a bondline temperature of 255.5°C, reducing the bondline limit is meant to simulate the uncertainty in calculating the thermal response of the material. The third case turns out to be the most limiting in

terms of sizing, however, the second case represents the highest heating and total heat load. The thickness that results from these sizing cases are root sum squared together and then an additional amount of thickness is added to account for uncertainty in the amount of recession being calculated. This becomes the minimum design thickness necessary to prevent the bondline temperature from being exceeded. Additionally, 0.889cm are added to create a feature for the Service Module connection to transfer the shear loads into the compression and the rest of the Command Module.

For the analysis shown in Figure 5.14 and Figure 5.15, the case 2 aeroheating was used since it would produce the highest surface temperatures and most thermal soak back into the pad. As the FEAR analysis has shown the bondline temperature limit does not come close to being violated which suggests the current design methodology is conservative.

In addition to the current deign practice; there are effects that the 1-D analysis cannot capture. The first effect is the fact that the in-plane virgin thermal conductivity of the compression pad material is roughly 35% greater than the through the thickness thermal conductivity. The in-plane char thermal conductivity is 36-50% greater depending on the temperature. Even though there is heating augmentation present, the higher in-plane conductivity tends to spread the heat out across the compression pad and away from the bondline. Another effect not captured by the 1-D sizing analysis is the 3-D geometric effect of having extra mass not directly in the path of the surfaces that are being heating. The area in question is highlighted with a circle in Figure 5.16. Notice there is additional compression pad material and the side wall of the Titanium insert in this region; both provide additional thermal mass and serve to regulate the heat being soaked towards the bondline. The CEV TPS ADP compression pad team designated this region as the "top hat" feature. The side which has the circle is also the side that has the highest heating augmentation factors. On the augmented heating side, notice the heat penetrates deeper into the top hat region, but the temperature towards the bondline is no more severe than

the side without the augmented heating. Again this is due to the extra thermal mass absorbing energy and the in-plane thermal conductivity allowing conduction in this direction. Had heating augmentation been applied to a 1-D analysis, the extra heat from the augmentation would be conducted directly to the bondline and would have given an incorrect higher bondline temperature.

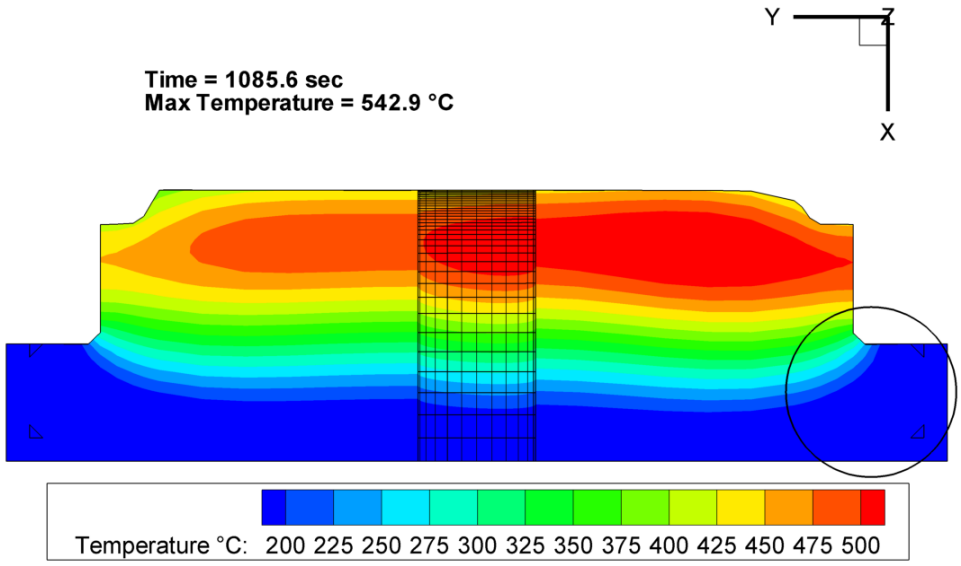

Figure 5.16: Zoomed in view of the compression pad lower corner

Another feature of FEAR is the computation of thermal stress during the simulation. The interval for stress computations is set by the user and in this case was set to 5 second intervals. It has been shown that the most critical stress in the MX4926N material is the across ply tensile stress [135, 139]. This is mainly due to the fact that there are no reinforcing fibers in-between plies and that the majority of the strength in this direction comes from the phenolic resin which is generally lower than the reinforcing fiber. In this dissertation, the across ply tensile stress will be tracked as the stress design specification.

There are many different opinions on the subject of when a charring material is considered to have failed. Some believe that if the stress allowable is exceeded at any time, whether it is in the char or virgin material, then it is a failure. Others ignore high stresses that occur in the char material all together. Another complicating factor is the

material's allowable stress is a function of temperature. For these reasons, failure of the MX4926N material will not be assessed in this dissertation, the goal will be to minimize the across-ply stress without adversely affected the stresses in the other directions and violating other imposed constraints which will be discussed in Section 5.4.1.3.

The peak across ply tensile stress occurs several seconds after peak heating at 150 seconds into the trajectory and is given Figure 5.17. The density distribution through the compression pad at 150 seconds is given in Figure 5.18. Notice the peak tensile stress is occurring where all the material has been converted to char and that the peak compressive stress is occurring at the leading edge of the pyrolysis zone.

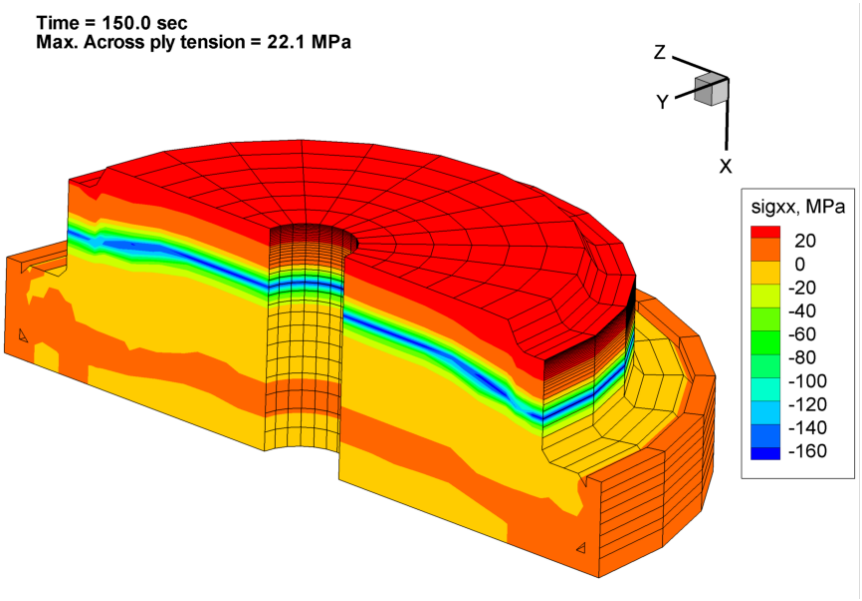

Figure 5.17: Peak across ply thermal stress at 150 seconds

Recall that the heating augmentation only gets applied to the convective heating, so at peak heating it will reach a maximum at the point where the augmentation is the highest which is approximately 2,300 W/cm^2. There is a non-trivial difference between the recession at the edge where the heating augmentation is the highest and where the heating augmentation is the lowest. The affect of the heating augmentation will be examined in the following section.

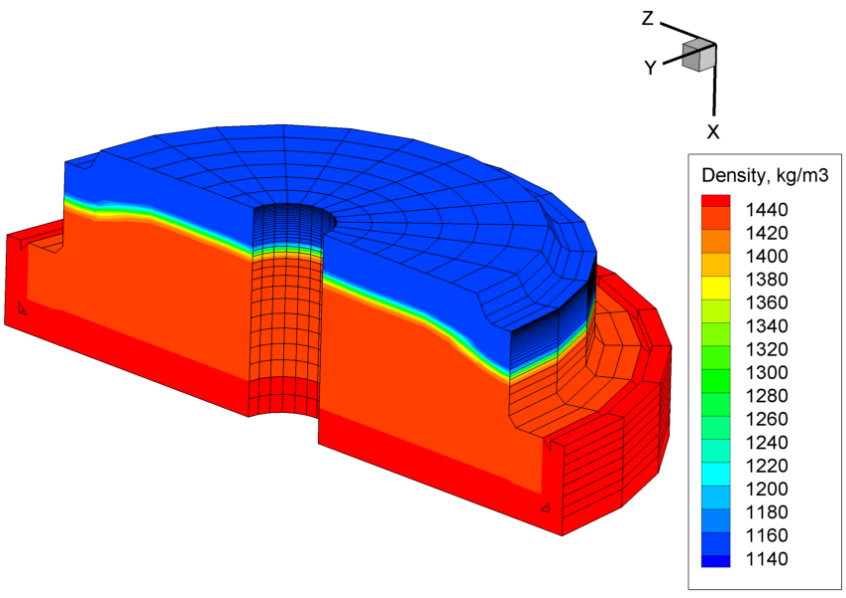

Figure 5.18: Density distribution at 150 seconds

5.4.1.2 Affect of Heating Augmentation on Recession

The recession rate for MX4926N carbon phenolic remains fairly low until surface temperatures reach the sublimation region of the B' table. This is evident in the compression pad analysis from the previous section where the side that had the highest heating augmentation significant recession and the downstream side of the pad where the augmentation was low showed very little recession. To examine the affect of heating augmentation, a closer look at the two regions of the compression pad is shown in Figure 5.19.

The surface temperature on the augmented side of the compression pad where the augmentation factors reach nearly 5.0 was 3,149.9°C at its peak. The temperature on the opposing side where augmentation factors were less than 1.0 was 2,757.5°C, or a difference of 392.4°C. This increase in temperature was significant enough to produce visible differences in recession. A comparison of the recession on the augmented side with the non-augmented side is given in Figure 5.19. In this case the recession on the augmented side is 3.178mm and on the non-augmented side 0.800mm, or a 297.3% difference.

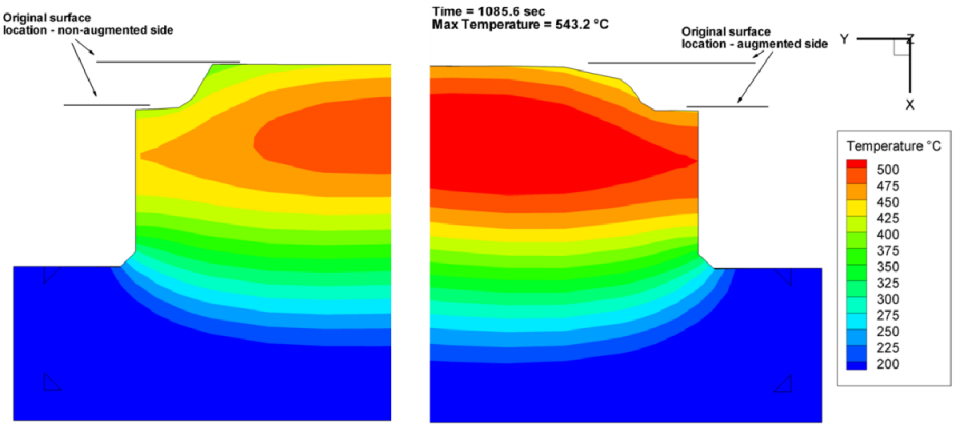

Figure 5.19: Affect of heating augmentation on recession

5.4.1.3 Optimum Compression Pad Design

Now that the baseline design has been analyzed, the objective is to optimize the design. This is the second step in the design process outlined in Figure 5.3. As mentioned in Section 5.1.2, the key design parameters of pad thickness, Titanium insert thickness, and material ply angle will be examined. Before the design space can be discretized, the ranges of design variable must be defined. Using engineering judgment and general knowledge of the design, the design variable values that would produce viable designs were defined and are summarized in Table 5.4.

Table 5.4: Design variable range

Design Variable	Maximum	Minimum
Compression pad thickness (cm)	5.486	8.026
Titanium insert thickness (cm)	0.254	1.270
Ply angle (degrees)	0.0	90.0

Once the design variable ranges have been defined, the process of discretizing them can begin. Generally, it is not known a priori how many levels each of the design variables should be broken into. A rule of thumb would be to discretize them into as few levels as possible in order to minimize the number of runs required, examine the results, and then add levels based on how each design variable affects the design specifications being tracked, which in this case would be the bondline temperature and across ply

tensile stress. The initial discretization for the design variables listed in Table 5.4 was three levels each. Upon examining the results, it was found that the across ply tensile stress was a strong function of ply angle, so the ply angle was broken down further so that it had seven levels. The design variable values were coded so that they varied between -1 and +1. Since the scale of each variable was significantly different, coding the variables in this way normalizes them with respect to one another and aids in the visual display of the results. The discrete values used and the corresponding coding is given in Table 5.5.

Table 5.5: Design variable discretization

Design Variable	Coding						
	-1.0	-0.667	-0.333	0.0	0.333	0.667	1.0
	Values						
Pad thickness (cm)	5.486	----	----	6.756	----	----	8.026
Ti insert thickness (cm)	0.254	----	----	0.762	----	----	1.270
Ply angle (degree)	0.0	15.0	30.0	45.0	60.0	75.0	90.0

The 3x3x7 full factorial design of experiments required 63 runs of FEAR to define the variation of the bondline temperature and across ply tensile stress over the ranges of the design variables. A contour plot showing the variation of the bondline temperature with the design variables is shown in Figure 5.20. It can be clearly seen that the bondline temperature varies non-linearly with the design variables. Also shown on Figure 5.20 are the known constraints of the compression pad and Titanium insert system.

The constraints can be categorized into three groups: material limitation, geometric configuration, and mission, or project management imposed. Generally, most of the constraints will fall into the material limitation category like the maximum bondline temperature, the maximum across ply stress, and ply angle. Often there are mission, or project management imposed constraints. System mass usually falls into this category

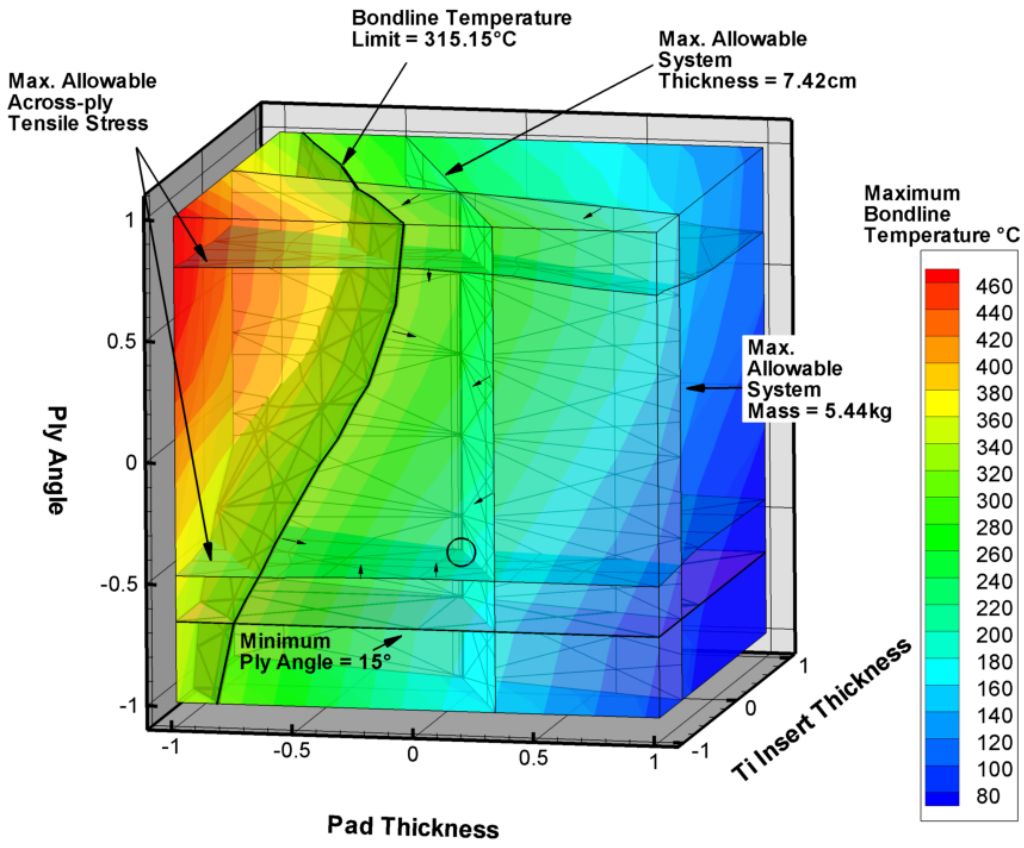

Figure 5.20: Compression pad bondline temperature variation with imposed constraints

since mass is a premium on any spacecraft. Sometimes there are configuration specific geometric constraints like the maximum total allowable thickness for the compression pad and Titanium insert. On the Orion CEV TPS, this is a real geometric constraint that must be met in order to allow a common service module interface height at every pad location and to avoid a forward facing step with respect to the upstream Avcoat TPS due to differential recession between the two.

Including the constraints on the bondline temperature contour shows how they affect the possible combinations of design variables and shows which combinations are viable. The constraints make finding the optimum somewhat easier since some combinations of the design variables can be eliminated immediately.

Finding the optimum design can be accomplished either numerically or by picking the values of the design values off the contour plot. In this example, the contour plot was used to get a reasonable estimate for the design variables which represented the starting point in the numerical determination of the optimum compression pad design. The starting point is shown on Figure 5.20 as a small circle at the intersection of the mass, stress, and total thickness constraints.

From the data generated from the 63 run full factorial design of experiments, a linear least squares fit of the bondline temperature was generated as a quadratic function of all the design variables. The across ply stress was also fit with a linear least squares fit and was found to be best represented by a sixth order polynomial which was quadratic in pad thickness and sixth order in ply angle. The system mass was a simple linear function of the pad and Titanium insert thicknesses. The ply angle and total thickness constraints were simply constants.

Since no assessment of failure is being made in terms of the across ply tensile stress, a metric, or target value for the across ply tensile stress must be established. Since the goal is to improve the as designed compression pad, the metric chosen was simply that the across ply tensile stress must be less than the 22.1 MPa calculated in the as designed compression pad and that no more than a 10% increase in the stresses in the other directions could be tolerated.

Using Microsoft Excel, a simple constrained optimization problem was set up and run. The result of the optimization was that the pad thickness should be 6.706cm, the Titanium insert thickness 0.655cm, and the ply angle 26°. Note that the ply angle was rounded up to the nearest degree since it is not practical to control the ply angle to the tenth of a degree, doing so introduces manufacturing inconsistencies and can lead to material failures [139]. The mass of the compression pad and Titanium insert system was increased slightly to 5.43kg; a 0.74% increase in mass compared to the as designed compression pad. This increase is deceiving since the optimized pad analysis included

heating augmentation. To make a better comparison, the one-dimensional RSS sizing process was performed again, this time with heating augmentation included. The result of performing the 1-D sizing with heating augmentation is that the required pad thickness would have to increase to 8.407cm making it 25.36% thicker than the optimized pad. The mass of the 1-D sized pad with heating augmentation would be 6.14kg making it 13.1% heavier than the optimized pad.

The bondline temperature for the optimized pad was calculated to be 169.9°C which is an increase of 17.1°C compared to the as designed compression pad. The temperature distribution at peak heating and at the end of the trajectory is shown in Figure 5.21 and Figure 5.22. Compared to the pad sized with heating augmentation, the bondline temperature increased 95.1°C. This suggests that performing a 1-D sizing for geometry that has three-dimensional features is highly conservative.

The maximum across ply tensile stress was reduced by 19.9% to 17.7MPa compared to the as designed compression pad. The design variables and objective functions, or design specifications, for the baseline as designed compression pad, the design including heating augmentation as determined by 1-D analysis, and the optimum design are summarized in Table 5.6. What remains to be determined is how these design changes affect the probabilities of exceeding the design specifications of bondline temperature and tensile stress.

Table 5.6: Design variable and specification comparison

Current 1-D Sized Compression Pad Design			3-D Optimized Design
	Baseline	Heating Augmentation	
Compression Pad Thickness (cm)	6.782	8.407	6.706
Titanium Insert Thickness (cm)	0.635	0.635	0.655
Ply Angle (degrees)	20	20	26
Mass (kg)	5.39	6.14	5.43
Max. Bondline Temperature (°C)	152.8	74.8	169.9
Max. Across Ply Tensile Stress (MPa)	22.1	22.1	17.7

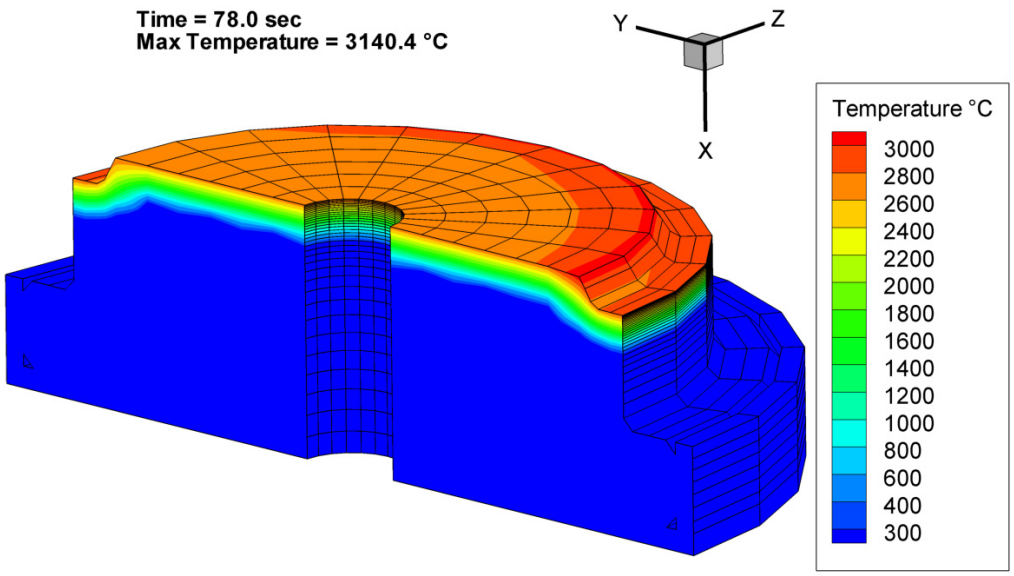

Figure 5.21: Optimum compression pad design temperature distribution at 78 seconds

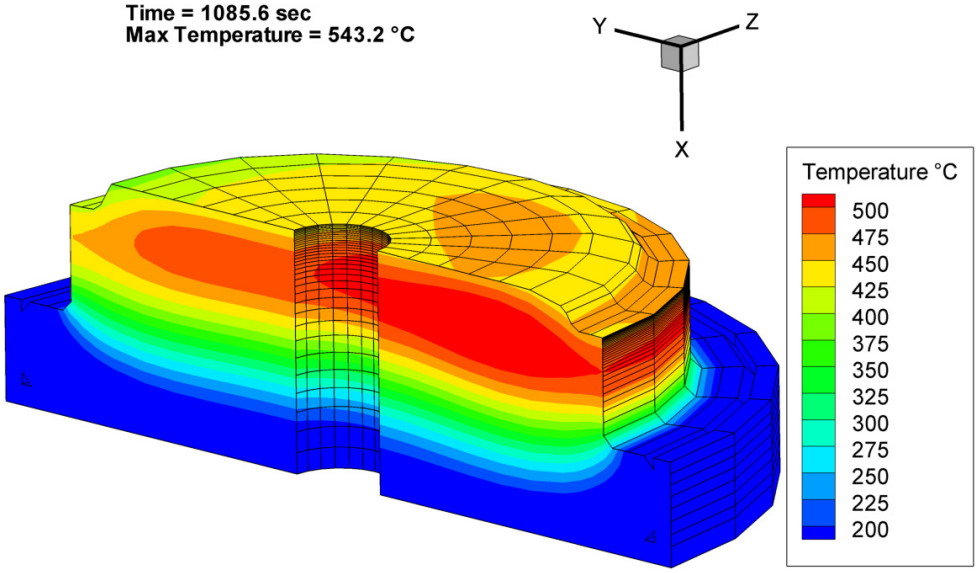

Figure 5.22: Optimum compression pad design temperature distribution at parachute deployment

5.4.2 Probabilistic Analysis

In the previous section, the optimum compression pad design which minimizes the bondline temperature and satisfies all the constraints was determined. The final step in the design process outlined in Figure 5.3 is to determine the probabilities that the bondline temperature and the across ply tensile stress target are exceeded. To do this, a Monte Carlo simulation is performed on the optimum design. Going back to the material

property sensitivity study, the top six properties influencing the thermostructural response were identified. These six properties were varied randomly according to an assumed Gaussian distribution. Other distributions are possible and may better represent a particular property, but for simplicity, all properties are assumed to follow Gaussian distributions.

A 500 sample Monte Carlo simulation was run on an Intel 2.93GHz Xeon quad core processor running 64 bit Fedora Core 9 Linux operating system. Only 500 samples were run due to the long run time for each sample. For demonstration purposes this is sufficient, however, in reality many more samples would need to be run to ensure enough samples were available to fit a suitable distribution through the response. The resulting distribution for the bondline temperature is given in Figure 5.23. According to the

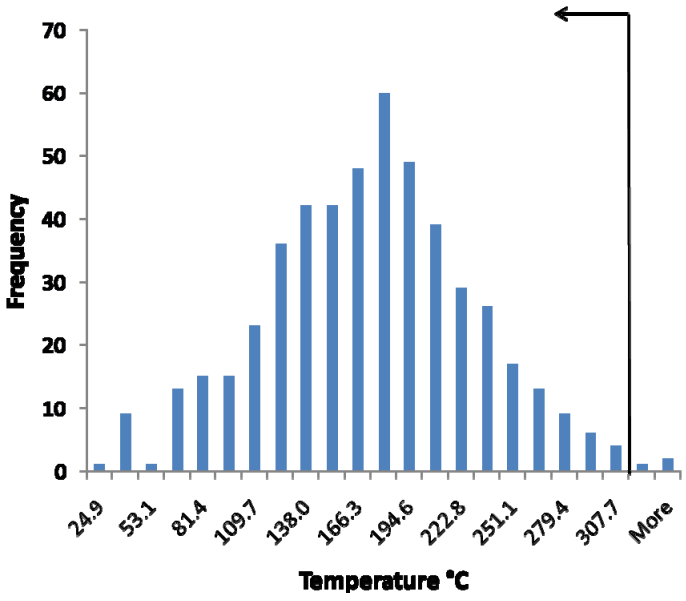

Figure 5.23: Bondline temperature distribution

distribution, the probability of exceeding the bondline temperature of 315.15°C is 0.43%, or in other words there is a 99.57% chance the bondline temperature will be below its limit. If this probability of exceeding the bondline temperature is not low enough, the constraints of the design space must be modified and a new optimum found. The designers, analysts, and mission managers are now armed with specific information as to

the probability the system will perform its function under the uncertain conditions encountered during flight. If mission managers desire a lower probability, the most obvious constraint to be modified would be the system mass. There is now a clear picture of how the mass affects bondline temperature and its relationship to the probability of exceeding it.

The across ply tensile stress distribution is shown in Figure 5.24. Since there is no assessment of failure being made due to stress, the stress will be measured against the as designed across ply tensile stress. According to the distribution, the probability of exceeding the across ply tensile stress in the as designed compression pad is 1.88%, or there is a 98.12% chance the stress will be below the as design stress. Again, an argument similar to that of the bondline temperature can be made with the across ply tensile stress. If the probability is not satisfactory, the design constraints would need to be modified and a new optimum derived.

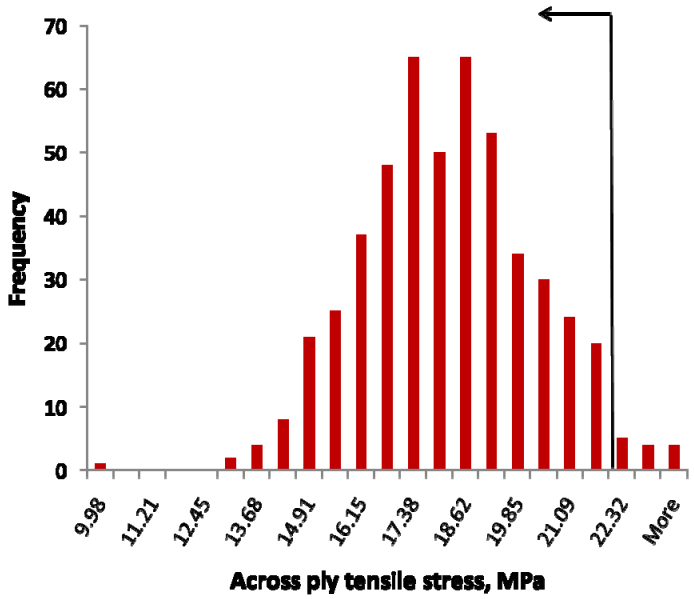

Figure 5.24: Across ply tensile stress distribution

The design process outlined in Figure 5.3 has been demonstrated with positive results. The link between the analysis and design has been established providing an increased knowledge about the design of the compression pad and the integrated compression pad-

Titanium insert system. Only a few parameters relating to the material properties were selected as the randomly varying variables in the Monte Carlo simulation. In reality many more parameters could have been chosen such including uncertainty in the aerodynamic heating. Also, there are more material properties that could have been selected for screening in the property sensitivity study phase of the process. Including specific material properties, or other parameters will depend on the specific problem being solved and should be evaluated each time this design process is used.

CHAPTER 6

CONCLUSION AND FUTURE WORK

6.1 Conclusion

In this dissertation, a review of ablative thermal protection systems analysis was presented. Specifically, the Orion CEV heatshield compression pads were described and the issues surrounding them were discussed. Historical compression pad designs were reviewed and their features compared. The need for a modern approach for designing and analyzing thermal protection systems was described. The governing differential equations for ablative thermal response were derived. In this dissertation, the finite element method was used to discretize and solve the resulting system of equations.

Galerkin's weak form of the governing differential equations was derived in both one and three-dimensions. Additionally, for the three-dimensional formulation, Darcy's Law was used to solve for the pyrolysis gas flow. Galerkin's weak form for Darcy's Law was derived and solved in conjunction with the thermal response. The equations for linear elasticity are solved alongside the thermal response equations. The linear elasticity equations serve two purposes; the first is to move the finite element mesh when there is recession, the second to calculate thermal stress. A computer code named FEAR has been developed to solve the system of equations in both one and three-dimensions. One-dimensional results were validated by comparing results for a selection of sample problems to the one-dimensional finite difference code FIAT. Three-dimensional results were validated by restricting the pyrolysis gas flow to one-dimension and using isotropic thermal properties and comparing to FIAT. The linear elasticity calculations for the mesh movement were validated by comparing the calculated recession by the resulting change in physical coordinates of the mesh in the output.

A new design approach was outlined and demonstrated by analyzing a CEV compression pad under augmented heating conditions. A link between the analysis of

thermal protection systems and their design was established. The link to design comes from understanding the variation in the thermostructural response over the range of the design variables.

6.2 Future Work

During the course of performing this research a number of features and additions to the code were identified but at this stage their implementation would have been premature or distracting from the primary goals and contributions of this research. Additionally, there were a few limitations identified with the current implementation that could be corrected with additional effort. The collection of features and additions, and limitation corrections are described in the sections that follow.

6.2.1 Coupled In-depth Thermal Response and Computational Fluid Dynamics Solution

One of the limitations of FEAR is that it uses trajectory heating which may, or may not be anchored to CFD calculations. A high fidelity method of supplying the distributed aerodynamic heating environment would be to couple a CFD calculation directly with the solution of the in-depth thermal response calculations. Another benefit of this scheme would be an improved prediction of the heating environment since the CFD solution would have direct access to a time accurate solution of the chemical species entering the boundary layer due to ablation of the heatshield.

Coupling of the CFD flow solution to the thermal response analysis must also include the affects of shape change on the resulting flow solution. This aspect would require the CFD computational grid to move along with the solid material finite element mesh. It may be possible to use the linear elasticity model used in this dissertation to move the CFD mesh, however caution would need to be exercised since the CFD mesh would be expanding vice contracting like the thermal response mesh.

The technique used to map the heating augmentation factors from the CFD results to the PATRAN mesh needs to be improved. Due to the dissimilarity of the CFD and PATRAN mesh, there may be some loss of fidelity when mapping from a fine mesh to a coarse mesh as was the case for the example shown in Chapter 5. Consistency in either the heat flux or total heat load must be maintained between the CFD result and the final mapped result. A modified mapping technique which maintains consistency should be developed. Furthermore, instead of mapping to the nodes, the mapping should be performed at the Gaussian points to maintain consistency with the finite element matrix integration. While this new technique won't be required for cases run in a coupled fashion, it will be important for cases that are run in an uncoupled mode.

6.2.1.1 Real Time Calculation of Surface Thermochemistry Data

One of the features identified which is related to the surface heating environment and would be required for a coupled CFD solution is the calculation of the thermochemistry data and non-dimensional ablation rates as the in-depth solution marches through time. Currently the thermochemistry data is supplied as a pre-calculated table as a function of pressure, temperature and B'_g. The tables generally attempt to cover a wide range of conditions, but in doing so there is some loss of accuracy since the data is interpolated linearly based on the current pressure, temperature and B'_g. If the two adjacent table entries are far apart in terms of one of the dependant variables, the linear interpolation may not be representative of the true solution. Generating an entire ACE table takes milliseconds on the 2.93Mhz Intel Xeon processor so the real time calculation would be no more expensive computationally than performing the triple interpolation of the table look up.

6.2.2 Implicit Decomposition Calculation

In Chapter 3 and Chapter 4, oscillations in the calculation of the pyrolysis gas flow were revealed. It was also shown that an increased number of elements and nodes in the regions undergoing pyrolysis could drastically reduce the oscillations albeit at the expensive of computation time. A potential solution to this problem could be bringing the pyrolysis flow calculation into the iterative non-linear in-depth temperature solution, thus making the solution fully implicit. Computational time, especially for three-dimensional problems could benefit from having the overhead of one of the equation systems removed. Additionally, the requirement to have a fine mesh in the regions undergoing pyrolysis may be able to be relaxed which would also reduce computational time.

6.2.3 Higher Order Elements

One of the direct benefits of the finite element method is the ability to employ higher order elements. Higher order elements utilize more nodes per element and thus allow quadratic, cubic, etc. interpolation functions. The benefit here is that curved boundaries can be approximated nearly perfectly which would reduce the number of elements required in the mesh and therefore decrease computational time. High order elements would also improve the Darcy flow calculation. Currently with 8-noded hexahedral elements, the pressure can only be calculated at the center of each element. This is due to the velocity-pressure formulation used where the interpolation functions for the pressure must be one order less than the interpolation functions for the velocity components. With the current linear 8-noded hexahedral element, the velocity components are interpolated linearly and defined at all eight nodes. Since the pressure must be one order lower, it becomes a constant for each element. With a quadratic 20-noded hexahedral element, the velocity components would again be known at every node, but this time the pressure would now be known at the eight corner nodes.

With an increase in the fidelity of the pressure calculation, the internal pressure could then be used with confidence in the structural analysis. By including the internal pressure as a boundary condition in addition to the temperature for the thermal stress, a more complete picture of the resultant stress could be provided. The ability to predict spallation, which is a phenomenon mostly related to the internal pressure, would greatly enhance the utility of FEAR.

6.2.4 Thermal Stress Improvements, General Stress Calculations

There is a limitation in the current implementation of the thermal stress calculation. In this dissertation, the linear elasticity equations only include the displacement degrees of freedom. Comparing the stress results for anything other than a completely constrained problem with NASTRAN is problematic since NASTRAN includes the rotational degrees of freedom in addition to the displacement. The rotational degrees of freedom allow for bending to occur. Although the displacement calculation has been fully validated, because of this limitation, the thermal stress has only been validated for a case where the problem is fully constrained and unable to displace. While this is a conservative assumption, it does not mirror reality. In the case of the compression pad, the top surface is unconstrained and free to expand in that direction and the stress would be lower than a fully constrained prediction. The rest of the compression pad is surrounded by either titanium or the Avcoat acreage TPS. In the region where the compression pad is surrounded by the Titanium, the Titanium would be strong enough to constrain the MX4926N carbon phenolic so the constrained assumption is valid. Around the perimeter, the Avcoat constrains the carbon phenolic from displacing, but the relative strength of the Avcoat is less than the carbon phenolic, so it would only partially constrain the compression pad.

As part of the future work, the rotational degrees of freedom need to be added to the formulation. This would allow more general problems to be solved in addition to being

able to validate the results against NASATRAN. With the ability to analyze more general stress problems, a distributed pressure load may be applied to the heatshield surface to simulate the pressure loading during entry. This additional capability would also require the ability to include an inertial constraint due to the mass of the vehicle. Implementation of such a constraint is not fully understood by the author at this time and additional research would be needed to accomplish this.

6.2.5 Code Optimization

Currently, the one-dimensional and the three-dimensional codes are separate entities. Additionally, the one-dimensional code does not make use of libMesh and PETSc libraries and there is currently no two-dimensional capability. In Section 5.2 the run time for the three-dimensional code was evaluated and was found to be fairly significant for large problems with long solution trajectories. These two limitations must be addressed and are described in the sections to follow.

6.2.5.1 Convert Three-Dimensional FEAR to General Multi-Dimensional

The libMesh finite element library is capable of solving finite element problems in one, two, or three dimensions. Furthermore, the library has the capability to mix two-dimensional and three-dimensional elements as well. To make FEAR more versatile, the one-dimensional version must be converted to use the libMesh and PETSc libraries. Additionally, support for two dimensional elements must be added to make FEAR a true multi-dimensional analysis tool.

Another versatility issue with FEAR is that it currently only supports 8-noded hexahedral elements in the three-dimensional version, and 2-noded bar elements for the one-dimensional version. There are numerous other families of elements available which libMesh has the ability to employ. Some examples would be 4-noded tetrahedral, and 5-

noded prism elements in three-dimensions, 4-noded quadrilateral, and 3-noded triangle elements in two-dimensions.

The current set of boundary conditions included in FEAR are specific to the compression pad problem being solved in this dissertation. Expansion of the allowed boundary conditions, such as including contact resistance between dissimilar materials would also make FEAR more versatile.

6.2.5.2 Increase Efficiency and Enable Parallel Processing

FEAR was developed by the author who does not have a computer science background and who is also a self-taught C++ programmer. Now that the FEAR code is functional and produces accurate results, coding inefficiencies must be identified and replaced with more efficient coding constructs. Data structures that are slow and can be replaced with faster structures must be identified as well. Other optimizations such as not looking up the thermal properties for every iteration in the non-linear solution must be examined to determine whether a computational benefit can be derived without adversely affecting the solution.

FEAR, along with libMesh and PETSc are capable of running in parallel on multiple processors. Unfortunately, this capability could not be demonstrated due to an improperly configured Linux cluster. This was an unfortunate unforeseen problem and will be the author's first priority after completion of this dissertation.

APPENDIX A

Newton-Raphson Method for Non-Linear Simultaneous Equations

A typical nonlinear problem where there are N functions to be zeroed, and N variables x_i may be written as [122],

$$F_i(x_1, x_2, ..., x_N) = 0 \tag{G.1}$$

Let $\boldsymbol{x}$ denote the vector of x_i variables and $\boldsymbol{F}$ denote the vector of functions F_i. In the neighborhood of $\boldsymbol{x}$ the functions F_i can be expanded in a Taylor series as,

$$F_i(\boldsymbol{x} + \delta\boldsymbol{x}) = F_i(\boldsymbol{x}) + \sum_{j=1}^{N} \frac{\partial F_i}{\partial x_j} \delta x_j + O(\delta \boldsymbol{x}^2) \tag{G.2}$$

The matrix of partial derivatives appearing in the second term on the right hand side is known as the Jacobian matrix $\boldsymbol{J}$ and is given by,

$$J_{ij} = \frac{\partial F_i}{\partial x_j} \tag{G.3}$$

Using matrix notation, neglecting terms of order $\delta \boldsymbol{x}^2$ and higher, and setting $\boldsymbol{F}(\boldsymbol{x} + \delta\boldsymbol{x}) = 0$ gives a set of linear equations for the corrections $\delta\boldsymbol{x}$ that move each function closer to zero simultaneously,

$$\boldsymbol{J} \cdot \delta\boldsymbol{x} = -\boldsymbol{F} \tag{G.4}$$

The matrix equation given in (G.4) may then be solved for the correction terms $\delta\boldsymbol{x}$ by either LU decomposition, Gaussian elimination, Gauss-Seidel iteration, or other standard matrix solver. The corrections are then added to the solution vector. Taking a full step with the corrections may be counterproductive and cause instability, so a fraction of the full step is taken based on comparing the new function vector norm with the previous function vector norm. The new solution vector is given as,

$$\boldsymbol{x}_{new} = \boldsymbol{x}_{old} + \alpha \cdot \delta\boldsymbol{x} \tag{G.5}$$

The norm of a vector is given as,

$$norm = \sum_{i=1}^{n} \left| F_i \left(\{x\} \right) \right| \tag{G.6}$$

If the norm of the new function vector is greater than that of the old, then assume that taking a full step would not be productive and take a partial step, α, defined as,

$$\alpha = \frac{\delta x}{5} \tag{G.7}$$

The process of forming the unbalanced load vector $\boldsymbol{F}$ and the Jacobian $\boldsymbol{J}$, then solving for $\delta \boldsymbol{x}$ is repeated until convergence is achieved.

In relation to the finite element equations in (3.43), the x_i*'s* would be the nodal temperatures, and the functions F_i would be

$$\begin{aligned} \{F\} = & \left(\left[\left[K_c(T_{n+1}, t_\theta) \right] - \left[K_{\dot{s}}(T_{n+1}, t_\theta) \right] \right] + \frac{1}{\Delta t} \left[C(T_{n+1}) \right] \right) \{T\}_{n+1} \\ & - \frac{1}{\Delta t} \left[C(T_{n+1}) \right] \{T\}_n - \{R(T_{n+1}, t_\theta)\} \end{aligned} \tag{G.8}$$

The Newton-Raphson method is a good all around method, but relies on an initial guess that is sufficiently close to the solution in order to guarantee convergence.

1-D Integration by parts [140]

$$\int_a^b u dv = uv\Big|_a^b - \int_a^b v du$$

$$u = N_i, \; and \; dv = \frac{\partial^2 T}{\partial x_S^2}$$

APPENDIX B

One-Dimensional Element Equation Matrix Multiplication and Integration

$$[N]=\begin{bmatrix}\left(1-\frac{x}{L}\right)\\ \frac{x}{L}\end{bmatrix}, \qquad [B]=\begin{bmatrix}-\frac{1}{L} & \frac{1}{L}\end{bmatrix}, \qquad \text{where L is the element length}$$

$$[N][N]^T=\begin{bmatrix}\left(1-\frac{x}{L}\right)^2 & \frac{x\left(1-\frac{x}{L}\right)}{L}\\ \frac{x\left(1-\frac{x}{L}\right)}{L} & \frac{x^2}{L^2}\end{bmatrix}, \qquad \int_0^L [N][N]^T=\frac{1}{3}\begin{bmatrix}1 & \frac{1}{2}\\ \frac{1}{2} & 1\end{bmatrix}$$

$$[B]^T[B]=\begin{bmatrix}\frac{1}{L^2} & -\frac{1}{L^2}\\ -\frac{1}{L^2} & \frac{1}{L^2}\end{bmatrix}, \qquad \int_0^L [B][B]^T=\frac{1}{L}\begin{bmatrix}1 & -1\\ -1 & 1\end{bmatrix}$$

$$[N][B]=\begin{bmatrix}-\frac{\left(1-\frac{x}{L}\right)}{L} & \frac{\left(1-\frac{x}{L}\right)}{L}\\ -\frac{x}{L^2} & \frac{x}{L^2}\end{bmatrix}, \qquad \int_0^L [N][B]=\frac{1}{2}\begin{bmatrix}-1 & 1\\ -1 & 1\end{bmatrix}$$

$$[B]^T[N]^T=\begin{bmatrix}-\frac{\left(1-\frac{x}{L}\right)}{L} & -\frac{x}{L^2}\\ \frac{\left(1-\frac{x}{L}\right)}{L} & \frac{x}{L^2}\end{bmatrix}, \qquad \int_0^L [B]^T[N]=\frac{1}{2}\begin{bmatrix}-1 & -1\\ 1 & 1\end{bmatrix}$$

Linear Elastic Matrix

Isotropic

$$[C_e] = \frac{E}{(1+\nu)(1-2\nu)} \begin{bmatrix} 1-\nu & \nu & \nu & 0 & 0 & 0 \\ \nu & 1-\nu & \nu & 0 & 0 & 0 \\ \nu & \nu & 1-\nu & 0 & 0 & 0 \\ 0 & 0 & 0 & \frac{1-2\nu}{2} & 0 & 0 \\ 0 & 0 & 0 & 0 & \frac{1-2\nu}{2} & 0 \\ 0 & 0 & 0 & 0 & 0 & \frac{1-2\nu}{2} \end{bmatrix}$$

Orthotropic

$$[C_e] = \begin{bmatrix} \frac{1-\nu_{23}\nu_{32}}{E_y E_z \Delta} & \frac{\nu_{21}-\nu_{31}\nu_{23}}{E_y E_z \Delta} & \frac{\nu_{31}-\nu_{21}\nu_{32}}{E_y E_z \Delta} & 0 & 0 & 0 \\ \frac{\nu_{12}-\nu_{13}\nu_{32}}{E_x E_z \Delta} & \frac{1-\nu_{31}\nu_{13}}{E_x E_z \Delta} & \frac{\nu_{32}-\nu_{31}\nu_{12}}{E_x E_z \Delta} & 0 & 0 & 0 \\ \frac{\nu_{13}-\nu_{12}\nu_{23}}{E_x E_y \Delta} & \frac{\nu_{23}-\nu_{13}\nu_{21}}{E_x E_y \Delta} & \frac{1-\nu_{12}\nu_{21}}{E_x E_y \Delta} & 0 & 0 & 0 \\ 0 & 0 & 0 & 2G_{23} & 0 & 0 \\ 0 & 0 & 0 & 0 & 2G_{31} & 0 \\ 0 & 0 & 0 & 0 & 0 & 2G_{12} \end{bmatrix}$$

Where

$$\Delta = \frac{1-\nu_{12}\nu_{21}-\nu_{23}\nu_{32}-\nu_{31}\nu_{13}-2\nu_{12}\nu_{23}\nu_{31}}{E_x E_y E_z}$$

APPENDIX C

Source Code Listing

The source code for the FEAR code is contained in the C++ source and header files shown in Table C-1. Some files contain ITAR restricted code and are not provided in their entirety; others are listed in their entirety within this appendix. The PETSc and libMesh libraries are open source and are not provided here.

Table C-1

File Name	Description
stdafx.h	Standard header used to include all other necessary header files
Stdafx.cpp	Standard driver for stdafx.h
Main.h	Header file to declare global functions and variables
Main.cpp	Main program entry point; global function definitions; global variable definitions
StaticHex8.h	Header file defining static objects
FEM.h	Header File for Hex8, Bar2, element classes, as well Node, Material and Decomp classes
FEM.cpp	Definitions of functions for Hex8, Bar2, element classes, as well Node, Material and Decomp classes
Flow.h	Header file for ENVIR class
Flow.cpp	Definitions of functions for ENVIR class
Math_Util.h	Header for mat utility functions
Math_Util.cpp	Math and vector utility functions, unit conversion functions
SolHelper.h	Header file for solution helper class
SolHelper.cpp	Helper class for solution management

REFERENCES

[1] Dec, J. A., Mitcheltree, R. A., "Probabilistic Design of A Mars Sample Return Earth Entry Vehicle Thermal Protection System", AIAA-2002-0910, 7-10 January 2002, 40th Aerospace Sciences Conference and Exhibit, Reno, NV.

[2] Anon, Planetary Mission Entry Vehicles Quick Reference Guide Version 3, NASA SP-2006-3401, NASA Ames Research Center, 2006.

[3] WILLCOCKSON, W. H., "Mars Pathfinder Heatshield Design and Flight Experience", *Journal of Spacecraft and Rockets*, Vol. 36, No. 3, pp 374-379, May-June 1999.

[4] WILLCOCKSON, W. H., "Stardust Sample Return Capsule Design Experience", *Journal of Spacecraft and Rockets*, Vol. 36, No. 3, pp 470-474, May-June 1999.

[5] WRIGHT, M. J., "CEV Thermal Protection System (TPS) Margin Management Plan", NASA Ames Research Center, C-TPSA-A-DOC-7005, Rev. v6d1, November 2006.

[6] WRIGHT, M. J., BOSE, D., AND CHEN, Y.-K., "Probabilistic Modeling of Aerothermal and Thermal Protection Material Response Uncertainties", AIAA Journal, Vol. 45, No. 2, pp 399-410, February 2007.

[7] CHEN, Y. –K, SQUIRE, T., LAUB, B., AND WRIGHT, M. J., "Monte Carlo Analysis for Spacecraft Thermal Protection System Design", AIAA-2006-2951, 5-8 June 2006, 9th Joint Thermophysics and Heat Transfer Conference, San Francisco, CA.

[8] Anon, "Apollo Block II Heatshield Final Stress Report", Avco Corporation, Willmington, MA, 1968.

[9] ERB,R. B., GREENSHIELDS, D. H., CHAUVIN, L. T., PAVLOSKY, J. E., AND STATHAM, C. L., "Apollo Thermal-Protection System Development", AIAA-1968-1142, 3-5 December 1968, AIAA Entry Vehicle Systems and Technology Meeting, Williamsburg, VA.

[10] LIECHTY, D. S., "Aerothermodynamic Testing of Protuberances and Penetrations on the NASA Crew Exploration Vehicle Heat Shield", AIAA 2008-1240, 7-10 January 2008, 46th AIAA Aerospace Sciences Meeting and Exhibit, Reno, NV.

[11] LESSARD, V., JENTINK, T., THOMPSON, R., AND ZOBY, V., "Computational Analysis of Beveled Compression Pad Geometries: Initial Results", CEV Aerosciences Project, NASA Langley Research Center, February 2008.

[12] Anon, "Marinite I Material Data Sheet", BNZ Materials, Inc., BNZ R-3261-W, November 1997.

[13] ANDREWS, T. L., "Detailed Heatshield Implementation Plan Boeing and Fiber Materials Inc. Phenolic Impregnated Carbon Ablator (PICA), PWD05-0122 Rev A, February 2006.

[14] Anon, "Apollo Heatshield, Monthly Progress report", January 1965, Avco Corporation, Research and Development Division

[15] JONES, R. A., and HUNT, J. L., "Effects of Cavities, Protuberances, and Recation Control Jets on Heat Transfer to the Apollo Command Module", NASA TM X-1063, March 1965.

[16] BERTIN, J. J., "The Effect of Protuberances, Cavities and Angle of Attack on the Wind Tunnel Pressure and Heat Transfer Distribution for the Apollo Command Module", NASA TM X-1243, October 1966.

[17] HUNT, J. L., and JONES, R. A., "Effects of Several Ramp Fairing, Umbilical, and Pad Configurations on Aerodynamic Heating to Apollo Command Module at Mach 8", NASA TM X-1640, September 1968.

[18] WALTON, T. E., WITTE, W. G., and O'HARE, B. J., "Flight Investigation of the Effects of Apollo Heatshield Singularities on Ablator Performance", NASA TN D-4791, September 1968.

[19] Phone conversation with Israel Taback, Lead Aeroshell Engineer Viking Project, March 2007.

[20] HOLMBERG, N. A., FAUST, R. P., HOLT, H. M., "Viking '75 Spacecraft Design and Test Summary: Volume I – Lander Design", NASA RP-1027, November 1980.

[21] LUNSFORD, V., "Genesis Mechanical Subsystems CDR", presentation package, Lockheed Martin, March 1999.

[22] CHEATWOOD, F. M., MERSKI, R. N., RILEY, C. J., and MITCHELTREE, R. A., "Aerothermodynamic Environment Definition for the Genesis Sample Return Capsule", AIAA-2001-2889, 35th AIAA Thermophysics Conference, Anaheim, CA June 11-14, 2001.

[23] Anon., "Space Shuttle Program Thermodynamic Design Data Book," Rockwell International, Report SD73-SH-0226, Downey, CA, Jan. 1981.

[24] SCOTTI, S. J. (compiled by), "Current Technology for Thermal Protection Systems", NASA-CP-3157, February 1992.

[25] KRATSCH, K. M., LOOMIS, W.C., RANDLES, P.W., "Jupiter Probe Heatshield Design", AIAA 1977-427, 21-23 March 1977, AIAA/ASME 18th Structures, Structural Dynamics & Materials Conference

[26] HURWICZ, H., "Aerothermochemistry Studies in Ablation", Combustion and Propulsion, 5th AGARD Colloquium on High-Temperature Phenomena, Braunschweig, Germany, April 9-13, 1962, Pergamon Press, New York, 1963.

[27] MOYER, C. B., and RINDAL, R. A., "An Analysis of the Coupled Chemically Reacting Boundary Layer and Charring Ablator – Part II. Finite Difference Solution for the In-Depth Response of Charring Materials Considering Surface Chemical and Energy Balances", NASA CR-1061, 1968.

[28] KOO, J. H., HO, D. W. H., and EZEKOYE, O. A., "A Review of Numerical and Experimental Characterization of Thermal Protection Materials – Part I. Numerical Modeling", AIAA 2006-4936, 9-12 July 2006, 42nd Joint Propulsion Conference and Exhibit, Sacramento, CA

[29] SCALA, S. M., "The Thermal Degradation of Reinforced Plastics During Hypersonic Re-Entry", General Electric Company, R59SD401, July, 1959.

[30] SCALA, S. M., "A Study of Hypersonic Ablation", General Electric Company, RS59SD438, September, 1959.

[31] SCALA, S. M., "The Ablation of Graphite in Dissociated Air, Part I: Theory", General Electric Company, R62SD72, September, 1962.

[32] LAFAZAN, S., and SIEGEL, B., "Ablative Thrust Chambers for Space Application", Paper No. 5, 46th National Meeting of the American Institute of Chemical Engineers, Los Angeles, CA., February 5th, 1962.

[33] SWANN, R. T., and PITTMAN, C. M., "Numerical Analysis of the Transient Response of Advanced Thermal Protection Systems for Atmospheric Entry". NASA TN-D-1370, July 1962.

[34] ROSENSWEIG, R. E., and BEECHER, N., "Theory for the Ablation of Fiberglas Reinforced Phenolic Resin Phenolic", *AIAA Journal*, Vol. 1, No. 8, pp 1802-1809, August, 1963.

[35] QUINVILLE, J. A., and SOLOMAN, J., "Ablating Body Heat Transfer", Aerospace Corporation, El Segundo, CA., SSD-TDR-63-159, January 15th, 1965.

[36] REINIKKA, E. A., and WELLS, P. B., "Charring Ablators on Lifting Entry Vehicles", Journal of Spacecraft and Rockets, Vol. 1, No. 1, January 1965.

[37] SWANN, R. T., DOW, M. B., and TOMPKINS, S. S., "Analysis of the Effects of Environmental Conditions on the Performance of Charring Ablators", Journal of Spacecraft and Rocket, Vol. 3, No. 1, January 1966.

[38] FRIEDMAN, H. A., and MCFARLAND, B. L., "Two-Dimensional Transient Ablation and Heat Conduction Analysis for Multi-material Thrust Chamber Walls", AIAA 1966-542, AIAA 2nd Joint Propulsion Specialist Conference, Colorado Springs, CO, June 13-17, 1966.

[39] TAVAKOLI, M. L., "An Integral Method for Analysis of the Aerothermochemical Behavior of Refractory-Fiber Reinforced Char-Forming Materials", AIAA 1966-435, AIAA 4th Aerospace Sciences Meeting, Los Angeles, CA, June 27-29, 1966.

[40] TRAN, H., K., JOHNSON, C. E., HSU, M., SMITH, M., DILL, H., and CHEN-JONSSON, A., "Qualification of the Forebody Heatshield of the Stardust Sample Return Capsule", AIAA-1997-2482, 32nd Thermophysics Conference, Atlanta, GA, June 23-25, 1997.

[41] OLYNICK, D. R., CHEN, Y-K, and TAUBER, M. E., "Aerothermodynamics of the Stardust Sample Return Capsule", *Journal of Spacecraft and Rockets*, Vol. 36, No. 3, May-June 1999, pp. 442-462.

[42] CHEATWOOD, F. M., MERSKI, N. R., RILEY, C. J., and MITCHELTREE, R. A., "Aerothermodynamic Environment Definition for the Genesis Sample Return Capsule", AIAA-2001-2889, 35th AIAA Thermophysics Conference, Anaheim, CA June 11-14, 2001.

[43] DESAI, PRASUN N. and CHEATWOOD, F. MCNEIL: "Entry Dispersion Analysis for the Genesis Sample Return Capsule," AS Paper 99-469, AAS/AIAA Astrodynamics Specialist Conference, Girdwood, AK, August 16-19, 1999.

[44] HOLLIS, B. R., STRIEPE, S. A., WRIGHT, M. J., BOSE, D., SUTTON, K., and TAKASHIMA, N., "Prediction of the Aerothermodynamic Enviornment of the Huygens Probe", AIAA-2005-4816, 38th AIAA Thermophysics Conference, Toronto, Ontario, Canada, June 6-9, 2005.

[45] TRAN, H., OLYNICK, D. R., CHEN, Y-K, WERCINSKI, P., and ALLEN, G. "TPS Requirements for Advanced Sample Return Capsule Design", AIAA-1998-2853 AIAA/ASME Joint Thermophysics and Heat Transfer Conference, 7th, Albuquerque, NM, June 15-18, 1998.

[46] MITCHELTREE, R. A., KELLAS, S., DORSEY, J. T., DESAI, P. N., and MARTIN, C. J. "A Passive Earth-Entry Capsule for Mars Sample Return", AIAA-1998-2851 AIAA/ASME Joint Thermophysics and Heat Transfer Conference, 7th, Albuquerque, NM, June 15-18, 1998.

[47] HOGGE, M. and GERREKENS, P., "Two-Dimensional Deforming Finite Element Methods for Surface Ablation", AIAA 1983-1555, June 1-3, 18th Thermophysics Conference, Montreal, Canada.

[48] HOGGE, M. and GERREKENS, P., "One-dimensional Finite Element Analysis of Thermal Ablation with Pyrolysis", Comp. Meth. in Appl. Mech. Eng., 33,609-634, 1982.

[49] J.H. CHIN. “Charring ablation by finite element”, in: R.W. Lewis et al., eds., Numerical Methods in Thermal Problems. Vol. 11 (Pineridge. Swansea. 1981) pp. 218-229.

[50] ANDERSON, D. A., TANNEHILL, J. C., and PLETCHER, R. H., *Computational Fluid Mechanics and Heat Transfer*, Hemisphere, Washington, DC, 1984.

[51] TU, S. Z., and RUFFIN, S. M., “Solution Adaptive, Unstructured Cartesian-Grid Methodology for Chemically Reacting Flow”, AIAA 2002-3097, 8th AIAA/ASME Joint Thermophysics and Heat Transfer Conference, St. Louis, MO, 24-26 June 2002.

[52] THOMPSON, J.F., THAMES, F. C., and MASTIN, C. W., “Automatic Numerical Generation of Body-fitted Curvilinear Coordinate System for Field Containing Any Number of Arbitrary Two-Dimensional Bodies.” *Journal of Computational Physics*, Vol. 15, pp 299-319, 1974.

[53] CHEN, Y. S., “A Numerical Method for Three-Dimensional Incompressible Flows Using Non-Orthogonal Body-Fitted Coordinate Systems”, AIAA-86-1654, 22nd AIAA/ASME/SAE/ASEE Joint Propulsion Conference, Huntsville, AL, 16-18 June 1986.

[54] SHYY, W., TONG, S. S., and CORREA, S. M., “Numerical Recirculating Flow Calculation Using a Body-Fitted Coordinate System”, *Numerical Heat Transfer*, Vol. 8, pp 99-113, 1985.

[55] MALISKA, C. R., and RAITHBY, G. D., “A Method for Computing Three-Dimensional Flows Using Non-Orthogonal Boundary-Fitted Coordinates”, *International Journal for Numerical Methods in Fluids*, Vol. 4, pp 519-537, 1984

[56] Anon.,”User's Manual, Aerotherm Charring Material Thermal Response and Ablation Program", Acurex Corporation, Aerotherm Division, Mountain View, California, November, 1987.

[57] CHEN, Y.-K., and MILOS, F. S., “Fully Implicit Ablation and Thermal Analysis Program (FIAT),” *Journal of Spacecraft and Rockets,* Vol. 36, No. 3, pp 475-483, May–June 1999

[58] HUEBNER, K. H., DEWHIRST, D. L., SMITH, D. E., BYROM, T. G., *The Finite Element Method for Engineers,* 4th ed., John Wiley & Sons, New York, 2001.

[59] LEWIS, R. W., NITHIARASU, P., SEETHARAMU, K. N., *Fundamentals of the Finite Element Method for Heat and Fluid Flow,* John Wiley & Sons, West Sussex, England, 2004.

[60] ZIENKIEWICZ, O. C., *The Finite Element Method*, 3rd ed., McGraw-Hill, New York, NY, 1977.

[61] REDDY, J. N., and GARTLING, G. K., *The Finite Element Method in Heat Transfer and Fluid Dynamics*, 2nd ed., CRC Press, 2000.

[62] Anon, "ProEngineer User's Manual"

[63] Anon, "MSC Software NASTRAN User's Manual"

[64] Anon, "MSC Software PATRAN Thermal User's Manual"

[65] Anon, "Thermal Desktop User's Manual"

[66] HURWICZ, H., FIFER, S., and KELLY, M., "Multidimensional Ablation and Heat Flow During Re-Entry", *Journal of Spacecraft and Rockets*, Vol. 1, No. 3, May-June 1964.

[67] FRIEDMAN, H. A., and MCFARLAND, B. L., "Two-Dimensional Transient Ablation and Heat Conduction Analysis for Multi-Material Thrust Chamber Walls", AIAA-1966-542, AIAA 2nd Propulsion Joint Specialist Conference, Colorado Springs, CO, June 13-17, 1966.

[68] CHEN, Y.-K., and MILOS, F. S., "Multidimensional Effects on Heatshield Thermal Response for the Orion Crew Module", AIAA-2007-4397, 39th AIAA Thermophysics Conference, Miami, FL, June 25-28 2007.

[69] MILOS, F. S., and CHEN, Y. –K., "Two-Dimensional Ablation, Thermal Response, and Sizing Program for Pyrolyzing Ablators", AIAA-2008-1223, 46th AIAA Aerospace Sciences Meeting and Exhibit, Reno, NV, 7-10 January 2008.

[70] CHEN, Y. –K., and MILOS, F. S., "Three-Dimensional Ablation and Thermal Response Simulation System", AIAA-2005-5064, 38th AIAA Thermophysics Conference, Toronto, Ontario Canada, 6-9 June 2005.

[71] PARK, G. –J., LEE, T. –H., KWON, H. L., and HWANG, K, -H., "Robust Design: An Overview", *AIAA Journal*, Vol. 44, No. 1, January 2006.

[72] TAGUCHI, G., CHOWDHURY, S., and TAGUCHI, S., *Robust Engineering*, McGraw-Hill, New York, 2000.

[73] TAGUCHI, G. "Introduction to Quality Engineering: Designing Quality into Products and Processes", Asian Productivity Organization, Tokyo, 1986.

[74] PHADKE, M. S., *Quality Engineering Using Robust Design*, Prentice-Hall, Englewood Cliffs, NJ, 1989.

[75] LEE, K. H., EOM, I. S., PARK, G. J., and LEE, W. I., "Robust Design for Unconstrained Optimization Problems Using the Taguchi Method," *AIAA Journal*, Vol. 34, No. 5, 1996, pp. 1059–1063.

[76] LEE, K. H., and PARK, G. J., "Robust Optimization in Discrete Design Space for Constrained Problems," *AIAA Journal*, Vol. 40, No. 4, 2002, pp. 774–780.

[77] SUNDARESAN, S., ISHII, K., and HOUSER, D. R., "A Robust Optimization Procedure with Variations on Design Variables and Constraints," *Engineering Optimization*, Vol. 24, No. 2, 1995, pp. 101–117.

[78] SUH, N. P., *Axiomatic Design: Advances and Applications*, Oxford Univ. Press, New York, 2001.

[79] SUH, N. P., *The Principles of Design*, Oxford Univ. Press, New York, 1990.

[80] STRIEPE, S.A., ET AL.: "Program to Optimize Simulated Trajectories (POST II), Vol. II Utilization Manual." Version 1.1.6.G, January 2004, NASA Langley Research Center, Hampton, VA.

[81] HAYTER, A. J., *Probability and Statistics for Engineers and Scientists*, 2nd Ed., Duxbury, Pacific Grove, CA, 2002.

[82] KEENEY, R. L., and VON WINTERFELDT, D., "Eliciting probabilities from Experts in Complex Technical Problems", IEEE Transactions on Engineering Management, Vol. 38, No. 3 August 1991.

[83] RANASINGHE, M., and RUSSELL, A. D., "Elicitation of Subjective Probabilities for Economic Risk Analysis: An Investigation", Construction Management and Economics, Vol. 11, pp 326-340, 1993.

[84] ISRAEL, M. H., and NARDO, S. V., "An Annotated Bibliography on Ablation and related Topics", PIBAL report no. 686, Polytechnic Institute of Brooklyn, May 1964.

[85] LEES, L., "Ablation in Hypersonic Flows", 7th Anglo-American Aeronautical Conference, New York, October 5-7, 1959.

[86] BAER, D., and AMBROSIO, A., "Heat Conduction in a Semi-infinte Slab with Sublimation at the Surface", Space Technology Lab. 59-0000-00610, Los Angeles, CA., February 1959.

[87] KATSIKAS, C. J., CASTLE, G. K., and HIGGINS, J. S., "Ablation Handbook – Entry Materials Data and Design", AFML-TR-66-262, September 1966.

[88] KENDALL, R. M., RINDAL, R. A., and BARTLETT, E. P., "Thermochemical Ablation", AIAA 65-642, AIAA Thermophysics Specialist Conference, Monterey, CA, September 13-15, 1965.

[89] KRATSCH, K. M., HEARNE, L. F., and MCCHESNEY, H. R., "Thermal Performance of Heatshield Composites During Planetary Entry", Lockheed Missiles and Space, LMSC-803099, Sunnyvale, CA, October 1963.

[90] BARRIAULT, R. J., "One-Dimensional Theory for a Model of Ablation for Plastics that Form a Charred Surface Layer", AVCO-RAD TM-58-130, November 1958.

[91] BEECHER, N., and ROSENSWEIG, R. E., "Ablation Mechanisms in Plastics with Inorganic Reinforcement", ARS Journal, Vol. 31, No. 4, April 1961, pp 530-539.

[92] MUNSON, T. R., and SPINDLER, R. J., "Transient Thermal Behavior of Decomposing Materials. Part I, General Theory and Application to Convective Heating", AVCO RAD-TR-61-10, AVCO Corp., Wilmington, MA, May 1961.

[93] BARRIAULT, R. J., and YOS, J., "Analysis of the Ablation of Plastic Heatshields that Form a Charred Surface Layer", ARS Journal, Vol. 30, No. 9, September 1960, pp. 823-829.

[94] CURRY, D. M., "An Analysis of a Charring Ablation Thermal Protection System", NASA TN D-3150, November 1, 1965.

[95] SCALA, S. M., and GILBERT, L. M., "Thermal Degradation of a Char Forming Plastic During Hypersonic Flight", ARS Journal, Vol. 32, No. 6, June 1962, pp 917-924.

[96] STEG, L., and LEW, H., "Hypersonic Ablation", *The High Temperature Aspects of Hypersonic Flow*, W. C. Nelson, ed., Proceedings of the AGARD-NATO Specialists Meeting, Rhode-Saint-Genèse, Belgium, April 3-6, 1962, MacMillian Co., New York, 1964, pp. 629-680.

[97] MORAN, M. J., and SHAPIRO, H. N., *Fundamentals of Engineering Thermodynamics*, John Wiley & Sons, New York, NY, 1988.

[98] GOLDSTEIN, H. E., "Kinetics of Nylon and Phenolic Pyrolysis", Lockheed Missiles and Space Company, Sunnyvale, CA. LMSC-667876, October 1965.

[99] GOLDSTEIN, H. E., "Pyrolysis Kinetics of Nylon 6-6, Phenolic Resin, and Their Composites", Marcel Dekker, Inc., New York, 1971

[100] HOGAN, R. E., BLACKWELL, B. F., and COCHRAN, R. J., "Application of Moving Grid Control Volume Finite Element Method to Ablation Problems", *Journal of Thermophysics and Heat Transfer*, Vol. 10, No. 2, April-June, 1996.

[101] BROGAN, J. J., "A Simple Numerical Solution for Heat Conduction in a Solid with a Receding Surface", *Journal of Spacecraft and Rockets*, Vol. 2, No.1, pp 112-113, Jan.-Feb. 1965.

[102] LEES, L., "Convective Heat Transfer With Mass Addition and Chemical Reactions", Third AGARD Colloquim on Combustion and Propulsion, Pergamon Press, New York, 1959.

[103] KENDALL, R. M., RINDAL, R. A., and BARTLETT, E. P., "A Multicomponent Boundary Layer Chemically Coupled to an Ablating Surface", *AIAA Journal*, Vol. 5, No. 6, June 1967, pp 1063-1071.

[104] BARTLETT, E. P, and GROSE, R. D., "An Evaluation of a Transfer Coefficient Approach for Unequal Diffusion Coefficients," Aerotherm Corporation, Mountain View, CA, Report 69-50, June 30, 1969.

[105] BARTLETT, E. P., NICOLET, W. E., AND HOWE, J. T., "Heat-Shield Ablation at Superorbital Re-entry Velocities", AIAA-1970-202, 19-21 January 1970, 8th Aerospace Sciences Meeting, New York, NY.

[106] KAYS, W. M., and CRAWFORD, M. E., *Convective Heat and Mass Transfer,* 3rd Edition, McGraw-Hill, New York, NY, 1993.

[107] SCHLITCHING, H., GERSTEN, K., *Boundary-Layer Theory*, 8th Edtion, Springer-Verlag, Berlin, Germany, 2000.

[108] ANDERSON, J. D., *Hypersonic and High Temperature Gas Dynamics*, McGraw-Hill, 1989, Published by AIAA with permission, Reston, VA, 2000.

[109] TURNS, S. R., *An Introduction to Combustion*, 2nd Edition, McGraw-Hill Series in Mechanical Engineering, Singapore, 2000.

[110] BIRD, R. B., "Diffusion in Multicomponent Gas Mixtures", 25th Anniversary Congress of the Society of Chemical Engineers, November 6-14, 1961.

[111] ROSNER, D. E., "Similitude Treatment of Hypersonic Stagnation Heat Transfer", ARS Journal, 29, 215-216, 1959.

[112] FAY, J. A. and RIDELL, R. F., "Theory of Stagnation-point Heat Transfer in Dissociated Air", Journal of Aeronautical Sciences, 25, 73-85, 121, 1958.

[113] Anon., "User's Manual Aerotherm Chemical Equilibrium Program", Acurex Report UM-81-11/ATD, August 1981.

[114] KENDALL, R. M., "An Analysis of the Coupled Chemically Reacting Boundary Layer and Charring Ablator – Part V. A General Approach to the Thermochemical Solution of Mixed Equilibrium-Nonequilibrium, Homogeneous or Heterogeneous Systems", NASA CR-1064, 1968.

[115] INCROPERA, F. P., and DEWITT, D. P., *Fundamentals of Heat and Mass Transfer,* 5th ed., Wiley, New York, 2002.

[116] TAUBER, M. E., and SUTTON, K., "Stagnation-Point Radiative Heating Relations for Earth and Mars Entires", *Journal of Spacecraft and Rockets*, Vol. 28, No. 1, January-February, 1991.

[117] FELIPPA, C. A., and CLOUGH, R. W., "The Finite Element Method in Solid Mechanics", in *SIAM-AMS Proceedings*, Vol. 2, American Mathematical Society, Providence, RI, 1970, pp 210-252.

[118] OLIVEIRA, E. R. A., "Theoretical Foundations of the Finite Element Method", *International Journal of Solids and Structures*, Vol. 4, 1968, pp 929-952.

[119] Wolfram Research Inc., *Mathematica Version 5.0*, Champaign, IL. 2003.

[120] WOOD, W. L., and LEWIS, R. W., "Comparison of Time Marching Schemes for the Transient Heat Conduction Equation", *International Journal for Numerical Methods in Engineering,* Vol. 9, 1975, pp 679-689.

[121] HUGHES, T. R. J., "Unconditionally Stable Algorithm for Nonlinear Heat Conduction", *Computer Methods in Applied Mechanics and Engineering*, Vol. 10, 1977, pp. 135-139.

[122] PRESS,W. H., TEUKOLSKY, S. A., VETTERLING, W. T., AND FLANNERY, B. P., *Numerical Recipes in C++: The Art of Scientific Computing*, 2nd ed., Cambridge University Press, Cambridge, UK, 2003.

[123] CHAPRA, S. C., and CANALE, R. P., *Numerical Methods for Engineers*, 2nd ed., McGraw-Hill, New York, 1988.

[124] Anon, "Intel Math Kernel Library Reference Manual", document number 630813-027US, September 2007.

[125] YAMADA, Y., ITO, K., YOKOUCHI, Y., TOAMANO, T., OHTSUBO, T. "Finite Element Analysis of Steady Fluid and Metal Flow", Proceedings of the Symposium on Finite Element Methods in Flow Problems, pp 73-94 University College of Swansea, Wales, 1974, Wiley, New York, 1975

[126] HOOD, P. and TAYLOR, C., "Navier-Stokes Equations Using Mixed Interpolation", pp121-132, *Finite Element Methods in Flow Problems*, Proceedings of the International Symposium on Fintie Element Methods in Flow Problems heal at University College of Swansea, Wales, January 1974

[127] OLSON, M. D. and TUANN, S. Y., "Primative Variables versus Stream Function Finite Element Solutions of the Navier-Stokes Equations", Ch. 4 of *Finite Elements in Fluids*, selected papers from the Second International Conference on Finite Elements in Flow Problems held at St. Margherita, Italy, 1976, Wiley, New York 1978, pp73-87.

[128] LYNCH, D. R., and O'NEIL, K., "Elastic Grid Deformation for Moving Boundary Problems in Two Space Dimensions", *Finite Elements in Water Resources III,* Vol. 2, edited by Wang et al., Mississippi University, Oxford, MS, 1980, pp 7.111-7.120.

[129] YE, J., *Laminated Composite Plates and Shells: 3D Modeling,* Springer-Verlag, London, 2003.

[130] KIRK, B., PETERSON, J. W., STOGNER, R. H., and CAREY, G. F., "libMesh: *A C++ Library for Parallel Adaptive Mesh Refinement/Coarsening Simulations"*. Engineering with Computers, vol. 22, no. 3-4, pp. 237-254, 2006.

[131] BALAY, S., BUSCHELMAN, K., GROPP, W. D., KAUSHIK, D., KNEPLEY, M. G., CURFMAN MCINNES, L., SMITH, B. F., AND ZHANG, H., "PETSc Web Page: http://www.mcs.anl.gov/petsc", 2001.

[132] BALAY, S., BUSCHELMAN, K., EIJKHOUT, V., GROPP, W. D., KAUSHIK, D., KNEPLEY, M. G., CURFMAN MCINNES, L., SMITH, B. F., AND ZHANG, H., "PETSc Users Manual", ANL-95/11 – Revision 2.1.5, Argonne National Laboratory, 2004.

[133] BALAY, S., GROPP, W. D., CURFMAN MCINNES, L., AND SMITH, B. F., "Efficient Management of Parallelism in Object Oriented Numerical Software Libraries", *Modern Software Tools in Scientific Computing*, editors Arge, E., Bruaset, A, M., and Langtangen, H. P., pp 163-202, 1997.

[134] THOMPSON, R.T.," DAC-3 Computational Analysis of Beveled Compression Pad Geometries", CEV Aerosciences Project, NASA Langley Research Center, August 2009.

[135] WILLIAMS, A. R., AND KOENIG, J. R., "Rayon Replacement Program Phase IV MX4926N MT Mechanical and Thermal Characterization", SRI-ENG-07-34-9714.09, January 2007.

[136] LADACKI, M., HAMILTON, J.V., and COHZ, S. N., "Heat of Pyrolysis of Resin in Silica-Phenolic Ablator," AIAA Journal, Vol. 4, No. 10, October 1966, pp. 1798-1802.

[137] DEC, J. A., and EMPEY, D., "Heatshield Compression Pads", Subsystem Design Review, Denver, CO, July 2009.

[138] Anon, Tecplot 360 2009, release 2 User's Manual, Tecplot Inc., Bellevue, WA, 2009

[139] DEC, J.A, "Arc Jet Test Failure Analysis", Compression Pad Technical Interchange Meeting, NASA Langley Research Center, October 2008.

[140] SWOKOSKI, E. W., OLINICK, M., PENCE, D., *Calculus*, 6th Ed., PWS Publishing Company, Boston, MA, 1994.